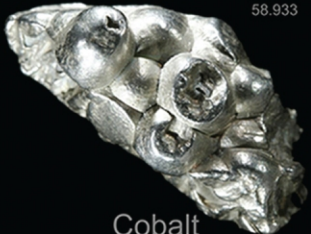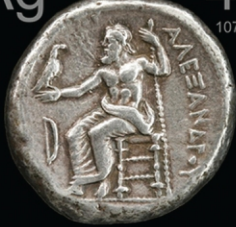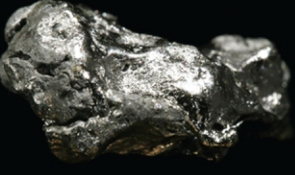# Конденсированные среды и межфазные границы

РЕЦЕНЗИРУЕМЫЙ НАУЧНЫЙ ЖУРНАЛ

Condensed Matter and Interphases

PEER-REVIEWED SCIENTIFIC JOURNAL

Co	27 58.933	Ni	28 58.693	Cu	29 63.546
Cobalt		Nickel		Copper	
Rh	45 102.91	Pd	46 106.42	Ag	47 107.87
Rhodium		Palladium		Silver	
Ir	77 192.22	Pt	78 195.08	Au	79 196.97
Iridium		Platinum		Gold	

Condensed Matter and Interphases
Kondensirovannye sredy i mezhfaznye granitsy

Condensed Matter and Interphases (Kondensirovannye Sredy i Mezhfaznye Granitsy) publishes articles in Russian and English dedicated to key issues of condensed matter and physicochemical processes at interfaces and in volumes.

The mission of the journal is to provide open access to the results of original research (theoretical and experimental) at the intersection of contemporary condensed matter physics and chemistry, material science and nanoindustry, solid state chemistry, inorganic chemistry, and physical chemistry, and to share scientific data in the **following sections**: atomic, electron, and cluster structure of solids, liquids, and interphase boundaries; phase equilibria and defect formation processes; structure and physical and chemical properties of interphases; laser thermochemistry and photostimulated processes on solid surfaces; physics and chemistry of surface, thin films and heterostructures; kinetics and mechanism of formation of film structures; electrophysical processes in interphase boundaries; chemistry of surface phenomena in sorbents; devices and new research methods.

The journal accepts for publication: reviews, original articles, short communications by leading Russian scientists, foreign researchers, lecturers, postgraduate and undergraduate students.

CONTENTS

Review

Selective ion-exchange sorbents for caesium extraction from alkaline radioactive solutions. Review

V. A. Ivanov✉, S. I. Kargov, O. T. Gavlina

*Lomonosov Moscow State University, the Faculty of Chemistry,
GSP-1, building 3, 1 Leninskiye Gory, Moscow 119991, Russian Federation*

Abstract

This review covers studies dedicated to the search for and development of sorbents for the extraction of the caesium-137 radioactive isotope from highly mineralised, highly alkaline solutions that are waste products of nuclear plants. This isotope with a half-life of 30.2 years is one of the most significant contributors to the radioactivity of the waste. It was shown that phenolic sorbents play the key role in caesium extraction from such solutions, they are able to exchange ions on phenolic groups in alkaline solutions, exhibiting high selectivity to caesium against large amounts of sodium and potassium ions. The sorbents make it possible to filter large solution flows, as well as to elute concentrated caesium quantitatively and rapidly with a small volume of acid. We compared the selectivity of sorbents obtained by the condensation of phenol and diatomic phenols with formaldehyde as well as modern materials obtained by the condensation of calixarenes and resorcinarenes with aldehyde. It was shown that the latter do not have any advantage in selectivity and are of lower chemical stability. Therefore, resorcinol-based materials are considered the key element in solving the problem of extracting the caesium-137 isotope from alkaline solutions. We analysed the current state of the problem. This article explains the nature of the high selectivity of phenolic sorbents for caesium ions and why the special arrangement of functional groups of calixarene and resorcinarene resins does not result in increased selectivity as compared with conventional phenol- and resorcinol-based materials.

Keywords: Caesium-137 isotope, Highly mineralised alkaline solutions, Ion exchange, Sorbtion, Selectivity, Resorcinol-formaldehyde resin, Calixarene, Resorcinarene

✉ Vladimir A. Ivanov, e-mail: minilana1954@mail.ru

Condensed Matter and Interphases / Конденсированные среды и межфазные границы   2022;24(3): 287–299

V. A. Ivanov et al.   Selective ion-exchange sorbents for caesium extraction from alkaline radioactive solutions...

1. Introduction

The reviewed authors have a number of publications concerning the properties and applications of sorbents and ion exchangers based on phenol-formaldehyde resins (PFRs). When one of these studies [1] underwent the review phase in an international journal, one of the reviews clearly questioned the relevance and practical value of the study of ion exchange on phenolic groups. The reviewer added that such materials were considered long outdated in the field of ion exchange.

The reviewer's doubt and bemusement are understandable. After all, the whole era of research, production, and widespread use of synthetic organic ion exchange resins began as early as 1935 with the condensation products of phenols with formaldehyde [2]. The PFR was a polymeric matrix onto which ion-exchange groups such as sulphonic acid, carboxylic acid, phosphorus, and amine groups were grafted [3–8]. Sulphonic acid cation exchangers were the most common as they were widely used in the softening and demineralisation of natural water and other solutions. By the mid-50s, such ion-exchange resins were produced in at least 15 countries (including the USSR [3, p. 204]). However, starting with the mid-1940s, they were promptly superseded by more chemically and mechanically stable resins based on styrene-divinylbenzene copolymer.

Nevertheless, the reviewer of [1], following our response to the comment, was surprised to admit that phenol-formaldehyde sorbents were still relevant even in the late 1990s, as they were produced, researched, and used. Since then, another two decades have passed. But even now, studies in this field still attract attention regularly, they are often cited. Therefore, it seems that the long established data on the properties of phenolic sorbents is still relevant for some areas of research, which have become a priority only in recent years.

In this review, the authors pointed out the most significant properties of phenolic sorbents, the issues they helped to solve, and the origin of their most important property, selectivity for caesium ions.

2. Some information on the properties of phenol-formaldehyde adsorbents and ion exchangers, and the problems they solve

In our review we did not cover the above-mentioned group of ion-exchange resins based on the PFRs with grafted acid or base groups, as they were described in a large number of monographs. We focused on the sorbents where the properties of the phenol-formaldehyde matrix and its ion-exchange properties play the key role.

In the 1970s, Diamond Shamrock Chemical Co. [9], a US company, produced the Duolite S-761 sorbent with irregularly shaped grains in the form of splinters resulting from the crushing of PFRs. The sorbent was proposed for the removal of colouring and other organic substances from food processing solutions. Rohm&Haas offered a similar product called Amberlite XAD 761 (previously known as Duolite XAD 761) [10]. These sorbents were synthesised by the condensation of phenol and formaldehyde, they did not have any other ion-exchange groups grafted into their structure other than phenolic groups. However, as the analysis in [11] showed, in addition to phenolic groups, they contained a rather large amount of methylol groups.

In addition, similar PFRs with grafted secondary and tertiary amino groups were produced under Duolite A-568, A-561, and A-7 brands as adsorbents of organic substances from liquid media. There are examples of their use in decolourisation of solutions of glucose and sodium glutamate and purification of citric acid during its extraction from products of enzymatic sugar processing.

PFR-based sorbents were used for these purposes due to a number of their specific properties [10]:

• Better adsorption properties towards substances with large molecules, which is attributed to the fact that their matrix is more hydrophilic compared to the polystyrene matrix and has a porous structure.

• Higher density (1.11 g/cm^3) compared to the polystyrene matrix (1.04 g/cm^3), which makes the adsorption layer more stable, and also gives other advantages for their practical use.

Condensed Matter and Interphases / Конденсированные среды и межфазные границы   2022;24(3): 287–299

V. A. Ivanov et al.   Selective ion-exchange sorbents for caesium extraction from alkaline radioactive solutions...

• Better fluid permeability through the layer of adsorbents and ion exchangers based on the phenol-formaldehyde matrix with irregularly shaped grains (obtained by crushing a polycondensation resin) compared to the layer of the spherical grains of polystyrene ion exchangers.

In the USSR, in the mid-1980s, the technology for the synthesis of macroporous PFRs with spherical granules was developed at the Nizhny Tagil branch of NPO *Plastmasy* [12], and the first batches were produced. In addition to being used as molecular sorbents for organic substances, they were also intended to be used as intermediates for further transformation into activated macroporous carbon with spherical granules. However, the current list of products by the manufacturing plant, which is now called Uralchimplast, does not include such products.

The main feature of the PFR-based sorbents is their high ion-exchange selectivity for caesium and rubidium ions. This property was long ago revealed and studied in sulphonic acid cation-exchangers based on PFRs in neutral and alkaline solutions [13–16]. In the USSR in the 1960s, processes for separating high purity caesium and rubidium compounds from alkali metal mixtures on sulphophenolic cationite [17–20] were developed as part of a state programme.

The PFRs without other types of ionogenic groups besides phenolic ones also exhibit high ion-exchange selectivity for caesium and rubidium ions in alkaline solutions [2–23]. When interacting with an alkaline solution, hydrogen from phenolic groups is substituted by alkali metal cations, and the interchange of metal cations may occur. It is possible to extract Cs^+ and Rb^+ ions from alkali metal mixtures using macroporous PFRs with spherical granules produced by the Nizhny Tagil branch of NPO *Plastmasy* [1, 24]. In the 1980s, as part of the state programme aimed at creating a technology for complex seawater processing with the recovery of valuable minerals, a method for rubidium extraction from seawater concentrates containing a large excess of potassium ions was developed. It was based on using macroporous PFRs [1, 24–26]. Due to the major changes in the former Soviet Union at the turn of the 1980s and 1990s, the programme was discontinued. However, the technologies developed at that time will undoubtedly be in demand in the future, when the use of the ocean's mineral resources will inevitably become a pressing issue.

3. Selective extraction of ^{137}Cs from alkaline waste from nuclear plants

The most significant issue that explains the ongoing attention to phenolic sorbents is the extraction of radioactive caesium during the processing of nuclear waste in many countries. The key challenge is to extract caesium from solutions that are characterised by high salt content (up to 300–350 g/l) and are highly alkaline. For example, there are five large radioactive waste sites in the USA [27], particularly in South Carolina (Savannah River Site) and Washington (Hanford Site), where weapons-grade plutonium was produced. The scale of this issue was outlined in [28]: "In the previous decade, the government spent about $60 billion on abatement measures, most of which, however, resulted only in isolation. At least another $200 billion and 70 years are estimated to be required for remedial measures in more than 100 areas in the United States that have been involved in the national nuclear weapons programme". In 1982, the US Congress passed the Nuclear Waste Policy Act. It launched a major project to develop a technology for processing accumulated radioactive waste into forms safe for long-term storage. A schedule for the construction of an underground facility for permanent storage of high-level radioactive waste was set [29, p. 537]. Since the late 1980s, extensive work was carried out to develop the technology and construct a processing facility for waste stored in the state of Washington [30]. The ultimate goal of the entire process is to compact the radioactive elements in order to reduce their volume, then vitrify them with borosilicate glass, and place them in stainless steel containers, first at the temporary storage facility, and then in a permanent storage facility. Already by 2005, the main stages of the technology had been designed [30] and construction had started [31]. However, there were uncertainties and concerns about the concentration of ^{137}Cs, even after construction had started. Even in 2020, the construction of the processing facilities, including the caesium removal unit, was far from complete [32]. Notably,

Condensed Matter and Interphases / Конденсированные среды и межфазные границы   2022;24(3): 287–299

V. A. Ivanov et al.   Selective ion-exchange sorbents for caesium extraction from alkaline radioactive solutions…

the US Government Accountability Office noted a steady increase in the cost of the project.

The ^{137}Cs and ^{90}Sr isotopes, which are β-emitters with half-lives of 30.2 years and 28.8 years, are major contributors to the radioactivity of the waste, and they also account for 95% of the heat release during waste storage. When radioactive waste is processed in the form of liquid solutions, these isotopes must be removed at the very beginning of the process, which turns out to be the most difficult challenge. This is why the separation of ^{137}Cs is called the bottleneck of the whole process. First, there are huge volumes of solutions from which ^{137}Cs has to be concentrated. Furthermore, the solutions have very high concentrations of alkali and sodium, reaching respectively ~1.7 M and 5.0 M (Table 1). It has also been noted that the composition of the solutions in different storage tanks may vary.

Table 1. Main components of the solution kept at the Hanford site in Washington before the extraction of radioactive caesium [33]

Ion	Concentration, mol/l	Ion	Concentration, mol/l
Na$^+$	4.99	OH$^-$	1.68
K$^+$	0.12	Al(OH)$_4^-$	1.72
Cs$^+$	$5.0 \cdot 10^{-4}$	NO$_3^-$	1.67
Rb$^+$	$5.0 \cdot 10^{-5}$	NO$_2^-$	0.43
		CO$_3^{2-}$	0.23
		SO$_4^{2-}$	0.15
		F$^-$	0.09

A large number of alternative materials for caesium extraction have been considered, including the most advanced ones (phenol-based extractants, crown ethers, calyxarenes, and inorganic sorbents and ion exchangers, etc.). Nevertheless, a key role in caesium extraction has been assigned to phenolic sorbents, which exhibit high ion-exchange selectivity for caesium against large excess of sodium and potassium ions. They also make it possible to filter large flow of solution and to elute concentrated caesium quantitatively and rapidly with a small volume of acid [34–36].

The use of the Duolite CS-100 ion exchanger was considered. It is a product of condensation of resorcylic acid with formaldehyde (besides two hydroxyl groups as substituents, the benzene ring also contains a carboxyl group). Its ability to sorb ^{137}Cs from low-activity solutions has been known since the 1960s. But the focus was on the resorcinol-formaldehyde sorbent (RFS), synthesised similarly to the PFRs, which turned out to be more selective and capacious. (It should be noted that obtaining of RFS was mentioned as early as in [2], 1935.) The technology for obtaining of sorbents with irregularly shaped grains was developed, it was implemented by Boulder Scientific Co, a US company [38–41].

Unfortunately, RFS, like all phenolic sorbents, has low chemical stability in alkaline media in the presence of oxygen dissolved in solutions and allows a relatively small number of sorption-desorption cycles [40]. (Our publication [42] was devoted to the issue of chemical stability of phenolic sorbents. It was shown that methylol groups were oxidised in alkaline media with formation of carboxylic groups and gradual destruction of the grains). Therefore, the US project further attempted to overcome this disadvantage. Sinvent A/S, a company from Norway, developed a method for introducing RFS into polystyrene-type spherical granules [43]. This method is based on the technology for obtaining low cross-linked monodisperse spherical styrene-divinylbenzene copolymer granules (0.1 wt. %), developed earlier by one of the authors of the method. The granules are hydrophilised by the introduction of sulpho groups or quaternary ammonium bases. To obtain the sorbent, water and reagents for the synthesis of RFS are added to a certain amount of dried monodisperse polystyrene granules. Once the granules have swollen substantially and the reagents are introduced, a polycondensation reaction is carried out. However, no details were disclosed regarding the type of granules used in the production of the sorbent for further testing in the extraction of radioactive caesium.

The possibility of producing sorbents with phenolic groups by condensation of calixarenes and resorcinarenes with formaldehyde or other aldehyde was also considered as a possible solution to the issue. Calixarenes and resorcinarenes, known since the 1940s [44–46], are products of cyclic oligomerisation of phenols with formaldehyde. Their molecules can be formed by different numbers of phenolic or resorcinol nuclei, for example, as shown in Figure 1.

Condensed Matter and Interphases / Конденсированные среды и межфазные границы 2022;24(3): 287–299

V. A. Ivanov et al. Selective ion-exchange sorbents for caesium extraction from alkaline radioactive solutions...

Interest in compounds of this type increased dramatically in the 1970s and 1980s. This was caused by an overall burst of activity in the new field of supramolecular chemistry. It was expected that they, as well as other "highly organised" compounds (crown ethers, cavitands, and spherands) would provide significantly higher selectivity for complexation with metal ions and bring separation technologies to a much higher level. It was taken into account that calixarene adopts a specific conformation so that the aromatic rings and alkyl substituents such as tert-butyl, as shown in Figure 2, form the central ring rim and the upper rim, while the hydroxy substituents are located in the lower part of the macrocycle. Such a structure is sometimes called a "basketball hoop", its characteristic parameters are expected to ensure high ionic selectivity.

In the early 1980s, it was found in [47, 48] that during the diffusion transfer of alkali metal hydroxides through a liquid membrane containing various calixarenes, it shows high selectivity for Rb+ and Cs+ ions versus other alkali metal ions (the experiment is shown schematically in Fig. 3). In these experiments, a solution of calixarene in an organic solvent was placed between a solution of alkali metal hydroxides and pure water. The diffusion transfer of alkali metal hydroxides into water gradually occurred. The caesium hydroxide output was 20 times that of rubidium and 50 times that of sodium. The p-tert-butyl- and p-tert-pentylcalix[4]arenes were observed to have the highest selectivity.

However, the use of calixarenes directly in such experiments or in conventional extraction techniques is complicated by many drawbacks.

Fig. 1. Structure of calyx[4]arene (a), calyx[6]arene (b), and calyx[8]arene (c) (R – alkyl substituents)
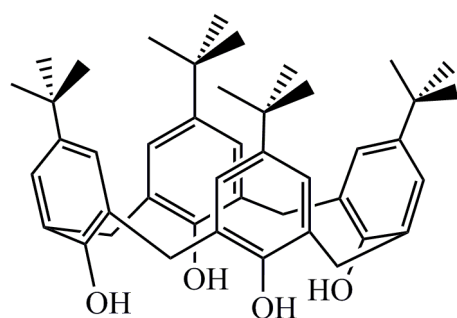
Fig. 2. The "basketball hoop" conformation of tert-butylcalix[4]arene

0.25 M CsOH + 0.25 M RbOH + 0.25 M KOH + 0.25 M NaOH solution in water

Water

Liquid membrane: of p-tert-butylcalix[4]arene solution in chloroform
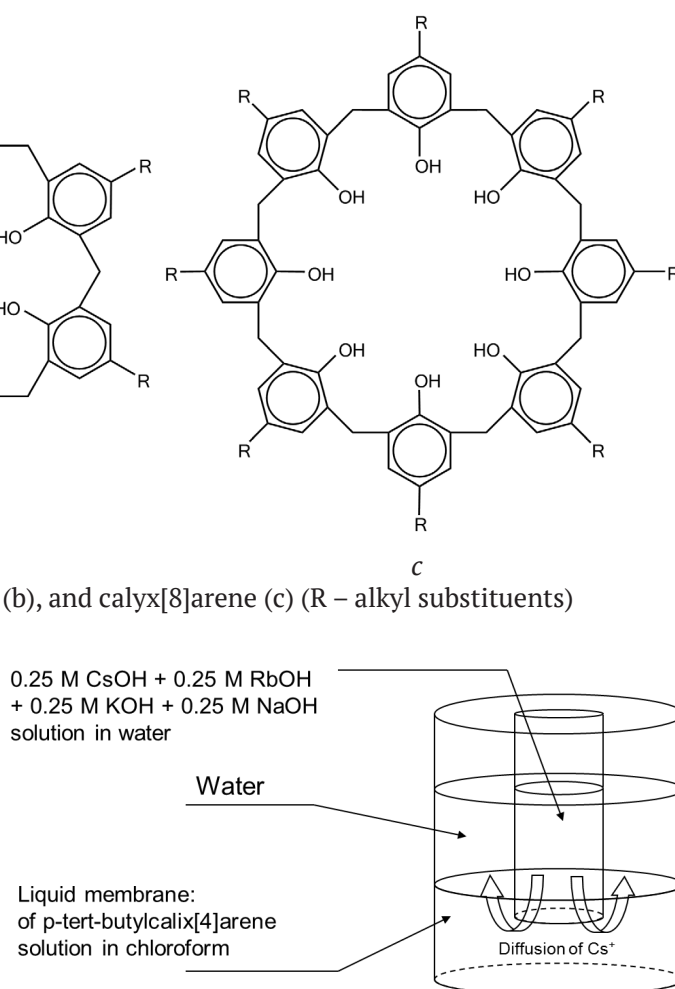
Diffusion of Cs+

Fig. 3. Schematic of a diffusion transfer experiment in a liquid membrane cell

Condensed Matter and Interphases / Конденсированные среды и межфазные границы   2022;24(3): 287–299

V. A. Ivanov et al.   Selective ion-exchange sorbents for caesium extraction from alkaline radioactive solutions...

Among them are the need to use hydrophobic solvents, the formation of emulsions, and solvent losses when using aqueous solutions. The most important disadvantage is a very low rate of diffusion of the extracted ions from one phase to another, etc. Subsequently, IBC Advanced Technologies, Inc. founded by the authors of works [47, 48] and specialising in obtaining and promoting macrocyclic reagents and technologies involving them, developed a method for obtaining sorbents with calixarene groups [49]. The patents describe the condensation of calyx[6]arene, calyx[8]arene, or propylresorcin[4]arene with phenol or resorcinol and formaldehyde in the presence of NaOH. The resulting resin is then crushed into fragments. From the information available in the open sources, it is not possible to say for sure, which of the materials under the trade mark SuperLig 644 obtained using this technology were chosen for further testing

in order to develop the technology for ^{137}Cs extraction from radioactive waste in Hanford (Washington State, USA) [33, 50–54].

The scheme of the caesium extraction by sorption includes: 1) filtration of the treated alkaline solution through a column filled with one of the ion-exchange materials mentioned above until the breakthrough of caesium, and 2) subsequent elution of caesium from the ion-exchanger with 0.5 M of nitric acid. Fig. 4 shows examples of the output curves of radioactive caesium sorption on the SuperLig 644 ion exchanger, and its elution with nitric acid from [27]. The two output curves in the upper figure represent two slightly different compositions of the initial solution, in particular, the sodium content was 5.0 M in one solution and 5.7 M in the other.

In experimental studies, SuperLig 644 showed no significant advantage in the volume of the
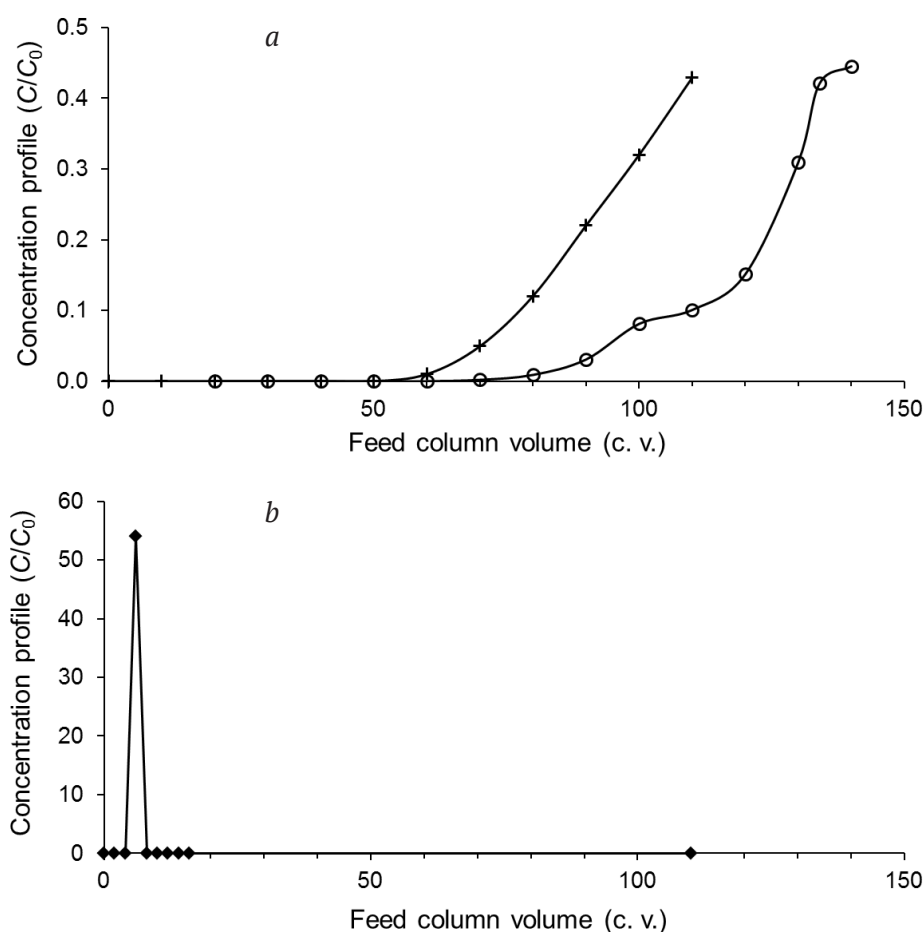
Fig. 4. Output curves of radioactive caesium sorption using the SuperLig 644 ion exchanger (a) and its elution with nitric acid (b) [27]

Condensed Matter and Interphases / Конденсированные среды и межфазные границы 2022;24(3): 287–299

V. A. Ivanov et al. Selective ion-exchange sorbents for caesium extraction from alkaline radioactive solutions...

treated solution (and hence selectivity) and in quality of acid elution (it was possible to achieve approximately 100-fold concentration of radioactive caesium) compared to the RFS. SuperLig 644 proved to be the least chemically stable sorbent, capable of withstanding only 5 or 6 sorption-desorption cycles. Upon reaching the limit, the used material has to be replaced and disposed of (it must be treated as a radioactive material). Moreover, SuperLig 644 turned out to be the most sensitive to temperature. At 45 °C, it almost lost its capacity for ^{137}Cs, while the conventional RFS retained its sorption capacity [51]. Another important consideration when selecting materials is that the SuperLig 644 ion exchanger is also the most expensive. Therefore, the RFS was considered a better option among these two materials, as it is more chemically stable.

In Russia, radioactive caesium in waste from nuclear facilities is mainly contained in nitric acid solutions. Highly selective ferrocyanide sorbents and corresponding technologies have been developed and successfully used for its extraction for a long time [55]. But there is a problem with caesium extraction from high salt alkaline boiler residues from evaporators at nuclear power plants, as their salt content reaches 300–350 g/l and their pH > 13 [56]. Ferrocyanide sorbents, like most inorganic sorbents, are unstable in such alkaline solutions. So, for the extraction of ^{137}Cs, Axion-RNM (from Perm) developed a technology and produced pilot batches of AXIONIT RCs-pk sorbents with granules obtained by crushing RFS and AXIONIT RCs-gran sorbents based on RFSs impregnated in spherical sulphonated polystyrene granules [56, 57]. During tests with solutions simulating high salt alkaline boiler residues from nuclear power plants evaporators, the sorbents showed high selectivity for caesium as well as good chemical and hydromechanical stability in alkaline media.

In Russia, the methods for the production of resorcinarene sorbents have also been developed. In particular, C-phenylcalix[4]resorcinarene (Fig. 5) is obtained by the condensation of resorcinol with benzaldehyde. It is used to produce a polymer in the form of spherical granules by catalytic resol polycondensation with formaldehyde, taken in the ratio of 1 : 3 [58].
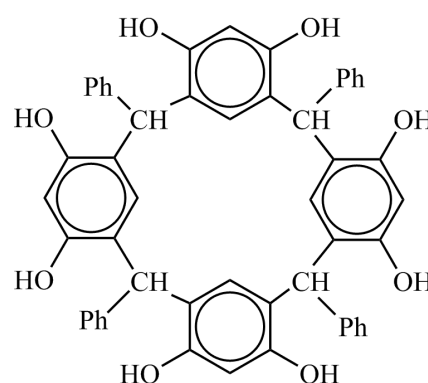
Fig. 5. Structure of C-phenylcalix[4]resorcinarene

In our article [59], we studied the selectivity of Cs$^+$–Rb$^+$ ion exchange (1 : 1) from 0.1 M of alkaline solutions using the RFS and a sorbent based on C-phenylcalix[4]resorcinarene. The results were compared with the data for the PFR-based sorbent. It turned out that this sorbent showed no advantage over PFR and even exhibited a slightly lower selectivity.

Thus, sorbents based on phenol, resorcinol, calixarenes, and resorcinarenes show high selectivity to caesium ion (and also rubidium) compared with other alkali metal ions. Particularly remarkable is the fact that the sorbents based on calixarenes and resorcinarenes did not exhibit the advantage over other materials of the group. Although we expected them to perform better, given the expectations which are usually associated with the use of macrocyclic reagents in the field of separation of substances. Therefore, the issue of explaining of such results remains urgent.

4. The origin of the ion-exchange selectivity of phenol-type sorbents for caesium ions

Previously [14, 60, pp. 65-88], the high selectivity for caesium and rubidium ions was explained by the fact that phenols or phenolic groups can form complexes with large caesium and rubidium ions. However, some researchers believe that this mechanism cannot explain the increased selectivity (61).

The features of the formation and structure of such complexes were studied using quantum chemistry methods. For instance, we used the density functional method in our study [62]. The calculations showed no particular binding

Condensed Matter and Interphases / Конденсированные среды и межфазные границы   2022;24(3): 287–299

V. A. Ivanov et al.   Selective ion-exchange sorbents for caesium extraction from alkaline radioactive solutions...

ability of caesium and rubidium ions to phenolate ions compared to other alkali metal ions. On the contrary, water molecules compete with the phenolate anion for binding to all alkali metal cations. Only three water molecules are enough to displace the phenolate anion into the second coordination sphere of any alkali metal ion. If more water molecules are added, the phenolate anion is always in the second coordination sphere (Fig. 6). The binding energy of $(CH_3)_2PhO^-$ with the $Me^+(H_2O)_n$ hydrated cation decreases irrespective of n, the number of water molecules in the aqua complex. It decreases in the same order as the hydration energy, i.e., $Li^+ > Na^+ > K^+ > Rb^+ > Cs^+$.

The calculations also showed that the calyx[4]arene anion, obtained by the removal of one hydrogen atom from one of the four OH-groups, also has no specific selectivity for caesium and rubidium ions in the absence of water molecules [59]. In this case, the energy of the cation binding to the calyx[4]arene anion also decreases under the sequence of $Li^+ > Na^+ > K^+ >$
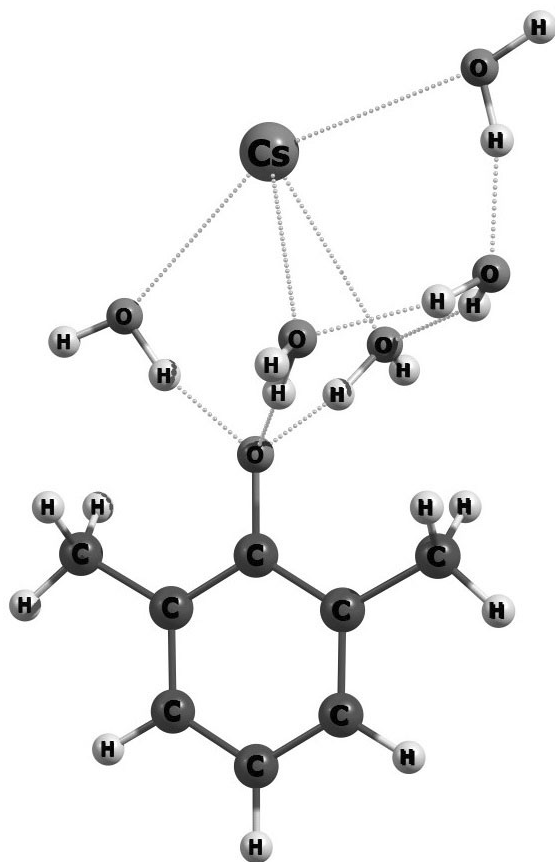
Fig. 6. Structure of the aqua complex of the $Cs^+(H_2O)_5$ ion with the 2,6-dimethyl-phenolate anion

$Rb^+ > Cs^+$. The numerical values of the energy of binding to the calix[4]arene anion are also close to the corresponding values for binding to the phenolate anion (even slightly lower than them). It should also be noted that the caesium ion in the optimised structure of the complex is positioned far away from the oxygen "crown", whereas the lithium ion is positioned almost in the plane of the crown. Thus, the modelling demonstrated that the special order of the functional groups of the calixarene and resorcinarene resins cannot cause an increase in selectivity for caesium ion compared to conventional PFRs and RFSs.

On our initiative, our colleagues in studies [63, 64] carried out molecular modelling of the interaction of alkali metal cations with the calyx[4]arene anion in the presence of 291 water molecules using the molecular dynamics method. The calculations showed that in the presence of water molecules the binding of Rb^+ and Cs^+ cations to the calyx[4]arene anion is much greater than that of Li^+, Na^+, and K^+ cations. The authors attributed this to the fact that smaller cations with a lower coordination number exhibit greater disruption of the hydrate shell when they bind to the calix[4]arene anion.

Thus, the selectivity for caesium and rubidium ions during ion exchange on all phenolic ion exchangers is due to other features.

Usually, during the ion-exchange process, the transfer of ions from an external solution into the ion-exchanger, which is a concentrated polyelectrolyte solution, is accompanied by their considerable dehydration. When an alkali metal ion is transferred from an external solution into the sorbent, its complex with the anion is broken. The ion undergoes partial dehydration with subsequent binding to phenolic groups:

$$Me_2^+(H_2O)_n \cdot Cl^- \xrightarrow{-mH_2O,\ -Cl^-}$$
$$\rightarrow Me_2^+(H_2O)_{n-m} \xrightarrow{+PhO^-} Me_2^+(H_2O)_{n-m} \cdot PhO^-. \tag{1}$$
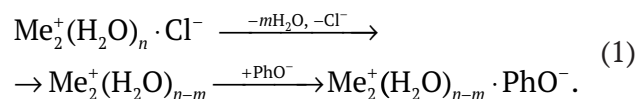
At the same time, the smaller ion 1, which was originally in the ion exchanger, is transferred in the opposite direction:

$$Me_1^+(H_2O)_n \cdot Cl^- \xleftarrow{+mH_2O,\ +Cl^-}$$
$$\leftarrow Me_1^+(H_2O)_{n-m} \xleftarrow{-PhO^-} Me_1^+(H_2O)_{n-m} \cdot PhO^-. \tag{2}$$
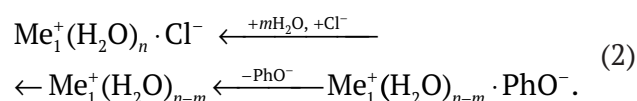
If we assume that the structures of similar complexes of the M_1^+ and M_1^+ и M_2^+ alkali metal

Condensed Matter and Interphases / Конденсированные среды и межфазные границы   2022;24(3): 287–299

V. A. Ivanov et al.   Selective ion-exchange sorbents for caesium extraction from alkaline radioactive solutions…

ions are the same (although this is not necessarily true), then the entropic component of the ion exchange reaction can be neglected. Thus, the Gibbs energy of the ion exchange reaction is determined by the hydration energies of ions and the energies of their interaction with fixed groups in the PFRs and with anions in the solution:

$$\Delta G = (\bar{E}_{\text{binding,Me}_2} - \bar{E}_{\text{binding,Me}_1}) - (E_{\text{binding,Me}_2} - E_{\text{binding,Me}_1}). \tag{3}$$

The first difference reflects the difference in binding energies of the ions (dehydrated) exchanged with the phenolate ions in the ion exchanger. The second reflects the difference in binding energies of the ions exchanged with water and the anion in the external solution. As shown by the calculations from [62], these two differences are positive and quite close. The selectivity in the ion-exchange system is determined by the delicate balance between them. Since the value of ∆G is determined simultaneously by four large values of the formation energies of the different complexes, it cannot be expected that quantum chemistry calculations can quantitatively predict selectivity in an ion-exchange system. However, expression (3) evidently shows that formation of aqua complexes of alkali metal ions in a solution contributes to a decrease in selectivity of smaller ions in comparison with larger ions in terms of binding to phenolic groups.

Thus, the only explanation for the selectivity of PFRs and other phenolic compounds for caesium and rubidium ions is the dominance of the ion dehydration stage during the transition from aqueous solution to the phenolic phase rather than the stage of binding to the ion-exchange groups. The phenolic ion exchangers have greater selectivity for caesium and rubidium ions than polystyrene-type sulphonic acid cation exchangers due to the fact that the former can bind much less water, and the ions in them are much more dehydrated. This is especially true for ion exchange on phenolic ion exchangers, which differ from other ion exchange resins and polyelectrolytes by considerably lower amounts of bound water (this can be seen, for example, from our data in [11]).

This conclusion is consistent with the explanation of the emergence of selectivity for the potassium ion in the ion channels of a biological cell. It says when the ion binds in the narrowest part of the channel, called the ion filter, it is also in a partially or completely dehydrated state [65]. The mechanisms of the emergence of selectivity of the ion channel and phenolic sorbents seem to be similar. The data [11] indicate a greater differentiation of water in phenol-formaldehyde sorbents in terms of its binding energy as compared to polystyrene sulphocationites. In general, the amount of water in such sorbents is quite large and comparable with the amount of water in polystyrene sulphocationites. However, the amount of strongly bound water is several times less. This seems to indicate that weakly bound "free" water is located in large pores, and relatively small amounts of water strongly bound to exchange groups can be located in narrow pores, which are similar to the ion channels in cells.

This conclusion about the mechanism of ion selectivity also coincides with the conclusion obtained in [66, 67]. The studies analysed the reasons for the preferential binding of potassium ion to guanine complexes and complexes with 18-crown-6-ether compared to sodium ions.

5. Conclusions

The sorbent obtained by condensation of resorcinol with formaldehyde plays the key role in caesium extraction from highly mineralised alkaline radioactive solutions. The sorbent of this type is capable of exchanging ions on phenolic groups in alkaline solutions, while exhibiting high selectivity for caesium against large excesses of sodium and potassium ions. It also makes it possible to filter large flows of solution and to elute concentrated caesium quantitatively and quickly with a small volume of acid. We compared the ion selectivity of sorbents obtained by condensation of phenol and diatomic phenols with formaldehyde and of modern materials obtained by condensation of calixarenes and resorcinarenes with aldehydes. The study showed that the latter had no advantage in selectivity and had a lower chemical stability.

Author contributions

All authors made an equivalent contribution to the preparation of the publication.

Condensed Matter and Interphases / Конденсированные среды и межфазные границы   2022;24(3): 287–299

V. A. Ivanov et al.   Selective ion-exchange sorbents for caesium extraction from alkaline radioactive solutions...

Conflict of interests

The authors declare that they have no conflict of interest.

References

1. Gorshkov V. I., Ivanov V. A., Staina I. V. Selectivity of phenol-formaldehyde resins and separation of rare alkali metals. *Reactive and Functional Polymers*. 1998;38(2–3): 157–176. https://doi.org/10.1016/S1381-5148(97)00165-X

2. Adams B. A., Holmes E. L. Adsorptive properties of synthetic resins. *Journal of the Society of Chemical Industry*. 1935;54(2): 1T–6T. https://doi.org/10.1002/jctb.5000540214

3. Saldadze K. M., Pashkov A. B. Titov V. S. Ion-exchange macromolecular compounds. Moscow: Goshimizdat Publ.; 1960. 356 p. (In Russ.)

4. Helfferich F. G. *Ion Exchange*. New York: McGraw-Hill; 1962. 624 p.

5. Helfferich F. G. Ion exchange: past, present, and future. In: *Ion exchange: science and technology*. Rodrigues A. E. (ed.). NATO ASI Series, vol. 107. Springer: Dordrecht; 1986. pp. 23–32. https://doi.org/10.1007/978-94-009-4376-6_2

6. Dorfner K. Introduction to ion exchange and ion exchangers. In: *Ion Exchangers*. Dorfner K. (ed.). Berlin, New York: De Gruyter; 2011. pp. 7–188. https://doi.org/10.1515/9783110862430.7

7. Ivanov V. A., Gorshkov V. I., Gavlina O. T., Obrezkova M. V. Phenolic ion exchangers. An outstanding role in the development of ion-exchange chromatography and amazing properties. *Sorptsionnye i khromatograficheskie protsessy*. 2003;3(4): 375–391. (In Russ.). Available at: https://www.elibrary.ru/item.asp?id=18201451

8. Ivanov V. A., Gorshkov V. I. 70 years of the history of the production of ion-exchange resins. *Sorptsionnye i khromatograficheskie protsessy*. 2006;6(1): 5–31. (In Russ.). Available at: https://www.elibrary.ru/item.asp?id=12051620

9. Abrams I. M. Macroporous condensate resins as adsorbents. *Product R&D*. 1975;14(2): 108–112. https://doi.org/10.1021/i360054a011

10. Bellamy S. A., Zaganiaris E. Dusting off the phenolic resins. In: *Ion exchange developments and applications: proceedings of IEX '96*. Greig J. A. (ed.). Cambridge: Royal Society of Chemistry; 1996. pp. 274–281.

11. Shelkovnikova L. A., Gavlina O. T., Vitkina D. E., Shkol'nikov E. I., Ivanov V. A. Acid-base properties of phenol formaldehyde sorbents. *Russian Journal of Physical Chemistry A*. 2012;86(5): 825–831. https://doi.org/10.1134/s0036024412050329

12. Vakulenko V. A., Smirnov Yu. A., Kurochkina R. N. Method for obtaining an ion-exchange sorbent. RF patent 2015996 C1. Publ. 07.15.1994. (In Russ.). Available at: https://www.freepatent.ru/patents/2015996

13. Kuznetsov I. A., Kustova L. V., Gorshkov V. I., Panchenkov G. M. Equilibrium of exchange of alkali metal cations on cation exchangers KU-1 and KU-2. *Moscow University Chemistry Bulletin*. 1963;2: 3–10. (In Russ.)

14. Gorshkov V. I., Korolev Yu. Z. Selectivity of sulfo- and sulfophenolic cations with respect to alkali metal ions. *Moscow University Chemistry Bulletin*. 1966;1: 16–20. (In Russ.)

15. Gorshkov V. I., Ivanova M. V., Ivanov V. A. Some features of the exchange of alkali metal cations on sulfophenol cation exchanger *Russian Journal of Physical Chemistry A*. 1977;51(8): 2084-2086. (In Russ.)

16. Gorshkov V. I., Ivanov V. A. Selectivity of sulfophenol cation exchanger KU-1 to alkali metal ions during exchange from alkaline and neutral solutions. *Russian Journal of Physical Chemistry A*. 1979;53(10): 2630–2632. (In Russ.)

17. Gorshkov V. I., Kuznetsov I. A., Panchenkov G. M., Kustova L. V. On the possibility of countercurrent ion-exchange separation of rubidium and cesium. *Russian Journal of Inorganic Chemistry*. 1963;8(12): 2795–2799. (In Russ.)

18. Gorshkov V. I., Panchenkov G. M., Savenkova N. P., Savostyanova S. U. Continuous countercurrent ion-exchange method for the separation of rubidium and cesium on the KU-1 cation exchanger. *Russian Journal of Inorganic Chemistry*. 1963;8(12): 2800–2805. (In Russ.)

19. Gorshkov V. I., Panchenkov G. M., Gulyaeva G. M., Dmitriev S. N., Savenkova N. P., Medvedev G. A. Continuous countercurrent ion-exchange method for the separation of rare alkali metals. In: *Rare alkaline elements: collection of reports of the II All-Union Conference on rare alkaline elements, October 13–16, 1964* / V. E. Plushev (ed.). Novosibirsk: Nauka Publ.; 1967. p. 287–295. (In Russ.). Available at: https://www.studmed.ru/plyuschev-v-i-otv-red-redkie-schelochnye-elementy-sbornik-dokladov-ii-vsesoyuznogo-soveschaniya-po-redkim-schelochnym-elementam-1964-_47f6b69e170.html

20. Gorshkov V. I., Panchenkov G. M., Chumakov V. A. Continuous countercurrent ion-exchange method for the separation of rubidium and potassium. *Russian Journal of Physical Chemistry A*. 1964;38(5): 1358–1361. (In Russ.)

21. Gorshkov V. I., Sverdlov N. Sh. Ion exchange on phenol ionites. I. The equilibrium of the exchange of alkali metal ions. *Russian Journal of Physical Chemistry A*. 1975;49(10): 2724. (In Russ.)

22. Ivanov V. A., Gorshkov V. I., Staina I. V., Vakulenko V. A., Tarasov V. N. Ion exchange on phenolic ionites. III. The equilibrium of the exchange

Condensed Matter and Interphases / Конденсированные среды и межфазные границы   2022;24(3): 287–299

V. A. Ivanov et al.   Selective ion-exchange sorbents for caesium extraction from alkaline radioactive solutions...

of alkali metal ions. *Russian Journal of Physical Chemistry A.* 1991;65(8): 2184–2188. (In Russ.)

23. Shelkovnikova L. A., Gavlina O. T., Ivanov V. A., Gorshkov V. I. The influence of temperature on the ion exchange properties of phenolformaldehyde sorbents. *Russian Journal of Physical Chemistry A.* 2009;83(12): 2122–2126. https://doi.org/10.1134/s0036024409120218

24. Gorshkov V. I., Ivanov V. A., Staina I. V. Method for extracting cesium and/or rubidium from mixtures of alkaline elements. Auth. certificate USSR No. 1781313, prior 08/20/90. Bull. No. 46, 1992. (In Russ.). Available at: https://patenton.ru/patent/SU1781313A1

25. Gorshkov V. I., Ivanov V. A., Staina I. V. Purification of rare alkali metal compounds using phenolic ion exchangers. *High-purity Substances.* 1995;6: 86–93. (In Russ.)

26. Khamizov R., Muraviev D. N., Warshawsky A. Recovery of valuable minerals from seawater by ion exchange and sorption methods. In: *Ion exchange and solvent extraction: a series of advances.* Marinsky J. A., Marcus Y. (eds.). Boca Raton: CRC Press; 1995. pp. 93–148. https://doi.org/10.1201/9781003208846-3

27. Izatt S. R., Bruening R. L., Krakowiak K. E., Izatt R. M. The selective separation of anions and cations in nuclear waste using commercially available molecular recognition technology (MRT) products. In: *Waste Management '03, Proc. Int. Conf., Tucson, AZ (USA), February 23–27, 2003.* pp. 1–11. https://www.researchgate.net/publication/255274313

28. Johnson J. Course change for DOE cleanups? *Chemical & Engineering News Archive.* 2002;80(12): 33–35. https://doi.org/10.1021/cen-v080n012.p033

29. Girard J. *Principles of environmental chemistry.* Sudbury, MA: Jones and Bartlett Publishers; 2005. 677 p.

30. Comprehensive review of the hanford waste treatment plant flowsheet and throughput. Assessment conducted by an independent team of external experts. Chartered by the hanford waste treatment and immobilization plant project at the direction of the US department of energy Ooffice of environmental management Washington, DC 20585. March 2005. Available at: http://www.em.doe.gov/Pages/ExternalTechReviews.aspx

31. Hamel W. F., Duncan G. M. The waste treatment plant, a work in progress. In: *WM'06 Conference, February 26 – March 2, 2006, Tucson, AZ.* Available at: http://archive.wmsym.org/2006/pdfs/6352.pdf

32. GAO-20-363. Report to Congressional Committees. Hanford waste treatment plan. May 2020. Режим доступа: https://www.gao.gov/assets/gao-20-363.pdf GAO-20-363. Report to Congressional Committees. Hanford waste treatment plan. May 2020. Available at: https://www.gao.gov/assets/gao-20-363.pdf

33. Ernest M. V., Bibler J. P., Whitley R. D., Wang N.-H. L. Development of a carousel ion-exchange process for removal of cesium-137 from alkaline nuclear waste. *Industrial & Engineering Chemistry Research.* 1997;36(7): 2775–2788. https://doi.org/10.1021/ie960729+

34. Collins J. L, Egan B. Z., Anderson K. K., Chase C. W., Mrochek J. E., Bell J. T., Jernigan G. E. *Evaluation of selected ion exchangers for the removal of cesium from MVST W-25 supernate.* ORNL/TM-12938. Oak Ridge National Laboratory. 1995. Available at: https://digital.library.unt.edu/ark:/67531/metadc793495

35. Brooks K. P., Kim A. Y., Kurath D. E. *Assessment of commercially available ion exchange materials for cesium removal from highly alkaline wastes.* PNNL-11121. Pacific Northwest National Laboratory. 1996. Available at: https://digital.library.unt.edu/ark:/67531/metadc668523

36. Hubler T. L., Franz J. A., Shaw W. J., Hogan M. O., Hallen R. T., Brown G. N., Linehan J. C. *Structure/function studies of resorcinol-formaldehyde (R-F) and phenol-formaldehyde (P-F) copolymer ion exchange resins.* PNNL-11347; Pacific Northwest National Laboratory. 1996. Available at: https://digital.library.unt.edu/ark:/67531/metadc685381

37. Roberts J. T., Holcomb R. R. *A phenolic resin ion exchange process for decontaminating low-radioactivity-level process water wastes.* ORNL-3036. Oak Ridge National Laboratory. 1961. Available at: https://books.google.ru/books?id=gfZEgZZ404c C&pg=PP1

38. Bibler J. P., Wallace R. M., Bray L. A. Testing a new cesium-specific ion exchange resin for decontamination of alkaline high-activity waste. In: *Waste Management '90, Proc. Int. Conf., Tucson, AZ (USA), February 25 – March 1, 1990.* Available at: https://digital.library.unt.edu/ark:/67531/metadc1319943

39. Favre-Réguillon A., Dunjic B., Lemaire M., Chomel R. Synthesis and evaluation of resorcinol-based ion-exchange resins for the selective removal of cesium. *Solvent Extraction and Ion Exchange.* 2001;19(1): 181–191. https://doi.org/10.1081/SEI-100001382

40. Pratt L. M., Szostak R., Khan I. M., Bibler J. Alkaline degradation of resorcinol-formaldehyde resins: solid-state NMR, thermal adsorption and desorption analysis, and molecular modeling. *Journal of Macromolecular Science, Part A.* 1997;34(2): 281–289. https://doi.org/10.1080/10601329708014955

41. Crawford C. L., Bibler N. E., Bibler J. P. An investigation of the radiolytic stability of a resorcinol-formaldehyde ion exchange resin. In: *Waste Management '94, Proc. Int. Conf., Tucson, AZ (USA), February 27 – March 3, 1994.* Available at: https://digital.library.unt.edu/ark:/67531/metadc1313751

Condensed Matter and Interphases / Конденсированные среды и межфазные границы   2022;24(3): 287–299

V. A. Ivanov et al.   Selective ion-exchange sorbents for caesium extraction from alkaline radioactive solutions...

42. Shelkovnikova L. A., Gavlina O. T., Ivanov V. A. Stability of phenol-formaldehyde ion-exchange sorbents in aqueous solutions. *Russian Journal of Physical Chemistry A.* 2011;85(9): 1652–1659.

43. Berge A., Nilsen T.-N., Bjorgun J.-O., Ugelstad J. *Process for preparing a dispersion and for preparing polymer particles*. US Patent 5,677,373. Oct 14. 1997.

44. Niederl J. B., Vogel H. J. Aldehyde-resorcinol condensations. *Journal of the American Chemical Society*. 1940;62(9): 2512–2514. https://doi.org/10.1021/ja01866a067

45. Zinke A., Ziegler E., Zur Kenntnis des Härtungsprozesses von Phenol-Formaldehyd-Harzen, VII. Mitteilung. *Berichte der deutschen chemischen Gesellschaft* (*A and B Series*). 1941;74(11): 1729–1736. https://doi.org/10.1002/cber.19410741102

46. Zinke A., Ziegler E. Zur Kenntnis des Härtungsprozesses von Phenol-Formaldehyd-Harzen, X. Mitteilung. *Berichte der deutschen chemischen Gesellschaft* (*A and B Series*). 1944;77(3-4): 264–272. https://doi.org/10.1002/cber.19440770322

47. Izatt R. M., Lamb J. D., Hawkins R. T., Brown P. R., Izatt S. R., Christensen J. J. Selective M⁺–H⁺ coupled transport of cations through a liquid membrane by macrocyclic calixarene ligands. *Journal of the American Chemical Society*. 1983;105(7): 1782–1785. https://doi.org/10.1021/ja00345a016

48. Izatt S. R., Hawkins R. T., Christensen J. J., Izatt R. M. Cation transport from multiple alkali cation mixtures using a liquid membrane system containing a series of calixarene carriers. *Journal of the American Chemical Society*. 1985;107(1): 63–66. https://doi.org/10.1021/ja00287a012

49. Tarbet B. J., Maas G., Krakowiak K. E., Bruening R. L. *Process for separating cesium from industrial streams containing other alkali metals using poly(hydroxyarylene) polymeric resins*. US Patent No 788526. Issued August 1998 and US Patent No 5,789,496. August 4, 1998.

50. Hassan N. M., Adu-Wusu K. Cesium removal from Hanford tank waste solution using resorcinol-formaldehyde resin. *Solvent Extraction and Ion Exchange*. 2005;23(3): 375–389. https://doi.org/10.1081/SEI-200056519

51. Burgeson I. E., Deschane J. R., Cook B. J., Blanchard Jr. D. L., Weier D. L. Evaluation of elution parameters for cesium ion exchange resins. *Separation Science and Technology*. 2006;41(11): 2373–2390. https://doi.org/10.1080/01496390600744423

52. Fiskum S. K., Blanchard D. L., Steele M. J., Thomas K. K., Trang-Le T., Thorson M. R. Spherical resorcinol-formaldehyde resin testing for cesium removal from Hanford tank waste simulant. *Separation Science and Technology*. 2006;41(11): 2461–2474. https://doi.org/10.1080/01496390600742740

53. Fiskum S. K., Arm S. T., Steele M. J., Thorson M. R. Spherical resorcinol-formaldehyde performance testing with Hanford tank waste. *Solvent Extraction and Ion Exchange*. 2008;26(4): 435–452. https://doi.org/10.1080/07366290802182691

54. Duignan M. R., Nash Ch. A., Punch T. M. High aspect ratio ion exchange resin bed – hydraulic results for spherical resin beads. *Separation Science and Technology*. 2008;43(9-10): 2943–2979. https://doi.org/10.1080/01496390802119051

55. Milyutin V. V., Nekrasova N. A., Kharitonov O. V., Firsova L. A., Kozlitin E. A. Sorption technologies in modern applied radiochemistry. *Sorptsionnye i khromatograficheskie protsessy*. 2016;16(3): 313–322. (In Russ., abstract in Eng.). Available at: https://www.elibrary.ru/item.asp?id=25919976

56. Milyutin V. V., Zelenin P. G., Kozlov P. V., Remizov M. B., Kondrutskii D. A. Sorption of cesium from alkaline solutions onto resorcinol-formaldehyde sorbents. *Radiochemistry*. 2019;61(6): 714–718. https://doi.org/10.1134/s1066362219060122

57. Tretyakov V. A., Kondrutsky D. A., Bobrov A. F., Milyutin V. V., Nesterov A. G. Method for obtaining a sorbent for the selective extraction of cesium. Patent RU 2521379. 02/13/2013 BI. 2014. No. 18. Available at: https://www.freepatent.ru/patents/2521379

58. Altshuler H. N., Abramova L. P., Malyshenko N. V., Shkurenko G. Yu., Ostapova E. V. Ion-exchange selectivity of a network calixarene-containing polymer obtained by the template synthesis on Na⁺, K⁺, and Ba²⁺ matrices. *Russian Chemical Bulletin*. 2005;54(8): 1978–1981. https://doi.org/10.1007/s11172-006-0067-8

59. Shelkovnikova L. A., Kargov S. I., Gavlina O. T., Ivanov V. A., Al'tshuler G. N. Selectivity of ion exchangers in extracting cesium and rubidium from alkaline solutions. *Russian Journal of Physical Chemistry A*. 2013;87(1): 125–128. https://doi.org/10.1134/s0036024413010251

60. Kholkin A. I., Gindin L. M., Markova L. S., Shtilman I. S. *Extraction of metals by phenols*. Novosibirsk: Nauka Publ.; 1976. 189 p. (In Russ.)

61. Samanta S. K., Misra B. M. Ion exchange selectivity of a resorcinol-formaldehyde polycondensate resin for cesium in relation to other alkali metal ions. *Solvent Extraction and Ion Exchange*. 1995;13(3): 575–589. https://doi.org/10.1080/07366299508918292

62. Kargov S. I., Shelkovnikova L. A., Ivanov V. A. The nature of ion exchange selectivity of phenol-formaldehyde sorbents with respect to cesium and rubidium ions. *Russian Journal of Physical Chemistry A*. 2012;86(5): 860–866. https://doi.org/10.1134/s0036024412050159

Condensed Matter and Interphases / Конденсированные среды и межфазные границы   2022;24(3): 287–299

V. A. Ivanov et al.   Selective ion-exchange sorbents for caesium extraction from alkaline radioactive solutions...

63. Kapusta D. P., Meteleshko Y. I., Babchuk I. V., Khrenova M. G. Applications of high performance computing: Born–Oppenheimer molecular dynamics of complex formation in aqueous solutions. *Supercomputing Frontiers and Innovations*. 2018;5(3): 70–73. https://doi.org/10.14529/jsfi180312

64. Kulakova A. M., Khrenova M. G. Molecular mechanism of the cesium and rubidium selective binding to the calix[4]arene revealed by Born–Oppenheimer molecular dynamics simulation and electron density analysis. *Mendeleev Communications*. 2021;31(2): 185–187. https://doi.org/10.1016/j.mencom.2021.03.013

65. Heginbotham L., Lu Z., Abramson T., MacKinnon R. Mutations in the K+ channel signature sequence. *Biophysical Journal.* 1994;66(4): 1061–1067. https://doi.org/10.1016/S0006-3495(94)80887-2

66. Glendening E. D., Feller D., Thompson M. A. An ab initio investigation of the structure and alkali metal cation selectivity of 18-Crown-6. *Journal of the American Chemical Society.* 1994;116(23): 10657–10669. https://doi.org/10.1021/ja00102a035

67. Gu J., Leszczynski J. Origin of Na^+/K^+ selectivity of the guanine tetraplexes in water: the theoretical rationale. *The Journal of Physical Chemistry A*. 2002;106(3): 529–532. https://doi.org/10.1021/jp012739g

Information about the authors

Vladimir A. Ivanov, Dr. Sci. (Chem.), Professor, Department of Chemistry, Lomonosov Moscow State University (Moscow, Russian Federation).

https://orcid.org/0000-0001-6022-9569
minilana1954@mail.ru

Sergey I. Kargov, Dr. Sci. (Chem.), Professor, Department of Chemistry, Lomonosov Moscow State University (Moscow, Russian Federation).

https://orcid.org/0000-0001-7834-6632
skargov@yandex.ru

Olga T. Gavlina, Cand. Sci. (Chem.), Research Fellow Department of Chemistry, Lomonosov Moscow State University (Moscow, Russian Federation).

https://orcid.org/0000-0001-5499-810X
ogavlina@mail.ru

Translated by Anastasiia Ananeva
Edited and proofread by Simon Cox

Original articles

Influence of magnetron sputtering conditions on the structure and surface morphology of In$_x$Ga$_{1-x}$As thin films on a GaAs (100) substrate

O. V. Devitsky[1,2] ✉, A. A. Zakharov[2], L. S. Lunin[1,2], I. A. Sysoev[2], A. S. Pashchenko[1,2], D. S. Vakalov[2], O. M. Chapura[2]

[1]Federal Research Center Southern Scientific Center of the Russian Academy of Sciences,
41 Chekhov str., Rostov-on-Don 344006, Russian Federation

[2]North Caucasian Federal University,
1 Pushkina str., Stavropol 355017, Russian Federation

Abstract

We present the results of the study of the structure and surface morphology of In$_x$Ga$_{1-x}$As thin films on a GaAs substrate. Thin films were obtained by magnetron sputtering from a specially formed In$_{0.45}$Ga$_{0.55}$As target in an argon atmosphere.

The obtained samples of thin films were studied by Raman scattering, atomic force microscopy, scanning electron microscopy, and energy-dispersive X-ray spectroscopy. It was shown that the grains of the films obtained at a substrate temperature below 600 °C were not faceted and were formed through the coalescence of grains with a size of 30–65 nm. At a substrate temperature of 600 °C, films consisted of submicron grains with a visible faceting.

It was determined that the average grain size increased and the root-mean-square roughness of thin films decreased due to an increase in the substrate temperature. Thin films obtained at a substrate temperature of 600 °C possessed the best structural properties.

Keywords: Magnetron sputtering, Thin films, Raman scattering, Surface morphology, A^{3}B^5 compounds

✉ Oleg V. Devitsky, e-mail: v2517@rambler.ru

Condensed Matter and Interphases / Конденсированные среды и межфазные границы   2022;24(3): 300–305

O. V. Devitsky et al.   Influence of magnetron sputtering conditions on the structure and surface...

1. Introduction

Semiconductor compounds A^3B^5 are widely used materials that are highly important in photovoltaics and optoelectronics. Today, among the most common methods for obtaining thin films and heterostructures of A^3B^5 compounds are the following: molecular beam epitaxy, metal organic chemical vapour deposition, ion-beam sputtering, and impulse laser deposition [15]. Magnetron sputtering is also used to obtain thin films of A^3B^5 compounds. Thin films of GaSb, $Al_xGa_{1-x}N$, $In_xAl_{1-x}N$, $GaAs_{1-y}N_y$, $In_xGa_{1-x}N$, and $In_xGa_{1-x}As$ on various substrates were obtained using this method [612]. $In_xGa_{1-x}As$ solid solution is widely used in modern optoelectronics [13], but the preparation of thin films using magnetron sputtering, although being highly relevant, still poses some challenges. They are mainly related to the fact that the effect of magnetron sputtering parameters on the properties of $In_xGa_{1-x}As$ thin films have not been thoroughly studied. In some works researchers either used the method of co-sputtering from high purity GaAs and In targets [14], or alternated the layers of GaAs and In, respectively. Although this method has certain advantages, it significantly complicates the process of magnetron sputtering. It is reasonable to use the targets with a set composition of the $In_xGa_{1-x}As$ solid solution the preparation of which was described in [5].

The goal of this work was to grow $In_xGa_{1-x}As$ thin films using magnetron sputtering and to study their structural properties and surface morphology.

2. Experimental

In this study, we reported the preparation of $In_xGa_{1-x}As$ thin films on GaAs (100) substrates using magnetron sputtering from a target with a calculated composition of $In_{0.45}Ga_{0.55}As$. The target was formed by sintering GaAs and InAs powders in the pure hydrogen atmosphere at a temperature of 700 °C for 120 minutes. Thin films of $In_xGa_{1-x}As$ were deposited on GaAs (100) using a PM1-60/1-02-02 IT magnetron in an argon atmosphere at a pressure of 8 Pa. The distance from the target to the substrate was 100 mm, the power of target sputtering was 1.8 W/cm². The duration of deposition was 60 minutes for all samples, and the temperature of the substrate varied from 400 to 600 °C. All thin film samples were 0.42 µm thick.

Micrographs of the surface and the composition were analysed using a scanning electron microscope MIRA3-LMH with a AZtecEnergy Standard/X-max20(standard) system that determines the elemental composition. The thickness of the layer was determined by micrographs of cleavages using contrast topography (SE detector). Structural properties were studied using Raman scattering on an inVia Raman Microscope (Renishaw) spectrometer with a laser wavelength of 514 nm at a room temperature. The surface morphology of thin films was studied on a Ntegra Aura atomic force microscope (AFM).

3. Results and discussion

Figs. 1 and 2 show SEM images of the surface of $In_xGa_{1-x}As$ thin films on GaAs grown at a temperature of the substrate 400 and 600 °C. The presented images show that the surface of both films consists of grains that become faceted when the substrate temperature increases up to 600 °C. There were also microdrops on the surface of all samples of thin films (Fig. 1b). The size of the microdrops was not more than 2 µm, and their density was approximately 0.06 µm⁻² for thin films obtained at 400 °C. There were almost no microdrops on thin films obtained at 500 and 600 °C. According to the presented results, a non-classical mechanism of crystal growth was observed for thin films obtained at 400 °C, which means that oriented attachment of small crystal grains occurred in the surface of a larger grain [15–16]. The surface of the films was very rough, and there were grains with the size of 260 µm that were not faceted and had interfaces that were not clearly visible. When the substrate temperature increased up to 500 °C, there were a greater number of larger grains (up to 320 µm) with a poorly visible faceting. There were a great number of homogeneous multifaceted grains on the surface of a film grown at 600 °C. These grains were no more than 560 µm in size. It is obvious that the structural properties of films increase with the growth of the size of grains.

Energy dispersive analysis showed that the composition of the films grown at 400 and 500 °C is similar to that of $In_{0.32}Ga_{0.68}As$, while

Condensed Matter and Interphases / Конденсированные среды и межфазные границы   2022;24(3): 300–305

O. V. Devitsky et al.   Influence of magnetron sputtering conditions on the structure and surface…
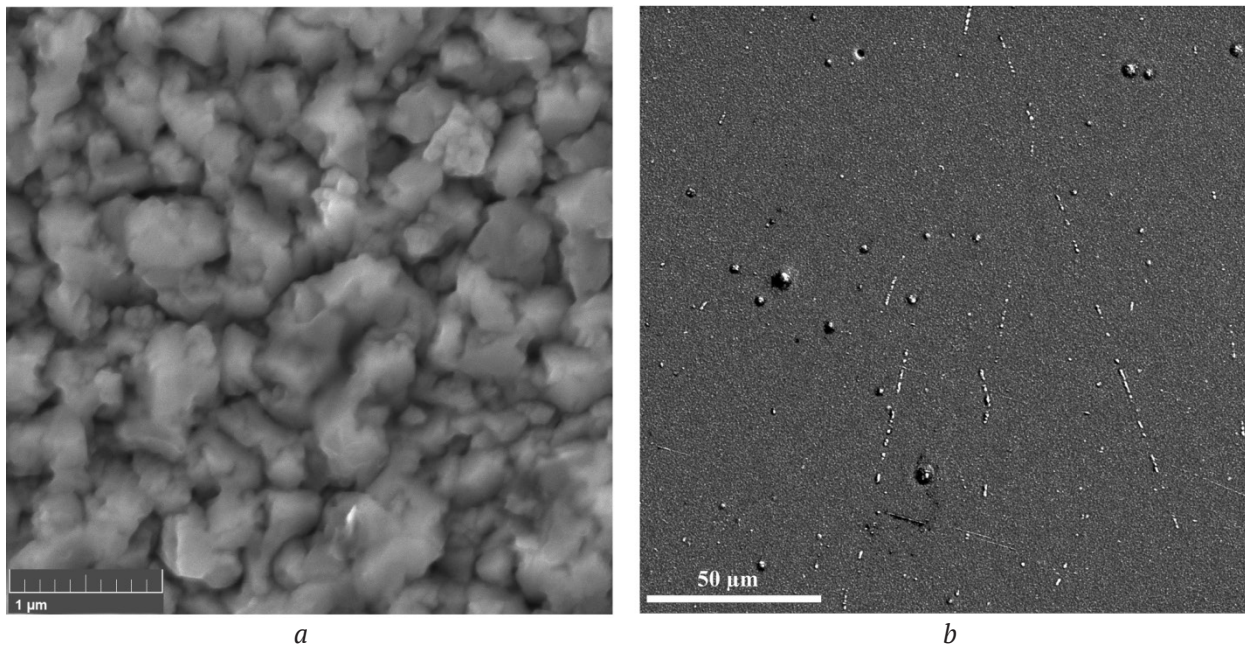
Fig. 1. SEM image of the surface of a thin In$_x$Ga$_{1-x}$As film on a GaAs substrate grown by magnetron sputtering at a temperature of 400 °C in the secondary electron detection mode at 10 kV, 64 kV (a), and 20 kV (b)
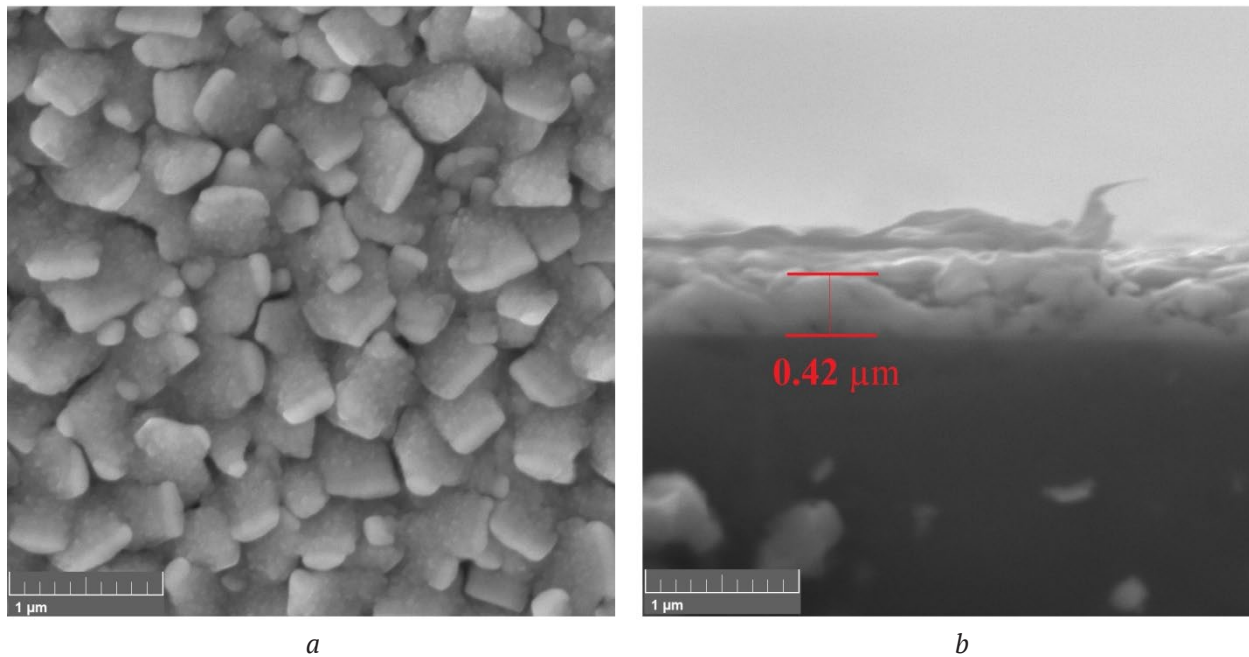
Fig. 2. SEM image of the surface (a) and cleavage (b) of a thin In$_x$Ga$_{1-x}$As film on a GaAs substrate grown by magnetron sputtering at a temperature of 600 °C

the composition of the film grown at 600 °C had a greater content of indium, In$_{0.43}$Ga$_{0.57}$As. This can probably be explained by the fact that the content of indium in a thin film decreased due to the segregation of indium at a lower temperature of a substrate.

To study the surface of thin films more thoroughly, we performed an AFM study of the surface morphology (Fig. 3) and determined root-mean-square roughness (RMS) of the surface. It was shown that when the substrate temperatures increased from 400 to 600 °C, RMS of thin films decreased from 32.62 to 26.75 μm, respectively.

The effect of the substrate temperature on the structural properties of In$_x$Ga$_{1-x}$As thin films was also studied by Raman spectra (Fig. 4). Two

Condensed Matter and Interphases / Конденсированные среды и межфазные границы 2022;24(3): 300–305

O. V. Devitsky et al. Influence of magnetron sputtering conditions on the structure and surface...
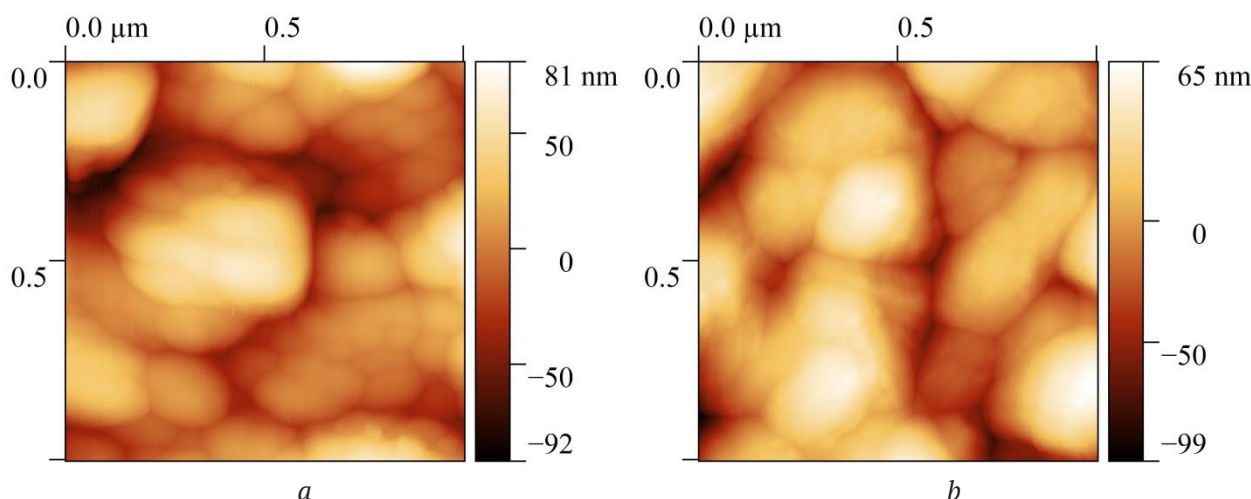
Fig. 3. AFM images of $In_xGa_{1-x}As$ thin films on a GaAs substrate grown by magnetron sputtering at 400 °C (a) and 600 °C (b)

high-intensity transverse (TO) phonon modes related to InAs and GaAs can be identified on the spectra in the frequency intervals of 219–223 cm⁻¹ and 245–257 cm⁻¹ respectively. It should be noted that in case of the film grown at 400 °C, we observed a longitudinal (LO) optical mode of InAs on the spectra located at the frequency of 223 cm⁻¹ as well as a low_intensity GaAs (LO) mode of 287 cm⁻¹. The region in the range of 110–130 cm⁻¹ can be associated with the presence of microdrops on the surface of films. According to the rules of selection, both LO and TO phonon modes must be allowed on Raman spectra for a perfect crystal [17]. The thin films grown at 500 and 600 °C obviously have the most perfect structure as InAs (TO) and GaAs (TO) modes are dominant in their spectra. A displacement in the position of an InAs (TO) phonon mode regarding the position of the frequency of an InAs (TO) mode for the voluminous InAs [14] (221 cm⁻¹) for 2 cm⁻¹ was observed only for the films grown at 400 and 500 °C, which is typical for thin films with a decreased content of In [18–21].

4. Conclusions

Thus, we grew $In_xGa_{1-x}As$ thin films on a GaAs substrate using magnetron sputtering. Using scanning electron microscopy and energy dispersion analysis, it was shown that $In_xGa_{1-x}As$ thin films obtained at the substrate temperature of 600 °C had the most similar composition to that of a sputtered target. The comparison of SEM images of the surface of $In_xGa_{1-x}As$ thin films on GaAs showed that the substrate temperature
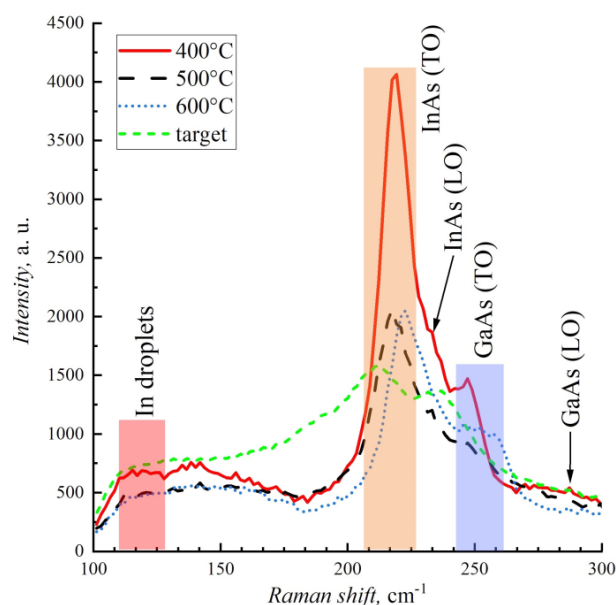
Fig. 4. Raman spectra of an $In_{0.45}Ga_{0.55}As$ target and $In_xGa_{1-x}As$ thin films on GaAs grown at different substrate temperatures

had a great effect on the surface morphology and structure of a film. The results of the study of Raman scattering spectra showed that $In_xGa_{1-x}As$ thin films obtained at the substrate temperature of 600 °C had the best structural properties. The presented experimental data showed that magnetron sputtering is a promising method that can be used for growing $In_xGa_{1-x}As$ thin films on GaAs.

Author contributions

Oleg Devitsky – the idea of experiments, text writing, final conclusions. Alexey Zakharov –

303

Condensed Matter and Interphases / Конденсированные среды и межфазные границы   2022;24(3): 300–305

O. V. Devitsky et al.   Influence of magnetron sputtering conditions on the structure and surface...

conducting research. Igor Sysoev – scientific leadership, research concept. Leonid Lunin – scientific leadership, review writing, and text editing. Alexander Pashchenko – review writing, text editing, final conclusions. Dmitry Vakalov – conducting research. Oleg Chapura – conducting research.

Conflict of interests

The authors declare that they have no known competing financial interests or personal relationships that could have influenced the work reported in this paper.

References

1. Wang W., Ma B., Chao Gao H., Long Yu H., Hui Li Z. Low surface roughness GaAs/Si thin-film deposition using three-step growth method in MBE. *Materials Science Forum*. 2020;1014(43): 43–51. https://doi.org/10.4028/www.scientific.net/MSF.1014.43

2. Devitsky O. V., Nikulin D. A., Sysoev I. A. Pulsed laser deposition of aluminum nitride thin films onto sapphire substrates. *Scientific and Technical Journal of Information Technologies, Mechanics and Optics*. 2020;20(2): 177–184. https://doi.org/10.17586/2226-1494-2020-20-2–177-184

3. Lunin L. S., Devitskii O. V., Sysoev I. A., Pashchenko A. S., Kas'yanov I. V., Nikulin D. A., Irkha V. A. Ion-beam deposition of thin AlN films on Al_2O_3 substrate. *Technical Physics Letters*. 2019;45(24): 1237. https://doi.org/10.1134/S106378501912023X

4. Zhu H., Chen Y., Zhao Y., Li X., Teng Y., Hao X., Liu J., Zhu H., Wu Q., Huang Y., Huang Y. Growth and characterization of InGaAs/InAsSb superlattices by metal-organic chemical vapor deposition for mid-wavelength infrared photodetectors. *Superlattices and Microstructures*. 2020;146: 106655. https://doi.org/10.1016/j.spmi.2020.106655

5. Pashchenko A. S., Devitsky O. V., Lunin L. S., Kasyanov I. V., Nikulin D. A., Pashchenko O. S. Structure and morphology of GaInAsP solid solutions on GaAs substrates grown by pulsed laser deposition. *Thin Solid Films*. 2022;743 139064. https://doi.org/10.1016/j.tsf.2021.139064

6. Bernal-Correaa R., Gallardo-Hernández S., Cardona-Bedoyac J., Pulzara-Mora A. Structural and optical characterization of GaAs and InGaAs thin films deposited by RF magnetron sputtering. *Optik*. 2017;145: 608–616. https://doi.org/10.1016/j.ijleo.2017.08.042

7. Zelaya-Angel O., Jiménez-Sandoval S., Alvarez-Fregoso O., Mendoza-Alvarez J.G., Gómez-Herrera1 M.L., Cardona-Bedoya J., Huerta-Ruelas J. Rhombohedral symmetry in $GaAs_{1-x}N_x$ nanostructures. *Semiconductor Science and Technology*. 2021;36(4): 045026. https://doi.org/10.1088/1361-6641/abe319

8. Mantarcı A. Comparison of optical, electrical, and surface characteristics of InGaN thin films at non-flow and small nitrogen flow cases. *Optical and Quantum Electronics*. 2021;53:544. https://doi.org/10.1007/s11082-021-03203-4

9. Nishimoto N., Fujihara J. Characterization of GaSb thin films with excess Ga grown by RF magnetron sputtering. *International Journal of Modern Physics B*. 2020;34(1020): 2050097. https://doi.org/10.1142/S0217979220500976

10. Othman N.A., Nayan N., Mustafa M.K., Azman Z., Hasnan M.M.I.M., Bakri A.S., Jaffar S.N., Abu Bakar A.S., Mamat M.H., Mohd Yusop M.Z., Ahmad M.Y. Structural and Morphological Properties of AlGaN Thin Films Prepared by Co-sputtering Technique. In: *Proceedings – 2021 IEEE Regional Symposium on Micro and Nanoelectronics. 13th IEEE Regional Symposium on Micro and Nanoelectronics, 2 4 August 2021*. Institute of Electrical and Electronics Engineers Inc., 2021. p. 20–23. https://doi.org/10.1109/RSM52397.2021.9511605

11. Mulcue L.F., de la Cruz W., Saldarriaga W. Efect of film thickness on morphological, structural and electrical properties of InAlN thin layers grown on glass at room temperature. *Applied Physics A*. 2021;127: 479. https://doi.org/10.1007/s00339-021-04618-2

12. Ferhati H., Djeffal F., Bendjerad A., Benhaya A., Saidi A. Perovskite/InGaAs tandem cell exceeding 29% efficiency via optimizing spectral splitter based on RF sputtered ITO/Ag/ITO ultra-thin structure. *Physica E: Low-dimensional Systems and Nanostructures*. 2021;128: 114618. https://doi.org/10.1016/j.physe.2020.114618

13. Kao Y. C., Chou H. M., Hsu S. C., Lin A., Lin C. C., Shih Z. H., Chang C. L., Hong H. F., Horng R. H. Performance comparison of III–V//Si and III–V//InGaAs multi-junction solar cells fabricated by the combination of mechanical stacking and wire bonding. *Scientific Reports*. 2019;9 4308. https://doi.org/10.1038/s41598-019-40727-y

14. Bernal-Correa R., Torres-Jaramillo S., Pulzara-Mora C., Montes-Monsalve J., Gallardo-Hernández S., López –López M., Cardona-Bedoya J., Pulzara-Mora A. $In_xGa_{1-x}As$ obtained from independent target via co-sputtering deposition. *Journal of Physics: Conference Series*. 2017;850: 012013. https://doi.org/10.1088/1742-6596/850/1/012013

15. Fedorov P. P., Mayakova M. N., Gaynutdinov R. V., Tabachkova N. Yu., Komandin G. A., Baranchikov A. E., Chernova E. V., Kuznetsov S. V., Ivanov V. K., Osiko V. V. Investigation of the deposition of calcium fluoride nanoparticles on the chips of CaF_2 single crystals. *Condensed Matter and Interphases*. 2021;23(4): 607–613. https://doi.org/10.17308/kcmf.2021.23/3681

Condensed Matter and Interphases / Конденсированные среды и межфазные границы   2022;24(3): 300–305

O. V. Devitsky et al.   Influence of magnetron sputtering conditions on the structure and surface...

16. Colfen H. Nonclassical nucleation and crystallization. *Crystals*. 2020;10(2): 61. https://doi.org/10.3390/cryst10020061

17. Loudon R., The Raman effect in crystals. *Advances in Physics*. 1964;52(13): 423-482. https://doi.org/10.1080/00018736400101051

18. Greene L. H., Dorsten J. F., Roshchin I. V., Abeyta A. C., Tanzer T. A., Feldmann W. L., Bohn P. W. Optical detection of the superconducting proximity effect: Raman scattering on Nb/InAs. *Czechoslovak Journal of Physics Supplement*. 1996;46(2): 741. https://doi.org/10.1007/BF02583678

19. Pulzara-Mora A., Montes-Monsalve J., Bernal-Correa R., Morales-Acevedo A., Gallardo-Hernández S., López-López M. Structural, optical and morphological properties of $In_xGa_{1-x}As$ layers obtained by RF magnetron sputtering. *Superficies y Vacío*. 2016;29(2) 32–37. Available at: https://superficiesyvacio.smctsm.org.mx/index.php/SyV/article/view/47/31

20. Kang S., Jeong T. S. Indium composition dependence of Raman spectroscopy and photocurrent of $In_xGa_{1-x}As$ strained layers grown by using MOCVD. *Journal of the Korean Physical Society*. 2020;76(3): 231. https://doi.org/10.3938/jkps.76.231

21. Groenen J., Carles R., Landa G. Optical-phonon behavior in $Ga_{1-x}In_xAs$: the role of microscopic strains and ionic plasmon coupling. *Physical Review B*. 1998;58(16): 10452–10462. https://doi.org/10.1103/physrevb.58.10452

Information about the authors

Oleg V. Devitsky, Cand. Sci. (Tech.), Senior Researcher, Laboratory of Physics and Technology of Semiconductor Nanoheterostructures for Microwave Electronics and Photonics, Federal Research Centre Southern Scientific Centre of the Russian Academy of Sciences *(Rostov-on-Don,* Russian Federation); Senior Researcher, Scientific and Educational Centre for Photovoltaics and Nanotechnology, North Caucasian Federal University *(Stavropol,* Russian Federation).

https://orcid.org/0000-0003-3153-696X

v2517@rambler.ru

Alexey A. Zakharov, Junior Researcher, Scientific and Educational Centre for Photovoltaics and Nanotechnology, North Caucasian Federal University *(Stavropol,* Russian Federation).

https://orcid.org/0000-0003-0379-9383

v2517@rambler.ru

Igor A. Sysoev, Dr. Sci. (Tech.), Director, Scientific and Educational Centre for Photovoltaics and Nanotechnology, North Caucasian Federal University *(Stavropol,* Russian Federation).

https://orcid.org/0000-0001-5415-0782

v2517@rambler.ru

Leonid S. Lunin, Dr. Sci. (Phys.–Math.), Chief Researcher, Laboratory of Physics and Technology of Semiconductor Nanoheterostructures for Microwave Electronics and Photonics, Federal Research Centre Southern Scientific Centre of the Russian Academy of Sciences *(Rostov-on-Don,* Russian Federation; Chief Researcher, Scientific and Educational Center for Photovoltaics and Nanotechnology, North Caucasian Federal University *(Stavropol,* Russian Federation).

https://orcid.org/0000-0002-5534-9694

lunin_ls@mail.ru

Alexander S. Pashchenko, Cand. Sci. (Phys.–Math.), Senior Researcher, Head of the Laboratory of Physics and Technology of Semiconductor Nanoheterostructures for Microwave Electronics and Photonics, Federal Research Center Southern Scientific Center of the Russian Academy of Sciences *(Rostov-on-Don,* Russian Federation; Senior Researcher, Scientific and Educational Center for Photovoltaics and Nanotechnology, North Caucasian Federal University *(Stavropol,* Russian Federation).

https://orcid.org/0000-0002-7976-9597

as.pashchenko@gmail.com

Dmitry S. Vakalov, Cand. Sci. (Phys.–Math.), Head of the Research Laboratory of Physicochemical Methods of Analysis, Scientific-laboratory Complex of Clean Rooms, Faculty of Physics and Technology, North Caucasian Federal University *(Stavropol,* Russian Federation).

https://orcid.org/0000-0001-6788-3811

megadims@gmail.com

Oleg M. Chapura, Engineer of the Department of Physical Electronics, Physics and Technology Faculty, North Caucasian Federal University, *(Stavropol,* Russian Federation).

https://orcid.org/0000-0002-6691-0010

chapurol-7@mail.ru

Original articles

Synthesis of magnetic chromium substituted cobalt ferrite Co(Cr$_x$Fe$_{1-x}$)$_2$O$_4$ adsorbents for phosphate removal

Qui Anh Tran[1, 2], Nhat Linh Tran[1,2], Dang Khoa Nguyen Anh[1, 2], Quynh Nhu Le Thi[1, 2], The Luan Nguyen[1,2], Huu Thinh Pham Nguyen[1,2], Anh Tien Nguyen[3], Quoc Thiet Nguyen[4], Tien Khoa Le[1,2] ✉

[1]Faculty of Chemistry, University of Science,
Ho Chi Minh city, Vietnam

[2]Faculty of Chemistry, University of Science, Vietnam National University,
Ho Chi Minh City, Vietnam

[3]Faculty of Chemistry, Ho Chi Minh City University of Education,
Ho Chi Minh City, Vietnam

[4]Institute of Applied Materials Science, Vietnam Academy of Science and Technology,
1B TL29 District 12, Ho Chi Minh City, Vietnam

Abstract

In this work, we aimed to prepare chromium substituted cobalt ferrite Co(Cr$_x$Fe$_{1-x}$)$_2$O$_4$ powders by a simple coprecipitation-annealing method with different Cr contents to create novel magnetic adsorbents for the removal of phosphate ions from water. The effects of Cr substitution on the crystal structure, phase composition, morphology, surface atomic composition, surface area and magnetic properties of our adsorbents were investigated by X-ray diffraction, scanning electron microscopy, energy-dispersive X-ray spectroscopy, Brunauer-Emmett-Teller nitrogen adsorption-desorption and vibrating sample magnetometry. According to the results, all our Co(Cr$_x$Fe$_{1-x}$)$_2$O$_4$ samples exhibited higher phosphate adsorption than CoFe$_2$O$_4$ powder but their magnetic properties were reduced for increasing Cr substitution. Among them, the Co(Cr$_{0.25}$Fe$_{0.75}$)$_2$O$_4$ sample was found to be the most promising material since its magnetic properties are still high to allow it to be easily separated from the solution and its maximum P adsorption capacity (according to the Langmuir model) was estimated to be 4.84 times higher than CoFe$_2$O$_4$, which can be attributed to the presence of Cr^{3+} ions on the surface and the enhanced surface specific area of this substituted sample. Moreover, the adsorption data of Co(Cr$_{0.25}$Fe$_{0.75}$)$_2$O$_4$ sample also fitted well to the pseudo second order kinetic model, revealing the adsorption rate constant of 0.87 mgP^{-1}s^{-1}, two times superior to CoFe$_2$O$_4$.

Keywords: Chromium substitution; Cobalt ferrite; Phosphate removal; Magnetic adsorbent; Surface Cr^{3+} content

✉ Tien Khoa Le, e-mail: ltkhoa@hcmus.edu.vn

Condensed Matter and Interphases / Конденсированные среды и межфазные границы   2022;24(3): 306–314

Qui Anh Tran et al.   Synthesis of magnetic chromium substituted cobalt ferrite Co(Cr$_x$Fe$_{1-x}$)$_2$O$_4$ adsorbents...

1. Introduction

For a long time, the presence of phosphate ions in wastewater has been largely considered as the main factor causing eutrophication [1, 2], a phenomenon characterized by the excessive algal growth, which can lead to numerous ecological disturbances, such as the bloom of cyanobacteria, the impairment of water quality and the hypoxia problem [3]. Hence, removing phosphate ions from wastewater before discharge is always a crucial task of environmental control strategies. In the literature, among different approaches including adsorption, chemical precipitation and biological removal, adsorption is found to be an economical, simple and effective method for the removal of phosphate ions in low concentration without formation of chemical waste sludge [4, 5]. However, most of phosphate adsorbent materials such as fly ash [6], porous metal oxides [7], metal organic frameworks [8] and layered double hydroxides [9] were developed in the form of fine powder which has the high suspendability in water and thus is very difficult to be separated from water bodies after treatment.

To address this problem, magnetically separable adsorbents based on ferrite materials were introduced. In fact, owing to their ferromagnetic properties, ferrite oxides have been extensively studied for various applications, including electromagnetic devices [10] magnetorheological fluids [11] and magnetic Fenton catalysts [12]. Hence, some recent studies have suggested to prepare magnetic phosphate adsorbents possessing the core-shell structure with ferrite particles as a magnetic core. For example, Lai et al. successfully prepared magnetic Fe$_3$O$_4$@SiO$_2$ core-shell nanoparticles functionalized by hydrous lanthanum oxide, which exhibited both high phosphate adsorption and good magnetic properties, facilitating the separation and recovery of core-shell materials [13]. Likewise, Lin et al. also reported the effective phosphate adsorption using Fe$_3$O$_4$@MgAl-LDH@La(OH)$_3$ composites with a hierarchical core-shell structure [14]. Thanks to their magnetite core, more than 79% of composite powders can be recovered from solution by a magnet [14]. However, the core-shell adsorbents were usually prepared by complicated procedures which increases their production cost. Besides, during phosphate removal, the shell component can be separated from the inner magnetic core since the bonding strength between the shell and the core is still a question mark.

Therefore, in this work, we proposed to developed novel magnetic phosphate adsorbents without core-shell structure, based on chromium substituted cobalt ferrite Co(Cr$_x$Fe$_{1-x}$)$_2$O$_4$ powders. These samples were prepared by a simple coprecipitation-annealing method with different Cr contents and then characterized in terms of phase composition, surface atomic composition, morphology, surface area and magnetic parameters. Their maximum P adsorption capacity and their adsorption kinetics for phosphate removal were also investigated.

2. Experimental

2.1. Synthesis of magnetic adsorbents

For the synthesis of Co(Cr$_x$Fe$_{1-x}$)$_2$O$_4$ with x = 0, 0.25, 0.50 and 0.75, the starting precursors including CoCl$_6$·6H$_2$O, Fe(NO$_3$)$_3$·9H$_2$O and Cr(NO$_3$)$_3$·9H$_2$O (> 98%, purchased from Sigma Aldrich) were separately dissolved in distilled water and then mixed together following the desired molar Co/Cr/Fe ratios. Subsequently, NaOH solution (4.0 mol/L^{-1}) was slowly added to the solution containing Co^{2+}, Fe^{3+} and Cr^{3+} under regular stirring until pH 7. This solution was heated and maintained at 90 °C for 2 hours. After that, the precipitates were filtered, washed with distilled water, dried at 150 °C for 8 hours and ground into a fine powder. The powders were annealed at 700 °C for 4 hours. Next, the products were washed with distilled water, separated from water by a magnet and finally dried again at 150 °C for 1 hour to obtain Co(Cr$_x$Fe$_{1-x}$)$_2$O$_4$ samples.

2.2. Material characterization

The magnetic measurement for Co(Cr$_x$Fe$_{1-x}$)$_2$O$_4$ adsorbents was carried out at room temperature by using a vibrating sample magnetometer PPMS6000 (Quantum Design). Their crystal structure and phase composition were investigated by powder X ray diffraction (XRD) using a BRUKER-Binary V3 X-ray diffractometer with Cu$K\alpha$ radiation (λ = 1.5406 Å) in the 2θ range of 10−80° (0.02° per step). The morphology of these samples was observed by a field emission

scanning electron microscope (FE-SEM) HITACHI S-48000 under an accelerating voltage of 10 kV. The energy-dispersive X-ray spectroscopy (EDS) analysis was also conducted using HITACHI S-4800 microscope to determine the surface atomic composition of our adsorbents. Moreover, their specific surface area was measured by using the Brunauer-Emmett-Teller (BET) method with N$_2$ adsorption-desorption isotherms recorded at 77 K on a NOVA 1000e analyzer (Quantachrome Instruments).

2.3. Preliminary tests for phosphate adsorption

The preliminary adsorption tests of our Co(Cr$_x$Fe$_{1-x}$)$_2$O$_4$ adsorbents toward phosphate ions were performed by dispersing adsorbent powder (0.20 g) in the glass beaker containing 100 mL of KH$_2$PO$_4$ solution (2 mgP/L^{-1}) without artificial pH adjustment. The beaker was sealed and placed in a circulation system of water to maintain the temperature at about 30 °C. The suspension was constantly stirred for 24 hours. Then, the magnetic adsorbent was separated from the phosphate solution by using a magnet and the phosphate concentration of this solution was determined by the molybdenum blue colorimetric method [15] using a Helios Omega UV – VIS spectrophotometer (Thermo Fisher Scientific, USA) to measure the absorbance at 880 nm. The phosphate removal yield (%) and the phosphate uptake capacity at equilibrium (q_e, mgP.g^{-1}) of Co(Cr$_x$Fe$_{1-x}$)$_2$O$_4$ samples were calculated by the following equations (Eq. 1 and 2):

$$\text{Yield (\%)} = \frac{C_0 - C_f}{C_0} \times 100, \tag{1}$$

$$q_e = \frac{(C_0 - C_f)V}{m_{\text{adsorbent}}}, \tag{2}$$

where C_0 and C_f are the initial and final concentration of phosphate solution (mgP/L^{-1}), V is the solution volume (L) and $m_{\text{adsorbent}}$ is the mass of adsorbent (g).

2.4. Adsorption isotherms

In order to determine the maximum phosphate adsorption capacity of our samples, the study of adsorption isotherms was conducted by adding 0.02 g of samples into 100 mL of KH$_2$PO$_4$ solutions with different phosphate concentrations (2–100 mgP.L^{-1}). These suspensions were regularly

stirred at about 30°C (by using a circulation system of water) for 24 hours. After that, the equilibrium adsorption capacity for phosphate of our samples was calculated according to Eq. 2. These isotherm data were consequently analyzed using two adsorption Langmuir and the Freundlich models which can be expressed by the Eq. 3 and Eq. 4, respectively:

$$\frac{C_e}{q_e} = \frac{C_e}{C_0} + \frac{1}{K_L \times q_m}, \tag{3}$$

$$\ln q_e = \ln K_F + \frac{1}{n} \times \ln C_e, \tag{4}$$

where C_e (mgP/L^{-1}) and q_e (mgP/g^{-1}) are the phosphate concentration and the phosphate adsorption capacity of Co(Cr$_x$Fe$_{1-x}$)$_2$O$_4$ at equilibrium, respectively, q_m is the maximum phosphate adsorption capacity (mgP/g^{-1}), K_L is a Langmuir constant associated with the affinity of binding sites (L/mg^{-1}), K_F is a Freundlich constant related to the adsorption capacity (mgP/g^{-1}) and n is the constant related to the adsorption density.

2.5. Adsorption kinetics

In order to investigate the phosphate adsorption kinetics of Co(Cr$_x$Fe$_{1-x}$)$_2$O$_4$ samples, the adsorption tests were carried out in the same way of our isotherm study except the fact that the initial phosphate concentration was fixed at 2 mgP/L^{-1}. At given time intervals, aliquots of solution were collected, followed by the separation of magnetic adsorbents by a magnet and the concentrations of remaining phosphate ions were determined. Then, two kinetic models, the pseudo first-order (Eq. 5) and the pseudo second-order (Eq. 6) were used to fit the adsorption data of our samples:

$$\log(q_e - q_t) = \log q_e - \frac{k_1 t}{2.303}, \tag{5}$$

$$\frac{t}{q_t} = \frac{1}{k_2 q_e^2} + \frac{t}{q_e}, \tag{6}$$

where q_e (mgP/g^{-1}) and q_t (mgP/g^{-1}) are the phosphate adsorption capacity of Co(Cr$_x$Fe$_{1-x}$)$_2$O$_4$ at equilibrium and time t (min), k_1 (min^{-1}) and k_2 (g/mgP^{-1}· min^{-1}) are the adsorption rate constants corresponding to the pseudo first-order and pseudo second-order kinetic models, respectively.

Condensed Matter and Interphases / Конденсированные среды и межфазные границы 2022;24(3): 306–314

Qui Anh Tran et al. Synthesis of magnetic chromium substituted cobalt ferrite Co(Cr$_x$Fe$_{1-x}$)$_2$O$_4$ adsorbents...

3. Results and discussion

3.1. Preliminary tests for phosphate adsorption

The phosphate removal yield and the phosphate uptake capacity at equilibrium of Co(Cr$_x$Fe$_{1-x}$)$_2$O$_4$ samples measured in our preliminary tests after 24 hours were presented in Table 1. Without Cr substitution, our CoFe$_2$O$_4$ sample only exhibited a low phosphate adsorption with the removal yield of 29.45 % and the uptake capacity of 0.31 mgP/g^{-1}. When Cr^{3+} ions were introduced into Co(Cr$_x$Fe$_{1-x}$)$_2$O$_4$ samples, the phosphate adsorption was greatly improved, indicating that the presence of Cr^{3+} ions may act as new and efficient adsorption sites toward phosphate ions. With $x = 0.25$, the phosphate removal yield and the phosphate uptake capacity reached 58.91% and 0.61 mgP/g^{-1}, respectively, which are about two times higher than CoFe$_2$O$_4$. However, when the substituent Cr content further increased ($x = 0.50, 0.75$), the adsorption capacity and the removal yield were only slightly enhanced, suggesting that the increase of Cr content did not strongly affect the adsorption capacity of Co(Cr$_x$Fe$_{1-x}$)$_2$O$_4$ samples.

3.2. Magnetic properties

Fig. 1 and Table 2 display the magnetic hysteresis loops and the magnetic parameters of our Co(Cr$_x$Fe$_{1-x}$)$_2$O$_4$ samples, respectively. Generally, magnetic adsorbent powders usually need high saturation magnetization (M_S) to be easily attracted by using an external magnetic field and low coercivity (H_C) to be easily redispersed for the next runs. It was observed that CoFe$_2$O$_4$ sample presented the hard ferromagnetic behavior at room temperature with the saturation magnetization of 65.90 emu/g^{-1} and the coercivity

of 646.32 Oe. For Co(Cr$_{0.25}$Fe$_{0.75}$)$_2$O$_4$ sample, these both magnetic parameters were clearly declined (M_S = 41.25 emu/g^{-1} and H_C = 181.60 Oe). This evolution can be attributed to the replacement of Fe^{3+} ions by Cr^{3+} ions in the oxide lattice. In fact, the magnetic moment of Cr^{3+} ion (3 μB) is lower than that of Fe^{3+} ion (5 μB) [16]. Hence, when an amount of Fe^{3+} ions at the octahedral sites were replaced by Cr^{3+} ions, the A-B super exchange interaction was declined, which causes the decrease in saturation magnetization of chromium substituted materials. Moreover, the reduction of magnetization could also turn our samples into soft magnetic materials, causing the decrease in coercivity [17]. These results are found to be in good agreement with previous works [17–19]. Fortunately, the saturation magnetization of Co(Cr$_{0.25}$Fe$_{0.75}$)$_2$O$_4$ is still high enough to allow the quick separation from the solution by a
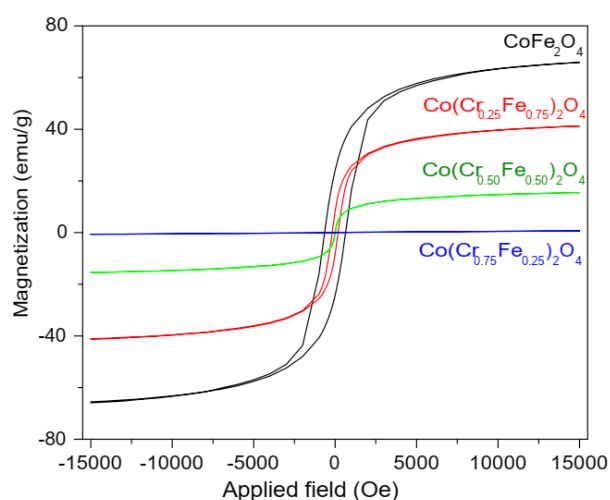
Fig. 1. Magnetic hysteresis loops of CoFe$_2$O$_4$, Co(Cr$_{0.25}$Fe$_{0.75}$)$_2$O$_4$, Co(Cr$_{0.50}$Fe$_{0.50}$)$_2$O$_4$ and Co(Cr$_{0.75}$Fe$_{0.25}$)$_2$O$_4$ samples

Table 1. Phosphate removal yield (Y %) and phosphate uptake capacity (q$_e$) of CoFe$_2$O$_4$, Co(Cr$_{0.25}$Fe$_{0.75}$)$_2$O$_4$, Co(Cr$_{0.50}$Fe$_{0.50}$)$_2$O$_4$ and Co(Cr$_{0.75}$Fe$_{0.25}$)$_2$O$_4$ in our preliminary tests after 24 hours

Samples	CoFe$_2$O$_4$	Co(Cr$_{0.25}$Fe$_{0.75}$)$_2$O$_4$	Co(Cr$_{0.50}$Fe$_{0.50}$)$_2$O$_4$	Co(Cr$_{0.75}$Fe$_{0.25}$)$_2$O$_4$
Y %	29.45	58.91	58.22	66.36
q_e (mgP g^{-1})	0.31	0.61	0.60	0.68

Table 2. Magnetic parameters of CoFe$_2$O$_4$, Co(Cr$_{0.25}$Fe$_{0.75}$)$_2$O$_4$, Co(Cr$_{0.50}$Fe$_{0.50}$)$_2$O$_4$, and Co(Cr$_{0.75}$Fe$_{0.25}$)$_2$O$_4$ samples

Samples	CoFe$_2$O$_4$	Co(Cr$_{0.25}$Fe$_{0.75}$)$_2$O$_4$	Co(Cr$_{0.50}$Fe$_{0.50}$)$_2$O$_4$	Co(Cr$_{0.75}$Fe$_{0.25}$)$_2$O$_4$
M_S (emu g^{-1})	65.903	41.251	15.492	0.671
H_C (Oe)	646.320	181.60	13.54	104.60

Condensed Matter and Interphases / Конденсированные среды и межфазные границы   2022;24(3): 306–314

Qui Anh Tran et al.   Synthesis of magnetic chromium substituted cobalt ferrite $Co(Cr_xFe_{1-x})_2O_4$ adsorbents...

magnet. However, for $Co(Cr_{0.50}Fe_{0.50})_2O_4$ and $Co(Cr_{0.75}Fe_{0.25})_2O_4$ samples, the M_S value was dramatically declined, making it very difficult to separate these samples by a magnet. Therefore, from the results of preliminary adsorption tests and magnetic analysis, the $Co(Cr_{0.25}Fe_{0.75})_2O_4$ sample can be considered as the most promising magnetic adsorbent among our chromium substituted materials.

3.3. Crystal structure and atomic composition

Figure 2 displays XRD patterns of our $CoFe_2O_4$ and $Co(Cr_{0.25}Fe_{0.75})_2O_4$ samples. The pattern of $CoFe_2O_4$ sample shows the pure phase of cubic spinel cobalt ferrite (space group Fd3m, JCPDS No.22-1086), identified by the XRD peaks at 18.33, 29.91, 30.70, 34.68, 36.01, 43.97, 58.09 and 62.15°. From this pattern, the cell parameter of cubic spinel lattice was found to be 8.375 Å. When Fe^{3+} ions were replaced by Cr^{3+} ions with $x = 0.25$, no additional phase and no evolution of cell parameters have been detected in the XRD pattern, indicating that the chromium substitution at the level of 25 mol% did not affect the crystal structure and the phase composition of ferrite adsorbents.

Although no additional Cr-containing phase was detected, according to the surface atomic composition determined by EDS analysis (Table 2), Cr^{3+} ions were still present in $Co(Cr_{0.25}Fe_{0.75})_2O_4$ sample with the surface atomic content up to 6.38%. It should be reminded that the ionic radius of Cr^{3+} ions at octahedral sites is 0.615 Å [20], which is very close to that of Fe^{3+} ions (0.645 Å) at the octahedral sites of cubic spinel lattice [20].
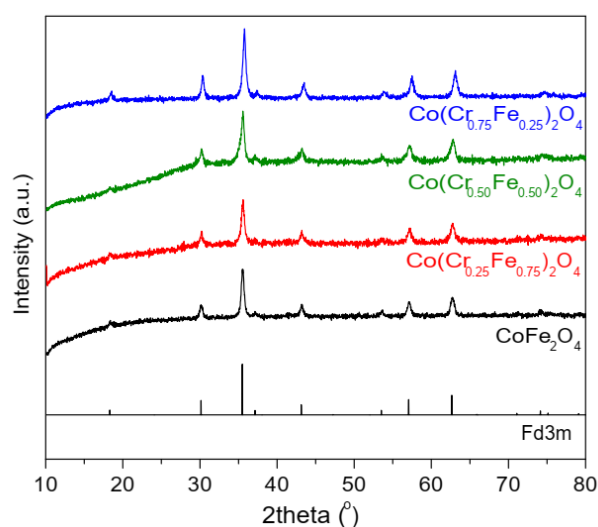
Fig. 2. XRD patterns of $CoFe_2O_4$, $Co(Cr_{0.25}Fe_{0.75})_2O_4$, $Co(Cr_{0.50}Fe_{0.50})_2O_4$ and $Co(Cr_{0.75}Fe_{0.25})_2O_4$ samples

This explained why Cr^{3+} ions can be substituted for Fe^{3+} ions in $CoFe_2O_4$ and why the formation of this solid solution is difficult to identify by XRD.

3.4. Morphology and specific surface area

The morphology of $CoFe_2O_4$ and $Co(Cr_{0.25}Fe_{0.75})_2O_4$ samples were investigated via their FE-SEM images. As shown in Fig. 3, both two samples consist of polyhedral particles with the particle size in the range of 30–50 nm. However, the particles of $CoFe_2O_4$ are found to be more strongly agglomerated than those of $Co(Cr_{0.25}Fe_{0.75})_2O_4$, which can be explained by the higher saturation magnetization of cobalt ferrite powders without Cr-substitution. Consequently, the $Co(Cr_{0.25}Fe_{0.75})_2O_4$ sample shows the enhanced
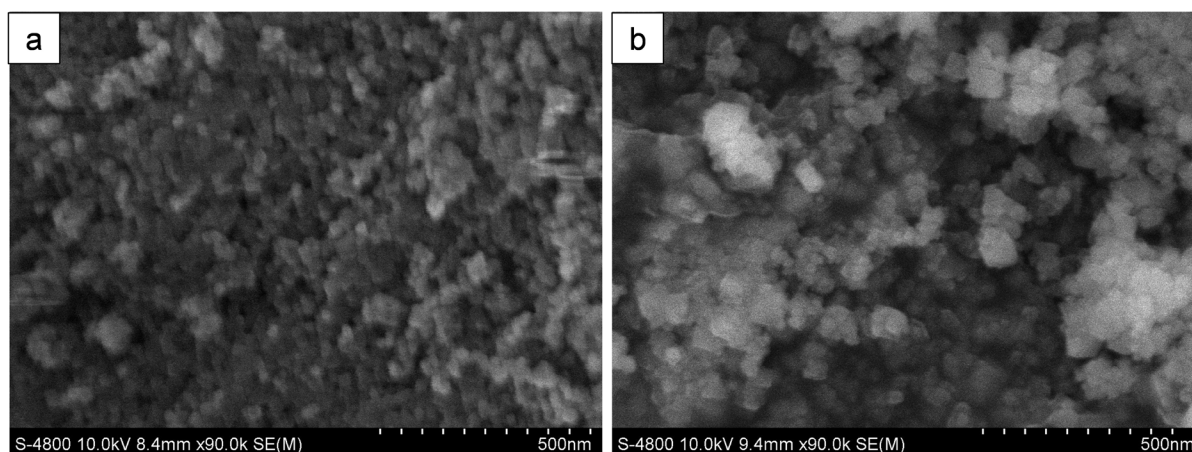
Fig. 3. FE-SEM images of $CoFe_2O_4$ (a) and $Co(Cr_{0.25}Fe_{0.75})_2O_4$ (b) samples

Condensed Matter and Interphases / Конденсированные среды и межфазные границы   2022;24(3): 306–314

Qui Anh Tran et al.   Synthesis of magnetic chromium substituted cobalt ferrite Co(Cr$_x$Fe$_{1-x}$)$_2$O$_4$ adsorbents...

specific surface area (23.258 m^2/g^{-1}) whereas the specific surface area of CoFe$_2$O$_4$ is only 14.331 m^2/g^{-1} (Table 3).

Table 3. Specific surface area (S_{BET}) of CoFe$_2$O$_4$ and Co(Cr$_{0.25}$Fe$_{0.75}$)$_2$O$_4$ samples

Ferrite	CoFe$_2$O$_4$	Co(Cr$_{0.25}$Fe$_{0.75}$)$_2$O$_4$
S_{BET} (m^2 g^{-1})	14.331	23.258

3.5. Adsorption isotherms

The experimental dataset obtained from the study of phosphate adsorption isotherms for CoFe$_2$O$_4$ and Co(Cr$_{0.25}$Fe$_{0.75}$)$_2$O$_4$ samples were fitted with the linear form by the Langmuir model (Fig. 4a) and Freundlich model (Fig. 4b). Then, their characteristic parameters were calculated and presented in Table 4. From the correlation coefficient R^2, it is noticed that all the adsorption isotherms are better described by the Langmuir model than Freundlich model. This result indicates that the precipitation of chromium phosphate or iron phosphate can be negligible [21] and the phosphate removal over our adsorbents follows the monolayer adsorption processes. Moreover, by using the Langmuir equation (Eq. 3), the adsorption rate constant of

Co(Cr$_{0.25}$Fe$_{0.75}$)$_2$O$_4$ sample was found to be 2.1160 mgP.g^{-1}, which is 4.85 times higher than CoFe$_2$O$_4$ (0.4365 mgP/g^{-1}).

3.6. Adsorption kinetics

In order to investigate the phosphate adsorption kinetics of Co(Cr$_x$Fe$_{1-x}$)$_2$O$_4$ samples, all kinetic data were fitted to the pseudo-first-order (Fig. 5a) and the pseudo-second-order (Fig. 5b). The calculated kinetic parameters were shown in Table 5. Owing to the higher correlation coefficients R^2, the pseudo-second-order model was proved to be more suitable for the phosphate adsorption on our materials. Accordingly, with the pseudo-second-order equation (Eq. 6), the phosphate adsorption rate constants of CoFe$_2$O$_4$ and Co(Cr$_{0.25}$Fe$_{0.75}$)$_2$O$_4$ samples were estimated to be 0.4767 and 0.8106 g/mgP^{-1}.min^{-1}, respectively (Table 5), confirming that the phosphate adsorption process on our Cr-substituted sample is clearly faster than CoFe$_2$O$_4$.

3.7. Discussion

According to our experimental results, the chromium substitution at the level of 25 mol% did not only improve the maximal phosphate
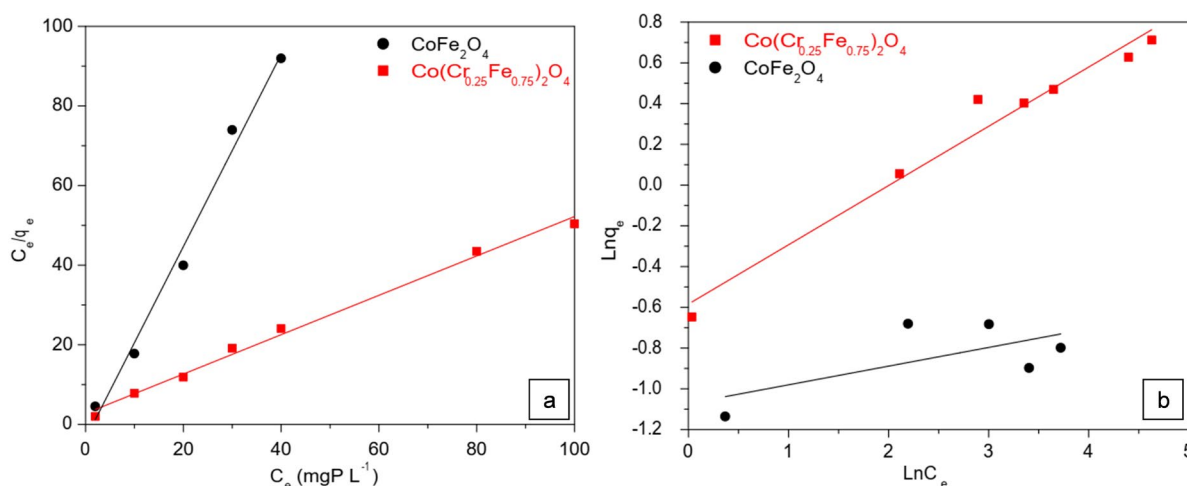
Fig. 4. F Linear fitting curves of C_e/q_e versus C_e for Langmuir model (a) and Lnq_e versus LnC_e for Freundlich model (b)

Table 4. Langmuir and Freundlich isotherm parameters for phosphate adsorption on CoFe$_2$O$_4$ and Co(Cr$_{0.25}$Fe$_{0.75}$)$_2$O$_4$ samples

	Langmuir		Freundlich	
	q_m (mgP/g^{-1})	R^2	K_F (mgP/g^{-1})	R^2
CoFe$_2$O$_4$	0.4365	0.9864	0.3422	0.4243
Co(Cr$_{0.25}$Fe$_{0.75}$)$_2$O$_4$	2.1160	0.9907	0.5576	0.9691

Condensed Matter and Interphases / Конденсированные среды и межфазные границы   2022;24(3): 306–314

Qui Anh Tran et al.   Synthesis of magnetic chromium substituted cobalt ferrite Co(Cr$_x$Fe$_{1-x}$)$_2$O$_4$ adsorbents...
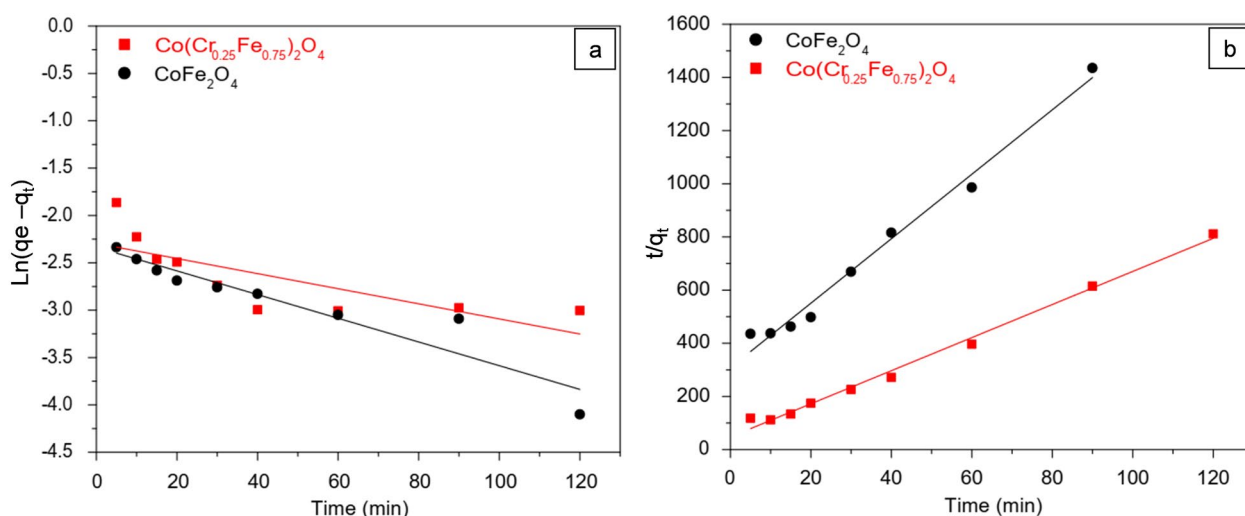
Fig. 5. Linear fitting curves of Ln(q_e- q_t) versus time for pseudo-first-order model (a) and (t/q_t) versus time for pseudo-second-order model (b)

Table 5. Kinetic parameters of phosphate adsorption on CoFe$_2$O$_4$ and Co(Cr$_{0.25}$Fe$_{0.75}$)$_2$O$_4$ samples

	Pseudo-first-order		Pseudo-second-order	
	k (min^{-1})	R^2	k (g mgP^{-1} min^{-1})	R^2
CoFe$_2$O$_4$	0.0086	0.8763	0.4767	0.9859
Co(Cr$_{0.25}$Fe$_{0.75}$)$_2$O$_4$	0.0081	0.5791	0.8106	0.9933

adsorption capacity but also increased the phosphate adsorption rate of CoFe$_2$O$_4$ powders. This evolution should be assigned to the increase in surface specific area of Cr-substituted sample as well as the presence of Cr^{3+} species in the lattice and on the surface of magnetic powders. In fact, when Cr^{3+} ions (x = 0.25) were substituted for Fe^{3+} ions in CoFe$_2$O$_4$, the specific surface area was enhanced by the factor of 1.62, which can increase the number of adsorption sites for phosphate ions. Since the adsorption rate constant of Co(Cr$_{0.25}$Fe$_{0.75}$)$_2$O$_4$ (k_2 = 0.8106 g/mgP^{-1}.min^{-1}) is also 1.70 times higher than that of CoFe$_2$O$_4$ (k_2 = 0.4767 g.mgP^{-1}.min^{-1}), we believe that the phosphate adsorption rate on our samples is strongly associated with their surface specific area. However, as mentioned in our isotherm study, when 25 mol% chromium was inserted to cobalt ferrite, the maximal adsorption capacity was greatly enhanced with the factor of 4.85, significantly outperforming the increase in surface specific area. Thus, in addition of large specific surface area, this enhancement of adsorption capacity should be attributed to the presence of Cr^{3+} species on the surface of Co(Cr$_{0.25}$Fe$_{0.75}$)$_2$O$_4$

sample. In literature, the formation constant of Cr(OH)$_3$H$_2$PO$_4^-$ complex was reported to be 10$^{2.78}$ [22] whereas that of FeHPO$_4^+$ complex is only 10$^{1.28}$ [23]. Therefore, it is suggested that the existence of Cr(III) species on the ferrite surface can promote bonding with phosphate ions through complex formation, which improves the phosphate removal from solution.

4. Conclusions

Herein, the synthesis of chromium-substituted cobalt ferrite particles by a simple coprecipitation – annealing method and their application as novel magnetic adsorbents to the removal of phosphate ions from the solution were reported. All the Cr-substituted samples exhibited the enhanced adsorption toward phosphate ions in solution but their magnetic properties tend to decline with Cr content. Among our different samples, the 25 mol% Cr-substituted CoFe$_2$O$_4$ sample was considered as the most promising magnetic adsorbent since its saturation magnetization is still high enough for the quick separation from the solution by a magnet and its maximal phosphate adsorption capacity as well

Condensed Matter and Interphases / Конденсированные среды и межфазные границы   2022;24(3): 306–314

Qui Anh Tran et al.   Synthesis of magnetic chromium substituted cobalt ferrite Co(Cr$_x$Fe$_{1-x}$)$_2$O$_4$ adsorbents...

as its phosphate adsorption rate constant are significantly superior to that of CoFe$_2$O$_4$, which can be attributed to the high surface specific area and the presence of Cr^{3+} species on the surface of Cr-substituted adsorbents.

Author contributions

The authors contributed equally to this article.

Conflict of interests

The authors declare that they have no known competing financial interests or personal relationships that could have influenced the work reported in this paper.

References

1. Cooperband L. R., Good L. W. Biogenic phosphate minerals in manure: implications for phosphorus loss to surface waters. *Environmental Science & Technology*. 2002;36(23): 5075–5082. https://doi.org/10.1021/es025755f

2. Oguz E., Gurses A., Canpolat N. Removal of phosphate from wastewaters. *Cement and Concrete Research*. 2003;33(8): 1109–1112. https://doi.org/10.1016/S0008-8846(03)00016-4

3. Smith V. H., Schindler D. W. Eutrophication science: where do we go from here? *Trends in Ecology & Evolution*. 2009;24(4): 201–207. https://doi.org/10.1016/j.tree.2008.11.009

4. Guo H., Li W., Wang H., Zhang J., Liu Y., Zhou Y. A study of phosphate adsorption by different temperature treated hydrous cerium oxides. *Rare Metals*. 2011;30: 58–62. https://doi.org/10.1007/s12598-011-0197-5

5. Cheng X., Huang X., Wang X., Sun D. J. Influence of calcination on the adsorptive removal of phosphate by Zn–Al layered double hydroxides from excess sludge liquor. *Journal of Hazardous Materials*. 2010;177: 516–523. https://doi.org/10.1016/j.jhazmat.2009.12.063

6. Lu S. G., Bai S. Q., Zhu L., Shan H. D. Removal mechanism of phosphate from aqueous solution by fly ash. *Journal of Hazardous Materials*. 2009;161: 95–101. https://doi.org/10.1016/j.jhazmat.2008.02.123

7. Delaneya P., Manamon C. M., Hanrahan J. P., Copley M. P., Holmes J. D., Morris M. A. Development of chemically engineered porous metal oxides for phosphate removal. *Journal of Hazardous Materials*. 2011;185: 382–391. https://doi.org/10.1016/j.jhazmat.2010.08.128

8. Zhang X., Sun F., He J., Xu H., Cui F., Wang W. Robust phosphate capture over inorganic adsorbents derived from lanthanum metal organic frameworks. *Chemical Engineering Journal*. 2017;326: 1086–1094. https://doi.org/10.1016/j.cej.2017.06.052

9. Santos L. C., da Silva A. F., dos Santos Lins P. V., da Silva Duarte J. L., Ide A. H., Meili L. Mg-Fe layered double hydroxide with chloride intercalated: Synthesis, characterization and application for efficient nitrate removal. *Environmental Science and Pollution Research*. 2020;27: 5890–5900. https://doi.org/10.1007/s11356-019-07364-4

10. Sunday K. J., Taheri M. L. NiZnCu-ferrite coated iron powder for soft magnetic composite applications. *Journal of Magnetism and Magnetic Materials*. 2018;463: 1–6. https://doi.org/10.1016/j.jmmm.2018.05.030

11. Anupama A. V., Kumaran V., Sahoo B. Application of Ni-Zn ferrite powders with polydisperse spherical particles in magnetorheological fluids. *Powder Technology*. 2018;338: 190–196. https://doi.org/10.1016/j.powtec.2018.07.008

12. Hoang N. T. P., Le T. K. Polyethylene glycol-assisted sol-gel synthesis of magnetic CoFe$_2$O$_4$ powder as photo-Fenton catalysts in the presence of oxalic acid. *Journal of Sol-Gel Science and Technology*. 2018;88: 211–219. https://doi.org/10.1007/s10971-018-4783-y

13. Lai L., Xie Q., Chi L., Gu W., Wu D. Adsorption of phosphate from water by easily separable Fe$_3$O$_4$@SiO$_2$ core/shell magnetic nanoparticles functionalized with hydrous lanthanum oxide. *Journal of Colloid and Interface Science*. 2016;465: 76–82. https://doi.org/10.1016/j.jcis.2015.11.043

14. Lin Z, Chen J. Magnetic Fe$_3$O$_4$@MgAl-LDH@La(OH)$_3$ composites with a hierarchical core-shell structure for phosphate removal from wastewater and inhibition of labile sedimentary phosphorus release. *Chemosphere*. 2021; 264: 128551. https://doi.org/10.1016/j.chemosphere.2020.128551

15. APHA (American Public Health Association). Standard methods for the examination of water and wastewater, 19th ed. *APHA*, Washington, DC. 1995.

16. Raghasudha M., Ravinder D., Veerasomaiah P. Magnetic properties of Cr-substituted Co-ferrite nanoparticles synthesized by citrate-gel autocombustion method. *Journal of Nanostructure in Chemistry*. 2013;3: 63. https://doi.org/10.1186/2193-8865-3-63

17. Li Z., Dai J., Cheng C., Suo Z., quing W. Synthesis and magnetic properties of chromium doped cobalt ferrite nanotubes. *Materials Research Express*. 2020;7: 086102. https://doi.org/10.1088/2053-1591/abae26

18. Fournier J. T., Landry R. J. ESR of Exchange coupled Cr^{3+} ions in phosphate glass. *The Journal of Chemical Physics*. 1971;55: 2522–2525. https://doi.org/10.1063/1.1676442

19. Worsztynowicza A., Kaczmareka S. M., Kurzawab M., Bosacka M. Magnetic study of Cr^{3+} ion in M$_2$CrV$_3$O$_{11-x}$ (M=Zn, Mg) compounds. *Journal of Solid State Chemistry*. 2005;178: 2231–2236. https://doi.org/10.1016/j.jssc.2005.04.033

20. Shannon R. D. Revised effective ionic radii and systematic studies of interatomic distances in halides

Condensed Matter and Interphases / Конденсированные среды и межфазные границы 2022;24(3): 306–314

Qui Anh Tran et al. Synthesis of magnetic chromium substituted cobalt ferrite Co(Cr$_x$Fe$_{1-x}$)$_2$O$_4$ adsorbents...

and chalcogenides. *Acta Crystallographica Section A*. 1976;32: 751–767. https://doi.org/10.1107/S0567739476001551

21. Del Bubba M., Arias C. A., Brix H. Phosphorus adsorption maximum of sands for use as media in subsurface flow constructed reed beds as measured by the Langmuir isotherm, *Water Research*. 2003;37: 3390–3400. https://doi.org/10.1016/S0043-1354(03)00231-8

22. Rai D., Moore D. A., Hess N. J., Rao L., Clark S. B. Chromium(III) hydroxide solubility in the aqueous Na$^+$–OH$^-$–H$_2$PO$_4^-$–HPO$_4^{2-}$–PO$_4^{3-}$–H$_2$O system: a thermodynamic model. *Journal of Solution Chemistry*. 2007;36: 1213–1242. https://doi.org/10.1007/s10953-007-9179-5

23. Lente G., Magalhães M. E. A., Fábián. I. Kinetics and mechanism of complex formation reactions in the iron(III)-phosphate ion system at large iron(III) excess. Formation of a tetranuclear complex. *Inorganic Chemistry*. 2000;39: 1950–1954. https://doi.org/10.1021/ic991017p

Information about the authors

Qui Anh Tran, 4th year student, Faculty of Chemistry, University of Science, Vietnam National University (Ho Chi Minh City, Vietnam).

trananh370@gmail.com

https://orcid.org/0000-0002-0365-8794

Nhat Linh Tran, 4th year student, Faculty of Chemistry, University of Science, Vietnam National University (Ho Chi Minh City, Vietnam).

tnllinh95@gmail.com

https://orcid.org/0000-0001-8527-1958

Dang Khoa Nguyen Anh, 3rd year student, Faculty of Chemistry, University of Science, Vietnam National University (Ho Chi Minh City, Vietnam).

nguyenkhoa260701@gmail.com

https://orcid.org/0000-0002-0968-0968

Quynh Nhu Le Thi, 3rd year student, Faculty of Chemistry, University of Science, Vietnam National University (Ho Chi Minh City, Vietnam).

ltqnhu2608@gmail.com

https://orcid.org/0000-0002-8081-5570

The Luan Nguyen, Master in Chemistry, Faculty of Chemistry, University of Science, Vietnam National University (Ho Chi Minh City, Vietnam).

ntluan@hcmus.edu.vn

https://orcid.org/0000-0001-6305-6878

Huu Thinh Pham Nguyen, Master in Chemistry, Faculty of Chemistry, University of Science, Vietnam National University (Ho Chi Minh City, Vietnam).

pnhthinh@hcmus.edu.vn

https://orcid.org/0000-0002-9308-5263

Anh Tien Nguyen, PhD in Chemistry, Chief of Inorganic Chemistry Department, Ho Chi Minh City University of Education (Ho Chi Minh City, Vietnam).

tienna@hcmue.edu.vn

https://orcid.org/0000-0002-4396-0349

Quoc Thiet Nguyen, PhD in Chemistry, Institute of Applied Materials Science, Vietnam Academy of Science and Technology (Ho Chi Minh City, Vietnam).

ngqthiet@yahoo.com

https://orcid.org/0000-0002-2218-9225

Tien Khoa Le, PhD in Chemistry, Chief of Inorganic Chemistry Department, University of Science, Vietnam National University (Ho Chi Minh City, Vietnam).

ltkhoa@hcmus.edu.vn

https://orcid.org/0000-0003-0058-0298

Condensed Matter and Interphases

Original articles

The effect of the moisture content in benzoic acid on the electrical conductivity of its melts

V. I. Kichigin[1], I. V. Petukhov[1✉], A. R. Kornilitsyn[1], S. S. Mushinsky[2]

[1]*Perm State University,
15 Bukireva str., Perm 614990, Russian Federation*

[2]*Perm Scientific Industrial Instrument-Making Company,
106 25th October str., Perm 614990, Russian Federation*

Abstract

The purpose of our study was to analyse the effect of the moisture content in benzoic acid on the electrical conductivity of its melts.

The measurements were performed using impedance spectroscopy in a hermetically sealed metal cell with the temperature of the melts being 160–200 °C. Samples of benzoic acid with different moisture content were used: (i) as-received benzoic acid; (ii) acid dried over anhydrous calcium chloride; (iii) acid exposed to air at 100 % relative humidity.

The study demonstrated that electrical conductivity increased with an increase in the amount of moisture in the acid (the conductivity of the sample with the highest moisture content was about 2.5 times higher than that of the driest sample).

The results obtained are of importance for understanding the mechanisms of proton exchange processes on lithium niobate crystals and can be used for the production of proton-exchange waveguides with stable characteristics.

Keywords: Electrical conductivity, Benzoic acid, Melt, Moisture, Proton exchange

✉ Igor V. Petukhov, e-mail: petukhov-309@yandex.ru

Condensed Matter and Interphases / Конденсированные среды и межфазные границы   2022;24(3): 315–320

V. I. Kichigin et al.   The effect of the moisture content in benzoic acid on the electrical conductivity of its melts

1. Introduction

Benzoic acid (BA) is widely used as a source of protons to perform proton exchange on lithium niobate (LN) $LiNbO_3$ crystals in order to produce integrated optical devices. During the proton exchange, a lithium niobate crystal is kept in a BA melt at a temperature of 170–200 °C. During this process, some of the lithium ions in the surface layer of the $LiNbO_3$ crystal are replaced with protons: $LiNbO_3 + xH^+ \leftrightarrow H_xLi_{1-x}NbO_3 + xLi^+$.

Furthermore, lithium ions in the lithium niobate crystal are replaced with hydrogen ions (protons) followed by the formation of a solid solution $H_xLi_{1-x}NbO_3$. This results in an increase in the refractive index of the surface layer of the crystal [1–4]. Due to the increase in the refractive index and the total internal reflection, light travels through the waveguide.

Some researchers believe that it is possible to control the intensity of the proton exchange process by reducing the acidity of the benzoic acid melt with lithium benzoate [5]. We should note that there are very few studies focusing on the state of benzoic acid in the melt. Thus, [6] demonstrates that the concentration of free protons in a benzoic acid melt is considerably low, and the protons required for proton exchange may result from dissociative adsorption of BA molecules in the surface of $LiNbO_3$. Analysis of the IR spectra of benzoic acid melts demonstrated that benzoic acid molecules are mostly present in the melt in the form of dimers [6]. Further studies [7, 8] determined that small amounts of water (about 0.5 wt%) added to benzoic acid intensify the proton exchange process. This could be explained by the increased dissociation of BA and increased concentration of protons in the BA melt. At the same time, only a few studies consider the effect of water added to benzoic acid on the result of proton exchange [9, 10]. Thus, they determined a significant influence of water in a melt of benzoic acid and lithium benzoate on the characteristics of the waveguides formed in lithium niobate [10].

The purpose of our study was to analyse the effect of moisture in benzoic acid on the concentration of free protons in a benzoic acid melt under conditions simulating those of the proton exchange process on lithium niobate. For this purpose, we measured the electrical conductivity of benzoic acid melts prepared in different ways and with different amounts of water in them.

2. Experimental

In our experiments we used benzoic acid prepared in the following ways.

1) As-received benzoic acid (analytical grade) stored in a closed container in a laboratory for 10 months (storage temperature 22–24 °C, the air humidity up to 60 %). This sample will be further on referred to as the BA with the "natural" moisture content.

2) The same BA after drying in a desiccator over calcined calcium chloride for 7 days (dried BA). The weight loss was 0.02 %.

3) The same BA after 5-7 days in a desiccator at 100 % relative air humidity. The weight increase was 0.02 %.

The method used in the experiment was practically the same as the one described in [6]. A hermetic aluminium cell was used (Fig. 1). The cell had two identical metal electrodes embedded in fluoropolymer. The diameter of the electrodes was 5 mm, and the distance between the electrodes was ~ 2 mm. The electrodes were placed parallel to each other. The electrodes were made of either titanium (as in [6]) or aluminium. Before the experiment the electrode surface was polished with fine abrasive cloth and cleaned with ethanol. The lid of the cell had a thermocouple inlet. The cell was sealed to prevent the release of benzoic acid and water vapours during the measurements. The range of operating temperatures T was 160–200 °C. The accuracy of the maintained operating temperature was ±1 °C. The cell was calibrated using 0.01 and 0.02 M solutions of potassium chloride.

Preliminary tests demonstrated that, when kept in BA melts for several hours, titanium and aluminium remain quite stable, and no corrosion products capable of affecting the electrical conductivity of the melt were observed. However, we should note that in the studied temperature range, thin oxide films formed on the surface of Ti and Al in BA melts.

To determine the conductivity of BA melts, we measured the frequency dependences of the impedance of the cell using a Solartron 1287/1255 analyser (Solartron Analytical). The amplitude

Condensed Matter and Interphases / Конденсированные среды и межфазные границы   2022;24(3): 315–320

V. I. Kichigin et al.   The effect of the moisture content in benzoic acid on the electrical conductivity of its melts
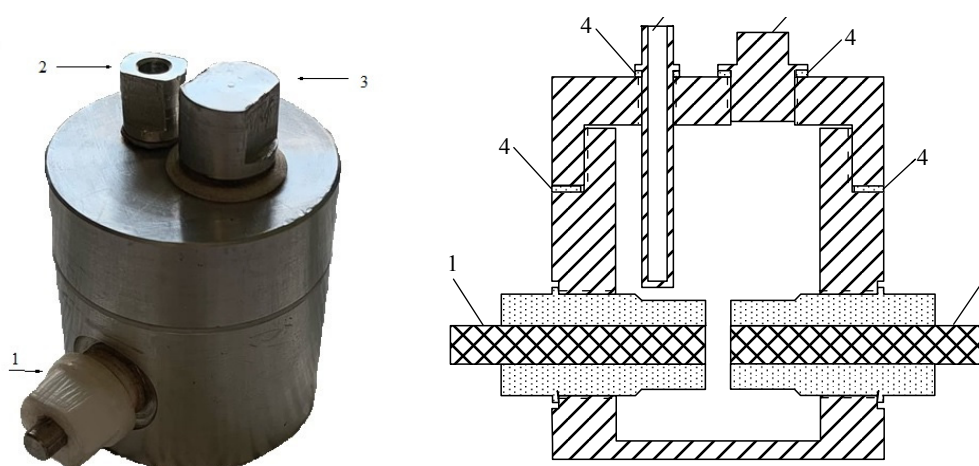
Fig. 1. External appearance and cross section of the cell used for conductivity measurements: *1* – titanium or aluminium electrodes; *2* – thermocouple inlet; *3* – plug; *4* – seal ring (fluoropolymer).

of the signal was up to 2 V. Large amplitudes of the alternating signal were used due to the high impedance (up to ~5×10⁷ Ohm). The resistance of the melt demonstrated a linear current-voltage characteristic. Therefore, a large amplitude signal can be used to reduce the noise in the impedance response [11].

3. Results and discussion

Experimental graphs of the impedance spectra on the complex plane are an almost perfect capacitive semicircle with a large diameter and a centre insignificantly displaced from the abscissa (Fig. 2). The semicircle is determined by the electrical resistance of the melt between the electrodes and the geometric capacitance of the measuring cell (not the double-layer capacity on the electrode-melt interface). The explanation for this is provided in [6]. The resistance of the melt is determined by the diameter of the capacitive semicircle (Fig. 2), rather than by the intercept of the capacitive arc on the abscissa at high frequencies f (when the influence of the geometric capacitance is observed, the real axis intercept at $f \rightarrow \infty$ practically equals zero).

Geometric capacitance $C_g = \varepsilon_0\varepsilon/d$ ($\varepsilon_0 = 8.854 \times 10^{-12}$, F/m is the electric constant, ε is the dielectric constant of the medium filling the cell, d is the distance between the electrodes) is parallel to series connection of the interfacial impedance and the resistance of the medium between the electrodes [12]. Geometric capacitance has very low values (usually 10^{-11} F [12]) and its impedance $1/(\omega C_g)$ has high values. However, if the resistance

of the medium between the electrodes and/or the interfacial impedance is high, then the effect of C_g on the measured impedance of the cell at high frequencies is dominant. Therefore, the effect of C_g is taken into account when studying high-resistance systems [13–16].

After the measurements in the BA melt (the highest temperature 200 °C) and cleaning the
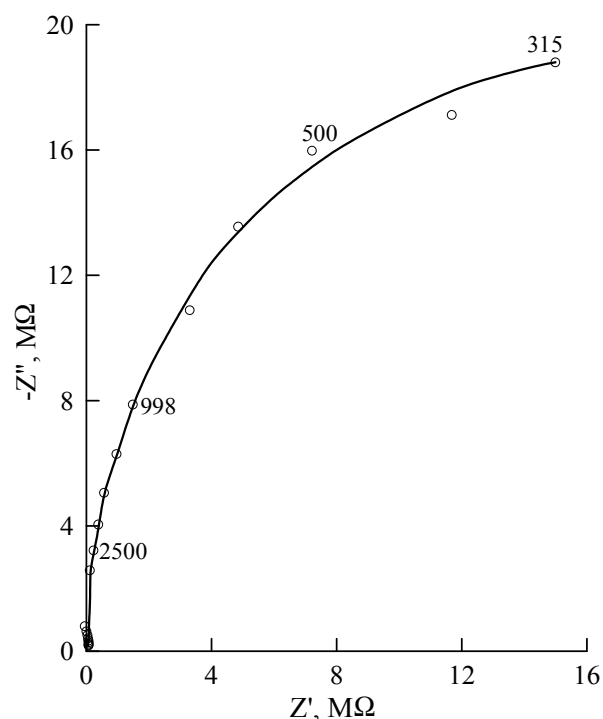
Fig. 2. The impedance graph for benzoic acid melt at 190 °C. Benzoic acid was exposed to air at 100 % relative humidity. The numbers next to the symbols are the frequencies in Hz

Condensed Matter and Interphases / Конденсированные среды и межфазные границы   2022;24(3): 315–320

V. I. Kichigin et al.   The effect of the moisture content in benzoic acid on the electrical conductivity of its melts

electrodes from the residues of benzoic acid in isopropyl and ethyl alcohol, the impedance was measured in a 0.02 M KCl aqueous solution with the same geometry of the cell. In this case the measured impedance was determined by the impedance of oxide layers, since the resistance of the solution between the electrodes (about 200 Ohm) was significantly lower than the impedance of the electrode with an oxide film on the surface. The study demonstrated that the diameter of the capacitive arc on the impedance graph of the cell with oxidised electrodes in an aqueous solution at room temperature is by about two orders of magnitude smaller than the diameter of the semicircle on the impedance graph of the cell with the BA melt, even at a higher temperature of the melt. At higher temperatures of the aqueous solution the impedance of the cell with oxidised electrodes reduced. We can thus assume that the difference in the resistance of the melt and the oxide film on the electrode surface at temperatures of 160–200 °C increases (more than two orders of magnitude). This proves that the high impedance of the cell with the BA melt is primarily accounted for by the resistance of the melt between the electrodes, rather than by the oxide film on the electrodes. In accordance with this, the obtained values of the electrical resistance of BA melts did not depend on the material of the electrodes (Ti or Al).

Based on the impedance graph (Fig. 2) we can calculate the capacitance of the cell with a BA melt using the relation [11] $\omega_m RC = 1$, where $\omega_m = 2\pi f_m$, f_m is the characteristic frequency, when the imaginary part of the impedance is maximum, and R is the resistance determined by the diameter of the semicircle. When $f_m \approx 315$ Hz, $R \approx 35$ MΩ (Fig. 2), we obtain $C \approx 1.4\times10^{-11}$ F, which complies with the geometric capacitance by the order of magnitude. When measured in an aqueous solution of electrolyte with oxidised electrodes (after the experiment with a BA melt), the values of the capacitance obtained based on the impedance graphs vary from several tenths of µF to several µF, i.e. they are noticeably different from the capacitance in the melt.

The results of the measurement of electrical conductivity κ of BA melts in the range of temperatures 160–200 °C are shown in Fig. 3. Curve 2 agrees well with the log κ, 1/T dependence

obtained in [6], where as-received benzoic acid was used. When more water is added to BA, the electrical conductivity naturally increases and the slope of log κ-1/T lines decreases (Fig. 3). Therefore, the initial moisture content in benzoic acid has a marked effect on the electrical conductivity of the melt. The changes are obviously caused by the presence of H_2O molecules in the melt. Removal of water from a BA melt can be hindered by the formation of BA-H_2O complexes [17] followed by their transformations:

$$(BH)_2 + H_2O = BH \times H_2O + BH \tag{1}$$

$$BH \times H_2O = B^- + H_3O^+ \tag{2}$$
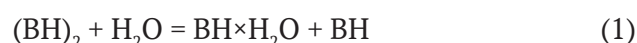
where $(BH)_2$ is a dimer of benzoic acid and $BH \times H_2O$ is a BA-H_2O complex.

The values of the activation energy E_a of the ion transfer process in the melt calculated based on the slopes of log κ−1/T lines using the formula $E_a = -2.303Rb$ (R is the gas constant, b is the slope), were 53.3 ± 6.2, 39.2 ± 3.1 and 37.6 ± 5.4 kJ×mol^{-1} for the dried BA, the BA with natural moisture content, and the BA kept at 100 % air humidity respectively. We can see that the two samples of BA containing some moisture have similar values
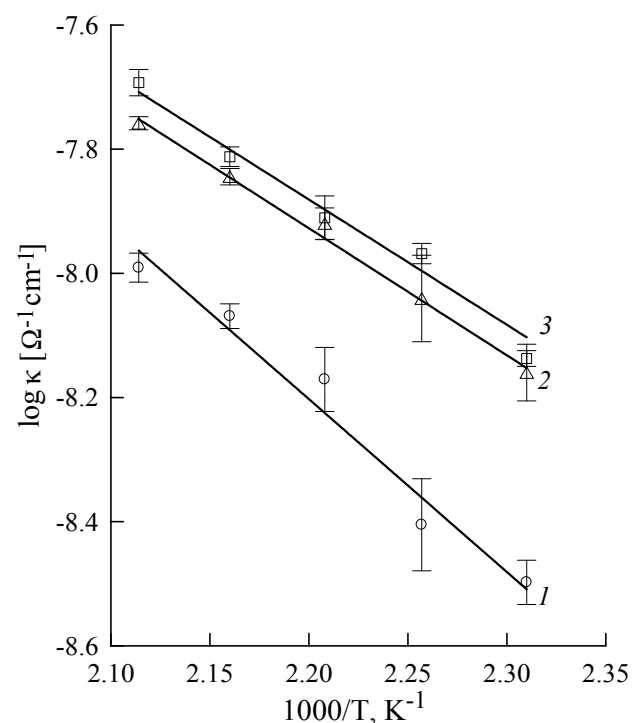
Fig. 3. Temperature dependence of electrical conductivity of benzoic acid melts: 1 – dried benzoic acid; 2 – benzoic acid with natural moisture content; 3 – benzoic acid exposed to air at 100 % relative humidity

Condensed Matter and Interphases / Конденсированные среды и межфазные границы   2022;24(3): 315–320

V. I. Kichigin et al.   The effect of the moisture content in benzoic acid on the electrical conductivity of its melts

of E_a, while E_a of the dried BA is significantly higher. In moisture containing BA, charge carriers can be formed by reactions (1) and (2). In dried BA, small number of ions is presumably formed according to the autoprotolysis reaction:

$$(BH)_2 = BH_2^+ + B^- \tag{3}$$

The difference in the nature and mechanism of charge carrier generation results in different values of E_a for moisture containing and dried samples of benzoic acid.

Thus, small amounts of water in benzoic acid melts result in an increase in electrical conductivity. Such an increase may result from a larger number of ions in the melt.

4. Conclusions

The obtained results demonstrate that the effect of moisture in benzoic acid on the electrical conductivity of BA melts and consequently on the concentration of free ions in the melt is noticeable (the sample with the highest moisture content differs from the dried one by 2.5 times at 160 °C), and should be taken into account during the proton exchange process on lithium niobate.

Author contributions

All authors made an equivalent contribution to the preparation of the publication.

Conflict of interests

The authors declare that they have no known competing financial interests or personal relationships that could have influenced the work reported in this paper.

References

1. Korkishko Yu. N., Fedorov V. A. Structural phase diagram of proton-exchange $H_xLi_{1-x}NbO_3$ waveguides in lithium niobate crystals. *Crystallography Reports*. 1999;44(2): 237–246. Available at: https://www.elibrary.ru/item.asp?id=13324513

2. Suchoski P. G., Findakly T. K., Leonberger F. J. Stable low-loss proton-exchanged $LiNbO_3$ waveguide devices with no electro-optic degradation. *Optics Letters*. 1988;13(11): 1050–1052. https://doi.org/10.1364/OL.13.001050

3. Korkishko Y. N., Fedorov V. A., Feoktistova O. Y. $LiNbO_3$ optical waveguide fabrication by high-temperature proton exchange. *Journal of Lightwave Technology*. 2000;18(4): 562–568. https://doi.org/10.1109/50.838131

4. Korkishko Yu. N., Fedorov V. A. Structural phase diagram of $H_xLi_{1-x}NbO_3$ waveguides: the correlation between optical and structural properties. *IEEE Journal of Selected Topics in Quantum Electronics*. 1996;2(2): 187–196. https://doi.org/10.1109/2944.577359

5. Korkishko Yu. N., Fedorov V. A., De Micheli M. P., Baldi P. Relationships between structural and optical properties of proton-exchanged waveguides on Z-cut lithium niobate. *Applied Optics*. 1996;35(36): 7056–7060. https://doi.org/10.1364/AO.35.007056

6. Kichigin V. I., Petukhov I. V., Mushinskii S. S., Karmanov V. I., Shevtsov D. I. Electrical conductivity and IR spectra of molten benzoic acid. *Russian Journal of Applied Chemistry*. 2011;84(12): 2060–2064. https://doi.org/10.1134/S1070427211120081

7. Petukhov I. V., Kichigin V. I., Mushinskii S. S., Minkin A. M., Shevtsov D. I. Effect of water contained in benzoic acid on the proton exchange process, the structure and the properties of proton-exchange waveguides in lithium niobate single crystals. *Condensed Matter and Interphases*. 2012;14(1): 119–123. (In Russ., abstract in Eng.). Available at: https://www.elibrary.ru/item.asp?id=17711946

8. Mushinsky S. S, Minkin A. M., Kichigin V. I., Petukhov I. V., Shevtsov D. I., Malinina L. N., Volyntsev A. B., Shur V. Ya. Water effect on proton exchange of X-cut lithium niobate in the melt of benzoic acid. *Ferroelectrics*. 2015;476(1): 84–93. https://doi.org/10.1080/00150193.2015.998530

9. Rambu A. P., Apetrei A. M., Doutre F., Tronche H., De Micheli M. P., Tascu S. Analysis of high-index contrast lithium niobate waveguides fabricated by high vacuum proton exchange. *Journal of Lightwave Technology*. 2018;36(13): 2675–2684. https://doi.org/10.1109/JLT.2018.2822317

10. Rambu A. P., Apetrei A. M., Tascu S. Role of the high vacuum in the precise control of index contrasts and index profiles of $LiNbO_3$ waveguides fabricated by high vacuum proton exchange. *Optics and Laser Technology*. 2019;118: 109–114. https://doi.org/10.1016/j.optlastec.2019.05.005

11. Orazem M. E., Tribollet B. *Electrochemical impedance spectroscopy*. Hoboken, New Jersey: John Wiley & Sons, Inc., 2008. 523 p. https://doi.org/10.1002/9780470381588

12. Sluyters-Rehbach M. Impedances of electrochemical systems: terminology, nomenclature and representation. Part I: Cells with metal electrodes and liquid solutions (IUPAC Recommendations 1994). *Pure Appl. Chem*. IUPAC Standards Online 1994;66(9) 1831–1891. https://doi.org/10.1351/pac199466091831

13. Faidi S. E., Scantlebury J. D. The limitations of the electrochemical impedance technique in the study of electrode reactions occurring in low conductivity media. *Journal of The Electrochemical Society*. 1989;136(4): 990–995. https://doi.org/10.1149/1.2096898

Condensed Matter and Interphases / Конденсированные среды и межфазные границы   2022;24(3): 315–320

V. I. Kichigin et al.   The effect of the moisture content in benzoic acid on the electrical conductivity of its melts

14. Yezer B. A., Khair A. S., Sides P. J., Prieve D. C. Use of electrochemical impedance spectroscopy to determine double-layer capacitance in doped nonpolar liquids. *Journal of Colloid and Interface Science.* 2015;449: 2–12. https://doi.org/10.1016/j.jcis.2014.08.052

15. SatyanarayanaRaju C. H. S. R. V., Krishnamurthy C. V. Charge migration model for the impedance response of DI water. *AIP Advances.* 2019;9: 035141. https://doi.org/10.1063/1.5078709

16. Lensch H., Bastuck M., Baur T., Schütze A., Sauerwald T. Impedance model for a high-temperature ceramic humidity sensor. *Journal of Sensors and Sensor Systems.* 2019;8: 161–169. https://doi.org/10.5194/jsss-8-161-2019

17. Schnitzler E. G., Jäger W. The benzoic acid–water complex: a potential atmospheric nucleation precursor studied using microwave spectroscopy and *ab initio* calculations. *Phys. Chem. Chem. Phys.* 2014;16(6): 2305–2314. https://doi.org/10.1039/c3cp54486a

Information about the authors

Vladimir I. Kichigin, Cand. Sci. (Chem.), Research Fellow, Research Fellow at the Department of Physical Chemistry, Perm State University (Perm, Russian Federation).

https://orcid.org/0000-0002-4668-0756
kichigin@psu.ru

Igor V. Petukhov, Cand. Sci. (Chem.), Associate Professor at the Department of Physical Chemistry, Perm State University (Perm, Russian Federation).

https://orcid.org/0000-0002-3110-668x
petukhov-309@yandex.ru

Andrey R. Kornilitsyn, Fourth year student, Faculty of Chemistry; Perm State University (Perm, Russian Federation).

https://orcid.org/0000-0002-8267-0168

Sergey S. Mushinsky, Head of department, Perm Scientific Industrial Instrument-Making Company (Perm, Russian Federation).

https://orcid.org/0000-0003-0567-2933

Original articles

The influence of the structure of carbon nanotubes in the polymer matrix on interfacial effects in nanocomposites

G. V. Kozlov, I. V. Dolbin✉

Kh.M. Berbekov Kabardino-Balkarian State University,
173 Chernyshevsky str., Nalchik 360004, Russian Federation

Abstract

It is now a well-known fact that interfacial effects play a decisive role in the formation of the properties of polymer composites on the whole and nanocomposites in particular. Therefore, this article investigates the relations between the structure of carbon nanotubes in the polymer matrix of a nanocomposite and the level of interfacial adhesion which is characterised by dimensionless parameter b_α.

It was shown that carbon nanotubes form ring-like structures, which are analogous to macromolecular coils of branched polymer chains and represent a specific type of aggregates for nanofillers of this type. Such ring-like structures can be geometrically described either by a full circle ("closed" structures) or by a part of it (arc) ("open" structures). The amplification of the aggregation process of carbon nanotubes characterised by a decrease in the radius of the ring-like structures is accompanied by a decrease in the fractal dimension of their surface compared to the nominal maximum value. When the ring-like structures reach the smallest possible (about 130 nm) radius, their surface is perceived by the polymer matrix as absolutely smooth, i.e. with a dimension of d=2. This determines the transition of the level of interfacial adhesion from nanoadhesion to perfect adhesion by Kerner. The nanoadhesion effect allows significantly improving the properties of polymer/carbon nanotube nanocomposites. The nanoadhesion effect only takes place if the surface of the ring-like structures of nanotubes is fractal.

Parameter b_α, which characterises the level of interfacial adhesion in polymer nanocomposites, linearly increases with an increase in the fractal dimension of the surface of carbon nanotube aggregates. In this case, the highest attainable nominal dimension of the nanotubes surface, equal to ~ 2.85, is only achieved for "open" ring-like structures. The proposed analytical methods make it possible to predict both interfacial characteristics and the properties of polymer/carbon nanotube nanocomposites.

Keywords: nanocomposite, carbon nanotubes, ring-like structures, aggregation, interfacial adhesion, surface, fractal dimension

✉ Igor V. Dolbin, e-mail: i_dolbin@mail.ru

Condensed Matter and Interphases / Конденсированные среды и межфазные границы   2022;24(3): 321–325

G. V. Kozlov, I. V. Dolbin   The influence of the structure of carbon nanotubes in the polymer matrix...

1. Introduction

Currently, carbon nanotubes, which have a number of unique properties (in particular, an elastic modulus of up to 1 TPa), are considered one of the most promising nanofillers for polymer nanocomposites [1]. However, a significant number of experimental studies have shown that an increase in the elastic modulus of the matrix polymer resulting from the introduction of the nanofiller is much smaller than expected [2, 3]. As a rule, this has been explained by a low degree of dispersion of carbon nanotubes or, which is just the same, a high degree of aggregation of the nanofiller [4, 5]. It should be noted that generally nanoparticles have a high tendency to aggregate due to very high values of specific surface [6, 7]. However, this effect has not been generalised to a proper theory.

As is known [8, 9], the structure of initially one-dimensional carbon nanotubes in any environment (melt, solution, solid phase) has its own specific features such as the formation of ring-like structures, which structurally are similar to macromolecular coils of branched polymer chains [8]. This ability is common to all one-dimensional (1D-dimensional) fillers [10]. Since it is currently believed that the properties of polymer nanocomposites are determined by the structure of the nanofiller (or more precisely, its aggregates) in the polymer matrix [11, 12], it seems necessary to take into account the formation of these ring-like formations. Thus, the purpose of this work is to quantitatively analyse the change in the characteristics of interfacial effects (fractal dimension of the nanotube surface and the level of interfacial adhesion) as a function of the structure of carbon nanotube aggregates modelled as ring-like formations, using epoxy polymer/multi-walled carbon nanotube (EP/MCNT) nanocomposites as an example [13].

2. Experimental

Multi-walled carbon nanotubes (MCNTs) obtained by deposition of chemical vapours in the Research Institute of Petroleum Industry (Iran) were used as nanofillers. They had an outer diameter of 10–50 nm, a length of 1–3 μm and their mass content in the studied nanocomposites varied in the range of 0.25–10.0 wt% [13].

A LY-5052 low-viscosity epoxy resin and a HY-5052 hardener were used to form the polymer matrix of EP/MCNT nanocomposites. First, MCNTs were dispersed in the hardener by sonication for 30 min. The sonication was carried by the pulse method at 60% amplitude to avoid overheating the material. The epoxy resin and hardener were mixed at a mass ratio of 100:30, after that the mixture was stirred at 900 rpm for 15 min. Then it was poured into metal molds and cured at 333 K for 15 hours [13].

Mechanical tests for uniaxial tension were performed using a Zwick/Roel machine at a temperature of 293 K and a slider speed of 1 mm/min. The used samples were 168 mm long, 13 mm wide, and 5 mm thick. The average value for 5 samples was taken as the test result [13].

3. Results and Discussion

Since the authors [13] did not use any methods of nanofiller processing (for example, functionalisation, *in situ* polymerisation, etc.) when preparing EP/MCNTs, the radius of ring-like MCNT formations R_{CNT} could be determined using the ratio [10, 14]:

$$\left(2R_{CNT}\right)^3 = \frac{\pi r_{CNT}^2 L_{CNT}}{\varphi_n}, \tag{1}$$

where r_{CNT} and L_{CNT} are the radius and the length of the carbon nanotube, respectively, φ_n is the volume content of the nanofiller estimated by the following simple formula [6]:

$$\varphi_n = \frac{W_n}{\rho_n}, \tag{2}$$

where W_n and ρ_n are the weight content and density of carbon nanofiller, respectively. For MCNT, the value of $\rho_n = 1500$ kg/m³ [15].

Further, it is possible to determine the effective (real) fractal dimension of the surface of ring-like MCNT formations d_{sur} using the following equation [16]:

$$\frac{E_n}{E_m} = 1 + 130\varphi_n\left[1 - \left(d - d_{sur}\right)^{1/1,7}\right], \tag{3}$$

where E_n and E_m are the elastic moduli of the nanocomposite and matrix polymer, respectively (the ratio E_n/E_m is commonly referred to as reinforcement degree of the nanocomposite) and d is the dimensionality of the Euclidean space in

which the fractal is considered (obviously, in our study, $d = 3$).

Fig. 1 shows the dependence of fractal dimension d_{sur} of the surface of nanotube aggregates (ring-like formations) on the radius of these formations R_{CNT} for EP/MCNT nanocomposites. As can be seen from the graph in Fig. 1, there was a linear decrease in d_{sur} as R_{CNT} decreased, i.e. as MCNT aggregation increased [9]. The value of $d_{sur} = 2.0$ determining the smooth Euclidean surface of MCNT aggregates was achieved at a certain finite value of $R_{CNT} \approx 0.13$ μm. The latter result was expected since the condition $R_{CNT} = 0$ is physically unrealistic and the minimum value of R_{CNT} cannot be less than two outer diameters of the nanotube, i.e. 0.10 μm in the studied case. The dependence $d_{sur}(R_{CNT})$ presented in Fig. 1 can be described analytically by the following empirical equation:

$$d_{sur} = 2 + 1,6\left(R_{CNT} - 0,13\right), \tag{4}$$

where the value of R_{CNT} was given in μm.

It should be noted that the value of d_{sur} for separate straight carbon nanotubes was ~ 2.85. From equation (4), it follows that such maximum value of d_{sur} is achieved for nanotubes with $R_{CNT} > 0.66$ μm. The authors [17] revealed a significant change in the properties of epoxy polymer/single-walled carbon nanotube nanocomposites during the transition of ring-like formations of these nanotubes from "closed" to "open" structures. The latter structure type referred to a nanotube in the shape of an arc, and the former could be approximated by a ring. It is obvious that boundary R_{CNT}^{cr} between these types of structures of ring-like formations can be determined purely geometrically by equation [17]:

$$R_{CNT}^{cr} = \frac{L_{CNT}}{2\pi}. \tag{5}$$

For the maximum length of the MCNT in the studied nanocomposites, $L_{CNT} = 3$ μm, the value of $R_{CNT}^{cr} \approx 0.48$ μm, which is quite close to the above value of $R_{CNT} \approx 0.66$ μm at which the condition of $d_{sur} = 2.85$ is fulfilled. This means that the maximum possible value of $d_{sur} = 2.85$ for carbon nanotubes is only achieved for fully "open" ring-like MCNT formations, i.e. under the condition of $R_{CNT} > R_{CNT}^{cr}$ [17].
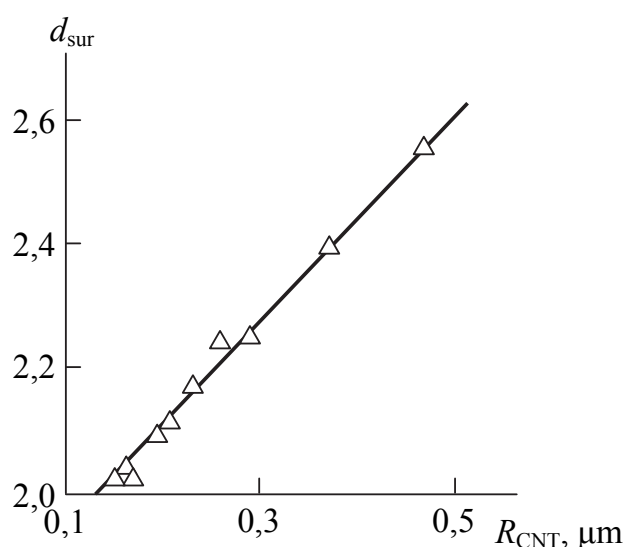
Fig. 1. Dependence of the dimension of the surface of ring-like formations of carbon nanotubes d_{sur} on their radius R_{CNT} for EP/MNCT nanocomposites

The level of interfacial adhesion between the polymer matrix and the nanofiller can be estimated quantitatively using dimensionless parameter b_α, which also allows the qualitative gradation of this level. Thus, when $b_\alpha = 0$, no interfacial adhesion is present; $b_\alpha = 1.0$ corresponds to perfect adhesion by Kerner; and $b_\alpha > 1.0$ defines the nanoadhesion effect [1]. The value of b_α can be determined according to the following percolation relation [6]:

$$\frac{E_n}{E_m} = 1 + 11\left(2,85 b_\alpha \varphi_n\right)^{1,7}. \tag{6}$$

Fig. 2 shows the dependence of the level of interfacial adhesion characterised by parameter b_α on fractal dimension d_{sur} of the surface of the MNCT aggregates for the studied nanocomposites. As can be seen, there is a linear increase in b_α with an increase in d_{sur}, which can be described analytically by the following equation:

$$b_\alpha = 1 + 11,2\left(d_{sur} - 2\right). \tag{7}$$

Equation (7) allows us to draw two important conclusions. First, the nanoadhesion effect ($b_\alpha > 1.0$) is only observed for the aggregates of a nanofiller with a fractal surface, i.e. for $d_{sur} > 2$. At $d_{sur} = 2.0$, i.e. a smooth Euclidean surface of the nanofiller, $b_\alpha = 1.0$, which corresponds to perfect interfacial adhesion by Kerner. Secondly, the

Condensed Matter and Interphases / Конденсированные среды и межфазные границы   2022;24(3): 321–325

G. V. Kozlov, I. V. Dolbin   The influence of the structure of carbon nanotubes in the polymer matrix...
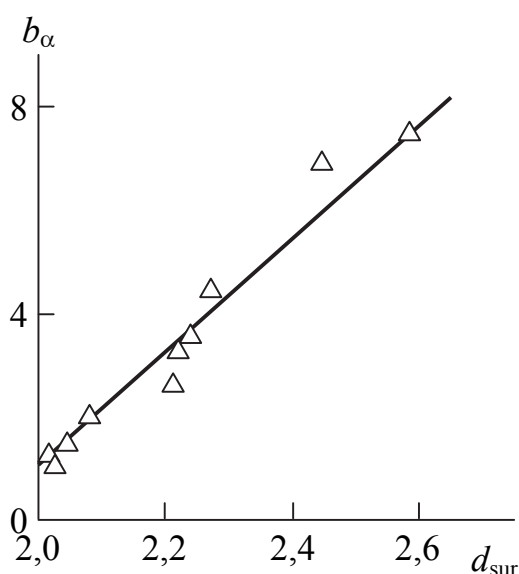
Fig. 2. Dependence of the level of interfacial adhesion characterised by parameter b_α on the dimension of the surface of ring-like formations of carbon nanotubes d_{sur} for EP/MNCT nanocomposites

combination of equations (6) and (7) indicates a very strong influence of the level of interfacial adhesion, or more precisely nanoadhesion, on the properties of nanocomposites. Thus, under the condition of $b_\alpha = 1.0$ (perfect adhesion) and the maximum value of $\varphi_n = 0.0667$ for the studied nanocomposites, the value of $E_n/E_m = 1.65$, which is close to the experimental value of 1.74, and the value of E_n in this case with $E_m = 3.11$ GPa, is 5.2 GPa. If at the specified value of φ_n the maximum value of $d_{sur} = 2.85$ is observed, then according to equation (7) $b_a = 10.5$. It follows from equation (6) that in the latter case $E_n/E_m = 36.6$ or $E_n = 113.9$ GPa. Thus, the transition from perfect adhesion to the maximum possible level of nanoadhesion for the studied nanocomposites ($b_\alpha = 10.5$) allows increasing the elastic modulus of nanocomposites by approximately 22 times.

4. Conclusions

Therefore, the results of this work have demonstrated that the dimension of the surface of aggregates (ring-like formations) of carbon nanotubes is controlled by their radius, i.e. the degree of aggregation. Nominal dimension of this surface can only be achieved for "open" ring-like formations. The nanoadhesion effect, which strongly affects the properties of nanocomposites, can only be observed in the case of fractal

surfaces, while the smooth Euclidean surface of the nanofiller corresponds to perfect interfacial adhesion by Kerner. The nanoadhesion effect in polymer nanocomposites opens up many opportunities for improving their properties.

Author contributions

All authors made an equivalent contribution to the preparation of the publication.

Conflict of interests

The authors declare that they have no known competing financial interests or personal relationships that could have influenced the work reported in this paper.

References

1. Moniruzzaman M., Winey K. I. Polymer nanocomposites containing carbon nanotubes. *Macromolecules*. 2006;39(16): 5194–5205. https://doi.org/10.1021/ma060733p

2. Coleman J. N., Khan U., Blau W. J., Gun'ko Y. K. Small but strong: A review of the mechanical properties of carbon nanotube-polymer composites. *Carbon*. 2006;44(6): 1624–1652. https://doi.org/10.1016/j.carbon.2006.02.038

3. Coleman J. N., Cadek M., Ryan K. P., Fonseca A., Nady J. B., Blau W. J., Ferreira M. S. Reinforcement of polymers with carbon nanotubes. The role of an ordered polymer interfacial regions. Experiment and modeling. *Polymer*. 2006;47(23): 8556–8561. https://doi.org/10.1016/j.polymer.2006.10.014

4. Yang K., Gu M., Guo Y., Pan X., Mu G. Effect of carbon nanotube functionalization on the mechanical and thermal properties of epoxy composites. *Carbon*. 2009;47(7): 1723–1737. https://doi.org/10.1016/j.carbon.2009.02.029

5. Supova M., Martynkova G. S., Barabashova K. Effect of nanofiller dispersion in polymer matrices: a review. *Science of Advanced Materials*. 2011;3(1): 1–25. https://doi.org/10.1166/sam.2011.1136

6. Mikitaev A. K., Kozlov G. V., Zaikov G. E. *Polymer Nanocomposites: Variety of Structural Forms and Applications*. New York: Nova Science Publishers, Inc., 2008; 319 p.

7. Kim H., Abdala A. A., Macosko C. W. Graphene/polymer nanocomposites. *Macromolecules*. 2010;43(16): 6515–6530. https://doi.org/10.1021/ma100572e

8. Schaefer D. W., Justice R. S. How nano are nanocomposites? *Macromolecules*. 2007;40(24): 8501–8517. https://doi.org/10.1021/ma070356w

9. Atlukhanova L. B., Dolbin I. V., Kozlov G. V. The physical characteristics of nanofiller and interfacial

Condensed Matter and Interphases / Конденсированные среды и межфазные границы   2022;24(3): 321–325

G. V. Kozlov, I. V. Dolbin   The influence of the structure of carbon nanotubes in the polymer matrix...

regions in nanocomposites with polymer/carbon nanotubes and elastomeric vitreous matrix. *Condenced Matter and Interphases*. 2019;21(4): 471–477. https://doi.org/10.17308/kcmf.2019.21/2358

10. Bridge B. Theoretical modeling of the critical volume fraction for percolation conductivity in fibre-loaded conductive polymer composites. *Journal of Materials Science Letters*. 1989;8(2): 102–103. https://doi.org/10.1007/BF00720265

11. Schaefer D. W., Zhao J., Dowty H., Alexander M., Orler E. B. Carbon nanofibre reinforcement of soft materials. *Soft Matter*. 2008;4(10): 2071–2078. https://doi.org/10.1039/b805314f

12. Kozlov G. V., Dolbin I. V. Theoretical basis for designing high-modulus polymer fibers and nanocomposites based on them. *Fibre Chemistry*. 2021;53(1): 46–49. https://doi.org/10.1007/s10692-021-10237-7

13. Omidi M., Rokni D. T., Milani A. S., Seethaler R. J., Arasteh R. Prediction of the mechanical characteristics of multi-walled carbon nanotube/epoxy composites using a new form of the rule of mixtures. *Carbon*. 2010;48(11): 3218–3228. https://doi.org/10.1016/j.carbon.2010.05.007

14. Kozlov G. V., Magomedov G. M., Magomedov G. M., Dolbin I. V. The structure of carbon nanotubes in a polymer matrix. *Condenced Matter and Interphases*. 2021;23(2): 223–228. https://doi.org/10.17308/kcmf.2021.23/3433

15. Thostenson E. T., Chou T.-W. Processing-structure-multi-functional properties relationship in carbon nanotube/epoxy composites. *Carbon*. 2006;44(12): 3022–3029. https://doi.org/10.1016/j.carbon.2006.05.014

16. Kozlov G. V., Dolbin I. V. Effect of the surface structure of a 2D Nanofiller on the elastic modulus of polymer nanocomposites. *Journal of Surface Investigation: X-ray, Synchrotron and Neutron Techniques*. 2019;13(4): 766–770. https://doi.org/10.1134/S1027451019040268

17. Kozlov G. V., Dolbin I. V. Interrelation between elastic moduli of filler and polymethyl methacrylate-carbon nanotube nanocomposites. *Glass Physics and Chemistry*. 2019;45(4): 277–280. https://doi.org/10.1134/S1087659619040060

Information about the authors

Georgii V. Kozlov, Research Fellow, Kabardino-Balkarian State University named after H. M. Berbekov (Nalchik, Russian Federation).

https://orcid.org/0000-0002-9503-9113
i_dolbin@mail.ru

Igor V. Dolbin, Cand. Sci. (Chem.), Associate Professor at the Department of Organic Chemistry and High-Molecular Compounds, Kabardino-Balkarian State University named after H. M. Berbekov (Nalchik, Russian Federation).

https://orcid.org/0000-0001-9148-2831
i_dolbin@mail.ru

Original articles

Research article
https://doi.org/10.17308/kcmf.2022.24/9855

Structural-phenomenological analysis of interrelation of microstructure indexes and properties of set cement systems

A. A. Ledenev[1] ✉, V. T. Pertsev[2], O. B. Rudakov[2], S. M. Usachev[2]

[1]Air Force Military Educational and Scientific Center «Air Force Academy
named after Professor N. E. Zhukovsky and Y. A. Gagarin» (Voronezh),
54a Starykh Bolshevikov str., Voronezh 394064, Russian Federation

[2]Voronezh State Technical University,
84 20-letiya Oktyabrya str., Voronezh 394006, Russian Federation

Abstract

The study of the chemical and physical processes of solidification of polydisperse cement systems until now is based predominantly on empirical approaches. The phenomenological analysis of the interrelation of structure coefficients of set cement systems at the microlevel with their physical-mechanical properties was proposed as one of scientifically-practical approaches to control of physical and chemical processes of structure formation of controlled-quality concretes. The comparison of the quantity indicators of a microstructure of cement rock and its functional properties can be used for the estimation of structural modifications with a variation in the composition of cement systems. The aim of the study was to obtain quantitative data of the structural-phenomenological analysis of set cement systems for determination of interrelation of microstructure indexes with their physical-mechanical properties.

For the analysis of the structure of cement systems we used fractal geometry and the theory of passing (percolation)-based methods as well as modern modelling methods and scanning electronic and atomic-power microscopy. Fractal index D and micro-coarseness index S were used for a quantitative estimation of the microstructure of cement rock obtained without an additive and with an organomineral additive. These indexes were compared with the properties of cement rock determined during standard physical-mechanical trials.

The calculation of microstructure indicators and determination of the optimal content of the components of the organomineral additive allowed increasing the understanding of the fractal-cluster mechanism of self-organization of cement systems, taking into account the topology of particle distribution. The interrelation between the D and S indicators, compressive resistance and the density of the cement stone was shown. The higher fractal parameter and a relatively low level of micro-coarseness were indicators of the material with improved physical-mechanical properties. The monitoring of changes of D and S indicators can be used to control the structural formation processes of cement systems.

Keywords: Polydisperse cement systems, Fractal-cluster microstructures, Electron microscopy, Fractality, Micro-coarseness, Physical-mechanical properties

For citation: Ledenev A. A., Pertsev V. T., Rudakov O. B., Usachev S. M. Structural-phenomenological analysis of interrelation of microstructure indexes and properties of set cement systems. *Condensed Matter and Interphases.* 2022;24(3): 326–334. https://doi.org/10.17308/kcmf.2022.24/9855

Для цитирования: Леденев А. А., Перцев В. Т., Рудаков О. Б., Усачев С. М. Структурно-феноменологический анализ взаимосвязи показателей микроструктуры и свойств затвердевших цементных систем. *Конденсированные среды и межфазные границы.* 2022;24(3): 326–334. https://doi.org/10.17308/kcmf.2022.24/9855

✉ Andrey A. Ledenev , e-mail: ledenoff@mail.ru

Condensed Matter and Interphases / Конденсированные среды и межфазные границы   2022;24(3): 326–334

A. A. Ledenev et al.   Structural-phenomenological analysis of interrelation of microstructure indexes...

1. Introduction

The phenomenological theory in the most general way is the formulation of regularities determining the relations between various observations of phenomena in accordance with the fundamental theory, but not following directly from this theory. In the natural sciences, the phenomenological analysis is an approach based on the correlation of various aspects and components of the phenomenon for the establishment of shapes and structures, modes and types of manifestation and functioning, in terms of relations with other phenomena and their mutual influence on each other. For construction materials science, further research aimed at improving methodological approaches for the analysis and assessment of the indexes of the structure of materials and the identification of their relationship with the physicochemical parameters that characterize the functional properties of the forming systems are important fundamental tasks. The development of ideas about the structure formation of the complex polydisperse heterogeneous systems, such as set cement stone, can be implemented comprehensively based on the system structural-phenomenological approach. The structural-phenomenological approach considers the interrelation between phenomena and their physical-mechanical properties, as well as a comprehensive microscopic analysis of quantitative indicators structures. This allows to establish the mechanisms of interaction between the components of cement systems and their influence on the physicochemical structural formation processes occurring at the microlevel.

The relevance of the implementation of the structural-phenomenological approach is associated with the widespread use of organomineral additives (OMA) for the production of cement concretes with improved physical and technical parameters based on multicomponent finely dispersed mixtures [1–18]. However, the control of the structural formation processes of cement systems have not yet been fully studied. The developed cement systems with OMA significantly differ from traditional concretes in terms of structural topology. As it is known, an inhomogeneous aggregated fractal-cluster structure is formed in the processes of hardening, as a result of chemical, physical intermolecular, interparticle and interfacial interaction of the components of cement systems in the solid phase. In the microvolume of set cement stone, the formed crystalline hydrate structure is a key element that determines the properties of the entire system [19–22]. At the same time, the formation of the microstructure is influenced by the properties of the surface of mineral components and the degree of dispersion, which manifests in the anisotropy of cement systems, their fractal-cluster heterogeneity [20–23].

The investigation of the structural formation processes of dispersed-disordered fractal-cluster systems at the microlevel can be successfully implemented based on the development of the provisions of fractal geometry, statistical physics, percolation theory with the involvement of modern numerical and computer models, physical and chemical research methods. One of the available methods for studying the microstructure of solids is electron and atomic force microscopy. In this case, the use of quantitative indicators of fractal dimension, micro-coarseness, which allow to assess the degree of homogeneity and ordering of complex fractal-cluster objects at the microlevel is efficient [24–29].

Thus, in our opinion, the development of a structural-phenomenological approach to the analysis of forming systems at the microlevel is one of the most important aspects of controlling the processes of structure formation and directed regulation of the properties of cement systems. New scientific knowledge in this direction allow to expand the understanding of the mechanism of interaction of components with various physical and chemical properties and their influence on the microstructure of cement concrete. This will become the basis for further improvement of the compositions and technology of concretes with improved functional characteristics, as well as the basis for the development of composites with unique properties.

The aim of the study was to obtain quantitative data based on the structural and phenomenological analysis of set cement systems for the identification of the interrelations of microstructure indicators with their physical-mechanical properties.

Condensed Matter and Interphases / Конденсированные среды и межфазные границы   2022;24(3): 326–334

A. A. Ledenev et al.   Structural-phenomenological analysis of interrelation of microstructure indexes...

2. Experimental

The object of research was model and set cement systems - cement stones with and without OMA additives. The characteristics of the microstructure and physical-mechanical properties of the set cement system were investigated. For comparative analysis, two series of samples with the size of 2.0×2.0×2.0 cm were prepared: 1) control composition - cement stone without additives; 2) cement stone of a composite system with a complex OMA additive – "Portland cement + OMA". For these purposes, Portland cement class CEM I 42.5N with a specific surface area of 3000 cm²/g, particle density 3.1 g/cm³ was used. The mineralogical composition of Portland cement (wt. %) was as follows: $3CaO \cdot SiO_2$ – 68.98; $3CaO \cdot SiO_2$ – 10.87; $3CaO \cdot Al_2O_3$ – 8.77; $4CaO \cdot Al_2O_3 \cdot Fe_2O_3$ – 11.38. Raw materials that showed high efficiency according to the results of preliminary studies [21–23] were used as components of the OMA. The chemical component of OMA was a plasticizing additive based on Melflux 2651F polycarboxylates, the dosage was 0.8% by weight of cement. The mineral component of the OMA was finely dispersed quartz sand with a fineness of 7000 cm²/g, SiO_2 content 97%, particle density 2.6 g/cm³, dosage 5, 10, 15, 20% by weight of cement.

The introduction of a pre-prepared complex OMA additive into the composition of the cement system was carried out in a dry form. Water content in the studied systems was selected based on constant rheological characteristic, estimated based on the cone flow diameter, which was 13–15 cm [21–23].

Technical tests of samples for compressive resistance (MPa) and average density (g/cm³) was carried out according to GOST 30744-2001 "Cements. Test methods using polyfractional sand." After testing, samples from the destroyed cement stone were prepared by mechanical grinding for the analysis of their microstructural characteristics. The size of the studied samples was 5×5×2 mm.

An analytical assessment of the indexes of the microstructure of the cement system, including OMA with different dosages of finely dispersed quartz sand, was carried out by numerical and computer simulation methods based on the concepts of the percolation theory [22, 29]. For the studied systems, the concepts of flow along tangent and overlapping spheres, which were models of particles of the solid phase of the microfiller - finely dispersed quartz sand and cement were used. During the calculation, the quantitative ratio (by volume) was evaluated, which characterizes the proportion of microfiller, determining the processes of formation of the structure and properties of the cement system according to the formula:

$$V = \frac{N\pi d^3}{6}, \qquad (1)$$

where V is volumetric content of spheres (models of particles of the solid phase of the microfiller); N is the number of spheres (models of particles of the solid phase of the microfiller); d is the diameter of the sphere (models of particles of the solid phase).

Also, during the analysis of the structural characteristics of the cement system, the ratio of microfiller particles to cement particles was calculated using the formula:

$$C = \frac{n_{mk}}{n_c}, \qquad (2)$$

where n_{mk}, n_c are concentrations (countable) of particles of microfiller and cement, which were calculated using the formulas:

$$n_{mk} = \frac{6m_{mk}}{\pi d_{mk}^3 \rho_{mk}}, \qquad (3)$$

$$n_c = \frac{6m_c}{\pi d_c^3 \rho_c}, \qquad (4)$$

where m_{mk}, m_c is the proportion of microfiller and cement particles (by weight); d_{mk}, d_c is average microfiller and cement particle diameter; ρ_{mk}, ρ_c is the density of microfiller and cement particles.

Visualization and geometric modelling of particles in the studied two-component cement system was carried out in the Unity 3D computer software environment. The program created spheres, representing models of solid phase particles, the calculated values of the characteristics of the components were entered and the indexes of the structure were calculated and its model was visualized [22].

Analysis of the formed structure of the set cement system at the microlevel was carried out

Condensed Matter and Interphases / Конденсированные среды и межфазные границы   2022;24(3): 326–334

A. A. Ledenev et al.   Structural-phenomenological analysis of interrelation of microstructure indexes...

using two methods of physicochemical studies: scanning electron microscopy and atomic force microscopy. Micrographs of the surface of the structure with a resolution of 5 nm at a magnification of 2000 times were obtained by scanning microscopy method using a "Jeol jsm-6380LV" scanning electron microscope. The resulting electronic images were used for fractal analysis of the microstructure. Quantification of the fractal dimension index D was carried out by the islands cross-section method using Fractall.Stat 3.1 software package [24]. For the implementation of this method, a digital image of the surface of the microstructure, obtained by an electron microscope in gray scale, was converted into black and white, while adjusting the brightness and contrast in the Paint.NET program. The transformed image was loaded into the Fractall.Stat 3.1 computer program, in which the structure image was sequentially divided into fragments (islands) and the area of dense zones A and perimeter P for each selected fragment were calculated. The fractal dimension index was calculated as the slope of the dependence of the perimeter of dense zones P from their area A, plotted in double logarithmic coordinates. To ensure the correctness and reliability of the obtained data, the number of fragments of the structure image was more than 10. An example of a graphical representation of the results of calculating the fractal dimension is shown in Fig. 1.

Three-dimensional topology images were obtained by atomic force microscopy using a NanoEducator unit and the surface micro-coarseness index S (nm) was determined based on the maximum peak of the three-dimensional image (along the z axis). The size of the scanning area for obtaining the image was 9×9 μm.

3. Results and discussion

Physical-mechanical tests demonstrated that the set cement system with the OMA complex additive predictably had significantly higher physical-mechanical properties (Table 1) than the system without additives. The obtained results were a consequence of the active influence of the organic and mineral components of the OMA complex additive on the formation of the microstructure of the cement stone. The

mechanism of action of the organic component "Melflux 2651F" based on polycarboxylates was due to the plastification and modification of the cement system, resulted from the effect of "steric" repulsion of watered particles of the solid phase during the adsorption of the surfactant [21, 23]. The action of the mineral OMA component - finely dispersed quartz sand was based on the modification of the structure of the cement system due to the presence of polar silanol groups capable of chemically participating in the process of hydration hardening on the amorphised surface of SiO_2 particles [23].

The physical factor of interparticle interaction also had an influence exhibited as the reshaping of the structure of the cement stone at the microlevel when OMA with a different ground quartz sand content was introduced [22]. According to the model representations of the percolation theory, the topological distribution of microfiller particles corresponding to the formation of a percolation "infinite" fractal cluster will determine the properties of the entire cement system (Fig. 2a) [22, 29]. It has been experimentally established that cement systems with a volume content of ground quartz sand $V \approx 0.1$–0.15 had the highest strength and density indicators (see Table 1). Convergence of the obtained experimental values and the
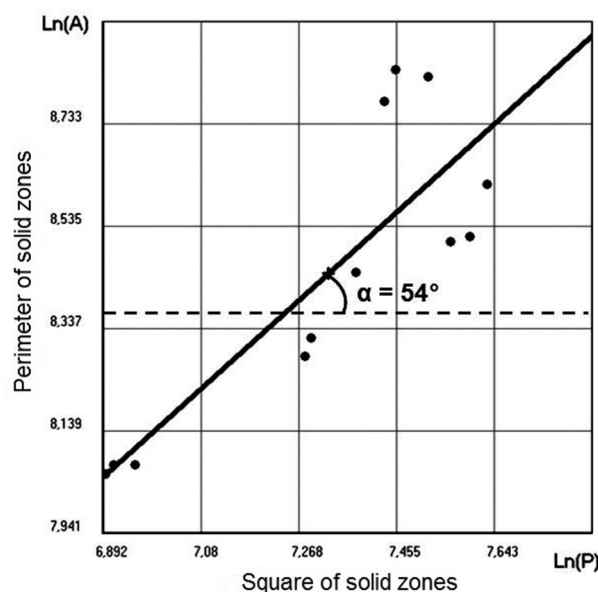
Fig. 1. Example of graphical representation of calculation results for determination of the fractal dimension using the Fractall.Stat 3.1 program [24]

Condensed Matter and Interphases / Конденсированные среды и межфазные границы   2022;24(3): 326–334

A. A. Ledenev et al.   Structural-phenomenological analysis of interrelation of microstructure indexes...

Table 1. Influence of OMA with different content of ground quartz sand on the physical-mechanical properties of the set cement system

Cement system	Contents of system components			Physical-mechanical properties	
	mass content of ground sand, %	volume content of ground sand, V	the ratio of components in the system, C	compressive resistance, MPa	density, g/cm^3
with complex OMA additive	5	0.054	0.47	114	2.26
	10	0.104	0.99	135	2.28
	15	0.149	1.57	121	2.26
	20	0.189	2.23	103	2.25
without additives	–	–	–	57	2.07
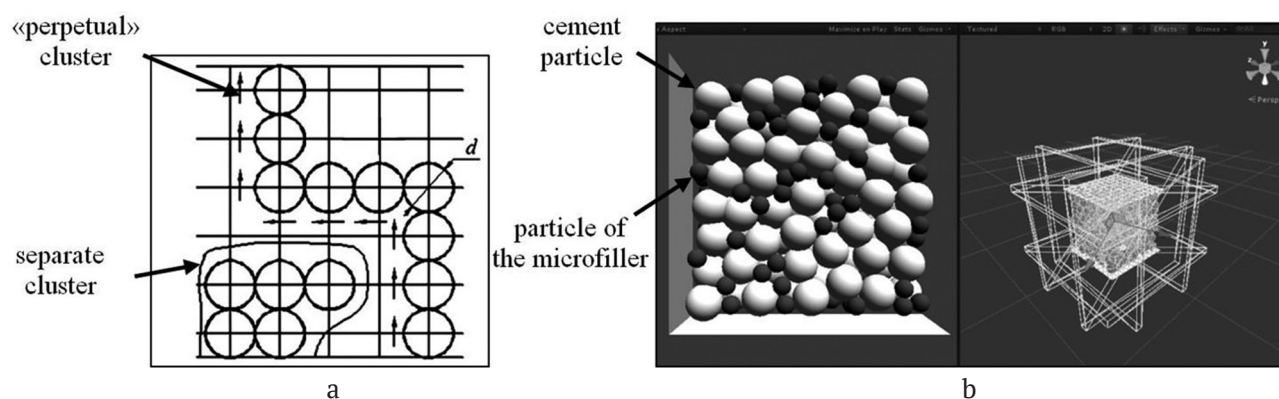
Fig. 2. Flat schematic model describing the flow of an "infinite" cluster (a) and geometric visualization of the model of the structure of the cement system with microfiller in the Unity 3D program (b) [22]

optimal indicators previously calculated for filled composites $V \approx 0.076–0.16$ confirmed the cluster mechanism of aggregation of particles of the solid phase and the possibility of the topological analysis of the structure using the percolation theory methods [22]. It was shown that the ratio of components in the system was $C \approx 1$ for a structure with a ground quartz sand content of 10% at $V \approx 0.1$ (see Table 1). A fragment of the visualization and geometric modelling of particles with the given structural characteristics of the cement system, carried out in the Unity 3D computer environment, is shown in Fig. 2b. Probably, under real conditions, the topological distribution of the aggregated microfiller provides its location in voids and between cement particles, which contributes to the compaction of the cement system. The obtained calculated values and the presented models characterize the optimal content of the OMA components for the formation of the microstructure and the improvement of the physical-mechanical properties of the filled cement system.

The analysis of images obtained using scanning electron microscope allowed to visually establish a qualitative change in the microstructure of the cement system formed during hydration hardening (Fig. 3). For the cement system, including the OMA complex additive, a distinctive feature was the formation of a more homogeneous and spatially ordered microstructure, including dense crystalline new growths (Fig. 3a). In turn, the microstructure of the set cement system without additives was characterized by a less uniform distribution of the solid phase with the presence of structural void elements - "dark" zones (Fig. 3b).

The images of the structure obtained using a scanning electron microscope were processed for quantitative evaluation by fractal analysis methods (Fig. 4). It was established that for a more homogeneous and ordered microstructure formed in a system with a complex OMA additive, the fractal index was higher $D = 1.85$ (Fig. 4a) in comparison with the index obtained for the structure without additives $D = 1.43$ (Fig. 4b). An increase in the fractal index quantitatively

Condensed Matter and Interphases / Конденсированные среды и межфазные границы   2022;24(3): 326–334

A. A. Ledenev et al.   Structural-phenomenological analysis of interrelation of microstructure indexes...
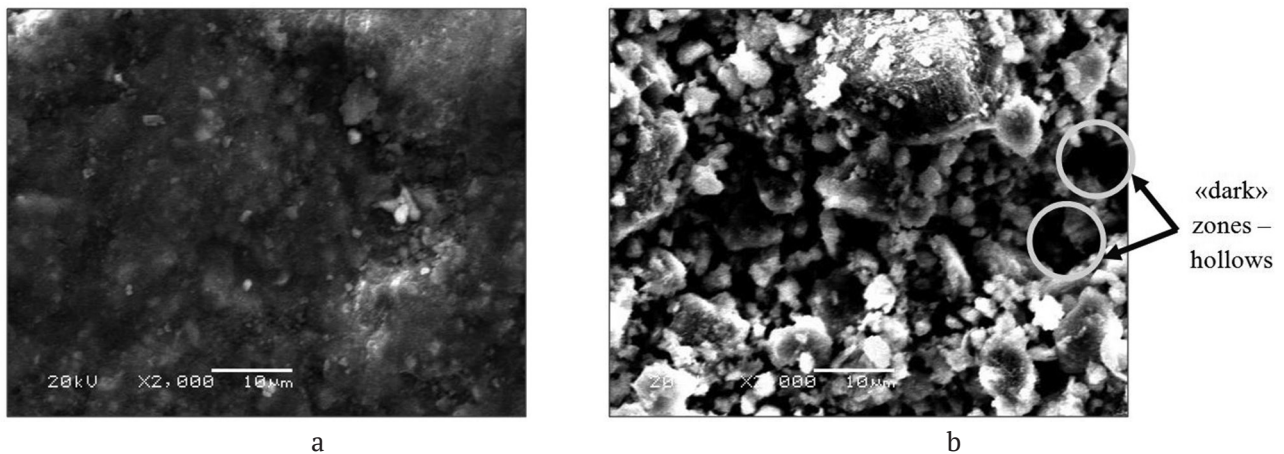
Fig. 3. Images of the microstructure of the set cement system obtained using a scanning electron microscope (×2000): a) cement system with the OMA additive; b) cement system without additives
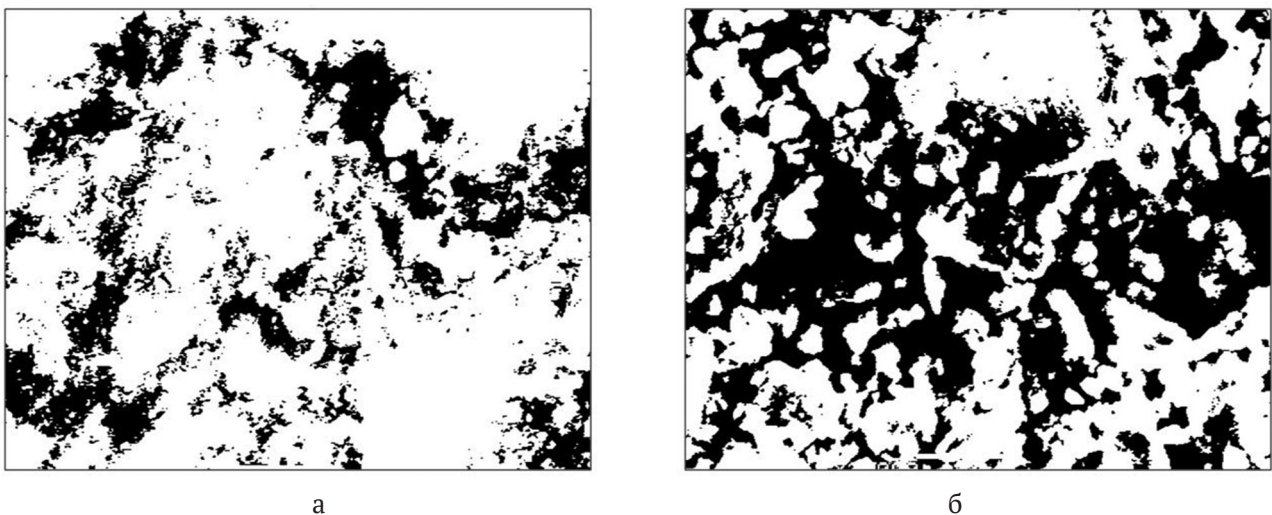
Fig. 4. Processed images of the microstructure of the set cement system: a) cement system with OMA additive (D = 1.85); b) cement system without additives (D = 1.43)

characterized the geometric restructuring of the formed microstructure and correlated with the strength indexes and density of the cement stone (Table 2). In particular, the higher the fractal index, and its value closer to D = 2, the more evenly dense elements (areas) are distributed in the microstructure space of the system and, respectively, the formed system of cement stone is denser and more durable.

The interrelation of the micro-coarseness index S with physical-mechanical properties of systems was revealed by the analysis of the microstructure using an atomic force microscope,(Fig. 5, see Table. 2). It was established, that denser and more durable cement system with the OMA additive was characterized by a more uniform and ordered surface relief (Fig. 5a). Complex relief surfaces

with a large number of protrusions and a higher value of micro-coarseness was characteristic for less homogeneous structure of the cement system (Fig. 5b).

4. Conclusions

The structural-phenomenological approach to the analysis and evaluation of the formed cement systems allowed to expand the understanding of the fractal-cluster mechanism of their structure formation. The relationship of microstructure indicators with the properties of cement systems was established by the comparison of quantitative data of modelling of the topology of particle distribution, and fractal geometry indicators of electronic images with microrelief indexes and physical-mechanical properties. The developed

Condensed Matter and Interphases / Конденсированные среды и межфазные границы   2022;24(3): 326–334

A. A. Ledenev et al.   Structural-phenomenological analysis of interrelation of microstructure indexes...

Table 2. Indicators of the physical-mechanical properties and the microstructure of the set cement system

Cement system	physical-mechanical properties		Indicators of microstructure	
	compressive resistance, MPa	density, g/cm³	fractality, D	microcoarseness, S, nm
with complex OMA additive	135	2.28	1.85	160
without additives	57	2.07	1.43	2656
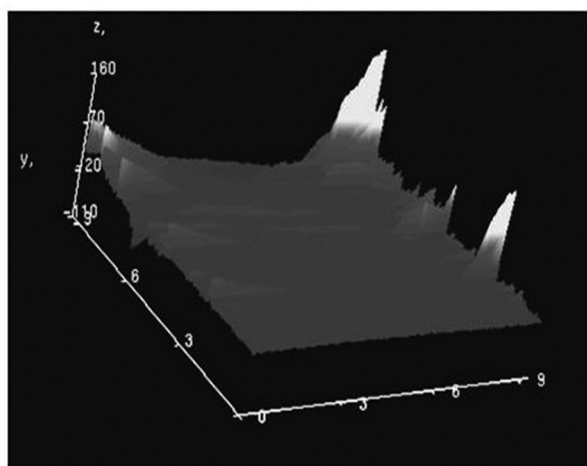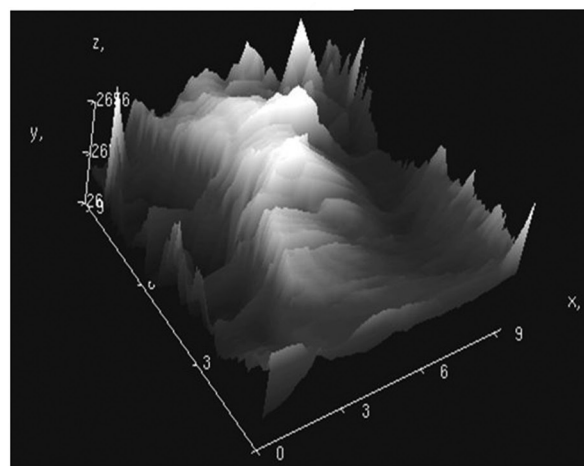
a   b

Fig. 5. Images of the microstructure of the surface of the set cement system, obtained using an atomic force microscope (dimensions x, y – μm, z – nm): a) cement system with OMA additive (S = 160 nm); b) cement system without additives (S = 2656 nm)

methodology can be used for further study of the factors controlling the processes of structure formation and regulation of the properties of cement systems.

Author contributions

All authors made an equivalent contribution to the preparation of the publication.

Conflict of interests

The authors declare that they have no known competing financial interests or personal relationships that could have influenced the work reported in this paper.

References

1. Kaprielov S. S., Sheinfeld A. V., Dondukov V. G. Cements and additives for producing high-strength concretes. *Stroitel'nye materialy = Construction Materials.* 2017;11. 4–10. (In Russ., abstract in Eng.). https://doi.org/10.31659/0585-430X-2017-754-11-4-10 https://www.elibrary.ru/item.asp?id=30744332

2. *Management of technology processes, structure and properties of concrete.* E. M. Chernyshov, E. I. Shmit'ko (eds.). Voronezh. VGASU Publ; 2002. 344 p. (In Russ.)

3. Tarakanov O. V., Akchurin T. K., Utyugova E. S. Efficiency of application of integrated organomineral additives for concretes. *Vestnik Volgogradskogo gosudarstvennogo arhitekturno-stroiteľnogo universiteta. Seriya: Stroiteľstvo i arhitektura = Bulletin of Volgograd State University of Architecture and Civil Engineering. Series: Civil Engineering and Architecture.* 2020;1(78): 174–181. (In Russ., abstract in Eng.). Available at: https://www.elibrary.ru/item.asp?id=42737922

4. Lesovik V. S., Fediuk R. S. New generation composites for special facilities. *Stroitel'nye materialy = Construction Materials.* 2021;3: 9–17. (In Russ., abstract in Eng.). https://doi.org/10.31659/0585-430X-2021-789-3-9-17

5. Nelyubova V. V., Usikov S. A., Strokova V. V., Netsvet D. D. Composition and properties of self-compacting concrete using a complex of modifiers. *Stroitel'nye materialy = Construction Materials.* 2021;12: 48–54. (In Russ., abstract in Eng.). https://doi.org/10.31659/0585-430X-2021-798-12-48-54

6. Svintsov A. P., Abbas Abdulhussein Abd Noor, Abbas Abdel-Sater, Sorokin A. N. Influence of nano-modified additives on the mobility of concrete mixture. *Stroitel'nye materialy = Construction materials.* 2020;7:

Condensed Matter and Interphases / Конденсированные среды и межфазные границы   2022;24(3): 326–334

A. A. Ledenev et al.   Structural-phenomenological analysis of interrelation of microstructure indexes…

54–59. (In Russ., abstract in Eng.). https://doi.org/10.31659/0585-430X-2020-782-7-54-59

7. Hagverdiyeva T. A., Jafarov R. Impact of fine ground mineral additives on properties of concrete. *Stroitel'nye materialy = Construction materials*. 2019;3: 73–76. (In Russ., abstract in Eng.). https://doi.org/10.31659/0585-430X-2019-768-3-73-76

8. Bazhenov Ju. M., Bulgakov B. I., Ngo Suan Hung. Hydraulic concrete with organomineral additive. *Construction materials technology: the present and the future: Proc. 1 All-Russia Scientific Conf., devoted to the 90 anniversary of the outstanding scientist- materials, academician RAACS Ju. M. Bazhenov, 1–2 October 2020, Moscow*. Moscow: MGSU publ.; 2020. pp. 114–117. (In Russ.)

9. Pan G., Li P., Chen L., Li G. A study of the effect of rheological properties of fresh concrete on shotcrete-rebound based on different additive components. *Construction and Building Materials*. 2019;224: 1069–1080. https://doi.org/10.1016/j.conbuildmat.2019.07.060

10. Zhang S., Qiao W.-G., Chen P.-C., Xi K. Rheological and mechanical properties of microfinecement-based grouts mixed with microfine fly ash, colloidal nanosilica and superplasticizer. *Construction and Building Materials*. 2019;212: 10–18. https://doi.org/10.1016/j.conbuildmat.2019.03.314

11. Hedayatinia F., Delnavaz M., Emamzadeh S. S. Rheological properties, compressive strength and life cycle assessment of self-compacting concrete containing natural pumice pozzolan. *Construction and Building Materials*. 2019;206: 122–129. https://doi.org/10.1016/j.conbuildmat.2019.02.059

12. Li Z., Cao G. Rheological behaviors and model of fresh concrete in vibrated state. Cement and Concrete Research. 2019;120: 217–226. https://doi.org/10.1016/j.cemconres.2019.03.020

13. Choi B. I., Kim J. H., Shin, T. Y. Rheological model selection and a general model for evaluating the viscosity and microstructure of a highly concentrated cement suspension. *Cement and Concrete Research*. 2019;123: 105775. https://doi.org/10.1016/j.cemconres.2019.05.020

14. Alatawna Amr, Birenboim Matan, Nadiv Roey, Buzaglo Matat, Peretz-Damari Sivan, Peled Alva, Regev Oren, Sripada Raghu. The effect of compatibility and dimensionality of carbon nanofillers on cement composites. *Construction and Building Materials*. 2020;232: 117141. https://doi.org/10.1016/j.conbuildmat.2019.117141

15. Svintsov A. P., Shchesnyak E. L., Galishnikova V. V., Fediuk R. S., Stashevskaya N. A. Effect of nano-modified additives on properties of concrete mixtures during winter season. *Construction and Building Materials*. 2020;237: 117527. https://doi.org/10.1016/j.conbuildmat.2019.117527

16. Chintalapudi K., Pannem R. M. R. An intense review on the performance of graphene oxide and reduced graphene oxide in an admixed cement system. *Construction and Building Materials*. 2020;259: 120598. https://doi.org/10.1016/j.conbuildmat.2020.120598

17. Zhu H., Gou H., Zhou H., Jiang Z. Microscopic analysis of nano-modified fly ash by fluidized bed reactor-vapor deposition. *Construction and Building Materials*. 2020;260: 120434. https://doi.org/10.1016/j.conbuildmat.2020.120434

18. Li D., Wang D., Ren C., Rui Y. Investigation of rheological properties of fresh cement paste containing ultrafine circulating fluidized bed fly ash. *Construction and Building Materials*. 2018;188: 1007–1013. https://doi.org/10.1016/j.conbuildmat.2018.07.186

19. Smirnov V. A., Korolev E. V. Building materials as disperse systems: multiscale modeling with dedicated software. *Construction and Building Materials*. 2019;1–2: 43–53. (In Russ., abstract in Eng.). https://doi.org/10.31659/0585-430X-2019-767-1-43-53

20. Ledenev A. A., Pertsev V. T., Rudakov O. B., Barabash D. E. Development of ideas about the rheological behaviour of building mixtures taking into account fractal-cluster processes in their structure formation. *Condensed Matter and Interphases*. 2020;22(4): 473–480. https://doi.org/10.17308/kcmf.2020.22/3059

21. Pertsev V. T., Khalilbekov Ya. Z., Ledenev A. A., Perova N. S. Composition and technology of complex additives for concrete based on industrial waste. *Cement i ego primenenie = Cement and its Applications*. 2019;3: 98–101. (In Russ., abstract in Eng.). Available at: https://www.elibrary.ru/item.asp?id=39321673

22. Ledenev A. A., Pertsev V. T. Modelling and estimation of structural characteristics of the cement stone, modified by microfillers. In: *Construction materials technology: the present and the future: Proc. 1 All-Russia Scientific Conf., devoted to the 90 anniversary of the outstanding scientist- materials, academician RAACS Ju. M. Bazhenov, 1–2 October 2020, Moscow*. Moscow: MGSU Publ.; 2020. pp. 59–64. (In Russ.)

23. Ledenev A. A., Kozodaev S. P., Pertsev V. T., Baranov E. V., Tzagoruiko T. V., Vnukov D. N. Mechanisms of act of various kinds organic-mineral additives in cement system. *Vestnik BGTU im. V.G. Shuhova = Bulletin of Belgorod State Technological University named after. V. G. Shukhov*. 2021;9. 99–105. https://doi.org/10.34031/2071-7318-2021-6-9-8-19

24. Golovinskij P. A., Ushakov I. I. Theory of fractal growth of shakes and accompanying acoustical emission. *Sbornik tezisov FiPS*. Moscow: Interkontakt-nauka Publ., 1999. pp. 20–24. (In Russ.)

25. Yablokov M. Ju. Fractal demension determination based on image analysis. n dimensions of a quantity on the basis of the analysis of the images.

Condensed Matter and Interphases / Конденсированные среды и межфазные границы   2022;24(3): 326–334

A. A. Ledenev et al.   Structural-phenomenological analysis of interrelation of microstructure indexes...

Russian Journal of Physical Chemistry A. 1999;2: 162–166. Available at: https://www.elibrary.ru/item.asp?id=13313798

26. Mandel'brot B. Fractal geometry of the nature. Moscow: Institut komp'juternyh issledovanij Publ.; 2002. 656 p. (In Russ.)

27. Korolev E. V., Grishina A. N., Aizenshtadt A. M. Analysis of structure formation of composites using fractal dimension. *Stroitel'nye materialy = Construction Materials.* 2020;9: 54–61. (In Russ., abstract in Eng.). https://doi.org/10.31659/0585-430X-2020-784-9-54-61

28. Krivonosova E. A., Rudakova O. A., Vstovskii G. V. Multifractal analysis of the structural composition of the heat affected zone of steels with carbonitride hardening. *Zavodskaya laboratoriya. Diagnostika materialov = Industrial Laboratory.* 2010;6(76): 26–30. (In Russ.). Available at: https://www.elibrary.ru/item.asp?id=14992942

29. Tarasevich Ju. Ju. Percolation: the theory, applications, algorithms. Moscow: Editorial URSS Publ.; 2002. 112 p. (In Russ.)

Information about the authors

Andrey A. Ledenev, Cand. Sci. (Eng.), Research Fellow, Air Force Military Educational and Scientific Center «Air Force Academy named after Professor N. E. Zhukovsky and Y. A. Gagarin» (Voronezh) (Voronezh, Russian Federation).

https://orcid.org/0000-0003-2493-8952
ledenoff@mail.ru

Victor T. Pertsev, Dr. Sci. (Eng.), Full Professor, Professor at the Department of Technology of Construction Materials, Products and Designs, Voronezh State Technical University (Voronezh, Russian Federation).

https://orcid.org/0000-0002-8882-4930
perec_v@mail.ru

Oleg B. Rudakov, Dr. Sci. (Chem.), Professor, Head of the Department of Chemistry and Chemical Technology of Materials, Voronezh State Technical University (Voronezh, Russian Federation).

https://orcid.org/0000-0003-2527-2857
robi57@mail.ru

Sergey M. Usachev, Cand. Sci. (Eng.), Associate Professor, Head of the Department of Technology of Construction Materials, Products and Designs, Voronezh State Technical University (Voronezh, Russian Federation).

https://orcid.org/0000-0002-3856-187X
sergey.usa4ev@mail.ru

Condensed Matter and Interphases

Original articles

Research article
https://doi.org/10.17308/kcmf.2022.24/9856

Phase equilibria in the MnTe–MnGa$_2$Te$_4$–MnIn$_2$Te$_4$ system

F. M. Mammadov[1] ✉, **S. Z. Imamaliyeva**[1], **Ya. I. Jafarov**[2], **I. B. Bakhtiyarly**[1], **M. B. Babanly**[1]

[1]*Institute of Catalysis and Inorganic Chemistry n.a. M. Nagiyev of the Azerbaijan National Academy of Sciences,
113 H. Javid av., Baku Az1143, Azerbaijan*

[2]*Baku State University,
23 Z. Khalilova str., Baku Az1148, Azerbaijan*

Abstract

A family of compounds with the general formula AB$_2$X$_4$ (A – Mn, Fe, Co, Ni; B – Ga, In, Sb, Bi; X – S, Se, Te) and complex phases of variable compositions based on them are among promising functional materials with thermoelectric, photoelectric, optical, and magnetic properties. In this article, we continued the study of multi-component systems based on the chalcogenides of transition metals and presented the results of the study of phase equilibria in the MnTe–MnGa$_2$Te$_4$–MnIn$_2$Te$_4$ system using differential thermal analysis and X-ray phase analysis.

Based on the experimental results, we built the polythermal cross sections MnTe–MnGaInTe$_4$ and MnGa$_2$Te$_4$–[A] (where [A] is a biphasic alloy of the 2MnTe–MnIn$_2$Te$_4$ side system of the 50.0 mol% MnIn$_2$Te$_4$ composition) as well as an isothermal section of a phase diagram at 800 K and a projection of the liquidus surface. It was established that the liquidus consists of the fields of primary crystallisation of 4 phases: 1 – Mn-ht; 2 – phases based on various modifications of MnTe; 3 – γ_1; 4 – γ_2. We also identified types and coordinates of non-variant and monovariant equilibria.

Based on triple compounds (MnGa$_2$Te$_4$, MnIn$_2$Te$_4$), we determined wide regions of solid solutions that are of particular interest as magnetic materials.

Keywords: Manganese-gallium telluride, Manganese-indium telluride, Phase diagram, Liquidus surface, Solid solutions, Magnetic materials

For citation: Mammadov F. M. Imamaliyeva S. Z., Jafarov Ya. I., Bakhtiyarly I. B., Babanly M. B. Phase equilibria in the MnTe–MnGa$_2$Te$_4$–MnIn$_2$Te$_4$ system. *Condensed Matter and Interphases*. 2022;24(3): 335–344. https://doi.org/10.17308/kcmf.2022.24/9856

Для цитирования: Мамедов Ф. М., Имамалиева С. З., Джафаров Я. И., Бахтиярлы И. Б., Бабанлы М. Б. Фазовые равновесия в системе MnTe–MnGa$_2$Te$_4$–MnIn$_2$Te$_4$. *Конденсированные среды и межфазные границы*. 2022;24(3): 335–344. https://doi.org/10.17308/kcmf.2022.24/9856

✉ Faik Mamedaga Mammadov, e-mail: faikmamadov@mail.ru

Condensed Matter and Interphases / Конденсированные среды и межфазные границы   2022;24(3): 335–344

F. M. Mammadov et al.   Phase equilibria in the MnTe–MnGa$_2$Te$_4$–MnIn$_2$Te$_4$ system

1. Introduction

A family of compounds with the general formula AB$_2$X$_4$ (A – Mn, Fe, Co, Ni; B – Ga, In, Sb, Bi; X – S, Se, Te) [1–8] and complex phases of variable compositions based on them [9–12] has been of considerable interest over the past thirty years. These magnetic compounds that contain three metal cations around each anion position, while the fourth empty position forms an ordered massif of vacancies, can exist in various crystal structures and show a number of physical and chemical properties related to the crystallographically ordered massif of the vacancies. The magneto-optical properties of these compounds are also of particular interest due to the presence of magnetic ions Fe^{+2} and Mn^{+2}. According to the results of [1-6], these compounds possess thermoelectric, photoelectric, and optical properties.

Recent studies showed that some layered compounds of the AB$_2$X$_4$ type exhibit properties of a magnetic and topological insulator [13–24]. Such a combination of magnetic and topological properties potentially leads to the development of multi-functional electronic and spintronic components that offer prospects of better energy efficiency and computing capabilities.

Considering the above, it can be said that the researches aimed at obtaining and studying solid solution based on the compounds of the AB$_2$X$_4$ type are relevant.

The search and development of methods for the directed synthesis of new multi-component phases and materials are based on reliable data on the phase equilibria of the corresponding systems [25–27].

In this article, we continued the study of multi-component systems based on the chalcogenides

of transition metals [28–31] and presented the results of the study of phase equilibria in the MnTe–MnGa$_2$Te$_4$–MnIn$_2$Te$_4$ system.

1.1. Starting compounds

The results of the study of starting binary and ternary compounds of the studied system are presented in [32–35]. MnTe telluride melts incongruently by a peritectic reaction at 1425 K. Several polymorphic transitions are inherent to this compound [32, 33]. The crystallographic parameters of various modifications of this compound are presented in Table 1.

The other two compounds of this system, MnGa$_2$Te$_4$ and MnIn$_2$Te$_4$, melt congruently at 1083 K [34] and 1025 K [35], respectively. The former crystallises in a pseudo-tetragonal structure, while the latter crystallises in a tetragonal structure (Table 1).

1.2. Boundary quasi-binary systems

A new specified variant of the phase diagram of the MnTe–MnGa$_2$Te$_4$ system was presented in [34], according to which was of eutectic type and had the following coordinates of the eutectic point: 84 mol% MnGa$_2$Te$_4$ and 1070 K.

The phase diagram of another boundary MnTe-MnIn$_2$Te$_4$ system of the eutectic type had the following coordinates of the eutectic point: 90 mol% MnIn$_2$Te$_4$ and 1015 K [35].

The authors of [30] studied the MnGa$_2$Te$_4$–MnIn$_2$Te$_4$ system (Fig. 1). It was established that it is quasi-binary and is characterised by the formation of wide regions of solid solutions based on the starting compounds. The MnGaInTe$_4$ phase had the highest temperature (1030 K) and crystallises in a tetragonal structure (Table 1). A comparison of MnGaInTe$_4$ crystal lattices and an MnIn$_2$Te$_4$ isostructural ternary compound

Table 1. Crystallographic data of binary and ternary phases of the MnTe-MnGa$_2$Te$_4$-MnIn$_2$Te$_4$ system

Phases	Crystal system, space group, and lattice parameters, nm	Source
MnTe – rt	hexagonal, $P6_3/mmc$: a = 0.41498, c = 0.67176 nm	[36]
MnTe – it	cubic, $F\bar{4}3m$: a = 0.634 nm	[36]
MnTe – ht	hexagonal, $P6_3/mmc$: a = 0.4148, c = 0.6721 nm	[36]
MnGa$_2$Te$_4$	pseudo-tetragonal: a = b = 0.847, c = 4.83 nm	[37]
	monoclinic, $C/2c$: a = b = 1.1999 нм, c = 2.4922 nm	[38]
MnIn$_2$Te$_4$	tetragonal, $I\text{-}42m$: a = 0.619490(5), c = 1.23956(2) nm	[30]
MnGaInTe$_4$	tetragonal, $I\text{-}42m$: a = 0.610293(7), c = 1.21766(2) nm	[30]

Condensed Matter and Interphases / Конденсированные среды и межфазные границы   2022;24(3): 335–344

F. M. Mammadov et al.   Phase equilibria in the MnTe–MnGa$_2$Te$_4$–MnIn$_2$Te$_4$ system
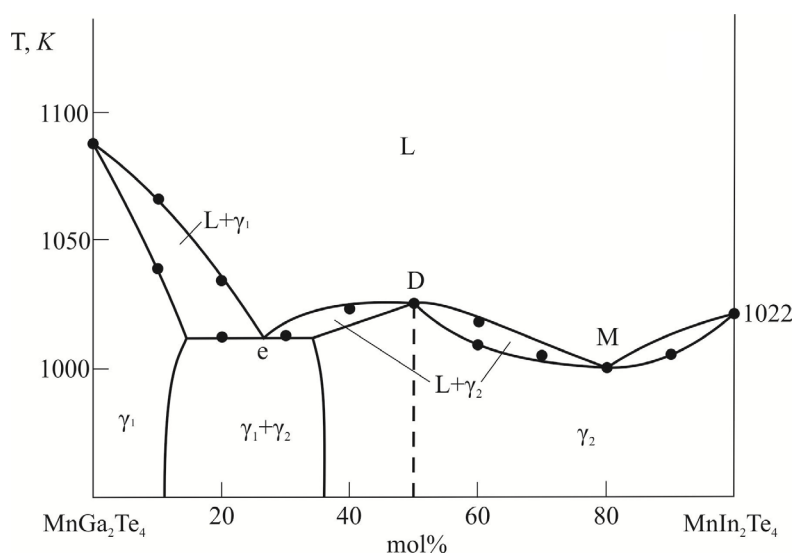
Fig. 1. Phase diagram of the MnGa$_2$Te$_4$–MnIn$_2$Te$_4$ system [30]

showed [30] that they were considerably different in the nature of colonisation of crystallographic positions and that MnGaInTe$_4$ could be characterised as an ordered phase.

2. Experimental

2.1. Synthesis

The starting compounds MnTe, MnGa$_2$Te$_4$, and MnIn$_2$Te$_4$ of the studied systems were synthesised by melting stoichiometric amounts of high purity elementary components (manganese, catalogue number 7439-96-5, indium – 7440-74-6, gallium – 7440-55-3, and tellurium – 13494-80-9) purchased from the German company Alfa Aesar. They were synthesised for 8 hours in sealed quartz ampoules that were evacuated to a residual pressure of 10^{-2} Pa. The temperatures were 20 K higher than the melting points. Then the furnace was turned off. To prevent the interaction of quartz with manganese, the starting compounds and intermediate alloys of the studied system were synthesised in graphitised ampoules. The graphitisation was performed by the thermal decomposition of toluene.

The single-phase composition of the synthesised samples was confirmed by means of differential thermal analysis (DTA) and X-ray diffraction (XRD).

According to DTA, the melting points of MnTe, MnGa$_2$Te$_4$, and MnIn$_2$Te$_4$ were 1425±3 K, 1083±3 K, and 1025±3 K, respectively, which corresponded with the results of [32–35].

Based on the XRD data, we calculated the crystallographic parameters of lattices, which corresponded well with the data from [36, 37, 30], (Table 1):

MnTe-rt – hexagonal, space group $P63/mmc$: $a = 0.41488(4)$, $c = 0.67166(6)$ nm;

MnGa$_2$Te$_4$ – pseudo-tetragonal $a = b = 0.84851(8)$, $c = 4.8402(2)$ nm;

MnIn$_2$Te$_4$ – tetragonal, I-42m: $a = 0.61949(5)$; $c = 1.23956(2)$ nm;

MnGaInTe$_4$ – tetragonal, I-42m: $a = 0.610293(7)$; $c = 1.21766(2)$ nm.

The alloys of the MnTe–MnGa$_2$Te$_4$–MnIn$_2$Te$_4$ system (Fig. 2) were synthesised by melting the above-mentioned compounds in different ratios in evacuated quartz ampoules with further long-term (500 h) thermal annealing at 800 K. In order to develop a diagram for the solid-phase equilibria, some alloys were hardened by dropping ampoules into cold water.

2.2. Research methods

DTA was conducted on a Netzsch STA 449 F3 unit (platinum-platinum/rhodium thermocouples) in the range of temperatures from room temperature to ~ 1450 K with a heating rate of 10 K·min^{-1}.

XRD was conducted by recording powder patterns on a D2 Phaser diffractometer. Crystal lattice parameters were calculated and specified using EVA and TOPAS 4.2 (Bruker, Germany, Cu$K\alpha$ radiation, angle range 5° ⩽ 2θ ⩽ 80°, recording rate 0.03°×0.2 min).

Condensed Matter and Interphases / Конденсированные среды и межфазные границы   2022;24(3): 335–344

F. M. Mammadov et al.   Phase equilibria in the MnTe–MnGa$_2$Te$_4$–MnIn$_2$Te$_4$ system
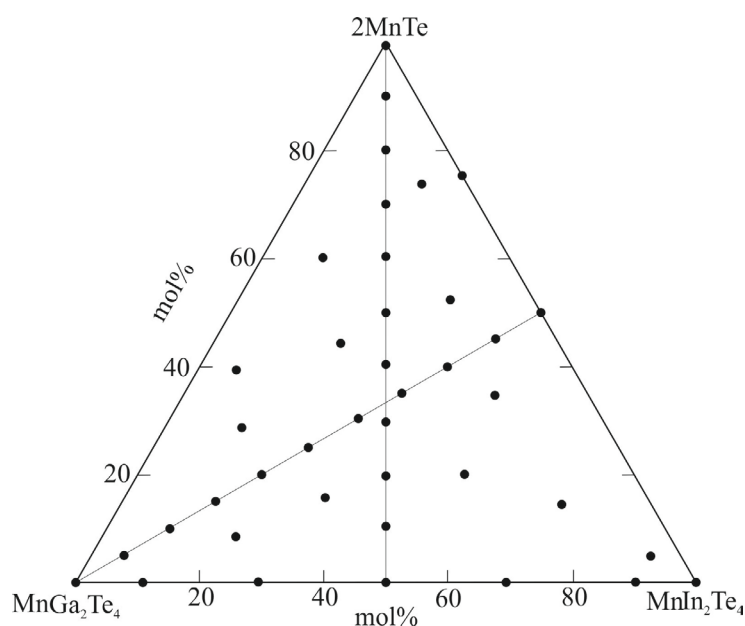
Fig. 2. Compositions of the studied samples in the MnTe–MnGa$_2$Te$_4$–MnIn$_2$Te$_4$ system

3. Results and discussion

We processed both experimental and published data on boundary systems [30, 34, 35] and obtained a general consistent pattern of phase equilibria in the MnTe–MnGa$_2$Te$_4$–MnIn$_2$Te$_4$ system. In tables and figures as well as in the article itself, solid solutions based on compounds and their various modifications were designated as follows: α – MnTe-lt, γ_1 – MnGa$_2$Te$_4$, γ_2 – MnIn$_2$Te$_4$.

3.1. Solid-phase equilibria
in the MnTe–MnGa$_2$Te$_4$–MnIn$_2$Te$_4$ system

Based on the XRD data of the samples hardened at 800 K, we developed a diagram for the solid-phase equilibria of the MnTe–MnGa$_2$Te$_4$–MnIn$_2$Te$_4$ system at 800 K (Fig. 3). As can be seen, wide regions of solid solutions based on ternary MnGa$_2$Te$_4$ (γ_1) and MnIn$_2$Te$_4$ (γ_2) compounds were formed in the system. These phases had the form of bands 2–4 mol% wide and 15 and 65 mol% long, respectively, along the boundary system MnGa$_2$Te$_4$-MnIn$_2$Te$_4$. Based on the low-temperature modification of MnTe, the α-phase took up a narrow area (5–6 mol%) of the corresponding angle. The listed phases formed a number of two-phase regions, $\alpha+\gamma_1$, $\alpha+\gamma_2$, and $\gamma_1+\gamma_2$ that were separated by a three-phase region $\alpha+\gamma_1+\gamma_2$.

All the phase regions presented in Fig. 3 were confirmed by XRD. Fig. 4 shows X-ray powder diffraction patterns of three alloys from different phase regions. It can be seen that the compositions of these samples correspond to the pattern of solid-phase equilibria presented in Fig. 3.

3.2. Liquidus surface

A projection of the liquidus surface of the MnTe–MnGa$_2$Te$_4$–MnIn$_2$Te$_4$ system consists of four fields of primary crystallisation (Fig. 5). The presence of field (1) corresponding to the primary crystallisation of high-temperature modification of manganese, which was not a component of this

Table 2. Non-variant and monovariant equilibria in the MnTe–MnGa$_2$Te$_4$–MnIn$_2$Te$_4$ system

Point or curve in Fig. 5.	Equilibrium	T, K
D	L $\leftrightarrow \gamma_2$ (MnGaInTe$_4$)	1030
M	L $\leftrightarrow \gamma_2$	1005
e_1	L $\leftrightarrow \gamma_1 + \gamma_2$	1012
e_2	L $\leftrightarrow \gamma_1 + \alpha$	1060
e_3	L $\leftrightarrow \gamma_2 + \alpha$	1015
e_4	L $\leftrightarrow \gamma_2 + \alpha$	1018
e_5	L $\leftrightarrow \gamma_2 + \alpha$	1310
E	L $\leftrightarrow \alpha + \gamma_1 + \gamma_2$	997
e_2E	L $\leftrightarrow \alpha + \gamma_1$	1060–997
e_1E	L $\leftrightarrow \gamma_1 + \gamma_2$	1012–997
e_4E	L $\leftrightarrow \alpha + \gamma_2$	1018–997
e_3e_5	L $\leftrightarrow \gamma + \gamma_2$	1015–995
$e_4 e_5$	L $\leftrightarrow \alpha + \gamma_2$	1018–995

Condensed Matter and Interphases / Конденсированные среды и межфазные границы   2022;24(3): 335–344

F. M. Mammadov et al.   Phase equilibria in the MnTe–MnGa$_2$Te$_4$–MnIn$_2$Te$_4$ system
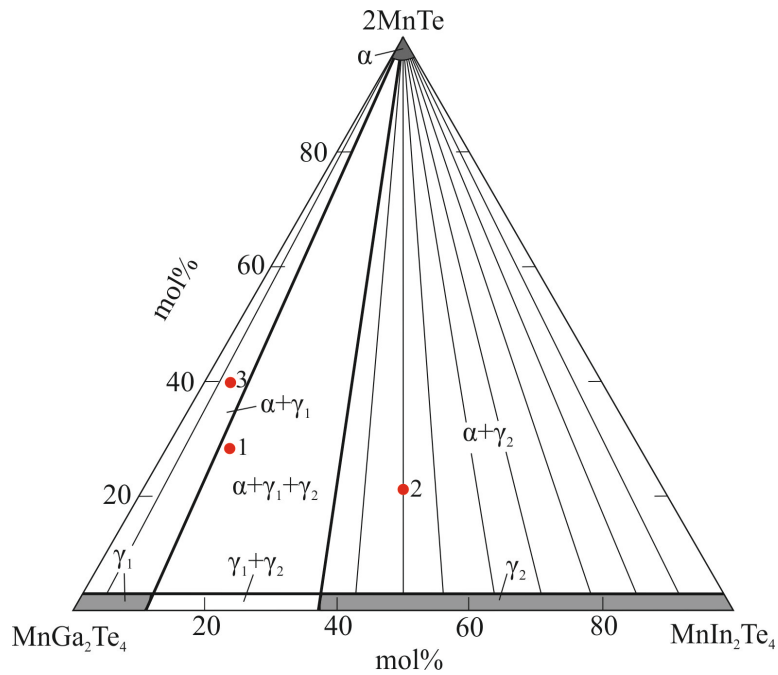
Fig. 3. Diagram of solid-phase equilibria in the MnTe–MnGa$_2$Te$_4$–MnIn$_2$Te$_4$ system at 800 K · 1-3 alloys for which X-ray powder diffraction patterns are presented in Fig. 4
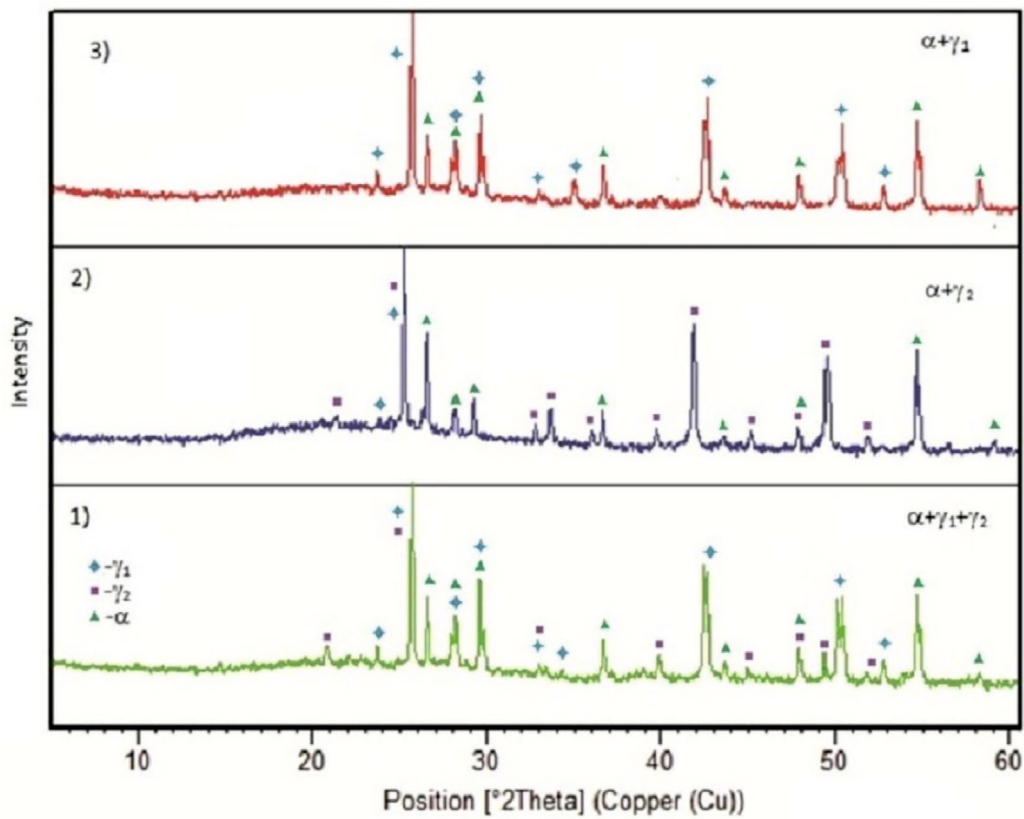
Fig. 4. X-ray powder diffraction patterns of the alloys (1-3) of the MnTe–MnGa$_2$Te$_4$–MnIn$_2$Te$_4$ system specified in Fig. 3
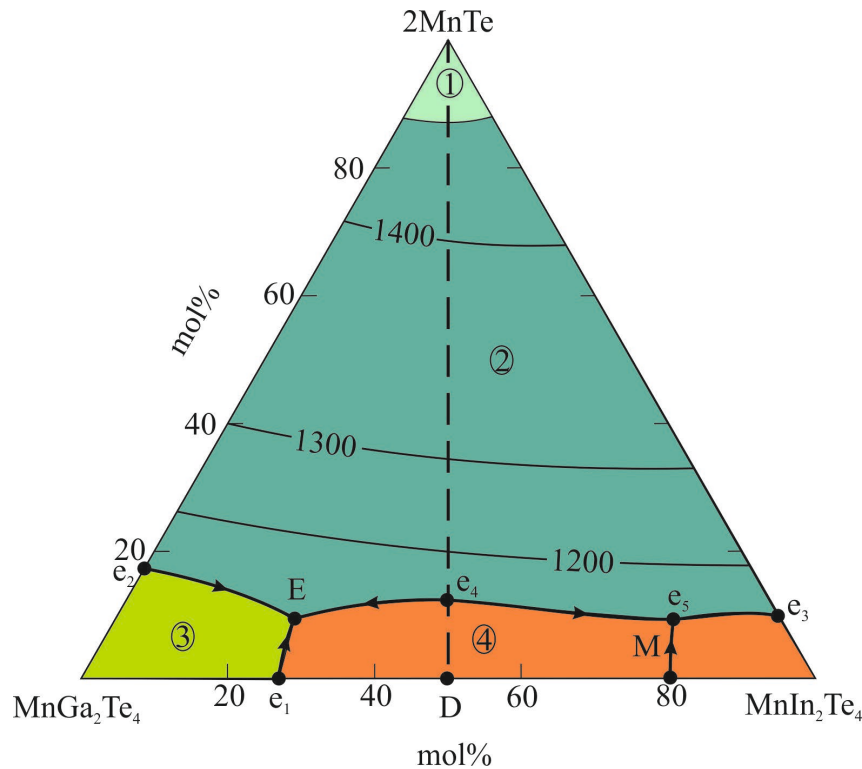
Fig. 5. Projection of the liquidus surface of the MnTe–MnGa2Te$_4$–MnIn$_2$Te$_4$ system. Primary crystallisation fields of the phases: *1* – Mn-ht; *2* – phases based on various modifications of MnTe; *3* – g$_1$; *4* – g$_2$

system, could be explained by the formation of MnTe by a peritectic reaction L + Mn-ht ↔ MnTe-ht [32]. Field (2) corresponds to the crystallisation of solid solutions based on various modifications of MnTe. The other two fields belong to the γ$_1$ and γ$_2$ phases. The specified fields are separated by a number of curves of monovariant equilibria and points of non-variant equilibria. The types and coordinates of non-variant and monovariant equilibria are presented in Table 2.

The MnTe–MnGa$_2$Te$_4$–MnIn$_2$Te$_4$ system had one partially quasi-binary section (Fig. 5, dotted line) that divided it into 2 subsystems. The MnTe–MnGa$_2$Te$_4$–MnGaInTe$_4$ subsystem belonged to the non-variant eutectic (E) type while the MnTe–MnGaInTe$_4$–MnIn$_2$Te$_4$ subsystem belonged to the monovariant eutectic type. It should be noted that the γ$_2$ phase of the MnGaInTe$_4$ composition had the highest melting point of 1030 K. As was shown in [30], the nature of colonisation of crystallographic positions in MnGaInTe$_4$ allowed considering it as an ordered phase. Taking into account that the MnGaInTe$_4$ phase was in non-variant eutectic equilibrium with the γ phase based on MnTe-rt (Fig. 5, point e$_4$), this section could be considered partially quasi-binary.

3.3. Polythermal sections

The **MnTe–MnGaInTe$_4$ section** (Fig. 6) was quasi-binary. The liquidus consists of three curves. Mn-ht crystallises from the melt in the regions of compositions rich in MnTe (> 90 mol%), while solid solutions based on various modifications of manganese monotelluride crystallise in the range of 13–90 mol% MnTe. The γ$_2$ phase crystallises in the range of 0–15 mol% MnTe. The formation of solid solutions based on MnTe leads to a decrease in temperature of its polymorphic transitions and establishment of metatectic equilibria. The coordinates of the eutectic points (e$_4$) are 13 mol% MnTe and 1018 K.

The **MnGa$_2$Te$_4$–[A] section** (Fig. 7) where [A] is a two-phase alloy of the 2MnTe–MnIn$_2$Te$_4$ side system with the 50 mol% MnIn$_2$Te$_4$ composition. This section crosses the 2MnTe–MnGaInTe$_4$ partially quasi-binary section and passes through the primary crystallisation fields of solid solutions based on various crystalline modifications of MnTe and the γ$_1$ phase. The following monovariant eutectic reactions procee below the liquidus: L ↔ α + γ$_1$ (55–97 mol% MnGa$_2$Te$_4$) and L ↔ α + γ$_2$ (< 55 mol% MnGa$_2$Te$_4$). The second reaction is

Condensed Matter and Interphases / Конденсированные среды и межфазные границы   2022;24(3): 335–344

F. M. Mammadov et al.   Phase equilibria in the MnTe–MnGa$_2$Te$_4$–MnIn$_2$Te$_4$ system
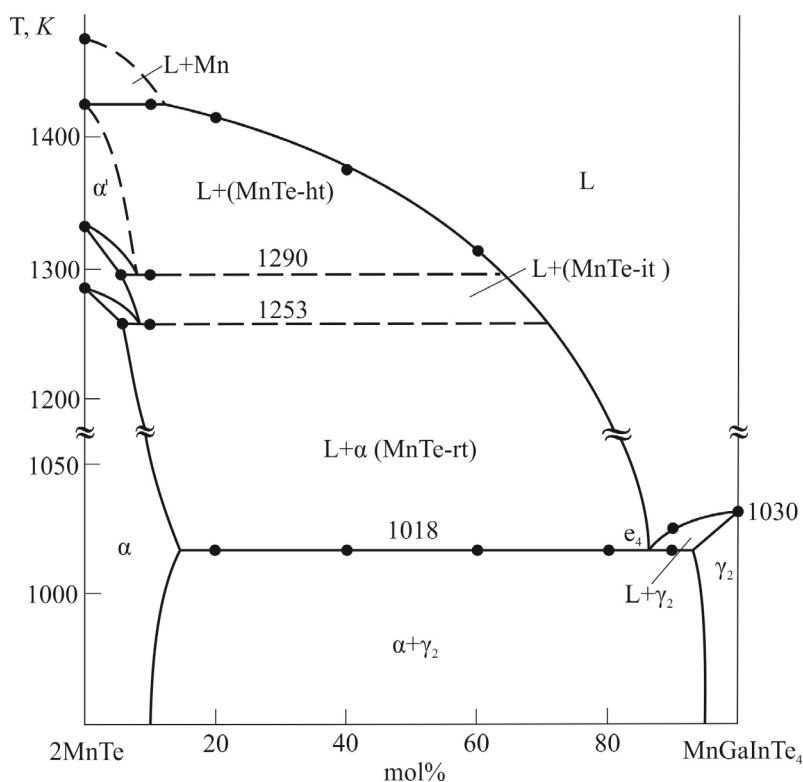
Fig. 6. Polythermal section of 2MnTe–MnGaInTe$_4$
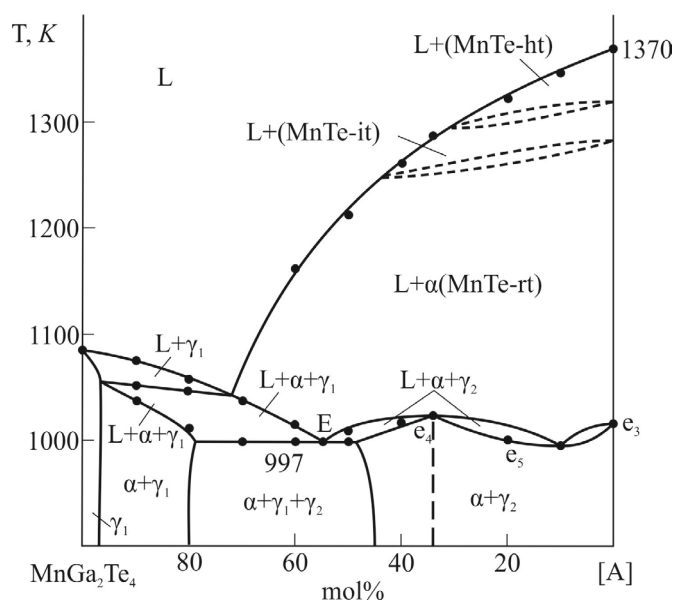
Fig. 7. Polythermal section of MnGa$_2$Te$_4$–[A], [A] is the alloy of the 2MnTe–MnIn$_2$Te$_4$ system with the composition of 50 mol% MnIn$_2$Te$_4$

non-variant in the extremum points (10 and 33.3 mol% MnGa$_2$Te$_4$ compositions). Three-phase fields are formed over the course of the specified eutectic processes: L + α + γ$_1$ and L + α + γ$_2$ (Fig. 7). In the range of the 0–48 and 80–97 mol% MnGa$_2$Te$_4$ compositions crystallisation ends with the formation of two-phase mixtures, α + γ$_2$ and α + γ$_1$, respectively. In the range of 48–80 mol% MnGa$_2$Te$_4$ crystallisation proceeds by a L$_E$ ↔ α + γ$_1$ + γ$_2$ non-variant eutectic reaction that resulted in the formation of a three-phase region α + γ$_1$ + γ$_2$ in the subsolidus.

Condensed Matter and Interphases / Конденсированные среды и межфазные границы   2022;24(3): 335–344

F. M. Mammadov et al.   Phase equilibria in the MnTe–MnGa$_2$Te$_4$–MnIn$_2$Te$_4$ system

4. Conclusions

Phase equilibria in the MnTe–MnGa$_2$Te$_4$–MnIn$_2$Te$_4$ system were studied by DTA and XRD methods. We built a projection of the liquidus surface of this system, an isothermal section at 800 K, and internal polythermal sections of the 2MnTe–MnGaInTe$_4$ and MnGa$_2$Te$_4$–[A] phase diagram. It was shown that the liquidus surfaces corresponded to 4 fields of primary crystallisation fields. We identified the types and coordinates of non-variant and monovariant equilibria. Wide regions of solid solutions along the MnGa$_2$Te$_4$–MnIn$_2$Te$_4$ section (10 and 65 mol%, respectively) that are of practical interest as potential magnetic materials were determined in the system.

Author contributions

F. M. Mammadov – research concept, writing the article, discussion of results. S. Z. Imamaliyeva – analysis of scientific literature, synthesis of compounds, conducting studies. Ya. I. Jafarov – analysis of scientific literature, discussion of results. I. B. Bakhtiyarly – discussion of results. M. B. Babanly – scientific supervision of research, concept of research, final conclusions.

Conflict of interests

The authors declare that they have no known competing financial interests or personal relationships that could have influenced the work reported in this paper.

References

1. Hyunjung K., Anand P. T., Eunhee H., Yunhee C., Heemin H., Sora B., Yeseul H., Hyoyoung L. FeIn$_2$S$_4$ nanocrystals: a ternary metal chalcogenide material for ambipolar field-fffect nransistors. *Advance Science.* 2018;1800068 (1-8). https://doi.org/10.1002/advs.201800068

2. Gao M. R., Xu Y. F., Jiang J., Yu S. H. Nanostructured metal chalcogenides: synthesis, modification, and applications in energy conversion and storage devices. *Chemical Society Reviews*. 2013;42(7): 2986–3017. https://doi.org/10.1039/C2CS35310E

3. Xia C., Li J. SnS thin films deposited by chemical bath deposition, dip coating and SILAR techniques. *Journal of Semiconductors*. 2016;37(5): 051001(1-9). https://doi.org/10.1088/1674-4926/37/5/053001

4. Karthikeyan N., Aravindsamy G., Balamurugan P., Sivakumar K. Thermoelectric properties of layered type FeIn$_2$Se$_4$ chalcogenide compound. *Materials Research Innovations.* 2018;22(5): 278–281. https://doi.org/10.1080/14328917.2017.1314882

5. Niftiyev N. N., Mamedov F. M., Quseynov V. I., Kurbanov S. Sh. AC electrical conductivity of FeIn$_2$Se$_4$ single crystals. *Semiconductors*. 2018;52(6): 683–685. https://doi.org/10.1134/S1063782618060167

6. Hwang Y., Choi J., Ha Y., Cho S., Park H. Electronic and optical properties of layered chalcogenide FeIn$_2$Se$_4$. *Current Applied Physics.* 2020; 20(1): 212–218. https://doi.org/10.1016/j.cap.2019.11.005

7. Yang J., Zhou Z., Fang J., Wen H., Lou Z., Shen G., Wei Z. Magnetic and transport properties of a ferromagnetic layered semiconductor MnIn$_2$Se$_4$. *Applied Physics Letters.* 2019;115(22): 222101(1-4). https://doi.org/10.1063/1.5126233

8. Sagredo V., Torres T. E., Delgado G. E., Rincón C. Effect of the paramagnetic to spin-glass phase transition on the fundamental absorption edge of MnIn$_2$Se$_4$ magnetic semiconducting compound. *Revista Mexicana de Física.* 2019;65(1): 14–19. https://doi.org/10.31349/RevMexFis.65.14

9. Djieutedjeu H., Lopez J. S., Lu R., Buchanan B., Zhou X., Chi H., Ranmohotti K. G. S, Uher C., Poudeu P. F .P. Charge disproportionation triggers bipolar doping in FeSb$_{2-x}$Sn$_x$Se$_4$ ferromagnetic semiconductors, enabling a temperature-induced Lifshitz transition. *Journal of the American Chemical Society*. 2019;141(23): 9249–9261. https://doi.org/10.1021/jacs.9b01884

10. Djieutedjeu H., Zhou X., Chi H., Haldolaarachchige N., Ranmohott K. G. S., Uher C., Young D., Poudeu P. F. P. Donor and acceptor impurity-driven switching of magnetic ordering in MnSb$_{2x}$Sn$_x$Se$_4$. *Journal of Materials Chemistry C*. 2014;2(30): 6199–6210. https://doi.org/10.1039/C4TC00672K

11. Moroz N. A., Lopez J. S., Djieutedjeu H., Ranmohotti K. G. S., Olvera A. R., Pan P. A., Takas N. J., Uher C., Poudeu P. F. P. Indium preferential distribution enables electronic engineering of magnetism in FeSb$_{2-x}$In$_x$Se$_4$ p-type high-Tc ferromagnetic semiconductors. *Chemical of Materials*. 2016;28(23): 8570–8579. https://doi.org/10.1021/acs.chemmater.6b03293

12. Haeuseler H., Srivastava S. K. Phase equilibria and layered phases in the systems A$_2$X$_3$-M$_2$X$_3$-M'X (A = Ga, In; M = trivalent metal; M' = divalent metal; X = S, Se). *Zeitschrift für Kristallographie*. 2000;215(4): 205–221. https://doi.org/10.1524/zkri.2000.215.4.205

13. Otrokov M. M., Klimovskikh I. I., Bentmann H., Zeugner A., Aliev Z.S., Gass S., Wolter A. U. B, Koroleva A. V., Estyunin D., Shikin A. M., BlancoRey M., Hoffmann M., Vyazovskaya A. Yu, Eremeev S. V., Koroteev Y. M., Amiraslanov I. R., Babanly M. B., Mamedov N. T., Abdullayev N. A., Zverev V. N., Büchner B., Schwier E. F., Kumar S., Kimura A., Petaccia L., Di Santo G., Vidal R. C., Schatz S., Kisner K., Min C. H., Moser S. K., Peixoto T. R. F., Reinert F.,

Condensed Matter and Interphases / Конденсированные среды и межфазные границы   2022;24(3): 335–344

F. M. Mammadov et al.   Phase equilibria in the MnTe–MnGa$_2$Te$_4$–MnIn$_2$Te$_4$ system

Ernst A., Echenique P. M., Isaeva A., Chulkov E. V. Prediction and observation of the first antiferromagnetic topological insulator. *Nature.* 2019;576(7787): 416–422. https://doi.org/10.1038/s41586-019-1840-9

14. Zhang D., Shi M., Zhu T., Xing D., Zhang H., Wang J. Topological axion states in the magnetic insulator MnBi$_2$Te$_4$ with the quantized magnetoelectric effect. *Physical Review Letters*. 2019;122(20): 206401(1-6). https://doi.org/10.1103/PhysRevLett.122.206401

15. Klimovskikh I. I., Otrokov M. M., Estyunin D., Eremeev S. V., Filnov S. O., Koroleva A., Shevchenko E., Voroshnin V., Rusinov I. P., Blanco-Rey M., Hofmann M., Aliev Z. S., Babanly M. B, Amiraslanov I. R., Abdullayev N. A., Zverev V. N., Kimura A., Tereshchenko O. E., Kokh K. A., Petaccia L., Di Santo G., Ernst A., Echenique P. M., Mamedov N. T., Shikin A. M., Chulkov E. V. Tunable 3D/2D magnetism in the (MnBi$_2$Te$_4$) (Bi$_2$Te$_3$)$_m$ topological insulators family. *npj Quantum Materials*. 2020; 5(54): 1–9. https://doi.org/10.1038/s41535-020-00255-9

16. Estyunin D. A. , Klimovskikh I. I. , Shikin A. M., Schwier E. F., Otrokov M. M., Kumira A., Kumar S., Filnov S. O., Aliev Z. S., Babanly M. B., Chulkov E. V. Signatures of temperature driven antiferromagnetic transition in the electronic structure of topological insulator MnBi$_2$Te$_4$. *APL Materials*. 2020;8(2): 021105(1-7). https://doi.org/10.1063/1.5142846

17. He K. MnBi$_2$Te$_4$-family intrinsic magnetic topological materials. *npj Quantum Mateials.* 2020;5(1): 90(1-4). https://doi.org/10.1038/s41535-020-00291-5

18. Jahangirli Z. A., Alizade E. H., Aliev Z. S., Otrokov M. M. Ismayilova N. A., Mammadov S. N., Amiraslanov I. R., Mamedov N. T., Orudjev G. S., Babanly M. B., Shikin A. M., Chulkov E. V. Electronic structure and dielectric function of Mn-Bi-Te layered compounds. *Journal of Vacuum Science & Technology B.* 2019;37(6): 062910(1-6). https://doi.org//10.1116/1.5122702

19. Yuan Y., Wang X., Li H., Li J., Ji Y., Hao Z., Wu Y., He K., Wang Y., Xu Y., Duan W., Li W., Xue Q. Electronic states and magnetic response of MnBi$_2$Te$_4$ by scanning tunneling microscopy and spectroscopy. *Nano Letters*. 2020;20(5): 3271–3277. https:/doi.org/10.1021/acs.nanolett.0c00031

20. Zhou L., Tan Z., Yan D., Fang Z., Shi Y., Weng H. Topological phase transition in the layered magnetic compound MnSb$_2$Te$_4$: Spin-orbit coupling and interlayer coupling dependence. *Physical Review B*. 2020;102: 085114(1-8). https://doi.org/10.1103/PhysRevB.102.085114

21. Garrity K. F., Chowdhury S., Tavazza F. M. Topological surface states of MnBi$_2$Te$_4$ at finite temperatures and at domain walls. *Physical Review Materials*. 2021;5: 024207(1-6). https://doi.org/10.1103/PhysRevMaterials.5.024207

22. Ovchinnikov D., Huang X., Lin Z. … Xu X. Intertwined topological and magnetic orders in atomically thin chern insulator MnBi$_2$Te$_4$. *Nano Letters*. 2021;21(6): 2544–2550. https://dx.doi.org/10.1021/acs.nanolett.0c05117

23. Swatek P., Wu Y., Wang L. L. Gapless dirac surface states in the antiferromagnetic topological insulator MnBi$_2$Te$_4$. *Physical Review* B. 2020;101(16): 161109(1-6). https://doi.org/10.1103/PhysRevB.101.161109

24. Zhu T., Bishop A. J., Zhou T., Zhu M., O'Hara D. J., Baker A. A., Cheng S., Walko R. C., Repicky J. J., Liu T., Gupta J. A., Jozwiak C. M., Rotenberg E., Hwang J., Žutic I., Kawakami R. K. Synthesis, magnetic properties, and electronic structure of magnetic topological insulator MnBi$_2$Se$_4$. *Nano Letters.* 2021;21(12): 5083–5090, https://doi.org/10.1021/acs.nanolett.1c00141

25. Babanly M. B., Mashadiyeva L. F., Babanly D. M., Imamaliyeva S. Z., Tagiev D. B., Yusibov Yu. A Some issues of complex studies of phase equilibria and thermodynamic properties in ternary chalcogenide systems involving Emf Measurements (Review). *Russian Journal of Inorganic Chemistry*. 2019;64(13): 1649–1671. https://doi.org/10.1134/S0036023619130035

26. Kertman A. V., Ruseikina A. V. Phase equilibria in BaS–In$_2$S$_3$ system. *Russian Journal of Inorganic Chemistry.* 2020;65(11): 1756–1761. https://doi.org/10.1134/S003602362011008X

27. Zlomanov V. P., Khoviv A. M., Zavrazhnov A. Yu. Physicochemical analysis and synthesis of nonstoichiometric solids. *Materials Science - Advanced Topics*. 2013, Chapter 5, pp. 103–128. https://doi.org/10.5772/54815

28. Mammadov F. M., Amiraslanov I. R., Imamaliyeva S. Z., Babanly M. B. Phase relations in the FeSe–FeGa$_2$Se$_4$–FeIn$_2$Se$_4$ system: refinement of the crystal structures of FeIn$_2$Se$_4$ and FeGaInSe$_4$. *Journal of Phase Equilibria and Diffusion.* 2019;40(6): 787–796. https://doi.org/10.1007/s11669-019-00768-2

29. Mammadov F. M., Imamaliyeva S. Z., Amiraslanov I. R., Babanly M. B. The phase diagram of the FeGa$_2$Se$_4$–FeIn$_2$ Se$_4$ system and the crystal structure of FeGaInSe. Condensed Matter and Interphases. 2018;20 (4): 604–610. (In Russ., abstract in Eng.). https://doi.org/10.17308/kcmf.2018.20/633

30. Mammadov F. M., Amiraslanov I. R., Aliyeva Y. R., Ragimov S. S., Mashadiyeva L. F., Babanly M. B. Phase equilibria in the MnGa$_2$Te$_4$-MnIn$_2$Te$_4$ system, crystal structure and physical properties of MnGaInTe$_4$. *Acta Chimica Slovenica.* 2019;66(2): 466–472. https://doi.org/10.17344/acsi.2019.4988

31. Mammadov F. M., Babanly D. M., Amiraslanov I. R., Tagiev D. B., Babanly M. B. FeS–Ga$_2$S$_3$–In$_2$S$_3$ system. *Russian Journal of Inorganic Chemistry*.

Condensed Matter and Interphases / Конденсированные среды и межфазные границы   2022;24(3): 335–344

F. M. Mammadov et al.   Phase equilibria in the MnTe–MnGa$_2$Te$_4$–MnIn$_2$Te$_4$ system

2021;66(10): 1533–1543. https://doi.org/10.1134/S0036023621100090

32. *Binary alloy phase diagrams.* Massalski T. B. (ed.). ASM International, Materials Park, Ohio, USA: 1990. 3875 p.

33. *Phase Diagrams for Binary Alloys.*.Okamoto H. (ed.), 2nd Edition. ASM International, Materials Park, Ohio, USA: 2010. 900 p.

34. Mammadov F. M. New version of the phase diagram of the MnTe–Ga$_2$Te$_3$ system. *New Materials, Compounds and Applications.* 2021;5(2): 116–121. Available at: http://jomardpublishing.com/UploadFiles/Files/journals/NMCA/V5N2/MammadovF.pdf

35. Mammadov F. M. Refinement of the phase diagram of the MnTe–In$_2$Te$_3$ system. *Azerbaijan Chemical Journal.* 2021;2: 37–41. https://doi.org/10.32737/0005-2531-2021-2-37-41

36. Chevalier P. Y., Fischer E., Marbeuf A. A thermodynamic evaluation system of the Mn–Te binary. *Thermochimica Acta.* 1993;223: 51–63. https://doi.org/10.1016/0040-6031(93)80119-U

37. Range K.-J., Hubner H.-J. MnGa$_2$Se$_4$ and MnGa$_2$Te$_4$. *Zeitschrift für Naturforschung B.* 1976;31(6): 886–887. https://doi.org/10.1515/ZNB-1976-0632

38. Cannas M., Garbato A., Garbato L., Ledda F., Navarra G. Crystal growth and structure of MnGa$_2$Te$_4$. *Progress in Crystal Growth and Characterization of Materials.* 1996;32: 171–183. https://doi.org/10.1016/0960-8974(95)00020-8

Information about the authors

Faig M. Mammadov, PhD (Chem.), Assistance Professor, Institute of Catalysis and Inorganic Chemistry, Azerbaijan National Academy of Sciences (Baku, Azerbaijan).
https://orcid.org/0000-0003-3317-7438
faikmamadov@mail.ru

Samira Z. Imamaliyeva, PhD (Chem.), Assistance Professor, Institute of Catalysis and Inorganic Chemistry, Azerbaijan National Academy of Sciences (Baku, Azerbaijan).
https://orcid.org/0000-0001-8193-2122
samira9597a@gmail.com

Yasin İ. Jafarov, Dr. Sci. (Chem.), Assistance Professor, Baku State University (Baku, Azerbaijan).
https://orcid.org/0000-0002-6597-2252
yasin_cafarov@mail.ru

Ikhtiyar B. Bakhtiyarly, Dr. Sci. (Chem.), Professor, Laboratory Manager Institute of Catalysis and Inorganic Chemistry, Azerbaijan National Academy of Sciences (Baku, Azerbaijan).
https://orcid.org/0000-0002-7765-0672
ibbakhtiarli@mail.ru

Mahammad B. Babanly, Dr. Sci. (Chem.), Professor, Associate Member of the Azerbaijan National Academy of Sciences, Executive Director of the Institute of Catalysis and Inorganic Chemistry, Azerbaijan National Academy of Sciences (Baku, Azerbaijan).
https://orcid.org/0000-0001-5962-3710
babanlymb@gmail.com

Original articles

Synthesis of chemically pure β-phase powders of gallium(III) oxide

A. M. Samoylov✉, S. S. Kopytin, K. V. Oreshkin, E. A. Shevchenko

Voronezh State University,
1 Universitetskaya pl., Voronezh 394018, Russian Federation

Abstract

The purpose of our study was to develop an optimal procedure for the synthesis of the β-phase of gallium(III) oxide with a high degree of chemical purity. Based on the analysis of the possible synthesis methods of the β-phase of gallium(III) oxide, we suggested a procedure which uses gallium(III) nitrate crystallohydrate as a precursor for obtaining the final product. The article demonstrates that during the synthesis of gallium(III) nitrate by means of direct interaction between metallic gallium and concentrated nitric acid, a hygroscopic crystallohydrate is formed with the formula $Ga(NO_3)_3 \cdot 9H_2O$.

Powders of the β-phase of Ga_2O_3 were synthesised by means of the thermal decomposition of gallium(III) nitrate in an oxygen atmosphere. Electron probe microanalysis (EPMA) and X-ray phase analysis (XRD) were used to determine the quantitative chemical composition, stoichiometry, and crystal structure of the gallium(III) oxide samples synthesised at different temperatures. The EPMA of the powders calcinated at temperatures T_{calc} = 500–950 °C demonstrated that the ratio of the elements was constant and corresponded to the stoichiometric composition of Ga_2O_3. A comparative analysis of the X-ray diffraction peaks demonstrated that with an increase in the decomposition temperature within the range T_{calc} = 500–950 °C, the symmetry of the structure of the Ga_2O_3 powders decreased from the cubic to the monoclinic. The study also determined that the samples of gallium(III) oxide synthesised at T_{calc} = 950 °C are single-phase and consist entirely of the monoclinic β-phase. The XRD data was used to calculate the crystal lattice parameters of the samples of the β-phase of Ga_2O_3 synthesised at T_{calc} = 950 °C.

Keywords: Gallium (III) oxide, Gallium (III) nitrate, Polymorphous modifications, Stoichiometry, Crystal structure, Monoclinic crystal system, Lattice parameters

✉ Alexander M. Samoylov, e-mail: samoylov@chem.vsu.ru

Condensed Matter and Interphases / Конденсированные среды и межфазные границы   2022;24(3): 345–355

A. M. Samoylov et al.   Synthesis of chemically pure β-phase powders of gallium(III) oxide

1. Introduction

The scientific progress at the turn of the 21st century and development of science-intensive technologies necessitated the creation of a new generation of microelectronic devices. Consequently, scientists began their search for semiconductor materials other than silicon and gallium arsenide [1, 2]. The range of promising materials for optical- and microelectronics has grown significantly, with experts focusing especially on studying wide-band semiconductor materials such as gallium nitride (GaN), aluminium nitride (AlN), silicon carbide (SiC), and solid solutions of gallium nitride and aluminium nitride (AlGaN).

The analysis of the literature data showed that of all the polymorphic modifications of gallium(III) oxide the β-phase of Ga_2O_3, which is thermodynamically stable in a wide range of temperatures, is the most promising material for optical- and microelectronics in the 21st century [2]. The obtained data on the physicochemical properties of single crystals and thin films of gallium(III) oxide demonstrates that this material has recently become a promising candidate for the production of certain types of devices in power electronics as well as solar energy converters and ultraviolet (UV) photodetectors [2–10]. Due to the large band gap of the β-phase of Ga_2O_3 (ΔE_g ~ 4.7 eV) this material can be used to produce ionizing radiation sensors and gas sensors which provide for more opportunities than the existing technologies [11–16].

Besides the above mentioned applications, gallium(III) oxide can also be used in doping of metal oxide semiconductors with hole conductivity, for instance palladium(II) oxide [17–20]. The studies of thin and nanocrystalline palladium(II) oxide films demonstrated that the heterostructures based on them can be effectively used to create resistive gas sensors [21–23]. Doping with gallium(III) oxide can enhance the sensitivity and selectivity of gas sensors produced using nanostructures with different morphological organization based on palladium(II) oxide due to the formation of active sites, as well as devices with *p*- *n*-transitions [24–25].

Analysis of the existing literature demonstrated that electrical properties of the β-phase of Ga_2O_3 have not been thoroughly studied yet [2]. Such studies are very much hindered by the presence of the so-called unintentional impurities in gallium(III) oxide [2]. Therefore, it is important to develop a method for synthesising gallium(III) oxide of high chemical purity.

The purpose of our study was to determine the optimal method of synthesis of the β-phase of Ga_2O_3 with high chemical purity, as well as to investigate its quantitative composition and crystal structure depending on the synthesis conditions.

2. Experimental

As follows from the literature data [26–28], there are several methods of synthesis of gallium(III) oxide. Fig. 1 presents the possible methods of synthesis of gallium(III) oxide. It might seem that the easiest way to synthesise β-phase powders of Ga_2O_3 is by the thermal decomposition of the precipitate of gallium(III) hydroxide according to the equation:

$$2Ga(OH)_3^{(S)} \rightarrow Ga_2O_3^{(S)} + 3 H_2O^{(G)}. \tag{1}$$
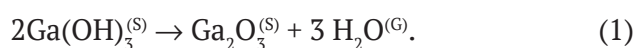
Since gallium(III) hydroxide (III) is characterised by a relatively small solubility product, $Ksp(Ga(OH)_3) = 1.6 \cdot 10^{-37}$ [29], it is possible to obtain enough precipitation of the substance with a minimum loss of the initial reagents. It is known [26–28] that gallium is an amphoteric metal. Therefore, gallium(III) hydroxide can be obtained by means of two methods.

First, the precipitate of gallium(III) hydroxide can be, in theory, synthesised in a single stage by direct interaction with hot water according to the equation:

$$2Ga^{(S)} + 6H_2O^{(L)} \rightarrow 2Ga(OH)_3^{(S)} + 3H_2^{(G)}. \tag{2}$$

In fact, this reaction (2) does not take place due to the quick oxidation of the metal's surface and formation of a thick layer of gallium(III) oxide which prevents the interaction between the metal and water.

The second way, as shown in Fig. 1, is to obtain the precipitate of $Ga(OH)_3$ in two stages. During the first stage, gallium is dissolved in strong inorganic acids (HCl, H_2SO_4, and HNO_3) followed by the deposition of $Ga(OH)_3$ by means of the effect of alkali on the solution of the corresponding salt, for instance:

$$GaCl_3^{(Aq)} + 3NaOH^{(Aq)} \rightarrow Ga(OH)_3^{(S)} + 3NaCl^{(Aq)}. \tag{3}$$

Condensed Matter and Interphases / Конденсированные среды и межфазные границы   2022;24(3): 345–355

A. M. Samoylov et al.   Synthesis of chemically pure β-phase powders of gallium(III) oxide
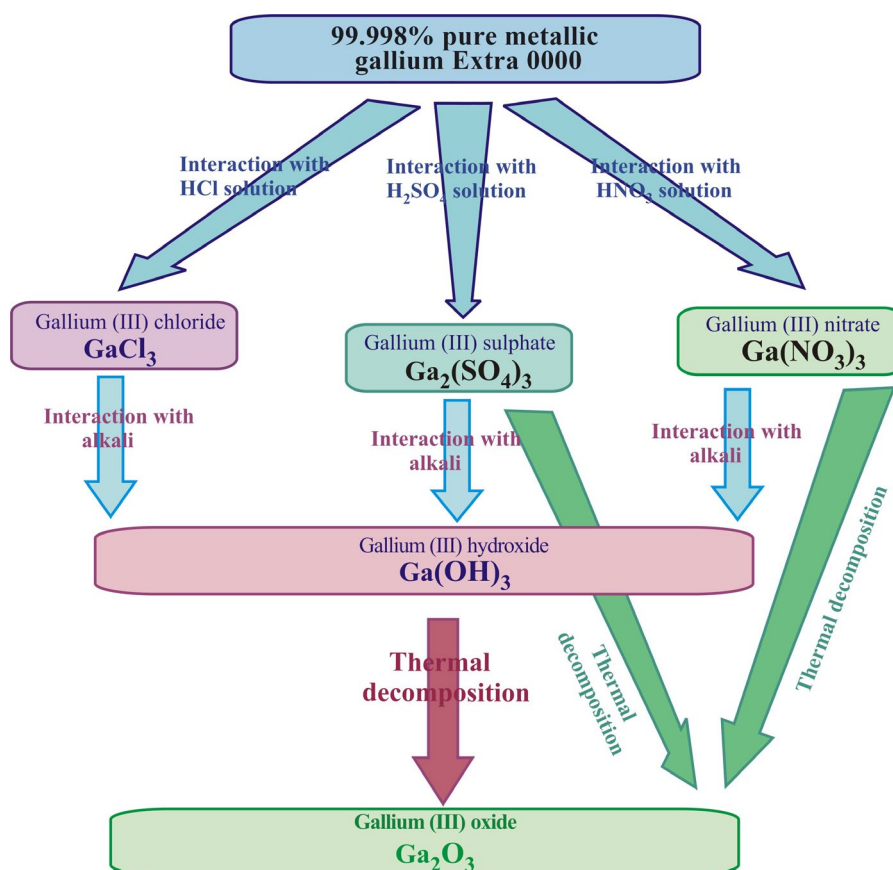
Fig. 1. Possible synthesis methods of different polymorphic modifications of gallium(III) oxide

However, this method of obtaining the precipitate of $Ga(OH)_3$ may result in smaller product yield of the reaction due to the incomplete deposition caused by the amphoterism of gallium(III) hydroxide:

$$Ga(OH)_3^{(S)} + 3NaOH^{(Aq)} \rightarrow 3Na[Ga(OH)_6]^{(Aq)}, \quad (4)$$

$$Ga(OH)_3^{(S)} + 3HCl^{(Aq)} \rightarrow GaCl_3^{(Aq)} + 3H_2O^{(L)}. \quad (5)$$
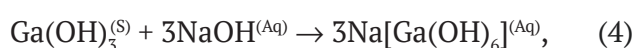
The existing literature does not provide any information about the dependence of the product yield of the deposition reaction of $Ga(OH)_3$ on the pH of the solution. There is also no data regarding the possible effect of the occurrence of sodium ions in the precipitate of $Ga(OH)_3$ obtained according to the equation (3). Nevertheless, the reviews demonstrated [2, 3] that the most common method of obtaining various polymorphic modifications of Ga_2O_3 is the thermal decomposition of $Ga(OH)_3$ hydroxide or GaOOH oxyhydroxide.

In this article, we suggest an optimal alternative method for the synthesis of gallium(III) oxide. It is based on the fact (Fig. 1)

that during the synthesis of Ga_2O_3 the precursor is gallium(III) nitrate.

The suggested method has two advantages over the synthesis methods of gallium(III) oxide described above. First, this method provides for the maximum product yield of Ga_2O_3, because it prevents the loss of the initial reagents during all the stages. Second, the method allows for obtaining a product of high chemical purity.

To obtain this result, we used the following initial reagents: 99.998% pure metallic gallium Extra 000 and concentrated nitric acid (reagent grade GOST 4461-77) which was additionally purified by means of distillation. As we know [30], nitric acid can contain a certain amount of hydrochloric acid impurities. Chloride anions in the samples of Ga_2O_3 are donor centres and therefore their presence in the samples of gallium(III) oxide is highly undesirable.

The degree of purity of the nitric acid was monitored based on the qualitative reaction with silver nitrate. The nitric acid was distilled until there were no chloride anions in the distilled

Condensed Matter and Interphases / Конденсированные среды и межфазные границы   2022;24(3): 345–355

A. M. Samoylov et al.   Synthesis of chemically pure β-phase powders of gallium(III) oxide

fraction of HNO_3. As a result, we obtained nitric acid of 1.40–1.45 g/cm³, which corresponds to the mass fraction $\omega\%$ (HNO_3) = 66 %.

As demonstrated in Fig. 1, in our study we used the process of decomposition of gallium(III) nitrate to synthesise crystalline powders of gallium(III) oxide. In this case, the synthesis of Ga_2O_3 includes two stages. During the first stage, gallium(III) nitrate was synthesised. The synthesis of $Ga(NO_3)_3$ was performed by means of direct interaction of 99.998 % pure metallic gallium Extra 000 with concentrated nitric acid at room temperature according to the equation:

$$Ga^{(S)} + 6HNO_3^{(Aq)} \rightarrow$$
$$\rightarrow Ga(NO_3)_3^{(Aq)} + 3NO_2^{(G)} + 3H_2O^{(L)} \qquad (6)$$
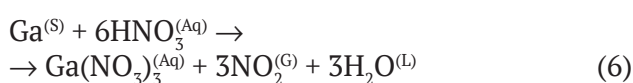
To initiate the formation of crystals, the solution was evaporated at the temperature of 50 °C until the first microscopic crystals appeared. The solution was then cooled to room temperature, after which it was further cooled to 0 °C in a mixture of ice and distilled water. The complete deposition of the gallium(III) nitrate crystallohydrate was obtained by keeping the solution at the temperature of 0 °C for 4 hours.

Using the calculations based on the results of the gravimetric analysis of the obtained crystals and the mass of the initial metallic gallium we determined that within the experimental error the formula of the obtained crystallohydrate is $Ga(NO_3)_3 \cdot 9H_2O$, or more precisely $[Ga(H_2O)_6](NO_3)_3 \cdot 3H_2O$.

The synthesised $Ga(NO_3)_3 \cdot 9H_2O$ crystals appeared to be highly hygroscopic and intensively absorbed moisture from air at room temperature. To prevent uncontrolled splashing of the $Ga(NO_3)_3 \cdot nH_2O$ samples, during the following calcination aimed at synthesising gallium(III) oxide, they were dehydrated by being heated to the temperature of 120 °C and exposed to isothermal endurance for 240 minutes. The temperature was monitored using chromel-alumel thermocouples and a digital voltmeter. As a result of the dehydration of $Ga(NO_3)_3 \cdot 9H_2O$ crystallohydrate under the described conditions, compact white samples were formed which practically did not absorb moisture from air. Prior to further calcination the dehydrated $Ga(NO_3)_3 \cdot nH_2O$ crystals were ground in an agate mortar for 30 minutes.

As a reactor for the decomposition of gallium nitrate we used a resistive heating tube furnace with dry oxygen delivered to the reaction zone. The quartz boat with the ground dehydrated $Ga(NO_3)_3 \cdot nH_2O$ crystals was put into the quartz reactor so that the galluim(III) nitrate sample was in the isothermal zone of the resistive heating furnace. The furnace was first slowly heated to T = 200 °C after which oxygen was delivered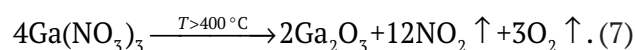 to the reaction zone. Thermal decomposition of the crystals of the precursor was performed in the temperature range of 300–950 °C for 6 hours. Gallium(III) nitrate was subjected to thermal decomposition to form gallium(III) oxide according to the equation:

$$4Ga(NO_3)_3 \xrightarrow{T>400\,°C} 2Ga_2O_3 + 12NO_2\uparrow + 3O_2\uparrow. \quad (7)$$

The qualitative and quantitative elemental composition of the synthesised samples was determined by means of the electron probe microanalysis (EPMA). The analysis was performed using a JEOL-JCM 6380 LV scanning electron microscope with an Oxford Instruments INCA X-sight LN2 energy dispersive analysis system.

The crystal structure of the Ga_2O_3 samples was studied by means of X-ray phase analysis (XRD) using a DRON-4-07 diffractometer with filtered CoK_α-radiation.

3. Results and discussion

Based on the quantity of gallium nitrate and the mass of the water, we determined the formula of the precursor used in the study. The synthesised gallium nitrate can be described by a molecular formula $Ga(NO_3)_3 \cdot 9H_2O$, or more precisely $[Ga(H_2O)_6](NO_3)_3 \cdot 3H_2O$. The X-ray analysis of the $Ga(NO_3)_3 \cdot 9H_2O$ crystallohydrate using DRON-4-07 did not present any diffraction pattern, which can be explained by the very high hygroscopy of gallium nitrate.

Using electron probe microanalysis (EPMA), we studied a number of samples obtained by means of calcination of dehydrated and ground $Ga(NO_3)_3 \cdot nH_2O$ samples in dry oxygen at the temperature range of T_{calc} = 300–950 °C.

Fig. 2 presents the typical spectrum of characteristic X-ray radiation and the scanning area of 400×400 µm of the surface of the samples obtained by means of the calcination of

Condensed Matter and Interphases / Конденсированные среды и межфазные границы   2022;24(3): 345–355

A. M. Samoylov et al.   Synthesis of chemically pure β-phase powders of gallium(III) oxide

dehydrated ground $Ga(NO_3)_3 \cdot nH_2O$ samples in the temperature range of T_{calc} = 300–950 °C. The synthesised samples of Ga_2O_3 showed very high resistance and very low electrical conductivity. To prevent the accumulation of static electricity and ensure the stability of the electronic probe, the surfaces of the studied Ga_2O_3 samples were coated with a thin layer of amorphous carbon (Fig. 2 a). This accounts for the presence of carbon lines in the characteristic X-ray radiation spectrum (Fig. 2 b). The figure demonstrates that the spectrum contains only gallium, oxygen, and carbon lines. No other elements were observed in the spectrum. This proves that the obtained samples are characterised by a high degree of chemical purity.

The data obtained my means of EPMA (Table 1) demonstrates that complete thermal decomposition of gallium(III) nitrate followed by the formation of a single-phase Ga_2O_3 according to the equation (7) takes place at the calcination temperature T_{calc} = 500 °C. The spectra of the samples obtained at lower temperatures (T_{calc} = 300 °C) contained nitrogen lines, which indicated that the decomposition of gallium(III) nitrate was not complete.

Having determined the quantitative composition of the single-phase gallium(III) oxide powders we can conclude that the quantity of gallium and oxygen atoms in the samples obtained at $T_{calc} \geq 500$ °C is constant within the systematic error of the EPMA method (Table 1).
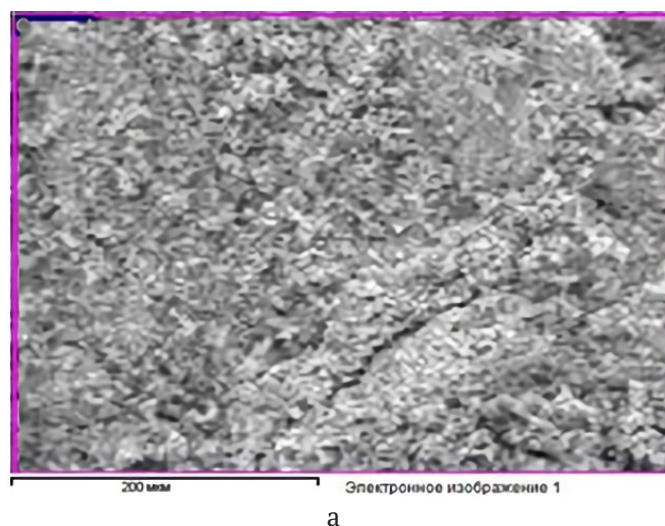
a
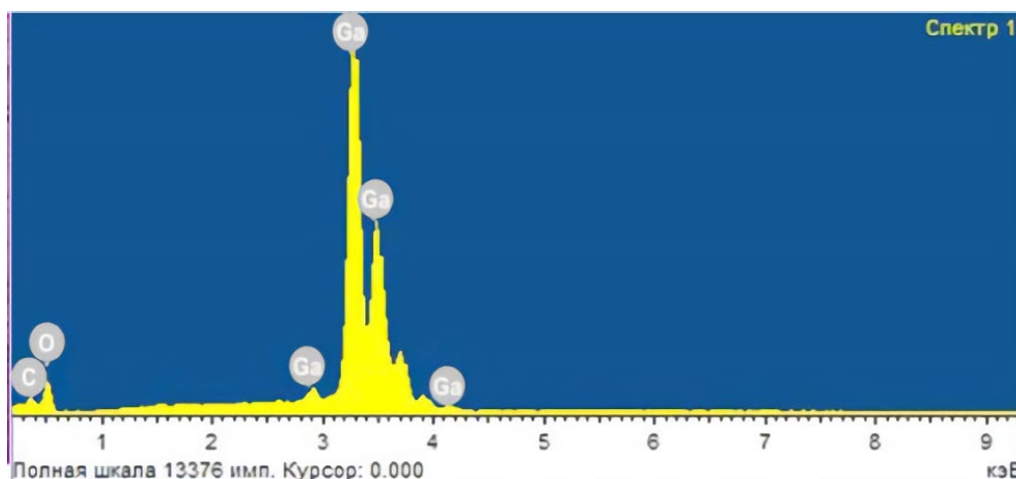
b

Fig. 2. a – SEM image of a section of the Ga_2O_3 sample scanned during the study of the quantitative composition by means of EPMA. b – Characteristic X-ray radiation spectrum of the Ga_2O_3 sample synthesized by calcination of $Ga(NO_3)_3 \cdot nH_2O$ in an oxygen atmosphere at T_{calc} = 750 °C

Condensed Matter and Interphases / Конденсированные среды и межфазные границы   2022;24(3): 345–355

A. M. Samoylov et al.   Synthesis of chemically pure β-phase powders of gallium(III) oxide

Table 1. The quantitative composition of samples obtained by calcination of dehydrated $Ga(NO_3)_3 \cdot nH_2O$ crystallohydrate in oxygen at different temperatures as determined by EPMA

Calcination temperature T_{calc} = 300 °C			
Element	Spectral line	Mass fraction ω, %	Mole fraction x, %
Gallium	L-line	63.26	18.985
Oxygen	K-line	30.42	65.895
Nitrogen	K-line	6.42	15.12
Total:		100%	100%
Phase composition of $Ga(NO_3)_3$ + Ga_2O_3			
Calcination temperature T_{calc} = 600 °C			
Element	Spectral line	Mass fraction ω, %	Mole fraction x, %
Gallium	L-line	74.005	39.515
Oxygen	K-line	25.995	60.485
Nitrogen	K-line	...	...
Total:		100 %	100 %
Quantitative composition of Ga_2O_3			
Calcination temperature T_{calc} = 850 °C			
Element	Spectral line	Mass fraction ω, %	Mole fraction x, %
Gallium	L-line	74.061	39.585
Oxygen	K-line	25.939	60.415
Nitrogen	K-line	...	...
Total:		100 %	100 %
Qualitative composition of Ga_2O_3			

Within the temperature range T_{calc} 500–950 °C, the ratio between the mole fractions of gallium and oxygen corresponds to the stoichiometric composition of Ga_2O_3 and does not depend on the calcination temperature. This data proved the assumption that the homogeneity region of Ga_2O_3 is rather narrow [2, 3].

Analysis of the literature data [2, 3, 31, 32] demonstrated that up to now five polymorphic modifications of gallium(III) oxide have been determined (Table 2). There is also data indicating the existence of a transitional form – the κ-phase of Ga_2O_3 [2, 3]. We should point out that the data regarding the crystal structure of most Ga_2O_3 modifications is rather controversial. Even more controversial is the information about the methods of obtaining most of the polymorphic modifications of Ga_2O_3, as well as about the temperatures at which each polymorphic modification of Ga_2O_3 is stable.

In our study, we used X-ray phase analysis to determine the phase composition of the Ga_2O_3 samples synthesised by means of calcination of gallium(III) nitrate in oxygen at a temperature of T_{calc} = 500–950 °C. The evolution of the X-ray diffraction pattern of the Ga_2O_3 samples synthesised at different temperatures is given in Fig. 3. The results of the identification of polymorphic modifications of the synthesised gallium(III) oxide samples based on the information in an international crystallographic database are presented in Table 3.

Fig. 3 shows that with an increase in the temperature of calcination of gallium(III) nitrate in an oxygen atmosphere the crystal structure of the Ga_2O_3 samples changes dramatically. According to the data presented in Fig. 3 and Table 3, the Ga_2O_3 samples synthesised at T_{calc} = 500 °C are single-phase and have the cubic crystal structure of a spinel (γ-phase of Ga_2O_3). When the synthesis temperature was increased to T_{calc} = 600 °C, the Ga_2O_3 samples were a mixture of two phases: the cubic γ-phase with an insignificant fraction of the δ-phase (Table 3). Further increase in the synthesis temperature of gallium(III) oxide samples in an oxygen atmosphere to T_{calc} = 750 °C resulted in the growth of the fraction of the δ-phase of Ga_2O_3

Condensed Matter and Interphases / Конденсированные среды и межфазные границы   2022;24(3): 345–355

A. M. Samoylov et al.   Synthesis of chemically pure β-phase powders of gallium(III) oxide

Table 2. Literature data on gallium(III) oxide polymorphous modifications [2, 3, 31 – 34].

Polymorphic modification	Crystal system	Space group	Pearson symbol
α-Ga$_2$O$_3$	Hexagonal (rhombohedral)	$R\bar{3}c$	hR30
β-Ga$_2$O$_3$	Monoclinic	$C2/m$	mS20
γ-Ga$_2$O$_3$	Cubic, defect spinel structure	$Fd\bar{3}m$	–
δ-Ga$_2$O$_3$	Cubic, possibly the structural type of bixbyite	$Ia\bar{3}$	–
ε-Ga$_2$O$_3$	Orthorhombic	$Pna2_1$	–

Table 3. Phase composition of the Ga$_2$O$_3$ samples obtained by calcination of dehydrated Ga(NO$_3$)$_3$×nH$_2$O crystallohydrate in oxygen at different temperatures

Calcination temperature T_{calc}, °C	Calcination temperature t, min.	Phase nature	Phase composition
500	360	Однофазный	γ-Ga$_2$O$_3$
600	360	Гетерофазный	γ-Ga$_2$O$_3$+ δ-Ga$_2$O$_3$
750	360	Гетерофазный	δ-Ga$_2$O$_3$ + γ-Ga$_2$O$_3$
850	360	Гетерофазный	δ-Ga$_2$O$_3$ + β-Ga$_2$O$_3$
950	360	Однофазный	β-Ga$_2$O$_3$
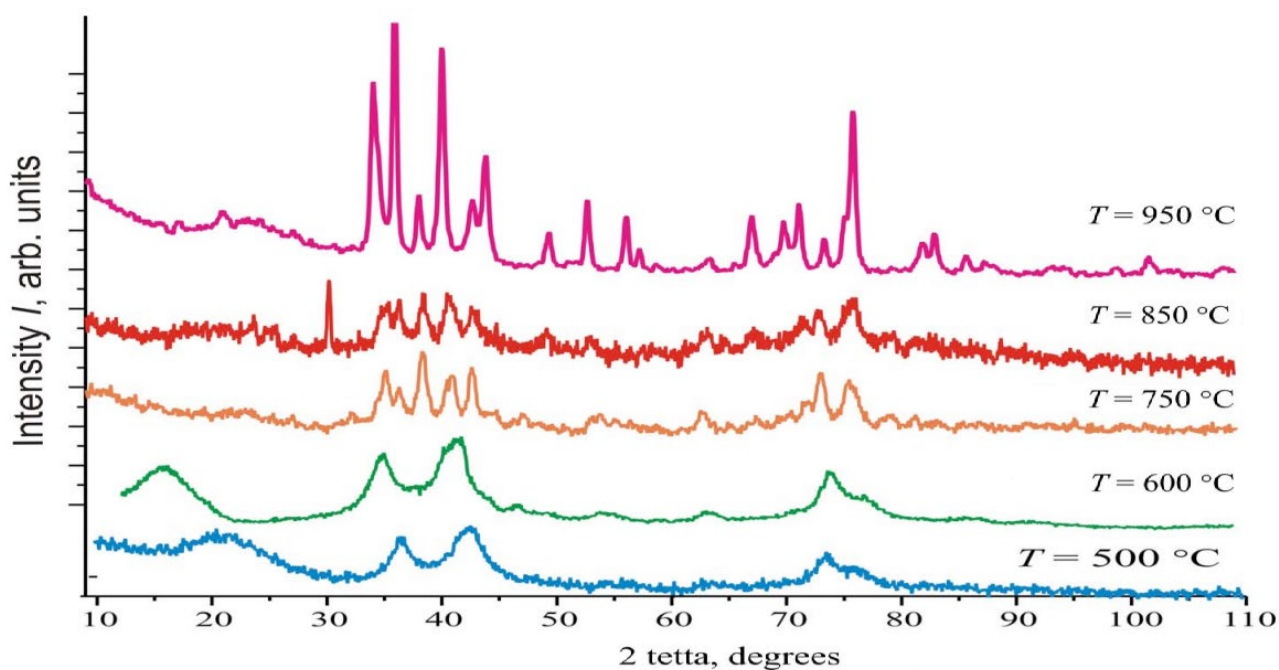
Fig. 3. X-ray diffraction patterns of gallium(III) oxide samples synthesized by calcination of dehydrated and ground Ga(NO$_3$)$_3$·nH$_2$O samples in an oxygen atmosphere at the temperature T_{calc} = 500–950 °C (CoKα-radiation)

Condensed Matter and Interphases / Конденсированные среды и межфазные границы   2022;24(3): 345–355

A. M. Samoylov et al.   Synthesis of chemically pure β-phase powders of gallium(III) oxide

with the presence of an insignificant fraction of the γ-phase of Ga_2O_3.

When the temperature was further increased to T_{calc} = 850 °C, the crystal structure of gallium(III) oxide powders also changed. The diffraction pattern did not show any peaks of the γ-phase, with the prevailing peaks of the cubic δ-phase of Ga_2O_3 being accompanied by a certain number of reflections characteristic of the monoclinic β-phase (Fig. 3 and Table 3). When the synthesis temperature was T_{calc} = 950 °C, the diffraction patterns of gallium(III) oxide samples showed only peaks of the monoclinic β-phase of Ga_2O_3 (Fig. 3 and 4). The absence of the reflections characteristic of other polymorphic modifications of gallium(III) oxide led us to the conclusion that in our study, at the temperature T_{calc} = 950 °C we synthesised chemically pure single-phase powders of the monoclinic β-phase of Ga_2O_3 (Fig. 4).

According to the obtained XRD data (Fig. 3 and Table 3), thermal decomposition of gallium(III) nitrate did not allow for obtaining of two of the polymorphic modifications of gallium(III) oxide, namely the hexagonal (rhombohedral) α-phase and the orthorhombic ε-phase (Table 2).

We should point out that the values of interplanar distances of the samples of the β-phase of Ga_2O_3 synthesised in our study are the closest to the recently obtained literature data [33, 34]. Based on the obtained X-ray diffraction patterns and the literature data [32 – 34] we calculated the parameters of the crystal lattice of the synthesised monoclinic b-phase of Ga_2O_3 (Table 4) using the UnitCell software and regression analysis [35]. The obtained parameters of the crystal lattice of the monoclinic β-phase of Ga_2O_3 and the unit cell volume were in maximum agreement with the results obtained in [34].

Table 4. Parameters of the crystal lattice of the β-phase of Ga_2O_3 synthesized at T_{calc} = 950 °C calculated by means of the method suggested by TJB Holland & SAT Redfern (1995) using the Unitcell software [35]

Crystal lattice parameter	Data source			
	[32]	[33]	[34]	The article
a, nm	0.58	1.2227(1)	1.2214(3)	1.22061
b, nm	0.304	0.30389(2)	0.30371(9)	0.30413
c, nm	1.223	0.58079(4)	0.57981(9)	0.57768
β, degrees	103.7	103.820(6)	103.83(2)	103.3706
Unit cell volume V_{uc}, nm³	0,2095	0.20955	0.20885	0.208636
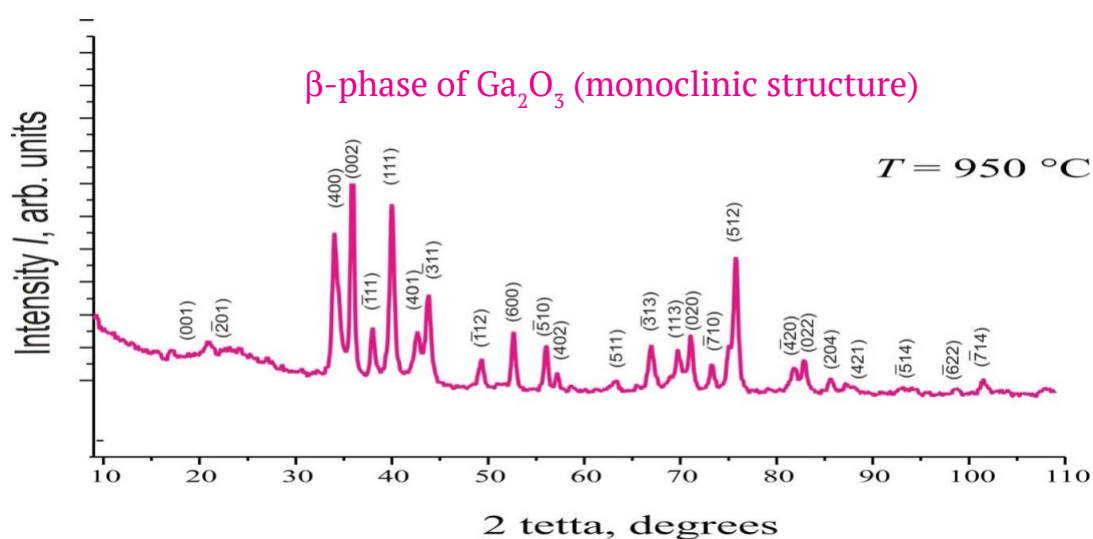
Fig. 4. X-ray diffraction patterns of the sample of the β-phase of gallium(III) oxide synthesized by calcination in oxygen at T_{calc} = 950 °C

Condensed Matter and Interphases / Конденсированные среды и межфазные границы   2022;24(3): 345–355

A. M. Samoylov et al.   Synthesis of chemically pure β-phase powders of gallium(III) oxide

4. Conclusions

In our study, we developed a synthesis method of gallium(III) oxide powders of high chemical purity with maximum product yield. The interaction between metallic gallium and concentrated nitric acid resulted in the formation of gallium(III) nitrate crystallohydrate with the general formula $Ga(NO_3)_3 \cdot 9H_2O$. The study determined that complete thermal decomposition of gallium(III) nitrate and formation of gallium(III) oxide occurs at the temperature $T_{calc} \geqslant 500$ °C. Based on the results of the EPMA we determined that within the range of calcination temperature $T_{calc} = 500–950$ °C, the ratio between gallium and oxygen atoms is stable within the systematic error, which corresponds to the stoichiometric composition of Ga_2O_3, and does not depend on the treatment temperature. The X-ray phase analysis proved that the crystal structure of the gallium(III) oxide powder whose synthesis temperature increased from $T_{calc} = 500$ °C to $T_{calc} = 950$ °C, changes with symmetry decreased from the cubic to the monoclinic structure. The determined parameters of the crystal lattice of the synthesised monoclinic phase are in full agreement with the reference data, which demonstrates great perfection of the structure of the synthesised samples of the β-phase of Ga_2O_3.

Author contributions

All authors made an equivalent contribution to the preparation of the publication.

Conflict of interests

The authors declare that they have no known competing financial interests or personal relationships that could have influenced the work reported in this paper.

References

1. Guo Y., Ma L., Mao K., Ju M., Bai Y., Zhao J., Zeng X. C. Eighteen functional monolayer metal oxides: wide bandgap semiconductors with superior oxidation resistance and ultrahigh carrier mobility. *Nanoscale Horiz.* 2019;4(3): 592–600. https://doi.org/10.1039/C8NH00273H

2. Pearton S. J., Jiancheng Yang, Cary Patrick H., Ren F., Jihyun Kim, Tadjer Marko J., Mastro Michael A. A review of Ga_2O_3 materials, processing, and devices. *Applied Physics Reviews*. 2018(5): 011301(1)–011301(56). https://doi.org/10.1063/1.5006941

3. Stepanov S. I., Nikolaev V. I., Bougrov V. E., Romanov A. E. Gallium oxide: properties and applications – a review. *Reviews on Advanced Materials Science*. 2016(44): 63–86. Режим доступа: https://elibrary.ru/item.asp?id=26987785

4. Shin S. S., Lee S. J., Seok S. I. Exploring wide bandgap metal oxides for perovskite solar cells. *APL Materials*. 2019;7(2): 022401. https://doi.org/10.1063/1.5055607

5. Shi J., Zhang J., Yang L., Qu M., Qi D.-C., Zhang K. H. L. Wide bandgap oxide semiconductors: from materials physics to optoelectronic devices. *Advanced Materials*. 2021;33(50): 2006230. https://doi.org/10.1002/adma.202006230

6. Mirzaei A., Lee J.-H., Majhi S., Weber M., Bechelany M., Kim S. Resistive gas sensors based on metal-oxide nanowires. *Journal of Applied Physics*. 2019;126: 241102. https://doi.org/10.1063/1.5118805

7. Neri G. First fifty years of chemoresistive gas sensors. *Chemosensors*. 2015;3(1): 1–20. https://doi.org/10.3390/chemosensors3010001

8. Vajhadin F., Mazloum-Ardakani M., Amini A. Metal oxide-based gas sensors for the detection of exhaled breath markers. *Medical Devices & Sensors*. 2021;4(1): e10161. https://doi.org/10.1002/mds3.10161

9. Shalini Devi K., Anantharamakrishnan A., Krishnan U., Yakhmi J. Chemical sensors based on metal oxides. In: *Smart Sensors for Environmental and Medical Applications*. Hamida Hallil, Hadi Heidari (eds.). The Institute of Electrical and Electronics Engineers, Inc.; 2020. pp 103–127. https://doi.org/10.1002/9781119587422.ch6

10. Pearton S., Yang J., Cary P. H., Ren F., Kim J., Tadjer M., Mastro M. A Review of Ga_2O_3 materials, processing, and devices. *Applied Physics Reviews*. 2018;5: 011301. https://doi.org/10.1063/1.5006941

11. Singh R., Lenka T. R., Panda D. K., Velpula R. T., Jain B., Bui H. Q. T., Nguyen H. P. T. The dawn of Ga_2O_3 HEMTs for high power electronics – a review. *Materials Science in Semiconductor Processing*. 2020;119: 105216. https://doi.org/10.1016/j.mssp.2020.105216

12. Alhalaili B., Al-Duweesh A., Popescu I. N., Vidu R., Vladareanu L., Islam M. S. Improvement of Schottky contacts of gallium oxide (Ga_2O_3) nanowires for UV applications. *Sensors*. 2022;22 (5): 2048. https://doi.org/10.3390/s22052048

13. Playford H. Y., Hannon A. C., Barney E. R., Walton R. I. Structures of uncharacterised polymorphs of gallium oxide from total neutron diffraction. *Chemistry – A European Journal*. 2013;19(8), 2803–2813. https://doi.org/10.1002/chem.201203359

14. Yoshioka S., Hayashi H., Kuwabara A., Oba F., Matsunaga K., Tanaka I. Structures and energetics of Ga_2O_3 polymorphs. *Journal of Physics: Condensed*

Condensed Matter and Interphases / Конденсированные среды и межфазные границы   2022;24(3): 345–355

A. M. Samoylov et al.   Synthesis of chemically pure β-phase powders of gallium(III) oxide

$Matter$. 2007;19(34): 346211. https://doi.org/10.1088/0953-8984/19/34/346211

15. McCandless J. P., Chang C. S., Nomoto K. ... Jena D. Thermal stability of epitaxial α-Ga_2O_3 and $(Al,Ga)_2O_3$ layers on m-plane sapphire: $Applied\ Physics\ Letters$. 2021;119(6): 062102. https://doi.org/10.1063/5.0064278

16. Xue H., He Q., Jian G., Long S., Pang T., Liu M. An overview of the ultrawide bandgap Ga_2O_3 semiconductor-based Schottky barrier diode for power electronics application. $Nanoscale\ Research\ Letters$. 2018;13(1): 290. https://doi.org/10.1186/s11671-018-2712-1

17. Ryabtsev S. V., Ievlev V. M., Samoylov A. M., Kuschev S. B., Soldatenko S. A. Microstructure and electrical properties of palladium oxide thin films for oxidizing gases detection. $Thin\ Solid\ Films$. 2017;636: 751–759. https://doi.org/10.1016/j.tsf.2017.04.009

18. Ryabtsev S. V., Shaposhnik A. V., Samoilov A. M., Sinelnikov A. A., Soldatenko S. A., Kushchev S. B., Ievlev V. M. Thin films of palladium oxide for gas sensors. $Doklady\ Physical\ Chemistry$. 2016;470(5): 550–553. (In Russ.). https://doi.org/10.7868/S0869565216290168

19. Samoylov A., Ryabtsev S., Shaposhnik A., Kuschev S., Soldatenko S., Ievlev V. Palladium oxide thin film for oxidizing gases detecting. $The\ 16\text{-}th\ International\ Meeting\ on\ Chemical\ Sensors\ IMCS\ 2016.\ Jeju,\ Jeju\ Island,\ Korea,\ July\ 10–13,\ 2016:\ Final\ Program\ \&\ Absrtacts\ Book$. 2016. 96 p.

20. Ryabtsev S. V., Iyevlev V. M., Samoylov A. M., Kuschev S. B., Soldatenko S. A. Real microstructure and electrical properties of palladium oxide thin films for oxidizing gases detecting. $Science\ and\ Application\ of\ Thin\ Films,\ Conference\ \&\ Exhibition\ (SATF\text{-}2016)\ Çeşme,\ Izmir,\ Turkey,\ September\ 19–23,\ 2016.\ Book\ of\ Abstracts:\ Izmir\ Institute\ of\ Technology$. 2016. 44 p.

21. Ievlev V. M., Ryabtsev S. V., Shaposhnik A. V., Samoylov A. M., Kuschev S. B., Sinelnikov A. A. Ultrathin films of palladium oxide for oxidizing gases detecting. $Procedia\ Engineering$. 2016;168: 1106-1109. https://doi.org/10.1016/j.proeng.2016.11.357

22. Ievlev V. M., Ryabtsev S. V., Samoylov A. M., Shaposhnik A. V., Kuschev S. B., Sinelnikov A. A. Thin and ultrathin films of palladium oxide for oxidizing gases detection. $Sensors\ and\ Actuators\ B:\ Chemical$. 2018;255(2): 1335–1342. https://doi.org/10.1016/j.snb.2017.08.121

23. Samoylov A. M., Ryabtsev S. V., Popov V. N., Badica P. Palladium (II) oxide nanostructures as promising materials for gas sensors. In book: $Novel$ $nanomaterials\ synthesis\ and\ applications$. George Kyzas (ed.). UK, London: IntechOpen Publishing House, 2018. pp. 211–229. http://dx.doi.org/10.5772/intechopen.72323

24. Marikutsa A. V., Rumyantseva M. N., Gaskov A. M., Samoylov A. M. Nanocrystalline tin dioxide: basics in relation with gas sensing phenomena. Part I. Physical and chemical properties and sensor signal formation. $Inorganic\ Materials$. 2015;51(13): 1329–1347. https://doi.org/10.1134/s002016851513004x

25. Marikutsa A. V., Rumyantseva M. N., Gaskov A. M., Samoylov A. M Nanocrystalline tin dioxide: basics in relation with gas sensing phenomena. Part II. Active centers and sensor behavior. $Inorganic\ Materials$. 2016;52(13): 1311–1338. https://doi.org/10.1134/S0020168516130045

26. Greenwood N. N., Earnshaw A. $Chemistry\ of\ elements$. 1997. https://doi.org/10.1016/b978-0-7506-3365-9.50005-5 (In Russ.)

27. Nekrasov B. V. $Fundamentals\ of\ general\ chemistry$: in 2 volumes. St. Petersburg: Jan'; 2003. 656 p. (In Russ.)

28. Ugay Ya. A. $Inorganic\ chemistry:\ a\ textbook\ for\ chemical\ specialties\ of\ universities$. Moscow: Vysshaya shkola Publ.; 1989. 483 p. (In Russ.)

29. Lurie Yu. Yu. $Handbook\ of\ analytical\ chemistry$. Moscow: 1979. pp. 92-101. (In Russ.)

30. Karyakin Yu. V., Angelov I. I. $Pure\ chemicals$. Moscow: Khimiya Publ.; 1974. 408 p. (In Russ.)

31. Yoshioka S., Hayashi H., Kuwabara A., Oba F., Matsunaga K., Tanaka I. Structures and energetics of Ga_2O_3 polymorphs. $Journal\ of\ Physics:\ Condensed\ Matter$. 2007;19(34): 346211. https://doi.org/10.1088/0953-8984/19/34/346211

32. Geller S. Crystal structure of β-Ga_2O_3. $The\ Journal\ of\ Chemical\ Physics$. 1960;33(3): 676–684. https://doi.org/10.1063/1.1731237

33. Welton-Holzer J., McCarthy G. North Dakota State University, Fargo, North Dakota, USA. ICDD Grant-in-Aid (1989).

34. Åhman J., Svensson G., Albertsson J. A reinvestigation of β-gallium oxide. $Acta\ Crystallographica\ Section\ C\ Crystal\ Structure\ Communications$. 1996;52 (6): 1336–1338. https://doi.org/10.1107/S0108270195016404

35. Holland T. J. B., Redfern S. A. T. Unit cell refinement from powder diffraction data: the use of regression diagnostics. $Mineralogical\ Magazine$. 1997;61(404): 65–77. https://doi.org/10.1180/minmag.1997.061.404.07

Information about the authors

Alexander M. Samoylov, Dr. Sci. (Chem.), Professor of the Department of Materials Science and Industry of Nanosystems*,* Voronezh State University (Voronezh, Russian Federation).

https://orcid.org/0000-0003-4224-2203
samoylov@chem.vsu.ru.

Stanislav S. Kopytin, postgraduate student, Department of Materials Science and Industry of Nanosystems, Voronezh State University (Voronezh, Russian Federation).

https://orcid.org/0000-0001-9353-0219
kopytin-stanislav@rambler.ru

Kirill V. Oreshkin, student, Department of Materials Science and Industry of Nanosystems, Voronezh State University (Voronezh, Russian Federation).

Elizaveta A. Shevchenko, student, Department of Materials Science and Industry of Nanosystems, Voronezh State University (Voronezh, Russian Federation).

liza15-99@mail.ru

Original articles

Engineering of biomimetic composite dental materials based on nanocrystalline hydroxyapatite and light-curing adhesive

P. V. Seredin[1]✉, D. L. Goloshchapov[1], Asaad A. H. AlZubaidi[2], V. M. Kashkarov[1], N. S. Buylov[1], Yu. A. Ippolitov[3], J. Vongsvivut[4]

[1]*Voronezh State University,*
1 Universitetskaya pl., Voronezh 394018, Russian Federation

[2]*Medical Instruments Techniques Engineering Department, Technical College of Engineering, Al-Bayan University, Baghdad, Iraq*

[3]*Department of Pediatric Dentistry with Orthodontia, Voronezh State Medical University,*
11 Studentcheskaya str., Voronezh 394006, Russian Federation

[4]*ANSTO-Australian Synchrotron,*
800 Blackburn Road, Clayton, Victoria 3168, Australia

Abstract

With the use of light-curing Bis-GMA (Bis-phenol-A glycidylmethacrylate) adhesive and nanocrystalline carbonate-substituted calcium hydroxyapatite (nano-cHAp), corresponding by an aggregate set of characteristics to the apatite of human enamel and dentin obtained from the biogenic source of calcium – egg's shell of birds biomimetic Bis-GMA/nano-cHAp adhesives were synthesized.

Introduction and distribution of nano-cHAp filler in the adhesive matrix as well as its interaction with molecular groups of the latter one resulted in the change of chemical bonds that was evidenced by the data of Fourier transform infrared (FTIR) spectroscopy. In summary, for the specified nanofiller concentration increased values of Vicker hardnesses (VH) and degree of conversion were attained simultaneously while light curing of Bis-GMA/nano-cHAp adhesive.

This result would provide a considerable influence on the following application of the developed biomimetic adhesives and clinical successes of teeth restoration with the use of these composites.

Keywords: Biomimetic strategies; Nanodentology; Calcium hydroxyapatite; Adhesives

✉ Pavel V. Seredin, e-mail: paul@phys.vsu.ru

Condensed Matter and Interphases / Конденсированные среды и межфазные границы   2022;24(3): 356–361

P. V. Seredin et al.   Engineering of biomimetic composite dental materials based on nanocrystalline...

1. Introduction

Numerous innovations with the application of biomimetic strategies and nanotechnologies (nanodentology) provided a considerable impetus in the area of engineering of the new class related with a new class of modern adhesion restoration materials [1]. It was repeatedly shown that the enhancement of trophic, mechanical (hardness and strength), physicochemical and performance properties of adhesive polymer matrix can be attained due to the introduction of various inorganic micro- and nanofillers into its composition [2, 3]. One of the applied fillers for dental materials and bonds is calcium hydroxyapatite (HAp). High efficiency in the use of this compound is due to the similarity of its physicochemical characteristics with the inorganic component of the bone and dental tissue of a human. However, the problem of the admissible content of nanocrystalline filler in the polymer matrix of an adhesive still remains a challenge.

Therefore, the main task of our work was the determination of the proper adaptive composition and molecular properties of biomimetic adhesive based on Bis-GMA (bis-phenol -A glycidylmethacrylate), filled with nanocrystalline carbonate-substituted hydroxyapatite (nano-cHAp), providing a high degree of polymerization and mechanical hardness.

2. Methods of production and studying of the samples

To obtain the samples of biomimetic samples in our work we used bisphenol-A-glycidyl methacrylate (Bis-GMA, Polysciences, Warrington, PA, USA, code 03344)-based commercial adhesive [11,25]. Nanocrystalline carbonate-substituted calcium hydroxyapatite (nano-cHaP) corresponding to the aggregate number of features in the human enamel and dentin [4–6] was applied as a filler for light-curing Bis-GMA aadhesive. Samples of nano-cHAp were obtained using the wet chemistry method. The raw calcium hydroxide was obtained by thermal annealing from the hen's eggshells [4].

Mixing of nano-cHAp component and adhesive was performed with the use of ultrasound homogenizer QSonica Q55 (Qsonica LLC, CT, USA) for 30 s.

To solve the problems stated in the work and connected with the determination of the adaptive composition and molecular properties of biomimetic nano-filled adhesives the following samples were obtained with different content of the raw components (see Table 1).

Table 1. Composition of the synthesized biomimetic adhesives samples

Samples	Bis-GMA, ml	nano-cHAp, g
A	250	0.2
B	250	0.16
C	250	0.12
D	250	0.08
E	250	0.04
F	250	0.01

The obtained samples were investigated with the use of Fourier transform infrared (FTIR) spectroscopy technique, including the application of Synchrotron FTIR microspectroscopy at the Infrared Microspectroscopy beamline (Australian Synchrotron, Victoria, Australia). Microhardness of the synthesized biomimetic adhesive samples after their photopolymerization was determined using Vicker's technique and employing optical microscope-hardness testing instrument.

3. Results and their discussion

Measuring of microhardness in the samples of biomimetic Bis-GMA/nano-cHAp adhesives was performed by Vicker's technique.

Microhardness number (HV) in this case is determined from the following expression:

$$H_\mu = \frac{2P\sin(\theta/2)}{d^2}, \tag{1}$$

where P – is the applied loading, d — is the size of indentation diagonal; $\theta = 136°$ — angle at the top of the diamond square Vickers tip.

From the analysis of data in Table 1 one can see that microhardness of biomimetic Bis-GMA/nano-cHAp adhesive begins at the addition of nanocrystalline hydroxyapatite and it attains maximum at the content of ~0.16 g nano-cHAp in 250 ml of Bis-GMA adhesive. After that a decay of microhardness value is observed. Non-linear behavior of the dependence of microhardness values on nano-cHAp content is due to the changes that occur in molecular composition of the samples [7–10].

Condensed Matter and Interphases / Конденсированные среды и межфазные границы   2022;24(3): 356–361

P. V. Seredin et al.   Engineering of biomimetic composite dental materials based on nanocrystalline...

It is well known that a degree of conversion for the adhesive material can be determined with the use of FTIR data [11]. To do this it is required to determine the ratio of integral intensities for the bands related to aliphatic (C = C) bonds/ aromatic (C = C) bonds before the process of polymerization and after its completion. The part of aliphatic C = C bonds can be determined from intensity of vibrations near 1637 cm^{-1}, while the part of aromatic (C = C) bonds can be determined from intensity of vibrations near 1610 cm^{-1}. Calculations were performed for 10 samples of standard Bis-GMA adhesive and each of the 10 biomimetic adhesive specimens in the samplings. After that mean values for the degree of conversion for each group of the specimens were determined and standard deviation was calculated which did not exceed 2%.

Results of the calculation show that in case of the use of original adhesive based on BisGMA the share of non-polymerized bonds is of about 22.0±1.4%, thus coinciding with the calculations presented for the adhesive on the basis of Bis-GMA/HEMA from [11]. At the same while adding nano-c-HAp the value of the degree of conversion (polymerization) starts increasing, attains its maximum at ~93%, while after that a decrease of polymerization degree (degree of conversion) is observed.

Spline-curves of microhardness and degree of polymerization for the samples in a dependence on nano-c-HAp in the composition of biomimetic adhesive are presented together in figure 1. It can be easily seen that both values representing as mechanical as molecular properties of the synthesized biomimetic adhesives are of the similar character in a dependence on the filler content. Simultaneous graphical analysis makes it possible to determine the range of the optimal compositions for bioadhesive providing maximal value of as microhardness as the value of the degree of conversion during polymerization. From the calculations it follows (see Fig. 1) that the content of nanocrystalline hydroxyapatite with characteristic morphological characteristics (20×20×50 nm) should be within the vicinity of the value ~0.125–0.135 g per 250 ml of Bis-GMA (Fig. 1).

Before our work has been performed it was shown that involvement of nanoparticles resulted in improvement of a number of mechanical properties for dental composites. Addition of the fillers (silicon nanoparticles) to the adhesion systems has an impact on the improvement
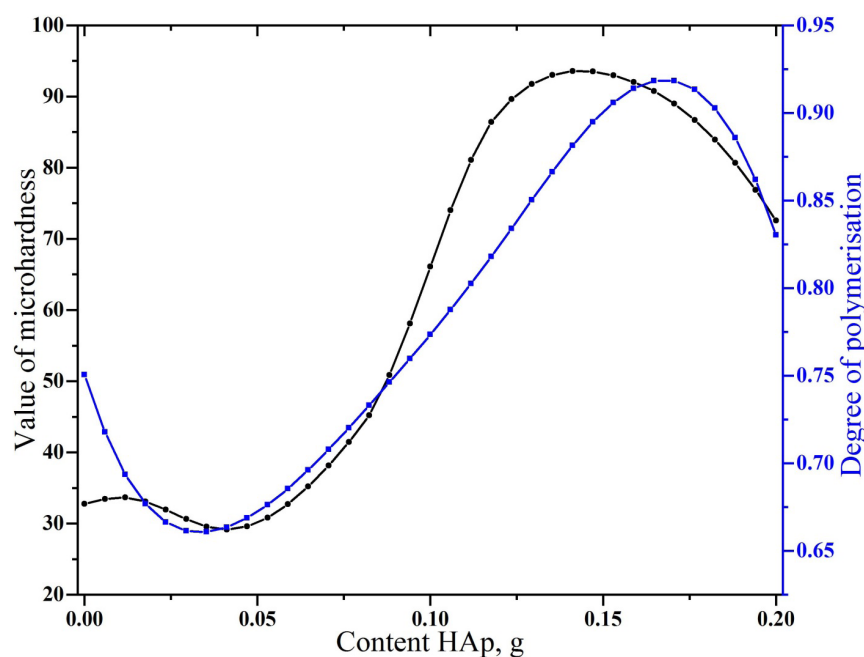
Fig. 1. Comparison of the microhardness value $H\mu$ (HV) and Degree of conversion for biomimetic adhesives in a dependence of nanofiller admixture

Condensed Matter and Interphases / Конденсированные среды и межфазные границы   2022;24(3): 356–361

P. V. Seredin et al.   Engineering of biomimetic composite dental materials based on nanocrystalline...

of mechanical properties and elastic modulus, improved the distribution of stresses caused by polymerization [12]. Results of modification for the adhesive systems on the basis of Bis-GMA, TEGDMA and HEMA with the use of HAp nanocrystallites from the work by Vicente Castelo Branco Leitune el al [9] correlate well with the dependence of mechanical properties of adhesive under increase of nanofiller addition observed in our research work. It was demonstrated that using HAp nanoparticles with the mean size of ~ 27 nm the enhanced values of microhardness can be attained somehow in the range of ~ 32,35 MPa. After that with an increase of HAp nanoparticles content in adhesive characteristic decay of mechanical properties was obtained. However, in our work we managed to get even greater values of microhardness (HV) with the account of increasing value of the conversion degree that considerably exceeds the value of 63.84%. The latter one was attained in the work by Vicente Castelo Branco Leitune el al for the addition of 1% HAp by mass [9].

As it follows from the obtained results (see Fig. 1) while modifying Bis-GMA with the use of nano-cHAp it is possible to attain the value of Vicker hardness exceeding dentin hardness but less than for dental enamel [13,14]. This would probably redistribute natural loads between the anatomic tissues in the efficient manner.

It was repeatedly noted that an important factor of the process is the size of nanofiller particles. The particles of large size can lead to agglomeration of the particles and degradation of mechanical properties of the interface [15]where nanoparticles (minimum size ~3 nm. However, the type of nanofiller has also a great impact on the final properties of the modified material. Unlike of the number of the previous similar investigations where HAp nanoparticles and other inorganic nanomaterials were applied for the filling of adhesion system, in our work used nanocrystals of carbonate-substituted hydroxyapatite with the mean sizes of 20×20×50 nm obtained according to our elaborated technology [4]. These nanocrystals are characteristic for the native dental tissue. Uniform distribution of nano-cHAp filler in the adhesive matrix as well the interaction with the filler molecular groups favors the changes in molecular bonds that is confirmed by FTIR data; as a result, this considerably improved mechanical characteristics of the material.

4. Conclusions

With the use of light-curing Bis-GMA (Bis-phenol-A glycidylmethacrylate) adhesive and nanocrystalline carbonate-substituted calcium hydroxyapatite (nano-cHAp), corresponding by an aggregate set of characteristics to the apatite of human enamel and dentin obtained from the biogenic source of calcium – egg's shell of birds biomimetic Bis-GMA/nano-cHAp adhesives were synthesized.

Introduction and distribution of nano-cHAp filler in the adhesive matrix as well as its interaction with molecular groups of the latter one resulted in the change of chemical bonds that was evidenced by the data of Fourier transform infrared (FTIR) spectroscopy. In summary, for the specified nanofiller concentration increased values of Vicker hardnesses (VH) and degree of conversion were attained simultaneously while light curing of Bis-GMA/nano-cHAp adhesive.

This result would provide a considerable influence on the following application of the developed biomimetic adhesives and clinical successes of teeth restoration with the use of these composites.

Author Contributions

Seredin P. V. – conceived and designed the experiments, analysed the data, performed the experiments, contributed reagents/materials/analysis tools and wrote the manuscript. Goloshchapov D. L. – contributed reagents/materials/analysis tools, performed the experiments, analysed the data, prepared the figures and/or tables and wrote the manuscript. Ippolitov Yu. A. – contributed reagents/materials/analysis tools and wrote the manuscript. AlZubaidi Asaad. A. H., Kashkarov V. M., Buylov N. S., Ippolitov Yu. A., Vongsvivut J. – performed the experiments. All authors have read and agreed to the published version of the manuscript.

Conflicts of interest

The authors declare no conflict of interest

References

1. Zafar M. S., Amin F., Fareed M. A., Ghabbani H., Riaz S., Khurshid Z., Kumar N. Biomimetic aspects of

Condensed Matter and Interphases / Конденсированные среды и межфазные границы   2022;24(3): 356–361

P. V. Seredin et al.   Engineering of biomimetic composite dental materials based on nanocrystalline...

restorative dentistry biomaterials. *Biomimetics*. 2020;5(3): 34. https://doi.org/10.3390/biomimetics5030034

2. Alhenaki A. M., Attar E. A., Alshahrani A., Farooq I., Vohra F., Abduljabbar T. Dentin bond integrity of filled and unfilled resin adhesive enhanced with silica nanoparticles – an SEM, EDX, Micro-Raman, FTIR and micro-tensile bond strength study. *Polymers*. 2021;13(7): 1093. https://doi.org/10.3390/polym13071093

3. Timpe N., Fullriede H., Borchers L., Stiesch M., Behrens P., Menzel H. Nanoporous silica nanoparticles with spherical and anisotropic shape as fillers in dental composite materials. *BioNanoMaterials*. 2014;15(3–4): https://doi.org/10.1515/bnm-2014-0010

4. Seredin P. V., Goloshchapov D. L., Prutskij T., Ippolitov Yu. A. Fabrication and characterisation of composites materials similar optically and in composition to native dental tissues. *Results in Physics*. 2017;7: 1086–1094. https://doi.org/10.1016/j.rinp.2017.02.025

5. Goloshchapov D. L., Gushchin M. S., Kashkarov V. M., Seredin P. V., Ippolitov Y. A., Khmelevsky N. O., Aksenenko A. Yu. XPS and XANES studies of biomimetic composites based on B-type nano-hydroxyapatite. *Results in Physics*. 2018;9: 1386–1387. https://doi.org/10.1016/j.rinp.2018.04.065

6. Goloshchapov D., Buylov N., Emelyanova A., Ippolitov I., Ippolitov Y., Kashkarov V., Khudyakov Y., Nikitkov K., Seredin P. Raman and XANES spectroscopic study of the influence of coordination atomic and molecular environments in biomimetic composite materials integrated with dental tissue. *Nanomaterials*. 2021;11(11): 3099. https://doi.org/10.3390/nano11113099

7. Provenzi C., Leitune V. C., Collares F. M., Trommer R., Bergmann C. P., Samuel S. M. Interface evaluation of experimental dental adhesives with nanostructured hydroxyapatite incorporation. *Applied Adhesion Science*. 2014;2(1): 2. https://doi.org/10.1186/2196-4351-2-2

8. Lezaja M., Jokic B. M., Veljovic D. N., Miletic V. Shear bond strength to dentine of dental adhesives containing hydroxyapatite nano-fillers. *Journal of Adhesion Science and Technology*. 2016;30(24): 2678–2689. https://doi.org/10.1080/01694243.2016.1197086

9. Leitune V. C. B., Collares F. M., Trommer R. M., Andrioli D. G., Bergmann C. P., Samuel S. M. W. The addition of nanostructured hydroxyapatite to an experimental adhesive resin. *Journal of Dentistry*. 2013;41(4): 321–327. https://doi.org/10.1016/j.jdent.2013.01.001

10. Al-Hamdan R. S., Almutairi B., Kattan H. F., Alresayes S., Abduljabbar T., Vohra F. Assessment of hydroxyapatite nanospheres incorporated dentin Aadhesive. A SEM/EDX, micro-Raman, microtensile and micro-indentation study. *Coatings*. 2020;10(12): 1181. https://doi.org/10.3390/coatings10121181

11. Daood U., Swee Heng C., Neo Chiew Lian J., Fawzy A. S. In vitro analysis of riboflavin-modified, experimental, two-step etch-and-rinse dentin adhesive: Fourier transform infrared spectroscopy and micro-Raman studies. *International Journal of Oral Science*. 2015;7(2): 110–124. https://doi.org/10.1038/ijos.2014.49

12. Kasraei S., Khamverdi Z. Effect of nanofiller addition to an experimental dentin adhesive on microtensile bond strength to human dentin. *Journal of Dentistry of Tehran University of Medical Sciences*. 2009;6(2): 1–5.

13. del Pilar Gutiérrez-Salazar M., Reyes-Gasga J. Microhardness and chemical composition of human tooth. *Materials Research*. 2003;6(3): 367–373. https://doi.org/10.1590/S1516-14392003000300011

14. Aydın B., Pamir T., Baltaci A., Orman M. N., Turk T. Effect of storage solutions on microhardness of crown enamel and dentin. *European Journal of Dentistry*. 2015;09(02): 262–266. https://doi.org/10.4103/1305-7456.156848

15. Souza G. M. D. Nanoparticles in restorative materials. In: *Nanotechnology in Endodontics*. Kishen A. (ed.). Springer International Publishing; 2015. pp. 139–171. http://link.springer.com/cГАПter/10.1007/978-3-319-13575-5_8

Information about the authors

Pavel V. Seredin, Dr. Sci. (Phys.–Math.), Full Professor, Chair of Department, Department of Solid State Physics and Nanostructures, Voronezh State University (Voronezh, Russian Federation).

https://orcid.org/0000-0002-6724-0063
paul@phys.vsu.ru

Dmitry L. Goloshchapov, Cand. Sci. (Phys.–Math.), Assistant Professor, Department of Solid State Physics and Nanostructures, Voronezh State University (Voronezh, Russian Federation).

https://orcid.org/0000-0002-1400-2870
goloshchapov@phys.vsu.ru

Asaad. A. H. AlZubaidi, PhD, Lecturer, Medical Instruments techniques Engineering Department, Technical College of Engineering, Al-Bayan University (Baghdad, Iraq).

https://orcid.org/0000-0003-4852-0825
Asaad.a@albayan.edu.iq

Vladimir M. Kashkarov, Cand. Sci. (Phys.–Math.), Senior Researcher, Department of Solid State Physic and Nanostructures, Voronezh State University (Voronezh, Russian Federation).

https://orcid.org/0000-0001-9460-9244
vmkashkarov@gmail.com

Condensed Matter and Interphases / Конденсированные среды и межфазные границы   2022;24(3): 356–361

P. V. Seredin et al.   Engineering of biomimetic composite dental materials based on nanocrystalline...

Nikita S. Buylov, Cand. Sci. (Phys.–Math.), Educator, Department of Solid State Physics and Nanostructures, Voronezh State University (Voronezh, Russian Federation).

https://orcid.org/0000-0003-1793-4400
buylov@phys.vsu.ru

Yury A. Ippolitov, Dr. Sci. (Med.), Full Professor, Head of Dentistry Institute of Postgraduate Medical Education Department, Voronezh State Medical University (Voronezh, Russian Federation).

https://orcid.org/0000-0001-9922-137X
dsvgma@mail.ru

Jitraporn (Pimm) Vongsvivut, Beamline Scientist, IR Microspectroscopy, Australian Synchrotron, Synchrotron Light Source Australia Pty LTD (Melburn, Australia).

https://orcid.org/0000-0003-0699-3464
jitrapov@ansto.gov.au

Translated by Pavel Seredin

Condensed Matter and Interphases

Original articles

Effect of pore size on phase transitions in rubidium tetrachlorozincate nanoparticles in porous glass matrices

L. S. Stekleneva[1,3]✉, A. A. Bryanskaya[1], M. A. Pankova[2], S. V. Popov[3], L. N. Korotkov[1]

[1]*Voronezh State Technical University,*
84 20-Letiya Oktyabrya str., Voronezh 394006, Russian Federation

[2]*Voronezh Institute of the Ministry of Internal Affairs of the Russian Federation,*
53 Prospekt Patriotov, Voronezh 394065, Russian Federation

Air Force Military Educational and Scientific Centre "Zhukovsky and Gagarin Air Force Academy"
54a Starykh Bol'shevikov ul., Voronezh 394064, Russian Federation

Abstract

It is well known that below a certain temperature (T_i), local displacements of individual atoms from their original positions occur in ferroelectric crystals with incommensurate phases. They form a spatial wave with a length of λ, which is incommensurate with the lattice period *a*, i.e. the λ/a ratio is irrational. The wavelength increases as the temperature decreases. Near the phase transition temperature T_C it reaches a length comparable to the size of the ferroelectric domains, as in the model rubidium tetrachlorozincate crystal (Rb_2ZnCl_4).

In ultrafine Rb_2ZnCl_4 crystals, the increase in λ is hindered by the size of the crystallite. Therefore, the physical properties of nanocrystalline rubidium tetrachlorozincate are expected to be considerably different from those of the bulk sample.

One of the methods for producing nanosized ferroelectric materials is a method based on embedding the material from a solution into porous matrices with nanometre-sized through-pores. We applied this method to study the effect of the size of ultrafine rubidium tetrachlorozincate crystallites on its dielectric properties and the phases occurring in the nanocrystallites.

For the experiment, we used samples of polycrystalline Rb_2ZnCl_4 and composites obtained by incorporation of Rb_2ZnCl_4 salt from aqueous solution into porous silicon oxide matrices with an average through-pore diameter of 46 and 5 nm (RS-46 and RS-5, respectively). The temperature dependencies of their dielectric permittivity were studied within the range of 100 to 350 K. We determined the temperatures of transition to the incommensurate (T_i) and ferroelectric (T_C) phases, as well as the mobility deceleration temperatures of ferroelectric domain boundaries in rubidium tetrachlorozincate nanocrystallites in the RS-46 composite. In Rb_2ZnCl_4 particles in the RS-5 composite, only the transition to the incommensurate phase occurs. In contrast to the bulk material, it shows features of the first-order phase transition.

Keywords: Incommensurate phase, Composite, Porous glass, Ferroelectric phase transition, Dielectric permittivity

For citation: Stekleneva L. S., Bryanskaya A. A., Pankova M. A., Popov S. V., Korotkov L. N. Effect of pore size on phase transitions in rubidium tetrachlorozincate nanoparticles in porous glass matrices. *Condensed Matter and Interphases.* 2022;24(3): 000-000. https://doi.org/10.17308/kcmf.2022.24/9859

Для цитирования: Стекленева Л. С., Брянская А. А., Панкова М. А., Попов С. В., Коротков Л. Н. Влияние размеров пор на фазовые переходы в наночастицах тетрахлорцината рубидия в пористых стеклянных матрицах. *Конденсированные среды и межфазные границы.* 2022;24(3): 000-000. https://doi.org/10.17308/kcmf.2022.24/9859

✉ Lyubov S. Stekleneva, e-mail: lubov_stekleneva@mail.ru

Condensed Matter and Interphases / Конденсированные среды и межфазные границы   2022;24(3): 362–368

L. S. Stekleneva et al.   Effect of pore size on phase transitions in rubidium tetrachlorozincate nanoparticles...

1. Introduction

Crystals with incommensurate phases are crystal structures where, at a certain temperature, local displacements of individual atoms from their initial positions occur. They form a spatial wave with a length of λ, that is incommensurate with the lattice period a, i.e. the ratio of λ/a is irrational. More generally, any material can be considered incommensurate, if there are two or more features of the translational symmetry which are mutually incompatible [1, 2].

Crystals with incommensurate phases attract interest, because the incommensurate modulation breaks the translational symmetry, so that the crystal is not in the true crystalline state. The spatial modulation waveform, originally described as sinusoidal, evolves with temperature. Its period increases as it gets farther from the incommensurate phase transition temperature (T_i), and the wave transforms into a soliton structure.

Rubidium tetrachlorozincate (Rb_2ZnCl_4) is a model ferroelectric material with an incommensurate phase [1–3].

The transition from the regular paraelectric to the incommensurate phase in the material is achieved at a temperature $T_i \approx 303$ K, called the Lifshitz temperature. The transition from the incommensurate to the commensurate ferroelectric phase occurs at $T_C \approx 192$ K [1, 3].

Below T_i, the wavelength λ in rubidium tetrachlorozincate increases with decreasing temperature, reaching the size comparable to the size of the ferroelectric domains near T_C [3].

However, the size of the crystallite in ultrafine crystals prevents an unlimited increase in the wavelength λ. Naturally, we can expect that this fact can significantly affect the phase states occurring in the material and considerably change its physical properties.

It should be noted that the properties of regular nanosized ferroelectrics have been intensively studied over a long time [4–10], whereas the physical processes in nanosized ferroelectrics with incommensurate phases have hardly been investigated so far.

Among various methods for obtaining nanocrystalline materials, the method of incorporation of the substance into porous matrices with nanometre-sized through-pores from the liquid state is probably the simplest [11].

We used this method to study the effect of the size of ultrafine rubidium tetrachlorozincate crystallites on its dielectric properties and the phases occurring in it.

2. Experimental

For the experiments, we used nanocrystalline Rb_2ZnCl_4 contained in the composites obtained by embedding rubidium tetrachlorozincate salt from aqueous solution into porous silicon dioxide plates with overall dimensions of 10×10×0.5 and 8.5×4.5×0.65 mm and average diameters of through-pores of ~ 46 and 5 nm, respectively. (The composites were abbreviated as RS-46 and RS-5).

The technology for the production of porous glass with a fine mesh of through-pores is described in detail in [12]. The porous glass used in our study initially had a relative volume of unfilled pores of 55% for RS-46 and 36% for RS-5.

Rubidium tetrachlorozincate salt was embedded into heat-treated porous glass plates from a saturated aqueous solution of Rb_2ZnCl_4 salt at temperatures of 90–98 °C, the process took about 3.5 hours. Following the procedure, the samples were dried in a thermostat with a gradual increase in temperature to 350 °C to remove residual moisture. The drying time was about 10 hours.

Using the weighing method, we found that the relative volume of embedded material in the porous matrix with an average pore diameter of about 46 nm was ≈ 19 %, and in the matrix with an average pore diameter of about 5 nm it was ≈ 15 %. In both cases, the proportion of Rb_2ZnCl_4 in relation to the total volume of the sample was about 8 %.

X-ray phase analysis of the synthesised composites was carried out using a Bruker D2 PHASER X-ray diffractometer (Cu-$K\alpha$-radiation). The diffraction pattern obtained for the RS-5 composite is shown in Fig. 1. It can be seen that the angular dependence of the X-ray scattering intensity can be represented as a blurred maximum characteristic of glass located near the angle $2\theta \approx 24°$ and distinct peaks of intensity corresponding to the crystal lattice of bulk rubidium tetrachlorozincate.

Condensed Matter and Interphases / Конденсированные среды и межфазные границы 2022;24(3): 362–368

L. S. Stekleneva et al. Effect of pore size on phase transitions in rubidium tetrachlorozincate nanoparticles...

The average particle size (d) of Rb_2ZnCl_4 in the composites was determined by X-ray diffraction analysis using the specialised TOPAS 4.2 software [13]. The estimates resulted in $d \approx 51$ for RS-46 and 18 nm for RS-5.

In addition to the composite materials, we also used a bulk (polycrystalline) rubidium tetrachlorozincate sample in the experiment for comparative analysis. It was obtained by compacting from the Rb_2ZnCl_4 salt.

The structural phase transitions were determined by analysing dielectric response measurements in the temperature range of 100–350 K.

Prior to the measurements, conductive paste was applied to the large surfaces of the samples to form the plane capacitor electrodes after drying. The samples were installed in a measuring cell fitted into a cryostat containing a platinum resistance thermometer, which allowed us to monitor the sample temperature with an error not exceeding ± 0.2 K. The dielectric permittivity (ε) was measured using an E7-20 LCR meter at a frequency of 10 kHz during sample cooling/heating at a rate of 1 to 2 K/min.

Each measurement cycle was preceded by heating the sample together with the measuring cell in a vacuum at about 380 K to remove moisture adsorbed from the air.

3. Results and discussion

The results of the experiment are shown in Fig.2 as temperature dependence ε diagrams. In the case of polycrystalline rubidium tetrachlorozincate (Fig. 2a), the curves $\varepsilon(T)$ show two maxima. The dielectric permittivity maximum near the temperature $T_i \approx 307$ K is due to the transition from the regular paraelectric phase to the incommensurate phase. Its position on the $\varepsilon(T)$ dependence diagrams when heating and cooling the sample remains almost unchanged, which is a characteristic feature of the second-order structural phase transition.

The second ε maximum occurs when the sample is cooled at $T_{Cc} \approx 187$ K, and when it is heated at $T_{Ch} \approx 196$ K. This ε maximum corresponds to the ferroelectric phase transition. Depending on the measurement mode (heating/cooling), its shift shows that the ferroelectric phase transition in the Rb_2ZnCl_4 bulk sample is
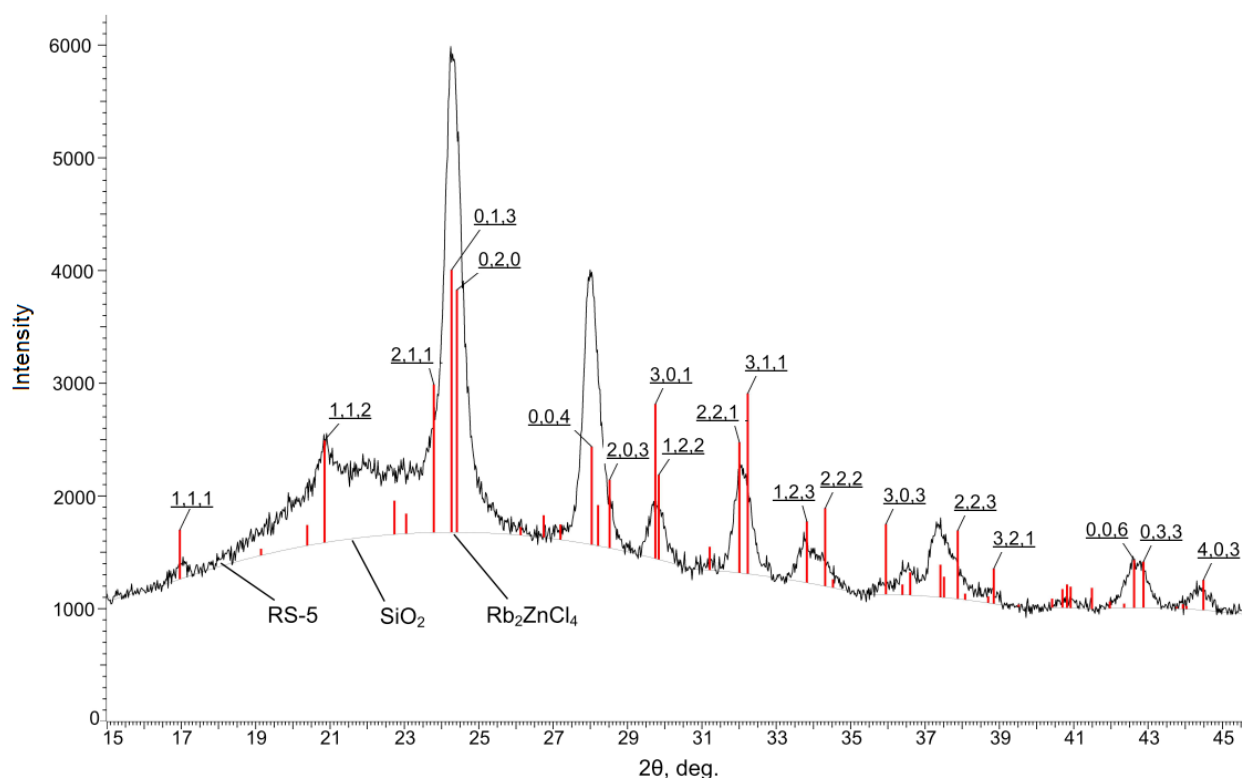

Fig. 1. The X-ray diffraction pattern of the RS-5 composite

Condensed Matter and Interphases / Конденсированные среды и межфазные границы   2022;24(3): 362–368

L. S. Stekleneva et al.   Effect of pore size on phase transitions in rubidium tetrachlorozincate nanoparticles...

a first-order phase transition, which is consistent with the known literature data [1, 2].

Some of the dielectric properties of the RS-46 composite were discussed in study [14]. The $\varepsilon(T)$ dependences show specific features around 160, 245, and 307 K (Fig. 2b). As in the polycrystalline sample, the maximum of ε, observed around 307 K, is due to the transition from the incommensurate to the paraelectric phase in the embedded Rb_2ZnCl_4 particles. Near this maximum, there is a blurred heat capacity peak C_p (Fig. 2, insert). It should be noted that the corresponding temperature (≈ 285 K) is slightly lower than T_i. Further research is required to clarify this issue.

The step-like anomaly of ε at about 240 K, registered when cooling the sample, corresponds to the maximum heat capacity observed near 232 K, as illustrated in the inset to Fig. 2. This C_p maximum has a specific shape characteristic of monocrystalline Rb_2ZnCl_4 in the temperature range corresponding to the ferroelectric phase transition [15].

In the temperature dependency of the dielectric permittivity measured when heating the sample, there were no dielectric response features indicative of a ferroelectric phase transition.

Moreover, we observed a blurred maximum of ε at $T^* \approx 160$ K (shifted towards 158 K on the cooling curve). It is almost symmetrical, the temperature hysteresis forming only its right slope. Remarkably, there were no specific features in the $C_p(T)$ dependence around T^*.

This fact suggests that the above maximum of ε is due to a phase transition at the boundaries of the ferroelectric domains and the consequent reduction in their mobility. The phenomenon has been reported for monocrystalline rubidium tetrachlorozincate [15–17]. In the case of crystals with a lot of lattice defects, a blurred maximum of the dielectric response was observed around T^*, the temperature at which the mobility of domain boundaries ceases [15].

Notably, the temperature dependences of dielectric permittivity obtained upon heating and cooling of the studied material do not coincide, forming a temperature hysteresis of ε over a wide temperature range. The range lies above the temperature T^*, where the mobility of
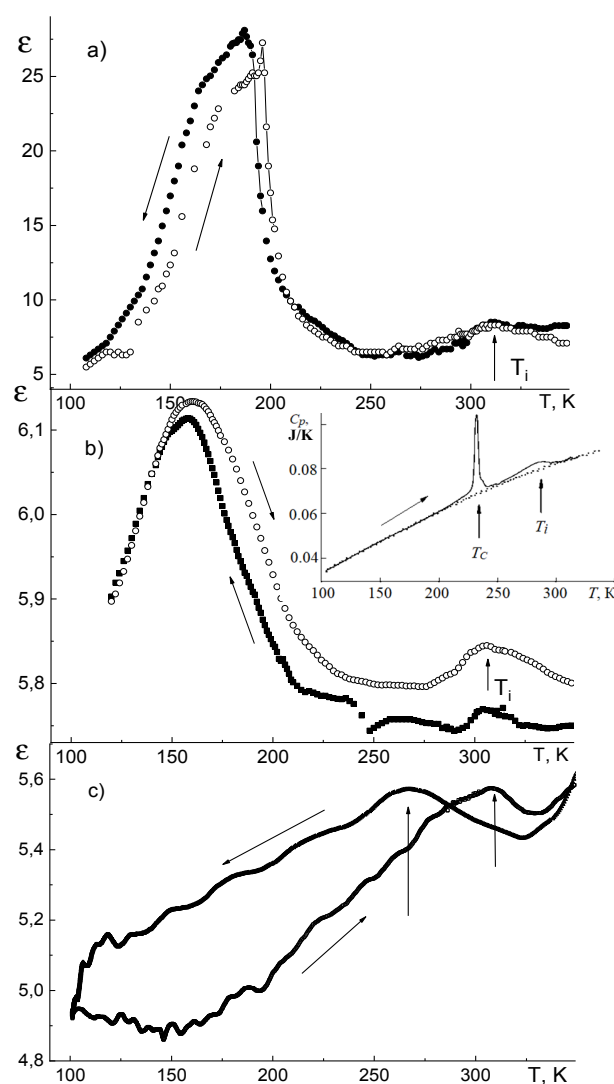
Fig. 2. Temperature dependences of dielectric permittivity for the crystalline Rb_2ZnCl_4 sample (a), and RS-46 (b) and RS-5 (c) composites obtained by heating and cooling. The insert shows the temperature dependence of the specific heat capacity of the RS-46 composite [11]

domain boundaries ceases. However, at $T < T^*$, the temperature hysteresis of e was not observed.

In the case of the monocrystalline sample, a similar dielectric response behaviour was reported [15–17]. However, unlike the above composite material, the temperature hysteresis of ε in Rb_2ZnCl_4 monocrystal is limited to T^* from below and to the Lifshitz temperature T_i from above. According to the authors who studied this phenomenon in Rb_2ZnCl_4 [15–17], the anomalously wide temperature hysteresis of dielectric permittivity is due to the fixation of the domain boundaries and solitons on lattice defects.

Condensed Matter and Interphases / Конденсированные среды и межфазные границы   2022;24(3): 362–368

L. S. Stekleneva et al.   Effect of pore size on phase transitions in rubidium tetrachlorozincate nanoparticles...

Due to the strong interaction with the defects, the polar domains can be "drawn" into the nonpolar phase from the ferroelectric phase during the heating of the sample [18]. This is probably the reason why the $\varepsilon(T)$ dependence when heating the RS-46 composite, goes above the ε temperature dependence obtained during its cooling.

Let us now consider the dielectric properties of the RS-5 composite (Fig. 2c). Near the value of T_i, there is a small peak of dielectric permittivity. On the cooling curve, its position corresponds to ≈ 268 K, and on the heating curve it is ≈ 307 K. The observed temperature hysteresis of T_i confirms that, in rubidium tetrachlorozincate crystallites embedded in porous silicon dioxide with an average pore diameter of about 5 nm, the transition from the regular paraelectric phase to the incommensurate phase exhibits the features of the first-order phase transition. The hysteresis of T_i is due to the fixation of the incommensurate wave of atomic displacements by the lattice defects, including the defects on the particle surface. Subsequently, the wave detaches from the stops upon "overheating" or "overcooling" of the sample compared to the phase equilibrium temperature.

No features of a dielectric response indicating a ferroelectric phase transition or a transition in the domain structure were observed in the $\varepsilon(T)$ dependences under the experimental conditions. Therefore, we can conclude that the ferroelectric phase does not occur in Rb_2ZnCl_4 particles in the RS-5 composite.

Moreover, the temperature hysteresis of ε for the RS-5 composite covers the entire temperature range used in the experiment, indicating the presence of metastable states in the material and their relaxation over a wide temperature range. Apparently, the existence of such a wide temperature hysteresis of ε is a common feature of ferroelectrics with incommensurate phases incorporated into porous matrices [19].

In contrast to the RS-46 composite, the $\varepsilon(T)$ dependence for heating goes below the ε, temperature dependence for cooling of the sample. This indirectly indicates that the ferroelectric phase domains, which usually make a significant contribution to the dielectric

response, were not formed in the case of the RS-5 composite.

4. Conclusions

Based on the results of the research, we made the following conclusions.

1. The Lifshitz temperature $T_i \approx 307$ K in Rb_2ZnCl_4 rubidium tetrachlorozincate crystallites localised in silicon dioxide pores with an average diameter of 46 and 5 nm changed little as compared to the temperature T_i in the bulk sample. At the same time, the phase transition exhibited the features of the first-order phase transition, which were most pronounced in the case of Rb_2ZnCl_4 particles in the RS-5 composite. For this material, the temperature of the transition from the incommensurate to the paraelectric phase remained approximately the same as that of the bulk sample. However, when the temperature change was reversed, the value of T_i decreased to ≈ 268 K. Thus, the interaction of rubidium tetrachlorozincate particles with the matrix stabilised the nonpolar commensurate phase. This interaction seems to be predominantly chemical, as the transition to the incommensurate phase was not accompanied by either polarisation or a noticeable deformation of the Rb_2ZnCl_4 lattice.

2. Under the experimental conditions, we observed no transition from the incommensurate to the commensurate ferroelectric phase in Rb_2ZnCl_4 nanocrystallites in the RS-5 composite.

3. In rubidium tetrachlorozincate particles in a porous silicon dioxide matrix with an average pore size of ≈ 46 nm, the transition to a ferroelectric phase was registered. According to the combined data of dielectric and calorimetric measurements, the temperature of the transition was around 240 K. This is approximately 50 K higher than in the monocrystalline material.

4. The dielectric permittivity maximum observed around 160 K for the RS-46 composite corresponds to the dielectric anomaly occurring due to rearrangement in the domain structure of monocrystalline Rb_2ZnCl_4 with a high defect concentration [15]. Thus, we can state that, at low temperatures, ferroelectric domains are formed in rubidium tetrachlorozincate crystallites embedded into silicon dioxide with through-pores averaging 46 nm in diameter. The domain

Condensed Matter and Interphases / Конденсированные среды и межфазные границы 2022;24(3): 362–368

L. S. Stekleneva et al. Effect of pore size on phase transitions in rubidium tetrachlorozincate nanoparticles...

mobility decelerates significantly at ≈ 160 K, as in bulk Rb_2ZnCl_4 monocrystal.

Author contributions

Korotkov L. N. – concept of the research. Stekleneva L. S. – carrying out the experiment. Bryanskaya A. A. – preparing samples for the experiment. Pankova M.A. – preparing the manuscript. Popov S. V. – attestation of samples, processing of experimental data, and making figures.

Conflict of interests

The authors declare that they have no known competing financial interests or personal relationships that could have influenced the work reported in this paper.

References

1. Cummins H. Z. Experimental studies of structurally incommensurate crystal phases. *Physics Keports*. 1990;185(5-6): 211–409. https://doi.org/10.1016/0370-1573(90)90058-a

2. Gridnev S. A., Korotkov L. N. *Disordered polar dielectrics. From crystal to dipole glass and chaos.* Palmarium Academic Publishing; 2013. 170 p. Available at: https://www.elibrary.ru/item.asp?id=26049698

3. Bagautdinov B. Sh., Shekhtman V. Sh. Evolution of the structure of Rb2ZnCl4 over the temperature range 4.2–310 K. *Physics of the Solid State*. 1999;41(6): 987- 993. https://doi.org/10.1134/1.1130929

4. Tarnavich V. V., Sidorkin A. S., Korotkova T. N., Rysiakiewicz-Pasek E., Korotkov L. N., Popravko N. G. "Restricted Geometry" Effect on Phase Transitions in KDP, ADP, and CDP Nanocrystals. *Crystals*. 2019;9(11): 593. https://doi.org/10.3390/cryst9110593

5. Mikhaleva E. A., Flerov I. N., Kartashev A. V., Gorev M. V., Molokeev M. S., Bogdanov E. V., Bondarev V. S., Korotkov L. N., Rysiakiewicz-Pasek E. Effect of restricted geometry and external pressure on the phase transitions in ammonium hydrogen sulfate confined in a nanoporous glass matrix. *Journal of Materials Science.* 2018;53(17): 12132–12144. https://doi.org/10.1007/s10853-018-2467-1

6. Naberezhnov A. A., Stukova E. V., Alekseeva O. A., Novikova S. A., Franz A. Effects Associated with Confined Geometry in Nanocomposites Based on Mesoporous 2D-SBA-15 and 3D-SBA-15 Matrices Containing Sodium Nitrite Nanoparticles. *Technical Physics*. 2019;64(12): 1866–1871. https://doi.org/10.1134/s106378421912020x

7. Beskrovny A. I., Vasilovskii S. G., Vakhrushev S. B., Kurdyukov D. A., Zvorykina O. I., Naberezhnov A. A., Okuneva N. M., Tovar M., Rysiakiewicz-Pasek E., Jaguś P. Temperature dependences of the order parameter for sodium nitrite embedded into porous glasses and opals. *Physics of the Solid State*. 2010;52(5): 1092–1097. https://doi.org/10.1134/s1063783410050410

8. Naberezhnov A. A., Vakhrushev S. B., Kumzerov Y. A., Fokin A. V. Mechanism of ferroelectric phase transition in ultra-dispersed sodium nitrite particles. *Ferroelectrics*. 2021;575(1): 75–83. https://doi.org/10.1080/00150193.2021.1888229

9. Nguyen H. T., Chau M. T. Structural and dielectric studies of three-phase composite containing multiwalled carbon nanotubes, nanodispersed silica AND KDP. *Phase Transitions*. 2020;93(10-11): 1080-1088. https://doi.org/10.1080/01411594.2020.1839753

10. Mikhaleva E. A., Flerov I. N., Bogdanov E. V., Bondarev V. S., Gorev M. V., Rysiakiewicz-Pasek E. Size effect on sensitivity to external pressure and caloric effects in TGS: ceramics and nanocomposites. *Materials Today Communications*. 2020;25: 101463. https://doi.org/10.1016/j.mtcomm.2020.101463

11. Kumzerov Y., Vakhrushev S. Nanostructures within porous materials. In: *Encyclopedia of Nanoscience and Nanotechnology. Volume 10*. H. S. Nalwa (ed.). New York: American Scientific Publishers; 2003. pp. 811–849.

12. Andreeva O. V., Obyknovennaja I. E. Nanoporous matrices NPS-7 and NPS-17 – possibilities of use in an optical experiment. *Nanosystems: Physics, Chemistry, Mathematics*. 2010;1(1): 37–53. (In Russ.). Available at: https://www.elibrary.ru/item.asp?id=15648759

13. Bruker AXS TOPAS V4. *General profile and structure analysis software for powder diffraction data.* User's Manual. Karlsruhe, Germany: Bruker AXS; 2008.

14. Korotkov L. N., Stekleneva L. S., Flerov I. N., Mikhaleva E. A., Rysiakiewicz-Pasek E., Molokeev M. S., Bondarev V. S., Gorev M. V., Sysoev O. I. X-Ray, dielectric, and thermophysical studies of rubidium tetrachlorozincate inside porous glasses. *Bulletin of the Russian Academy of Sciences: Physics*. 2019;83(9): 1072–1076. https://doi.org/10.3103/s1062873819090132

15. Strukov B. A., Belov A. A., Gorshkov S. N., Kozhevnikov M. Ju. Thermal conductivity and heat capacity of Rb2ZnCl4 crystals in the region of the incommensurate phase. *Bulletin of the Academy of Sciences of the USSR. Physical Series*. 1991;55(3): 470–473. (In Russ.)

16. Gridnev S. A., Prasolov B. N., Gorbatenko V. V. On the phase in the domain wall of Rb2ZnCl4 near 150 K. *Crystallography Reports*. 1997;42(4): 670–673. Available at: https://www.elibrary.ru/item.asp?id=13261163

17. Gridnev S. A., Shuvalov L. A., Gorbatenko V. V., Prasolov B. N. "Freezing" of domain structure in

Condensed Matter and Interphases / Конденсированные среды и межфазные границы   2022;24(3): 362–368

L. S. Stekleneva et al.   Effect of pore size on phase transitions in rubidium tetrachlorozincate nanoparticles...

Rb$_2$ZnCl$_4$. *Ferroelectrics*. 1993;140(1): 145–149. https://doi.org/10.1080/00150199308008277

18. Gridnev S. A., Shuvalov L. A., Gorbatenko V. V., Prasolov B. N. "Freezing" of domain structure in Rb2ZnCl4. *Ferroelectrics*. 1993;140(1): 145–149. https://doi.org/10.1080/00150199308008277

19. Korotkov L. N., Stekleneva L. S., Logoshina E. M., Pankova M. A. Dielectric response of Rb$_2$ZnCl$_4$ within porous aluminum oxide. *Ferroelectrics*. 2020;567(1): 74–81. https://doi.org/10.1080/00150193.2020.1791589

Information about the authors

Lyubov S. Stekleneva, instructor at the Department of Solid State Physics of Voronezh State Technical University, Voronezh, Russian Federation; lecturer at the Department of Physics and Chemistry of the Air Force Military Educational and Scientific Centre of Zhukovsky and Gagarin Air Force Academy, Voronezh, Russian Federation.

https://orcid.org/0000-0002-5460-2870

lubov_stekleneva@mail.ru

Aleksandra A. Bryanskaya, student at the Department of Solid State Physics of Voronezh State Technical University, Voronezh, Russian Federation.

https://orcid.org/0000-0002-1848-0554

Aleksbrianskaya@yandex.ru

Margarita A. Pankova, Cand. Sci. (Tech.), Senior Lecturer at the Department of Mathematics and Systems Modelling of Voronezh Institute of the Ministry of Internal Affairs of the Russian Federation, Voronezh, Russian Federation.

https://orcid.org/0000-0002-5985-9018

m_a_pankova@mail.ru

Sergey V. Popov, Cand. Sci. (Phys.–Math.), Associate Professor at the Department of Physics and Chemistry of the Air Force Military Educational and Scientific Centre of Zhukovsky and Gagarin Air Force Academy, Voronezh, Russian Federation.

https://orcid.org/0000-0003-2218-5811

nikiforovatl@yandex.ru

Leonid N. Korotkov, Dr. Sci. (Phys.–Math.), Professor at the Department of Solid State Physics, Voronezh State Technical University, Voronezh, Russian Federation.

https://orcid.org/0000-0002-5350-5841

l_korotkov@mail.ru

Translated by Anastasiia Ananeva
Edited and proofread by Simon Cox

Condensed Matter and Interphases

Original articles

Analysis of the variations in the surface properties of SiO_2 and Al_2O_3 nanoparticles obtained by different synthesis methods

V. V. Syzrantsev✉

Grozny State Oil Technical University,
100 Isaeva av., Grozny 364051, Russian Federation

Abstract

The article presents a comparative study of the surface properties of silica and alumina nanoparticles synthesized by various methods.

Using the IR spectroscopy we demonstrated that the synthesis method affect the surface properties of nanoparticles while maintaining the phase composition of the material. The article demonstrates the relationship between the types of surface sites, their strength, and the interaction of nanoparticles with the dispersed medium. In particular, a significant difference was observed in the strength of the active sites for all samples, which was reflected in the rheology of nanofluids based on epoxy resin. This demonstrates the importance of accurate descriptions of the surface properties of nanoparticles, as they determine their interaction with other materials.

The article also considers the possibility to evaluate the intensity of the particle-medium interaction based on the fractal dimension. Our study showed that it varies significantly depending on the synthesis method. The article discussed the possibility to determine the intensity of the particle-medium interaction using the values of the nanoparticle's zeta potential and the interfacial layer.

Keywords: Keywords: Nanoparticles, Surface sites, Interfacial layer, Zeta potential, Nanoparticle synthesis

✉ Vyacheslav V. Syzrantsev, e-mail: vvveliga@mail.ru

Condensed Matter and Interphases / Конденсированные среды и межфазные границы   2022;24(3): 369–378

V. V. Syzrantsev   Analysis of the variations in the surface properties of SiO$_2$ and Al$_2$O$_3$ nanoparticles...

1. Introduction

Nanoparticles are a common class of materials, whose properties have been studied in much detail. However, few researchers pay attention to the fact that, having the same chemical and phase compositions, some of the properties of nanoparticles depend on the conditions of their synthesis and may vary significantly [1]. At the moment, there are dozens, and for some substances even hundreds, of approaches to the synthesis of nanoparticles. The synthesis is always performed under certain conditions resulting in the formation of particles with specific crystal and surface structures. Therefore, powders synthesised using different methods are effective for different applications, and it is only possible to determine a suitable option for a particular application by trial and error. This appears to be the only reliable method, since there is no uniform approach to the characterisation of nanoparticles.

The significant difference between the characteristics of nanoparticles and bulk materials is quite often explained by the growing influence of the surface area, whose fraction in relation to the volume increases with the decrease in the size of the particles [2]. However, the changes in the properties of the surface itself, although crucial, are never taken into account. These changes may include surface defects (variations in the local coordination number, twinning, changes in the crystallographic planes, and porosity), the presence and composition of functional groups, and their inhomogeneity. These factors, except for lyophobic behaviour, are widely underestimated, even though they play an important role in the process of interaction of particles with a dispersed medium.

It is known that surface energy is proportional to the number of broken bonds in the surface atoms multiplied by the energy of these bonds. For particles with a metallic crystal structure this parameter helps to determine the melting point [3–5], as well as other thermodynamic parameters [6, 7] and the surface energy [8].

For oxides and more complex particles, the situation is more complicated.

Firstly, the existing descriptions of such nanoparticles, similar to bulk materials, mostly focus on their composition (purity) and size.

Secondly, such particles may be a combination of crystalline phases or be X-ray amorphous only in the order of short ranges [9, 10]. Since the surface energy can be different for different crystallographic planes on the surface of the particle [11], the identity of such particles can be questionable.

Thirdly, the surface of nanoparticles can have unique features which must be taken into account as opposed to the features of the surface of bulk materials. These features might include: porosity of the surface, the strength and concentration of Brønsted acid sites (BAS) and Lewis acid sites (LAS) [12], and ductility and elasticity of the neighbouring clusters comprising the particle.

For the gas-phase synthesis the key factors are the cooling rate and the mechanical and thermal properties of the cooling gas and the evaporated materials [13–16]. Additionally, the fast cooling rate of the vapour may result in a fixed metastable state of some of the clusters thus creating a ratio between the surface and the bulk energy characteristic for nanoparticles of a different size. In the case of a liquid-phase synthesis the result depends on the type of the process, the type of the reagent, the pH, the concentration of the precursor, the temperature, and the duration of the process [17]. The multicomponent sensitivity to the conditions of the synthesis results in significant variations of the size of the nanopaticles, their size distribution, and surface characteristics. Thus, during cryochemical condensation of silver vapour [18] different fractal dimensions of the particles were observed depending on the solvent: 1.9 (isopropanol), 1.7 (acetonitrile), 1.5 (toluene). The average sizes of the primary particles in the fractal cluster were 16.0, 21.0, and 9.4 nm respectively.

One of the most obvious methods to determine the difference in the interaction of nanoparticles of various origin with the medium they are dispersed in, is to measure its viscosity. The experimental studies [19, 20] demonstrated that higher concentrations and smaller size of the particles result in an increase in viscosity. However, the results obtained by different researchers vary greatly and are significantly higher than the values calculated using the the Batchelor–Green formula [21] commonly used for suspensions with microparticles. This can

Condensed Matter and Interphases / Конденсированные среды и межфазные границы   2022;24(3): 369–378

V. V. Syzrantsev   Analysis of the variations in the surface properties of SiO$_2$ and Al$_2$O$_3$ nanoparticles...

be accounted for only by the variations in the interaction intensity between the liquid and nanoparticles [22] which differ in their surface structure, namely the thickness of the interfacial layer.

The variability of the surface properties occurring during the synthesis can be identified using IR and UV spectroscopy, which determine characteristic vibrations of bridging, terminal, and other bonds between the surface atoms. Thus, [1, 23] demonstrated that when different methods of synthesis of SiO$_2$ nanoparticles are used, their structure changes from close-packed (aerosils) to ribbon (silica gels). When the composition of the surface group is the same, the key factor is their inhomogeneity, i.e. their reactivity distribution. In particular, the ratio between the terminal and bridging OH groups may vary for nanoparticles [24]. A change in the number of Lewis acid sites can result from a number of factors including the changes in the local coordination number of oxygen, aluminium, silicon, or other elements of the oxide [25], thus reflecting the value of the surface energy of a particular sample.
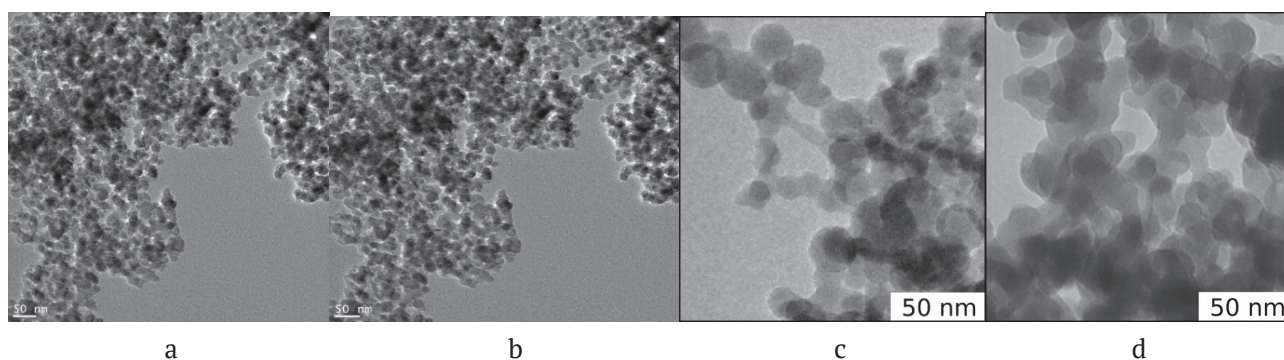
Another way to determine the concentration of the active sites is by means of adsorption of acid-base indicators [[26]. Analysis of the adsorption spectra distribution makes it possible to predict the sorption capacity of the surface and other properties of nanoscale materials. In particular, it helps to determine the variations in the strength and concentration of BAS and LAS during the treatment of the surface and show their relation to the properties of the material, such as dielectric permittivity [27] and the coefficient of friction of the surface [28].

However, it is difficult to use the results of the IR spectroscopy and the indicator method directly due to their complexity and lack of transparency. Besides, the theoretical and practical aspects of the process need to be further elaborated by both researchers and manufacturers. Therefore, in our study, we analysed the results of the spectroscopy, particle-particle interaction based on the fractal dimension, and particle-medium interaction based on the viscosity measurements [29]. A fractal dimension is assumed to be a common factor which demonstrates the specifics of the interaction between particles and their environment or a material.

2. Materials and methods

To compare SiO$_2$ and Al$_2$O$_3$ nanoparticles we used samples obtained by several synthesis methods: SiO$_2$ and Al$_2$O$_3$ obtained by means of electron beam evaporation (Ts and Ta samples); commercially available SiO$_2$ and Al$_2$O$_3$ powders synthesised by pyrogenic process (As and Aa samples), (Evonik Industries, Germany); commercially available SiO$_2$ and Al$_2$O$_3$ powders obtained by liquid phase method (Ls and La samples), (Nanjing XFNANO Materials Tech Co., China); commercially available SiO$_2$ powders obtained using the plasma arc method (Psp sample), (Plasmotherm, Russia); commercially available Al$_2$O$_3$ AKP50 powders synthesised by means of chemical deposition (Sa sample) (Sumitomo Chemical, Japan); and commercially available Al$_2$O$_3$ powders obtained using the exploding wire method (Ea sample), (Perspektivnye Materialy, Russia). Their TEM photographs and particle size distribution are presented in Fig. 1–3. All silica particles were X-ray amorphous. Analysis performed by the Rietveld method demonstrated that their structural parameters and binding energies were similar. Aa and Ta samples were a gamma phase of aluminium oxide, and La, Ea, and Sa samples were an alpha phase of aluminium oxide. All particles were of spherical shape and had a similar average diameter. However, the range of particle size distribution varies greatly, which means that the particles will behave differently when applied for practical purposes.

For the IR spectroscopy, tablets were formed with the ratio of the mass to the geometric area being 15–49 mg/cm^2. The tablets were put into a vacuum IR cuvette and were vacuumized for 1 hour at 10^{-3} Pa. Then, without contact with the atmosphere, the samples were put into a measuring chamber, which measured the spectra at temperatures of up to 77 K. The spectra were then recorded at room temperature and at 77–110 K. The spectra were recorded using a Shimadzu IRTracer-100 spectrometer in the range of 600–6000 cm^{-1} with a resolution of 4 cm^{-1}. The number of accumulated scans was 100 which ensured the signal-to-noise ratio of at least 75000. The adsorption was performed at 77 K in doses which ensured the pressures of 0.1, 0.4, 0.9, 1.4, and 10 Torr in the cuvette.

Condensed Matter and Interphases / Конденсированные среды и межфазные границы   2022;24(3): 369–378

V. V. Syzrantsev   Analysis of the variations in the surface properties of SiO$_2$ and Al$_2$O$_3$ nanoparticles...

Fig. 1. TEM photographs of SiO$_2$ nanoparticles: a) – sample Ls, b) – sample Ps, c) – sample Ts, d) – sample As
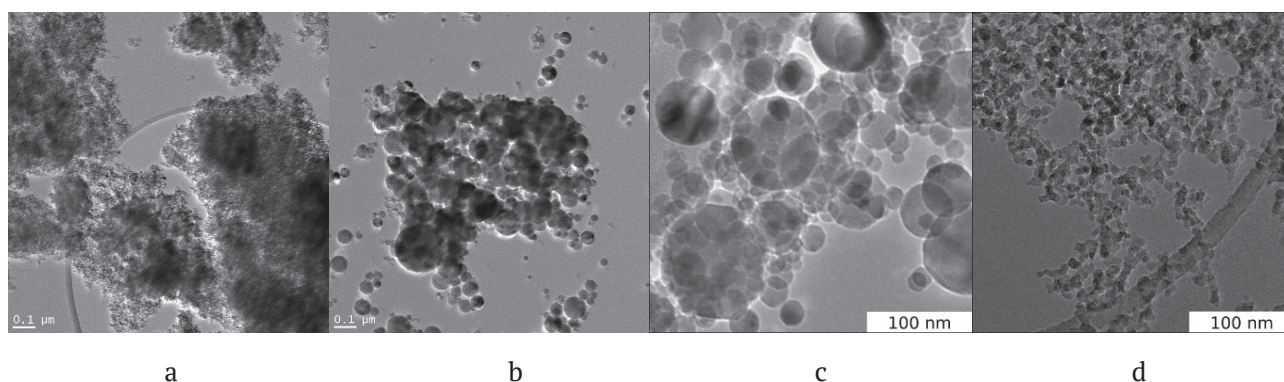
Fig. 2. TEM photographs of Al$_2$O$_3$ nanoparticles: a) – sample La, b) – sample Ea, c) – sample Ta, d) – sample Aa
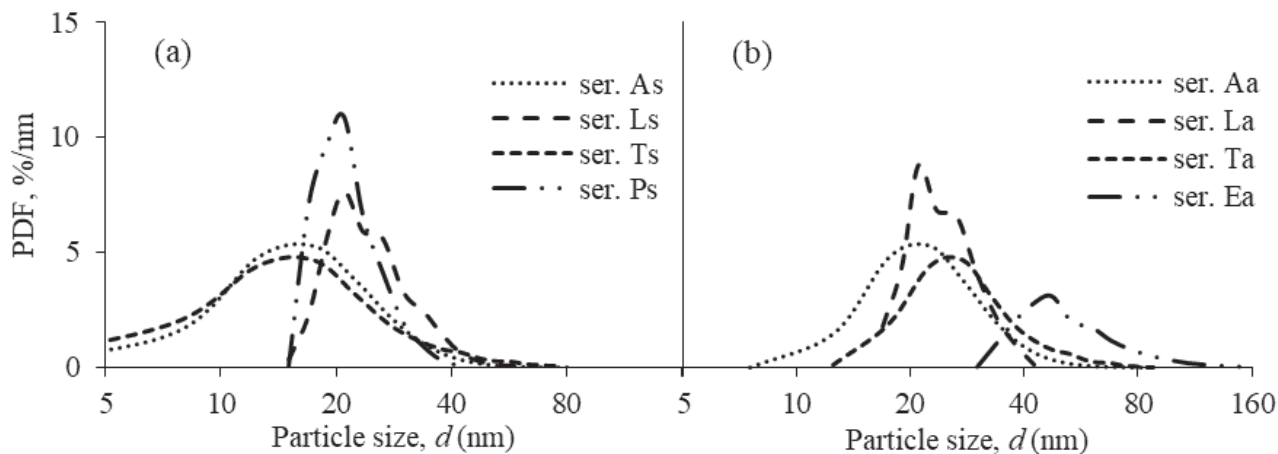
Fig. 3. Probability density function (PDF) of nanoparticle size distributions: (a) SiO$_2$; (b) Al$_2$O$_3$.

To measure the IR spectra of the adsorbed pyridine, the initial powders were mixed with barium fluoride at a ratio of 1:2. Barium fluoride was transparent in the region of 1000 cm^{-1} and thus did not distort the spectra in the region of OH groups. Prior to the adsorption of pyridine, the samples were vacuumized at 450 °C for 2 hours. The final pressure was below 10^{-3} Torr. Pyridine was adsorbed at a temperature of 150–160 °C for 15–20 minutes and then the air was evacuated for 60 minutes at the same temperature until the vacuum level was at least 10^{-2} Torr. The spectra were recorded with a resolution of 4 cm^{-1} in the region 1000–4000 cm^{-1} using a Shimadzu-8300 IR-Fourier spectrometer until 200 spectra were accumulated. The strength of the acid sites was qualitatively evaluated based on the position of two bands showing the vibrations of the pyridine ring in the regions 1440–1460 and 1590–1630 cm^{-1}.

Condensed Matter and Interphases / Конденсированные среды и межфазные границы   2022;24(3): 369–378

V. V. Syzrantsev   Analysis of the variations in the surface properties of SiO$_2$ and Al$_2$O$_3$ nanoparticles...

The calculation methodology of the fractal dimension [30] is based on the linear dependence of the area of the agglomerate on its perimeter on double logarithmic scale. The calculation was performed based on the analysis of TEM photographs. Using photographs of various scales, for instance 50, 100, 200, and 500 nm, we obtained data on the similarity of particle agglomerations depending on the scale. Then from $\log S = C + 2/D \cdot \log P$ we obtained the fractal dimension D2 as the slope of the linear dependence of logS on logP. To obtain 3D fractal dimension D3 we recalculated the 2D values of D2 using the formula $D3 = 1.5 \cdot D2$. The measurement error was 0.005–0.01, which allowed us to use this parameter to assess the intensity of interaction between the particles and the medium.

3. Results

3.1. Variations in the fractal dimension

The fractal dimensions calculated for SiO$_2$ and Al$_2$O$_3$, nanoparticles are given in Fig. 4. As we can see, for all groups of SiO$_2$ nanoparticles fractal dimensions grow almost linearly with the growth of the specific surface in the range of 0.1–0.15. At the same time, the effect of the synthesis method can be stronger, reaching up to 0.4–0.5. The fractal dimension of Al$_2$O$_3$ nanoparticles (Fig. 4b) generally demonstrates a similar dependence. When the specific surface varies, the fractal dimensions of the particles of the same type are very close. When a different synthesis method is used, the difference is 0.3–

0.5. The difference can also be accounted for by a different phase, since samples of Aa and Ta are gamma phase, and samples of La, Ea, and Sa are alpha phase. Nevertheless, the difference in the fractal dimension caused by the use of different synthesis methods is significant even for the same phase.

Summing up the data on all the types of particles, we can see that the particles synthesised using electron beam evaporation have smaller fractal dimension (2.3–2.6) than the particles synthesised by any other method. The largest fractal dimension, often close to the limit value ($D3_{max} = 3$), was observed in particles synthesised by liquid phase methods (Ls, La, Sa). Nanoparticles obtained by means of the pyrogenic process have intermediate values of fractal dimension whose range (2.3–2.7) varies significantly depending on the type of the synthesised material. Based on this data, we can assume that the fractal dimension reflects the difference in the force field of the surface of nanoparticles which forms agglomerates of various complex forms: sphere-like, ribbon, chain, jellyfish-like, etc. Under certain conditions it can be used as a basic identification parameter for the application of nanoparticles.

3.2. Variations in the surface properties

The most common surface defects are porosity and plane distortions (steps, depressions, twinning of the crystal lattice, and other distortions). In any case, the coordination numbers of the first and the last atoms change, affecting their ability to interact with the medium. This is how LAS appear,
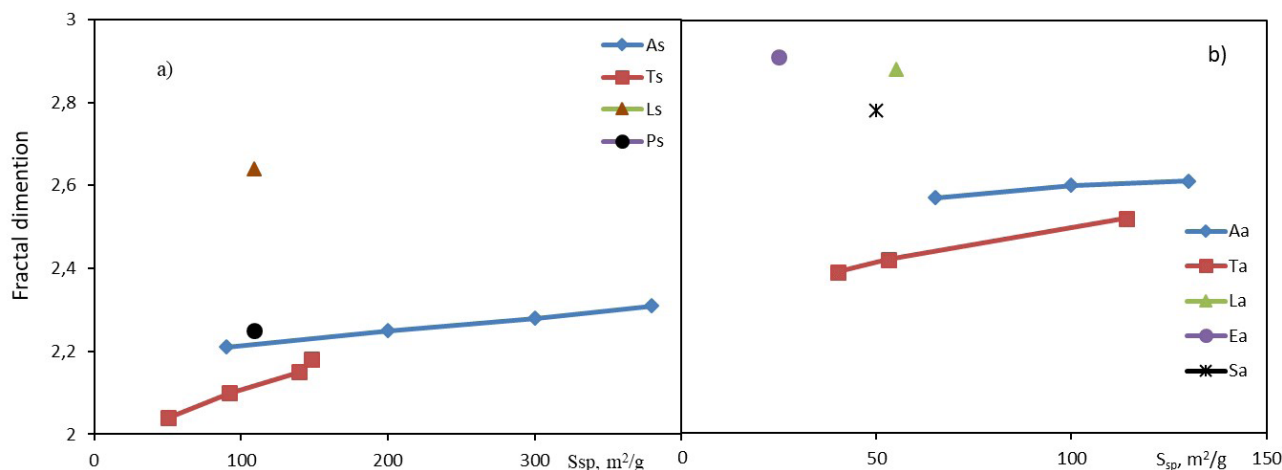

Fig. 4. The fractal dimension D3 of nanoparticles: a) – SiO$_2$ and b) – Al$_2$O$_3$

Condensed Matter and Interphases / Конденсированные среды и межфазные границы   2022;24(3): 369–378

V. V. Syzrantsev   Analysis of the variations in the surface properties of SiO$_2$ and Al$_2$O$_3$ nanoparticles...

which result from coordinatively saturated metal cations in various coordination environment of, for instance, oxygen atoms (Fig. 5).

Another peculiar feature of the surface is the formation of OH groups, for instance terminal or bridge groups, which are easily identified in IR spectra based on the occurrence of absorption bands at 3400–3800 cm^{-1}. They are considered to be BAS. There can also be basic sites, i.e. bridge oxygen atoms or OH group oxygen atoms. Such surface properties are determined by means of IR spectroscopy, which can ensure the quite accurate identification of characteristic bands in the spectrum.

For SiO$_2$, the strength of the sites is determined based on the frequency shift of the OH stretching vibrations towards the region of low frequencies during the adsorption of CO. For Al$_2$O$_3$, the LAS strength is determined based on the shift of the bands of adsorbed pyridine at 1440–1460 cm^{-1} and 1590–1630 cm^{-1} to the region of high frequencies. The larger the shift, the stronger the asidic site. A number of studies of the said nanoparticles were carried out, and the difference in their structures was determined [10, 31, 32]. The results of the measurements are given in Table 1.

From the point of view of interactions with the medium, the strongest are the LAS which interact through the valence bonds of metals in the oxide. The next are basic sites interacting through oxygen atoms. The terminal OH groups,

i.e. BAS are the weakest. Based on the analysis of the data on the SiO$_2$ samples, we can assume that the As sample demonstrates the highest intensity of the interaction with the medium due to the observed LAS (2200 cm^{-1}) and a significant shift of the frequency of stretching vibrations. The next is the Ps sample due to a significant shift in the frequency of stretching vibrations of the OH group (87 cm^{-1}) during the adsorption of CO. The third should be the Ts sample with a significant shift of the frequency of CO stretching vibrations (83 cm^{-1}). The Ls sample, with a shift of the frequency of stretching vibrations (79 cm^{-1}) and a strong BAS (2170 cm^{-1}), demonstrates the weakest interaction with the medium.

Similar conclusions can be made for the nanoparticles As and Ts obtained using the indicator method in [33]. The indicator method demonstrated that the surface of the As nanoparticles was mostly covered in LAS, while for the Ts sample, Lewis basic sites and BAS were observed.

As for the aluminium oxide, we can assume that the Aa sample (1454 and 1622 cm^{-1}) has the strongest interaction with the environment. The second is the Ta sample (1447 and 1604 cm^{-1}). At the same time, the La sample demonstrated medium LAS in the range of 2180–2197 cm^{-1}. The same for the Ea sample at 2189 cm^{-1}. They are thus compatible with regard to the intensity of their interaction with the medium.
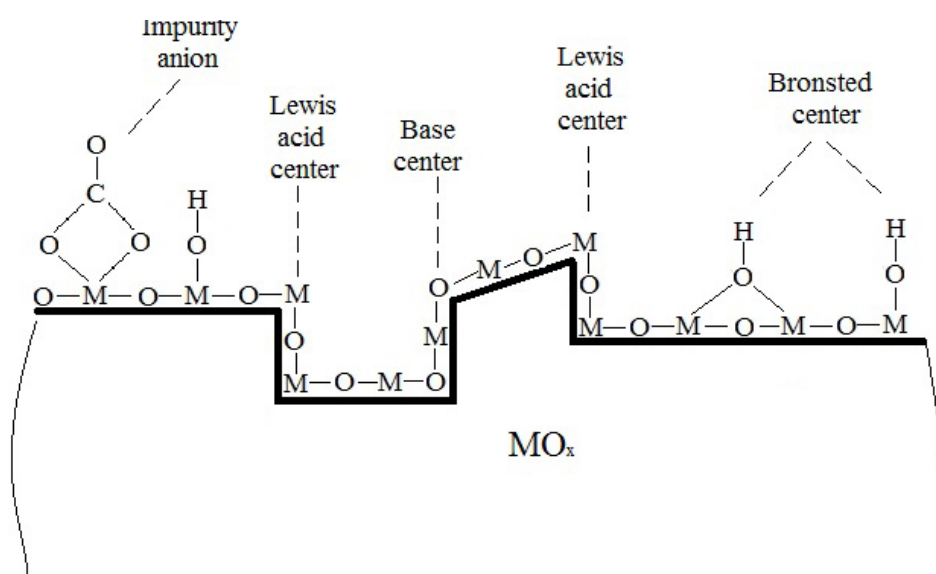

Fig. 5. Possible types of surface structures and sites

Condensed Matter and Interphases / Конденсированные среды и межфазные границы   2022;24(3): 369–378

V. V. Syzrantsev   Analysis of the variations in the surface properties of SiO$_2$ and Al$_2$O$_3$ nanoparticles...

Table 1. Interpretation of the IR spectra (cm^{-1})

Sample SiO$_2$	Ls	Ps	Ts	As
Shift in the frequency of OH stretching vibrations of the SiOH groups	79	87	83	83
Medium LAS*	2170	none	none	none
Strong BAS*	none	none	none	2200
Hydrogen-bonded OH groups	none	weak 3650	3690, 3580	3690, 3580
Stressed Si-O-Si bridges	927	930	810	810
Stressed bridges	none	none	886, 946	886, 946
Sample Al$_2$O$_3$	La	Ea	Ta	Aa
Terminal OH groups (over 3750)	very weak 3795, 3780	very weak 3783	3785	strong 3785
Bridge OH groups (3650–3745)	weak 3680, 3695, 3732	3721, 3680 weaker than those of La	medium 3685, 3745, weak 3660	strong 3685, medium 3745, weak 3660
Medium LAS*	2180-2197	2189	none	none
Medium BAS**	2164	none	none	none
LAS** in the ranges of:				
1440–1460	none	none	1447	1454
1590–1630	none	none	1604	1622

* according to the stretching vibrations of the adsorbed CO
** according to the spectra of the adsorbed pyridine

3.3. Variations in the interaction intensity

Experimental measurements of the ζ-potential and the thickness of the interfacial layer [29] according to the model presented in [22] demonstrated that there is a strong correlation between these values, which indicates their affinity. From the point of view of colloidal chemistry, the ζ-potential is determined by the intensity of the interaction between the particle and the medium and corresponds to the thickness of the layer where the medium connected with the particle and divided from it is dispersed (Stern layer [34]). The result of the comparison (Table 2) demonstrates the presence of a linear dependence of the thickness of the interfacial layer δ, obtained based on the measurements of the viscosity of the nanofluid on the value of the ζ-potential. This means that the surface structure and the value of the ζ-potential connected with it, which determine the intensity of the interaction of the particles with the medium, depend more on the synthesis method rather than on the size of the particles.

Comparing the data from Table 2 and the assumptions regarding the interaction intensity based on the IR spectroscopy, we can see that they are almost identical. The thickness of the interfacial layer corresponding to the interaction intensity is the largest for the the As sample, and then deteriorates in the same order as determined by the IR spectroscopy. A slight difference can be accounted for by the possible affinity of the resin to the specific surface groups, or by some additional factors. Aluminium oxide samples demonstrated the same correlation. The only difference is the use of electroexplosive particles (Ea) in the epoxy resin, where their effect on the viscosity is significantly stronger than the expected value.

The fractal dimension is not so obviously connected with the interaction intensity. We assume that the most effective is the value of 2.3–2.5, while the almost ideal values (D3$_{max}$ = 3) make the interaction with the medium less intensive. This is analogous to the process of cluster formation up to the point when a metastable isomer state is reached. It is known that at this point diffusion-limited aggregation of molecules is no longer a priority, because the system is ideal, and therefore it is more profitable to grow new clusters. In this case, the effective interaction between the particles and the environment

Condensed Matter and Interphases / Конденсированные среды и межфазные границы   2022;24(3): 369–378

V. V. Syzrantsev   Analysis of the variations in the surface properties of SiO$_2$ and Al$_2$O$_3$ nanoparticles...

Table 2. Characteristics of SiO$_2$ and Al$_2$O$_3$ nanoparticles

Sample SiO$_2$	Ls	Ps	Ts	As
Fractal dimension	2.640±0.005	2.250±0.006	2.04-2.18±0.01	2.21-2.31±0.01
ζ-potential, mV	−21.2±0.5	−24.2±0.7	−30.2±0.6	−36.2±0.5
Thickness of the interfacial layer in ED-20, δ, nm	2.82	3.03	3.29	3.67
Sample Al$_2$O$_3$	La	Ea	Ta	Aa
Fractal dimension	2.880±0.005	2.910±0.005	2.39−2.52±0.01	2.57-2.61±0.01
ζ-potential, mV	13.3±0.5	−17.5±0.4	−7.8±0.3	−12.8±0.6
Thickness of the interfacial layer in ED-20, δ, nm	0.5	2.54	1.89	2.23

requires available LAS bonds, which form on the defects of the surface. At the same time, low D3 prevents the formation of stable bonds between the atoms of the nanoparticles and the medium, also resulting in an insignificant increase in viscosity.

Therefore, the conducted study of the connection between the properties of the nanoparticles and their interaction with the medium demonstrated that it is possible to identify the particles by certain available parameters. The study thus provides researchers with a tool for forecasting the technological processes in this very complicated segment of nanotechnologies.

4. Conclusions

The article discussed the necessity to take into account the synthesis method when designing the technological processes with nanoparticles, since it determines the effectiveness of interaction of the particles with the medium. We suggest that the composition of the surface particle sites, which determine the intensity of their interaction with the environment, should be taken into account, namely LAS, basic sites, and BAS. The article demonstrated examples of the effect of such sites for the silica and alumina nanoparticles synthesised by means of several methods. The correspondence with the surface properties is not uniform and it is necessary to take into account surface forces. Therefore, the quality control of the full-scale production requires the control over the stability of size distribution of the particles and the fractal dimensions.

Conflict of interests

The author declares that they have no known competing financial interests or personal relationships that could have appeared to influence the work reported in this paper.

References

1. Sheka E. F., Khavryuchenko V. D., Markichev I. V. Techonological polymorphism of disperse amorphous silicas: inelastic neutron scattering and computer modelling. *Russian Chemical Reviews*. 1995;64(5): 389–414. https://doi.org/10.1070/rc1995v-064n05abeh000156

2. Vollath D., Fischer F. D., Holec D. Surface energy of nanoparticles – influence of particle size and structure. *Beilstein Journal of Nanotechnology*. 2018;9: 2265–2276. https://doi.org/10.3762/bjnano.9.211

3. Cluskey P. D., Newport R. J., Benfield R. E., Gurman S. J., Schmidt G. Z. An EXAFS study of some gold and palladium cluster compounds. *Zeitschrift for Physik D Atoms, Molecules and Clusters*. 1993;26: 8–11. https://doi.org/10.1007/bf01425601

4. Eckert J., Holzer J. C., Ahn C. C., Fu Z., Johnson W. L. Structural and thermodynamic properties of nanocrystalline fcc metals prepared by mechanical attrition. *Nanostructured Materials*. 1993;2: 407–413. https://doi.org/10.1016/0965-9773(93)90183-c

5. Coombes C. J. The melting of small particles of lead and indium. *Journal of Physics F: Metal Physics*. 1972;2: 441–449. https://doi.org/10.1088/0305-4608/2/3/013

6. Shandiz A., Safaei M. A. Melting entropy and enthalpy of metallic nanoparticles. *Materials Letters*. 2008;62: 3954–3956. https://doi.org/10.1016/j.matlet.2008.05.018

7. Safaei A., Shandiz M. A. Size-dependent thermal stability and the smallest nanocrystal. *Physica E: Low-dimensional Systems and Nanostructures*. 2009;41: 359–364. https://doi.org/10.1016/j.physe.2008.07.023

8. Ouyang G., Tan X., Yang G. Thermodynamic model of the surface energy of nanocrystals. *Physical Review B*. 2006;74: 195408. https://doi.org/10.1103/physrevb.74.195408

9. Abzaev Y. A., Syzrantsev V. V., Bardakhanov S. P. Simulation of the structural state of amorphous phases in nanoscale SiO$_2$ synthesized via different methods.

Condensed Matter and Interphases / Конденсированные среды и межфазные границы   2022;24(3): 369–378

V. V. Syzrantsev   Analysis of the variations in the surface properties of SiO$_2$ and Al$_2$O$_3$ nanoparticles...

Physics of the Solid State. 2017;59(9): 1874–1878. https://doi.org/10.1134/S1063783417090025

10. Syzrantsev V., Paukshtis E., Larina T., Chesalov Y., Bardakhanov S., Nomoev A. Features of surface structures of alumina and titanium dioxide nanoparticles produced using different synthesis methods. *Journal of Nanomaterials*. 2018;2018: 1-10. https://doi.org/10.1155/2018/2065687

11. Fried E., Gurtin M. E. A unified treatment of evolving interfaces accounting for small deformations and atomic transport with emphasis on grain-boundaries and epitaxy. In: *Advances in Applied Mechanics.* Aref H., van der Giessen E. (eds.). Academic Press: San Diego, CA, U.S.A.; 2004. pp. 1–177. https://doi.org/10.1016/s0065-2156(04)40001-5

12. Chukin G. D., Smirnov B. V., Malevich V. I. Formation of the structure of an amorphous aluminosilicate catalyst and its Lewis acid sites. *Kinetics and Catalysis.* 1988;29(3): 609-615.

13. Yumozhapova N. V., Nomoev A. V., Syzrantsev V. V., Khartaeva E. C. Formation of metal/semiconductor Cu-Si composite nanostructures. *Beilstein Journal of Nanotechnology*. 2019;10: 2497–2504. https://doi.org/10.3762/bjnano.10.240

14. Grammatikopoulos P., Steinhauer S., Vernieres J., Singh V., Sowwan M. Nanoparticle design by gas-phase synthesis. *Advances in Physics: X.* 2016;2: 1–20. https://doi.org/10.1080/23746149.2016.1142829

15. Swiatkowska-Warkocka Z., Koga K., Kawaguchi K., Wang H., Pyatenko A., Koshizaki N., Pulsed laser irradiation of colloidal nanoparticles: a new synthesis route for the production of non-equilibrium bimetallic alloy submicrometer spheres *RSC Adv.* 2013;3: 79–83. https://doi.org/10.1039/c2ra22119e

16. Li C., Yamauchi Y. Facile solution synthesis of Ag@Pt core-shell nanoparticles with dendritic Pt shells. *Physical Chemistry Chemical Physics*. 2013;15: 3490–3496. https://doi.org/10.1039/c3cp44313b

17. Kaabipour S., Hemmati S. A review on the green and sustainable synthesis of silver nanoparticles and one-dimensional silver nanostructures. *Beilstein Journal of Nanotechnology*. 2021;12: 102–136. https://doi.org/10.3762/bjnano.12.9

18. Kato M. Preparation of ultrafine particles of refractory oxides by gas-evaporation method. *Japanese Journal of Applied Physics*. 1976;15(5): 757–760. https://doi.org/10.1143/JJAP.15.757

19. Minakov A., Rudyak V. Ya, Pryazhnikov M. I. Systematic experimental study of the viscosity of nanofluids. *Heat Transfer Engineering.* 2021;42(12): 1024–1040. https://doi.org/10.1080/01457632.2020.1766250

20. Bashirnezhad K., Bazri S., Safaei M., Goodarzi M., Dahari M., Mahian O., Dalkılıça A., Wongwises S. Viscosity of nanofluids: a review of recent experimental studies. *International Communications in Heat and Mass Transfer.* 2016;73(4): 114–123. https://doi.org/10.1016/j.icheatmasstransfer.2016.02.005

21. Batchelor G. K. The effect of Brownian motion on the bulk stress in a suspension of spherical particles. *Journal of Fluid Mechanics*. 1977;83(1): 97-117. https://doi.org/10.1017/S0022112077001062

22. Syzrantsev V. V., Zavyalov A. P., Bardakhanov S. P. The role of associated liquid layer at nanoparticles and its influence on nanofluids viscosity. *International Journal of Heat and Mass Transfer.* 2014;72: 501. https://doi.org/10.1016/j.ijheatmasstransfer.2013.12.082

23. Khavryuchenko V. D., Sheka E. F. Computational modeling of amorphous silica. 4. Modeling the initial structures. Aerogel. *Journal of Structural Chemistry.* 1994;35(3): 305–308. https://doi.org/10.1007/BF02578281

24. Lamberov V. F., Romanova A. A., Shmelev R. G., Sopin I. G., Characterization of acid-modified alumina as a support for reforming catalysts. *Kinetics and Catalysis.* 2020;61(1): 130–136. https://doi.org/10.1134/s0023158420010097

25. Morterra G., Bolis C., Magnacca V. IR spectroscopic and microcalorimetric characterization of Lewis acid sites on (transition phase) Al$_2$O$_3$ using adsorbed CO. *Langmuir.* 1994;10(6): 1812–1824. https://doi.org/10.1021/la00018a033

26. Nechiporenko A. P. *Donor-acceptor properties of the surface of solid-phase systems. Indicator method.* St. Petersburg: Lan' Publ.; 2017. 284 p.

27. Sychev M. M., Cheremisina O. A. Relationship between the acid-base properties of the filler surface and the dielectric constant of polymer composite materials based on it. *ChemChemTech.* 2014;57(12): 67–71. (In Russ.). Available at: https://elibrary.ru/item.asp?id=23206884

28. Syrkov A. G., Silivanov M. O., Sychev M. M., Rozhkova N. N. Alteration of the acid-base properties of the oxidized surface of disperse aluminum during the adsorption of ammonium compounds and the antifriction effect. *Glass Physics and Chemistry.* 2018;44(5): 474–479. https://doi.org/10.1134/s1087659618050206

29. Syzrantsev V. V., Arymbaeva A. T., Zavjalov A. P., Zobov K. V. The nanofluids' viscosity prediction through particle-media interaction layer. *Materials Physics and Mechanics.* 2022; 48(3): 386-396. http://dx.doi.org/10.18149/MPM.4832022_9

30. Nomoev A. V., Vikulina L. S. Fractal dimension of the grain boundaries in ceramics with nanodispersed additions. *Technical Physics.* 2012;57(12): 1746–1748. https://doi.org/10.1134/s1063784212120225

31. Syzrantsev V. V., Larina T. V., Abzaev Yu. A., Paukstis E. A., Kostyukov A. I. Structural, surface and optical properties of nanoalumina produced by various

Condensed Matter and Interphases / Конденсированные среды и межфазные границы 2022;24(3): 369–378

V. V. Syzrantsev Analysis of the variations in the surface properties of SiO$_2$ and Al$_2$O$_3$ nanoparticles...

ways. *IOP Conference Series: Materials Science and Engineering/* 2020;1000(1): 012001. https://doi.org/10.1088/1757-899x/1000/1/012001

32. Syzrantsev V. V., Paukstis E. A., Larina T. V. Surface polymorphism of silica nanoparticles. *IOP Conference Series: Materials Science and Engineering.* 2020;1008(1): 012030. https://doi.org/10.1088/1757-899x/1008/1/012030

33. Bardakhanov S. P., Vasiljeva I. V., Mjakin S. V., Kuksanov N. K. Surface functionality features of nanosized silica obtained by electron beam evaporation at ambient pressure. *Advances in Materials Science and Engineering.* 2010;2010: 241695. https://doi.org/10.1155/2010/241695

34. Mewis J., Wagner N. J. Colloidal suspension rheology. Cambridge University Press; 2011. https://doi.org/10.1017/CBO9780511977978

Information about the authors

Vyacheslav V. Syzrantsev, Cand. Sci. (Phys.–Math.), Director of the Research Centre for Collective Use of Scientific Equipment "Nanotechnologies and Nanomaterials", Grozny State Oil Technical University (Grozny, Russian Federation).

https://orcid.org/0000-0001-5388-8224
vvveliga@mail.ru

Condensed Matter and Interphases

Original articles

Influence of the method of formation a nanosized CoFe₂O₄/nontronite composite on its structure and properties

E. V. Tomina[1,2✉], N. A. Khodosova[2], A. A. Sinelnikov[1], A. V. Zhabin[1], N. A. Kurkin[1], L. A. Novikova[2]

[1]*Voronezh State University,
1 Universitetskaya pl., Voronezh 394018, Russian Federation*

[2]*Voronezh State University of Forestry and Technologies named after G. F. Morozov
8 Timiryazeva str., Voronezh 394087, Russian Federation*

Abstract

The aim of the study was to establish the influence of the method of formation of the $CoFe_2O_4$/nontronite nanocomposite on its structure and properties.

Impurity-free nanoparticles of cobalt ferrite $CoFe_2O_4$ (XRD), close to spherical in shape, with a predominant particle fraction in the range of 8-20 nm (TEM), were synthesized using the citrate combustion method. The formation of the $CoFe_2O_4$/nontronite nanocomposite was carried out by two methods: mechanical mixing of available precursors followed by annealing and combustion of iron-cobalt citrate with the formation of spinel in the presence of nontronite in the reactor.

The $CoFe_2O_4$/nontronite nanocomposite formed by the first method is characterized by the decomposition of natural aluminosilicate aggregates and a higher sorption activity with respect to formaldehyde than the original clay mineral and spinel. The second method of composite formation leads to the formation of coarse-grained silica structures with worse sorption activity in comparison with natural aluminosilicate and $CoFe_2O_4$.

Keywords: Nanocomposite, Citrate combustion method, Cobalt ferrite, Aluminosilicate

✉ Elena V. Tomina, e-mail: tomina-ev@yandex.ru

Condensed Matter and Interphases / Конденсированные среды и межфазные границы   2022;24(3): 379–386

E. V. Tomina et al.   Influence of the method of formation a nanosized CoFe$_2$O$_4$/nontronite composite...

1. Introduction

Demand for nanosized ferrites as magnetic materials [1, 2], catalysts [3], and recently also as sorbents [4], is determined, first of all, by the possibility of controlling their magnetic, structural, catalytic, and sorption characteristics by changing the methods for synthesizing nanocrystals and doping them with various cations [5–9]. Catalysts based on nanosized ferrites are significantly cheaper than those based on platinum and rare earth metals, precursors for their manufacture are readily available, and synthesis methods are reproducible and scalable [1, 2]. The prospects of using MeFe$_2$O$_4$ (Me = Co, Ni, Zn, Cu) as catalysts and sorbents is also determined by their chemical stability in acidic environments, thermal and temporal stability, highly developed surface, high saturation magnetization and residual magnetization, which opens up the possibility of their extraction by magnetic separation methods [10, 11]. In the areas of catalysis and sorption, composite materials based on a less expensive dispersed matrix and nanosized ferrite as a magnetic component are often used. The clay mineral nontronite, which is a highly dispersed natural sorbent, was chosen as the basis for the composite. The structure of nontronite is represented by a three-layer package, including two layers of silicon-oxygen tetrahedra separated by one octahedral FeO$_6$ package, between which water molecules with exchangeable cations are located [12]. The chemical composition of nontronite is variable, the most probable formula is Fe$_2^{3+}$[Al$_x$Si$_{4-x}$O$_{10}$](OH)$_2$·Na$_{0.35}$(H$_2$O) [13]. The mineral from the Voronezh deposit (Russia), which, according to [14], contains 80% of nontronite and 10% of illite and kaolinite was used in the study.

The aim of the study was to establish the influence of the method of formation of the CoFe$_2$O$_4$/nontronite nanocomposite on its structure and properties.

2. Experimental

The synthesis of ferrite-spinel CoFe$_2$O$_4$ using the citrate combustion method was carried out according to [15]. The first approach to the formation of the CoFe$_2$O$_4$/nontronite nanocomposite consisted of mechanical mixing the available precursors followed by annealing (method 1). To obtain a composite material, 20 wt. % cobalt ferrite and 80 wt. % nontronite, a small amount of ethanol was added to the mixture and mixed thoroughly. The resulting paste was air dried for 2 h and annealed in a muffle furnace (SNOL 8.2/1100) to remove alcohol at 500°C for 1 h. The second method for the formation of a composite (method 2) consisted in preparing a solution of iron citrate and cobalt citrate according to [15]. Then nontronite with the weight required to form a composite with the composition 20% CoFe$_2$O$_4$/80% nontronite was added to the solution. The reaction mixture was heated until the water had completely evaporated. In this case, a grey-red paste, a mixture of nontronite and iron-cobalt citrate was formed. During further heating, the decomposition of iron-cobalt citrate occurred with the formation of cobalt ferrite:

$$Fe_2Co(C_6H_6O_7)_4 \xrightarrow{[O],t} CoFe_2O_4 + 24CO_2 \uparrow + 12H_2O \uparrow$$

The resulting dark grey insoluble powder was annealed in a muffle furnace (SNOL 8.2/1100) to remove water at 300°C for 1 h.

Phase composition of the cobalt ferrite and the CoFe$_2$O$_4$/nontronite composite were studied by X-ray diffractometry (XRD, Empyrean BV diffractometer with Cu anode (λ = 1.54060 nm)). The scanning was performed within a range of angles 2θ = 10–80° with a step of 0.0200. The JCPDC database [16] was used to identify the phases. The size of the coherent scattering regions of the CoFe$_2$O$_4$ particles based on the broadening of X-ray diffraction lines calculated using the Debye-Scherrer formula (1) [17]:

$$D_{hkl} = \frac{kx\lambda}{\beta_{hkl} \times \cos\theta}, \tag{1}$$

where D_{hkl} is the average particle size, Å, k is the correction factor (for spherical particles k = 0.9), λ is the X-ray tube wavelength, θ is the position of the peak maximum, deg., β_{hkl} is the intrinsic physical broadening of the diffraction maximum, rad.

The size and morphology of the composite particles synthesized by different methods was determined based on the data of transmission electron microscopy (TEM, transmission electron microscope CarlZeiss Libra-120). The particle size distribution histogram was plotted using the ImageJ program version 1.53k.

Condensed Matter and Interphases / Конденсированные среды и межфазные границы   2022;24(3): 379–386

E. V. Tomina et al.   Influence of the method of formation a nanosized CoFe₂O₄/nontronite composite...

The sorption capacity of natural nontronite, pure $CoFe_2O_4$ and $CoFe_2O_4$/nontronite nanocomposite was tested in relation to formaldehyde, a toxicant of the 2nd hazard class [18]. For the determination of the sorption capacity 0.025 dm³ formaldehyde solution were added to 0.5 g of the composite, the static sorption time was 2 h. After the end of sorption, the solution was filtered. The content of formaldehyde in the filtrate was determined using the sulphite method. The relative error of determination was 1–3%.

3. Results and discussion

According to XRD data (Fig. 1), the cobalt ferrite sample synthesized by the citrate method is completely single-phase. All reflections in the diffraction pattern corresponded to that of cobalt ferrite with a $CoFe_2O_4$ spinel structure [16].

According to TEM data (Fig. 2), the cobalt ferrite particles had a shape close to spherical, and agglomeration was clearly expressed. The particle size was in the range from 6 to 34 nm. The predominant particle size fraction was in the range of 8–24 nm.

Nontronite belongs to layered silicates of the group of clay-like smectite minerals [19]. Nontronite is usually found in the form of finely dispersed scaly, vermiform, radial-spherical mineral aggregates, which was confirmed by the TEM data (Fig. 3).

Nontronite aggregates were characterized by layered formations up to 100 nm wide, elongated

in one direction (Fig. 3a). The dark-field image confirmed the ultrafine nature of nontronite mineral aggregates. At the same time, rounded particles with a size of about 10–20 nm could be seen in the images, which was probably a consequence of the insignificant decomposition of nontronite microaggregates into individual flakes as the result of the dispersion during sample preparation.

The $CoFe_2O_4$/nontronite nanocomposite, synthesized as a mechanical mixture of available precursors, was presented by separate round-shaped particles up to 20 nm in size, probably predominantly crystalline. As can be seen from the TEM image, there were no clay particles of the natural layered shape characteristic of nontronite, which probably was associated with the decomposition of natural aluminosilicate aggregates into individual flakes during nanocomposite annealing. Insignificant agglomeration of particles was expressed. The particle size of the composite did not exceed 20 nm. The predominant particle size fraction was in the size range of 6–12 nm.

The general scheme of dehydration of smectites during heating according to [20] is as follows: interlayer water is almost completely released at 250–300 °C, then a slow release of constitutional water (OH-groups) starts, which ends completely at T ~ 750 °C. The process of dehydration is partially reversible, until it is fully completed. Complete destruction of the structure usually
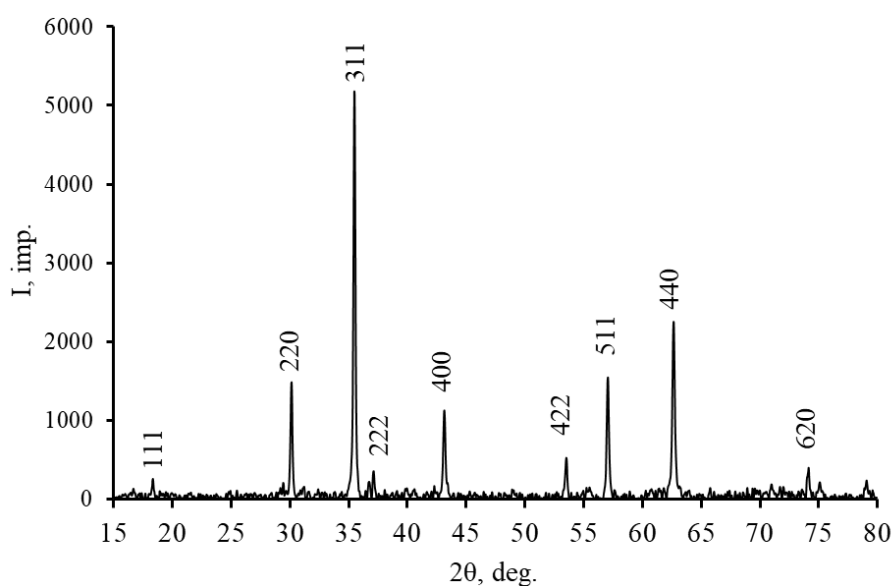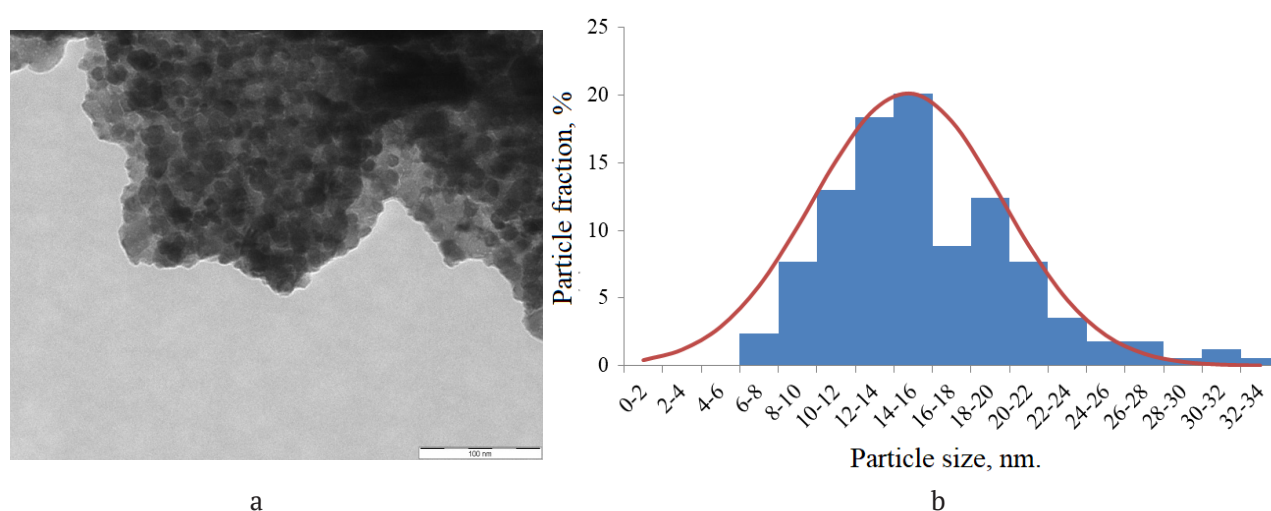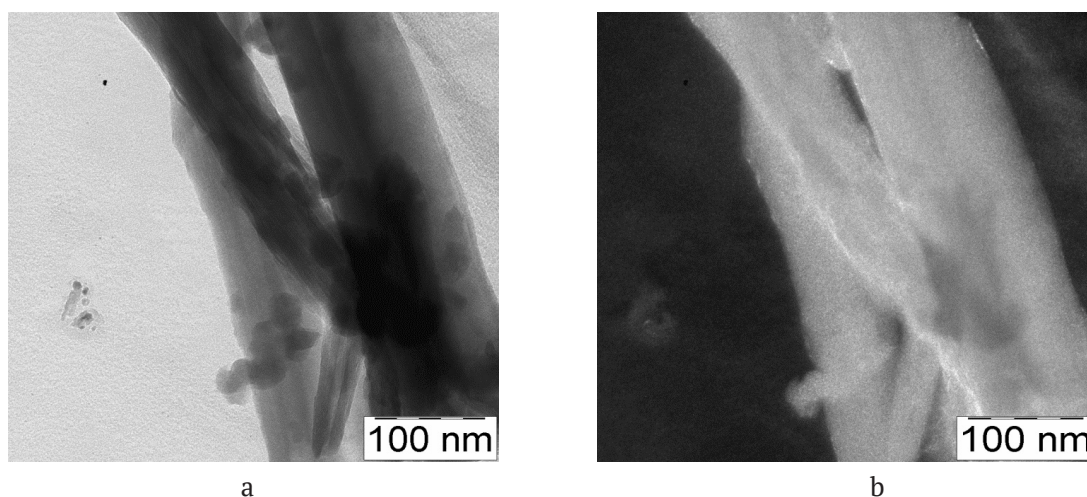

Fig. 1. X-ray diffraction pattern of a $CoFe_2O_4$ sample synthesized by the citrate method

Condensed Matter and Interphases / Конденсированные среды и межфазные границы   2022;24(3): 379–386

E. V. Tomina et al.   Influence of the method of formation a nanosized $CoFe_2O_4$/nontronite composite...

a   b

Fig. 2. TEM image (a) and particle size distribution histogram (b) of $CoFe_2O_4$
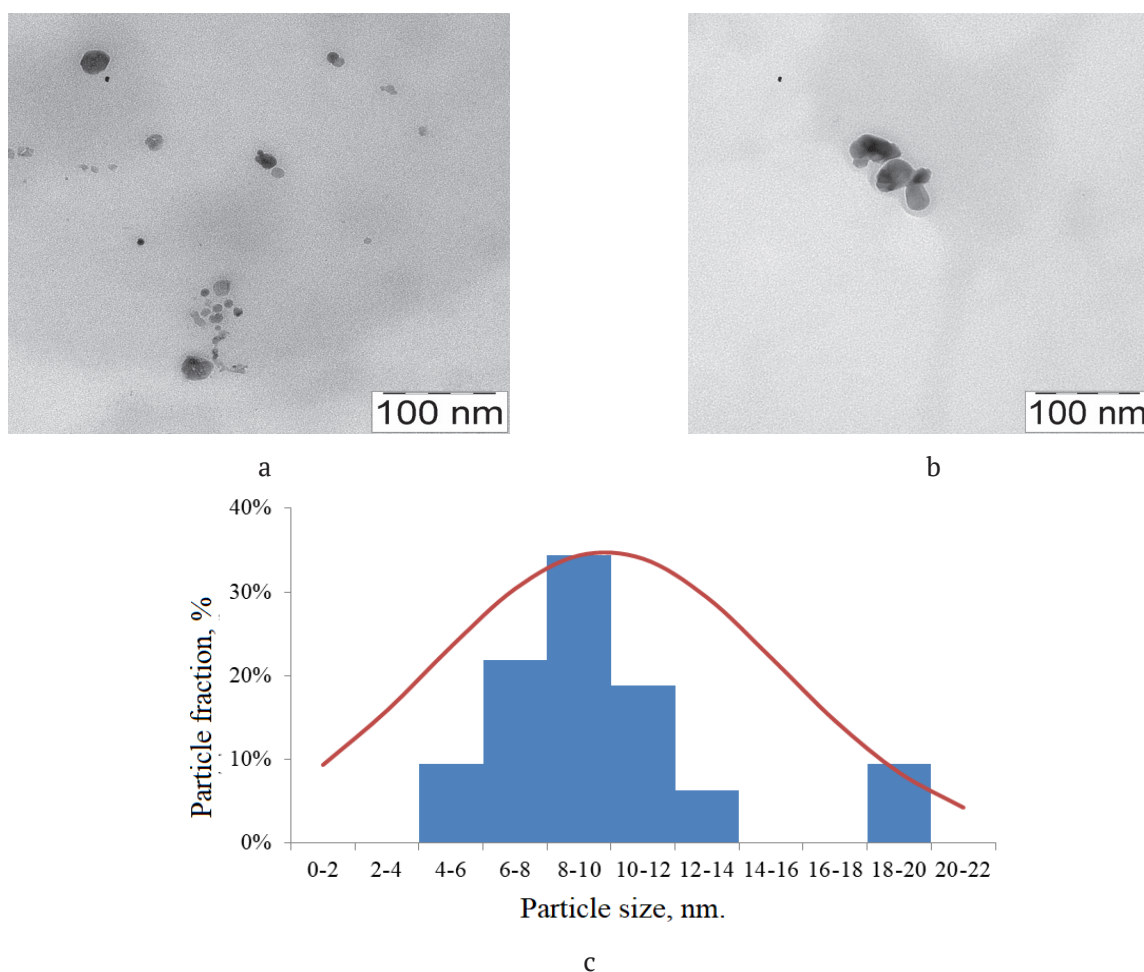

a   b

Fig. 3. TEM image of nontronite (a) and dark-field image (b)

occurs in the range of 800–900°C. Later studies [21] showed that the process of smectite dehydration is more complex. The transition boundaries are vaguer and do not have clear and stable values on the temperature scale, the transition stages are determined by temperature intervals. For nontronite, dehydroxylation starts already in the range of 400–500°C. At the same time the layered structure is preserved, however, the interlayer spaces are destroyed, the surface area and porosity are reduced. The layered silicate completely loses water and contracts with the formation of micaceous structure with heat treatment at 550 °C. X-ray diffraction patterns of dehydroxylates were quite blurred, XRD study demonstrated the gradual degradation of minerals.
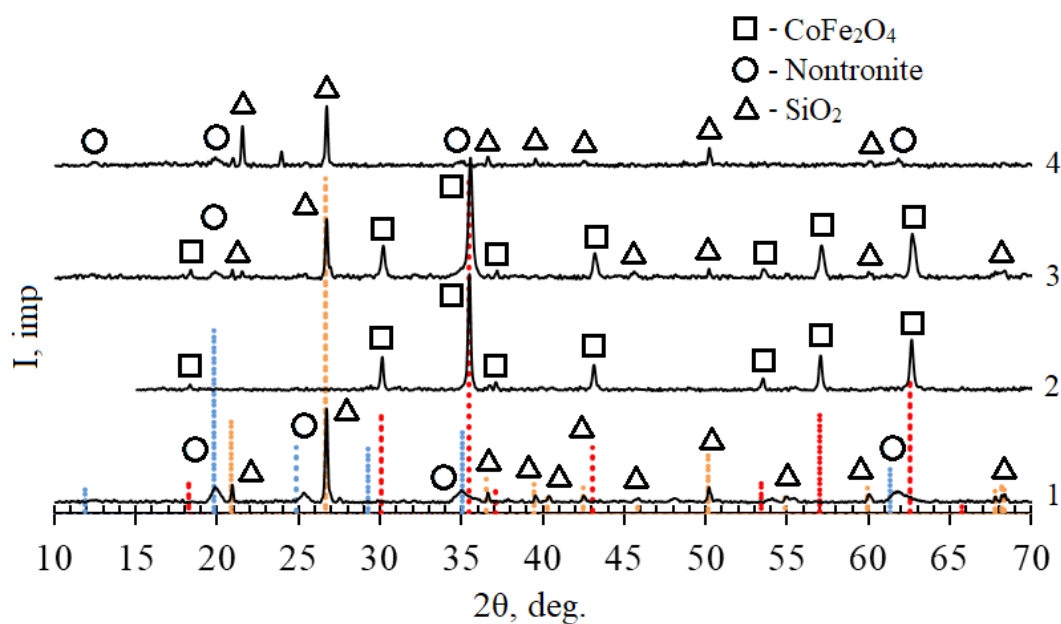
On the diffraction pattern of the $CoFe_2O_4$/nontronite nanocomposite formed by method 1 (Fig. 5, diffraction pattern 3), all the main

reflections of the cobalt spinel were identified (Fig. 5, diffraction pattern 2). Despite the fact that the conditions for recording the diffraction patterns of the composite did not allow to identify one of the main reflections of nontronite in the region of 5°, the remaining reflections can be identified according to the JCPDC database (Fig. 5, diffraction pattern 1), but their relative intensity was significantly reduced. This finding indicates a general increase in the defectiveness of the structure and dispersion of particles and may be associated with the destruction of aggregates of natural aluminosilicate, the loss of water due to the dehydration processes and partial dehydroxylation.

A completely different diffraction pattern was characteristic of the nanocomposite formed by method 2 (Fig. 5, diffraction pattern 4). The absence of cobalt ferrite reflections indicated that the spinel formed during the combustion of

Condensed Matter and Interphases / Конденсированные среды и межфазные границы   2022;24(3): 379–386

E. V. Tomina et al.   Influence of the method of formation a nanosized CoFe₂O₄/nontronite composite…

Fig 4. TEM image of a CoFe$_2$O$_4$/nontronite nanocomposite synthesized by method 1, (a), (b) and particle size distribution histogram (c)

Fig. 5. X-ray diffraction pattern of samples of nontronite (1), spinel CoFe$_2$O$_4$ (2), nanocomposite CoFe$_2$O$_4$/nontronite, method 1 (3), nanocomposite CoFe$_2$O$_4$/nontronite, method 2 (4)

Condensed Matter and Interphases / Конденсированные среды и межфазные границы   2022;24(3): 379–386

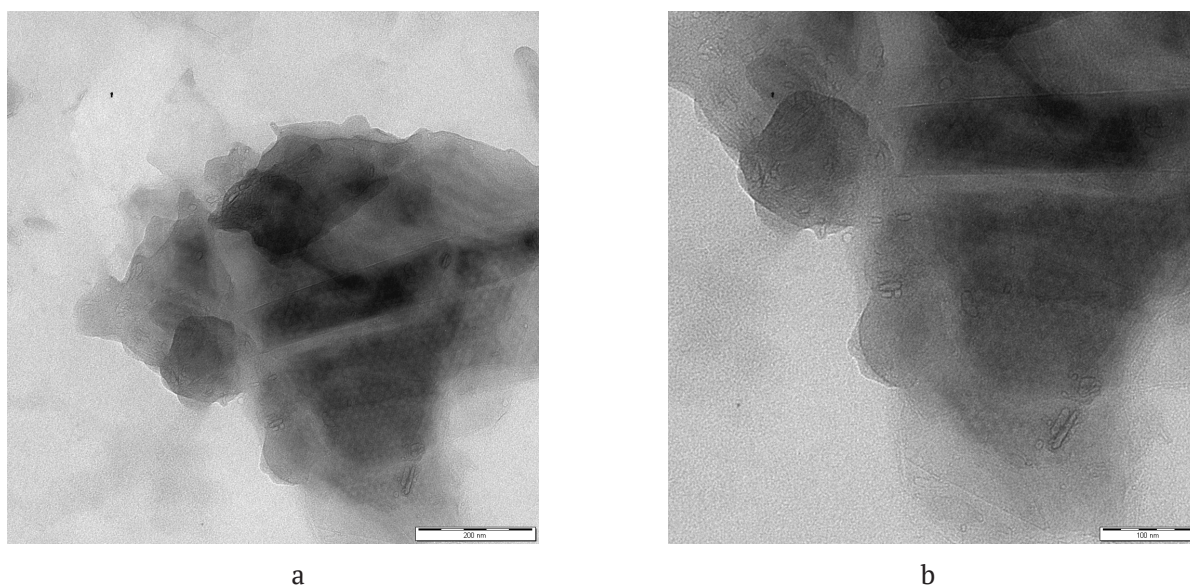E. V. Tomina et al.   Influence of the method of formation a nanosized CoFe₂O₄/nontronite composite...

the polymer gel was predominantly in the X-ray amorphous state. At the same time, reflections of SiO_2 in the form of quartz, which were also present in the diffraction pattern of natural nontronite, were identified. However, in the region of the diffraction angle of 22°, according to ICDD PDF, the most intense reflection of cristobalite was identified. This reflection was absent in the diffraction patterns of both the natural aluminosilicate and $CoFe_2O_4$/nontronite composite synthesized by method 1. Probably, the transition of quartz to cristobalite occurs during the combustion of gel-like iron-cobalt citrate under strongly non equilibrium conditions. The possibility of forming a metastable cristobalite at relatively low temperatures outside the classical equilibrium transition scheme quartz - tridymite - cristobalite was also emphasized in [22]. During further heating, metacristobalite transformed into tridymite and then into stable cristobalite.

On the TEM image (Fig. 6) of the $CoFe_2O_4$/nontronite nanocomposite synthesized by method 2, the overlapping of fairly large flat-crystalline objects up to 400 nm in size can be seen. This was a consequence of the dehydroxylation of nontronite and the formation of a micaceous structure. High iron content, according to [23], is the reason for the relatively low thermal stability of nontronite. A peculiar net structure from chequered holes can be seen at the bottom of Fig. 6b. Such formation is characteristic of the skeletal remains of some species of diatoms. On the

image for Fig. 6a, which was reordered at a lower magnification, parallel dark stripes are visible in its upper right corner. These strips represent a fragment of the skeleton of another diatom species. Colloidal solutions (sols) of silica serve as food for diatoms and it contributes to the perfect preservation of skeletons of these organisms in a fossil state even in the most ancient deposits.

Pure nontronite, cobalt spinel $CoFe_2O_4$ and composites formed by methods 1 and 2 were tested as formaldehyde sorbents (Table 1). Cobalt ferrite had the weakest sorption activity towards formaldehyde, determined based on the value of specific adsorption (a = 13 mg/g). For natural nontronite, the adsorption capacity is higher - 27 mg/g. Formaldehyde adsorption on CoFe $CoFe_2O_4$/nontronite composite synthesized by method 1 exceeded that on cobalt ferrite and pure nontronite (a = 30 mg/g). For the $CoFe_2O_4$/nontronite formed by method 2, the value of specific sorption at all formaldehyde concentrations was lower than that of nontronite and composite synthesized by method 1. This was caused, first of all, by the dehydroxylation of nontronite during the synthesis of the composite, which led to the destruction of the octahedral layer and a strong decrease in porosity.

Thus, the first method of forming a composite based on nontronite with the addition of cobalt ferrite opens up prospects for obtaining economically efficient sorbents sensitive to an external magnetic field.

a   b

Fig. 6. TEM image of the CoFe₂O₄/nontronite nanocomposite synthesized by method 2

Condensed Matter and Interphases / Конденсированные среды и межфазные границы   2022;24(3): 379–386

E. V. Tomina et al.   Influence of the method of formation a nanosized $CoFe_2O_4$/nontronite composite...

Table 1. Sorption capacity of nontronite, cobalt ferrite, and composites based on them with respect to formaldehyde solutions of various concentrations

Sample	Specific adsorption, mg/g			
	0.038 M	0.102 M	0.201 M	0.388 M
Nontronite	3.15	14.2	20.8	27.0
$CoFe_2O_4$	4.2	10.5	11.2	13.2
$CoFe_2O_4$/Nontronite method 1	4.1	15.6	22.6	30
$CoFe_2O_4$/Nontronite method 2	4.0	12.0	19.5	22.5

4. Conclusions

The impurity-free cobalt ferrite nanopowder with a predominant particle fraction in the range of 8–24 nm was synthesized using the citrate combustion method. Two methods for the formation of 20 % $CoFe_2O_4$/80 % nontronite nanocomposite were proposed for the production of inexpensive magnetically active sorbent. The effect of synthesis methods on the composition, structure of the composite, and sorption activity with respect to formaldehyde solutions of various concentrations has been established. The $CoFe_2O_4$/nontronite nanocomposite formed by mechanical mixing of available precursors followed by annealing, despite the destruction of submicroaggregates of natural nontronite and partial dehydroxylation, is a more effective sorbent compared to the original clay mineral. The formation of a composite by combustion of iron-cobalt citrate in the presence of nontronite led to the formation of coarse-grained silica structures with worse sorption activity compared to natural aluminosilicate.

Author contributions

All authors made an equivalent contribution to the preparation of the publication.

Conflict of interests

The authors declare that they have no known competing financial interests or personal relationships that could have influenced the work reported in this paper.

References

1. Kefeni K. K., Msagati A. M., Mamba B. B. Ferrite nanoparticles: synthesis, characterisation and applications in electronic device. *Materials Science and Engineering B.* 2017;215: 37–55. http://dx.doi.org/10.1016/j.mseb.2016.11.002

2. Tomina E. V., Mittova I. Y., Stekleneva O. V., Kurkin N. A., Perov N. S., Alekhina Y. A. Microwave synthesis and magnetic properties of bismuth ferrite nanopowder doped with cobalt. *Russian Chemical Bulletin.* 2020;69(5): 941–946. https://doi.org/10.1007/s11172-020-2852-1

3. Leila Roshanfekr Rad, Babak Farshi Ghazani, Mohammad Irani, Mohammad Sadegh Sayyafan, Ismaeil Haririan. Comparison study of phenol degradation using cobalt ferrite nanoparticles synthesized by hydrothermal and microwave methods. *Desalination and Water Treatment.* 2014;56(12): 1–10. https://doi.org/10.1080/19443994.2014.977960

4. Tkachenko I. A., Panasenko A. E., Odinokov M. M., Marchenko Y. V. Magnetoactive composite sorbents $CoFe_2O_4$–SiO_2 *Russian Journal of Inorganic Chemistry.* 2020;65(8): 1142–1149. https://doi.org/10.1134/S0036023620080173

5. Mittova I. Ya., Perov N. S., Tomina E. V., Pan'kov V. V., Sladkopevtsev B. V. Multiferroic nanocrystals and diluted magnetic semiconductorsas a base for designing magnetic materials. *Inorganic Materials.* 2021;57(13): 22–48. https://doi.org/10.1134/S0020168521130033

6. Rashidi S., Ataie A. One-step synthesis of $CoFe_2O_4$ nano-particles by mechanical alloying. *Advanced Materials Research.* 2014;829: P. 747–751. https://doi.org/10.4028/www.scientific.net/AMR.829.747

7. Agú U. A., Oliva M. I., Marchetti S. G., Heredia A. C., Casuscelli S. G., Crivello M. E. Synthesis and characterization of a mixture of $CoFe_2O_4$ and $MgFe_2O_4$ from layered double hydroxides: band gap energy and magnetic responses. *Journal of Magnetism and Magnetic Materials.* 2014;369: 249–259. https://doi.org/10.1016/j.jmmm.2014.06.046

8. Rao K. S., Nayakulu S. V. R., Varma M. C., Choudary G. S. V. R. K., Rao K. H. Controlled phase evolution and the occurrence of single domain $CoFe_2O_4$ nanoparticles synthesized by PVA assisted sol-gel method. *Journal of Magnetism and Magnetic Materials.* 2018;451(1): 602–608. https://doi.org/10.1016/j.jmmm.2017.11.069

9. Tomina E. V., Pavlenko A. A., Kurkin N. A. Synthesis of bismuth ferrite nanopowder doped with erbium ions. *Condensed Matter and Interphases.* 2021;23(1): 93–100. https://doi.org/10.17308/kcmf.2021.23/3309

Condensed Matter and Interphases / Конденсированные среды и межфазные границы   2022;24(3): 379–386

E. V. Tomina et al.   Influence of the method of formation a nanosized CoFe$_2$O$_4$/nontronite composite...

10. Rehman F., Sayed M., Khan J. A., Shah L. A., Shah N. S., Khan H. M., Khattak R. Degradation of crystal violet dye by fenton and photo-fenton oxidation processes. *Zeitschrift Fur Physikalische Chemie*. 2018;232(12): 1771–1786. https://doi.org/10.1515/zpch-2017-1099

11. Indu Sharma Somnath, Kotnala R. K., Singh M., Kumar Arun, Dhiman Pooja, Singh Virender Pratap, Verma Kartikey, Kumar Gagan. Structural magnetic and mössbauer studies of Nd-doped Mg-Mn ferrite nanoparticles. *Journal of Magnetism and Magnetic Materials*. 2017;444: 77–86. https://doi.org/10.1016/j.jmmm.2017.08.017

12. Tsipursky S. I., Drits V. A., Chekin S. S. Revealing the structural ordering of nontronites by the oblique texture electron diffraction method. *Proceedings of the Academy of Sciences of the USSR, geological series*. 1978;10: 105-113. (In Russ.)

13. Al-Ahmed A. (Ed.). Advanced applications of micro and nano clay II: synthetic polymer composites. *In: Materials Research Foundations*. Millersville, PA: Material Research Forum LLC; 2022. 290 p. https://doi.org/10.21741/9781644902035

14. Bel'chinskaya L. I., Khodosova N. A., Novikova L. A., Strel'nikova O. Y., Roessner F., Petukhova G. A., Zhabin A. V. Regulation of sorption processes in natural nanoporous aluminosilicates. 2. Determination of the ratio between active sites *Protection of Metals and Physical Chemistry of Surfaces*. 2016:52(4); 599–606. https://doi.org/10.1134/s2070205116040055

15. Khodosova N. A., Tomina E. V., Belchinskaya L. I., Zhabin A. V., Kurkin N. A., Volkov, A. S. Physical and chemical characteristics of the nanocomposite nontronite/CoFe$_2$O$_4$ sorbent. *Sorbtsionnye i khromatograficheskie protsessy*. 2021:21(4); 520–528. (In Russ., abstract in Eng.). https://doi.org/10.17308/sorpchrom.2021.21/3636

16. JCPDC PCPDFWIN: A Windows retrieval/display program for accessing the ICDD PDF – 2 Data Base, International Centre for Diffraction Data, 1997.

17. Brandon D., Kaplan W.D. *Microstructural characterization of materials*. John Wiley & Sons Ltd; 1999. 409 p. https://doi.org/10.1002/9780470727133

18. The list of substances, products, production processes, domestic and natural factors that are carcinogenic to humans. GN 1.1.029-98. Moscow: Goskomsanepidnadzor Russia; 1995. 17 p.

19. Stefan W: *The Great Reference Book of Lapis Minerals. All minerals from A to Z and their properties. 5th edition completely revised and enlarged*. Weise, Munich 2008, ISBN 978-3-921656-70-9.

20. Nurizyanov R. M. *Geology minerals and rocks*. Almetyevsk: Almetyevsk State Oil Institute Publ., 2012. 84 p. (In Russ.)

21. Bergaya F., Lagaly G. *Handbook of Clay Science. Developments in Clay Science 5*. Amsterdam: Elsevier; 2013. 787 p. Available at: https://www.sciencedirect.com/bookseries/developments-in-clay-science/vol/5/suppl/C

22. Gorshkov V. S., Savelyev V. G., Fedorov N. F. *Physical chemistry of silicates and other refractory compounds*. Moscow: Vysshaya shkola Publ.; 1988. 400 p.

23. Krupskaya V. V., Zakusin S. V., Tyupina E. A., Dorzhieva O. V., Chernov M. S., Bychkova Ya. V. Transformation of structure and adsorption properties of montmorillonite under thermochemical treatment. *Geochemistry International*. 2019;57(3): 314-330. https://doi.org/10.1134/s0016702919030066

Information about the authors

Elena V. Tomina, Dr. Sci. (Chem.), Head of the Department of Chemistry, Voronezh State University of Forestry and Technologies named after G. F. Morozov (Voronezh, Russian Federation).

tomina-e-v@yandex.ru

https://orcid.org/0000-0002-5222-0756

Nataliya A. Khodosova, Cand. Sci. (Chem.), Associate Professor at the Department of Chemistry, Voronezh State University of Forestry and Technologies named after G. F. Morozov (Voronezh, Russian Federation).

nhodosova@mail.ru

https://orcid.org/0000-0002-2809-717X

Alexander A. Sinelnikov, Cand. Sci. (Phys.–Math.), Head of Laboratory, Department of Materials Science and Industry of Nanosystems, Voronezh State University (Voronezh, Russian Federation).

rnileme@mail.ru

https://orcid.org/0000-0002-0549-4615

Aleksandr V. Zhabin, Cand. Sci. (Geologo-Mineralogical), Associate Professor at the Department of General Geology and Geodynamics, Voronezh State University (Voronezh, Russian Federation).

zhabin01@gmail.com

https://orcid.org/0000-0002-3844-6302

Nikolay A. Kurkin, PhD student, Department of Materials Science and Industry of Nanosystems, Voronezh State University (Voronezh, Russian Federation).

kurkin.nik@yandex.ru

https://orcid.org/0000-0002-0468-8207

Lyudmila A. Novikova, Cand. Sci. (Chem.), Associate Professor at the Department of Chemistry, Voronezh State University of Forestry and Technologies named after G. F. Morozov (Voronezh, Russian Federation).

yonk@mail.ru

https://orcid.org/0000-0002-1635-7739

Original articles

Up-conversion luminescence in mixed crystals $BaY_{1.8}Lu_{0.2}F_8$ doped with Er^{3+} ions excited at 1532 nm

A. S. Nizamutdinov[1]✉, S. A. Bukarev[2], S. V. Gushchin[2], A. A. Shavelev[1], M. A. Marisov[1,3], A. A. Shakirov[1], A. G. Kiiamov[1], A. V. Astrakhantseva[1], A. A. Lyapin[2]

[1]Kazan Federal University,
18 Kremlevskaja str., Kazan 420008, Russian Federation

[2]National Research Mordovia State University,
68 Bolshevitskaya str., Saransk 430005, Russia

[3]Zavoisky Physical-Technical Institute, FRC Kazan Scientific Center of the Russian Academy of Sciences,
10/7 Sibirsky av., Kazan 420029, Russian Federation

Abstract

Increasing the efficiency of upconversion luminophores is an important problem in materials science. Here we report on approach of use of disordered crystals namely solid solutions $BaY_{1.8}Lu_{0.2}F_8$ doped with Er^{3+} ions to improve spectral characteristics and efficiency of upconversion from near IR spectral region. It is shown that investigated compound provide up to 9.4% of external energy yield of the up-conversion luminescence at an excitation power density of 6 W/cm² at 1532 nm for the 10 at.% of Er^{3+} doping. Also the investigated crystals of $BaY_{1.8}Lu_{0.2}F_8$:Er^{3+} allow the control of the CCT parameter in the range of 2384–5149 K by changing the concentration and power density of the excitation. Advantages revealed in this work for crystalline compounds $BaY_{1.8}Lu_{0.2}F_8$:Er^{3+} such as wide absorption bands in the infrared spectral range, a high external energy yield, and a controllable distribution of intensity of luminescence bands makes them prospective to improve the efficiency of double-sided solar cells.

Keywords: Upconversion luminescence, External energy yield, Correlated color temperatures, Er^{3+}, Fluoride crystals, Solid solutions

✉ A. S. Nizamutdinov, e-mail: anizamutdinov@mail.ru

Condensed Matter and Interphases / Конденсированные среды и межфазные границы   2022;24(3): 387–396

A. S. Nizamutdinov et al.   Up-conversion luminescence in mixed crystals BaY$_{1.8}$Lu$_{0.2}$F$_8$ doped with Er^{3+} ions...

1. Introduction

Up-conversion materials doped with rare earth ions are widely used for various practical applications. These materials are used as markers to detect counterfeit products, laser radiation visualizers, solid-state lasers, biological sensors, and in solar panels to increase their efficiency. Fluoride matrices are characterized by large band gap and low energy spectrum of phonons which provides low level of nonradiative losses of excited population of levels and make them efficient in luminescent and upconversion applications [1–4].

One of the approaches to increase the efficiency of luminophores is to investigate disordered crystal lattices. First, such lattices may provide broadening of spectral lines which leads to increase of energy transfer efficiency between impurity ions and upconversion luminescence efficiency. Second, distortions of crystal lattice may lead to increase of electronic transitions probabilities which are relatively low for forbidden intraconfigurational *f-f* transitions of rare-earth ions. Despite low probabilities the *f-f* transitions of rare earth ions are widely used since they possess spectral lines in a variety of spectral ranges. One of the most popular luminescent ions for upconversion investigation is Er^{3+} ion [5,6]. Due to relatively large lifetime of excited states and significant manifestation of cross-relaxation processes it provide efficient upconversion with emitting photons of energy of two and higher photons of excitation radiation [7]. High efficiency of upconversion process in Er^{3+}-doped fluorides make it possible to achieve the laser oscillation at wavelengths of about 0.55 μm (the $^4S_{3/2}$–$^4I_{15/2}$ transition) when pumping at 980 nm [8]. Also the record value for internal photoluminescence quantum yield for upconversion luminescence was measured for Er^{3+}–Yb^{3+} ion pair [9, 10]. More interesting that Er^{3+} ions allow excitation of anti-stokes luminescence under pumping at 1530 nm where intensity of the sun light is still significant and photo effect from crystalline silicon is already absent. As it is known from literature the efficiency of Er^{3+} upconversion luminescence excited at 1530 nm can be even higher than that for 980 nm excitation most

probably due to longer lifetime of $^4I_{13/2}$ state [11] and it can provide efficient energy harvesting due to stronger absorption cross-section at 1.5 micrometers spectral range [11,12]. For example, the microcrystalline powder of β-phase NaYF$_4$ with 20% of Er^{3+} have shown 0.34% of external quantum efficiency at an irradiance of 1090 W·m^{-2} (0.03 cm^2·W^{-1}) at 1522 nm, polycrystalline samples of the same NaYF$_4$: Er^{3+} (20%) have provided 2.5% being incorporated into an optically transparent (refractive index similar to that of the phosphors) acrylic adhesive medium (weight ratio 0.4:0.6) [13] and 6.5% being incorporated into perfluorocyclobutane (PFCB) host matrix [14] external quantum efficiency when irradiated at 1523 nm.

The material under investigation is from family of BaY$_2$F$_8$ fluoride matrices which are characterized by monoclinic structure and significant vibrational broadening. It is already known that it provides significant efficiency of conversion from IR spectral range, for example, the external quantum efficiency (EQE) at 1557 nm measured values of 6.5% and 4.1% have been reached under 8.5 W cm^{-2} power density illumination for the 30% Er^{3+} and 20% Er^{3+} samples, respectively [15]. We studied the upconversion luminescence of mixed crystals BaY$_{1.8}$Lu$_{0.2}$F$_8$ doped with Er^{3+} ions upon excitation by infrared laser radiation at a wavelength of 1532 nm to the $^4I_{13/2}$ energy level of Er^{3+} ions.

Aim of this work is to study the efficiency of light conversion in BaY$_{1.8}$Lu$_{0.2}$F$_8$:Er crystals from the spectral range of photon energies lower than perovskite and silicon photoeffect maxima to near IR and visible spectral ranges. Namely, the spectral characteristics of up-conversion luminescence and its efficiency under laser excitation to the $^4I_{13/2}$ energy level of Er^{3+} ions have been investigated.

2. Research methods and characterization of materials

Single crystals of BaY$_{1.8}$Lu$_{0.2}$F$_8$:Er (1 at.%, 5 at.%, 10 at.%, 20 at.%, 30 at.%) were grown in Kazan Federal University by the Bridgman method, which consists in moving the crucible with the melt from the high-temperature zone to the lower-temperature. Crystal growth was implemented in graphite crucibles.

Condensed Matter and Interphases / Конденсированные среды и межфазные границы   2022;24(3): 387–396

A. S. Nizamutdinov et al.   Up-conversion luminescence in mixed crystals BaY$_{1.8}$Lu$_{0.2}$F$_8$ doped with Er^{3+} ions...

The absorption spectra of Er^{3+} ions in the studied fluoride crystals were registered in a Perkin Elmer Lambda 950 double-beam spectrophotometer with a double monochromator. The upconversion luminescence spectra of Er^{3+} ions were registered using spectroradiometer OL-770 VIS/NIR (slit spectral width 100 μm). To excite the upconversion luminescence of Er^{3+} ions to the $^4I_{13/2}$ level, we used a CW fiber laser with λ$_{rad}$~1532 nm. The diameter of the laser beam incident on the sample was measured using a BEAMAGE-3.0 beam analyzer (GenTec-EO) and appeared to be 420±10 μm.

To calculate the chromaticity coordinates and correlated color temperatures (CCT), the CIE 1931 (X, Y) standard colorimetric system was used.

To determine the internal energy yield (B$_{in}$) of up-conversion luminescence, an experimental setup was elaborated based on OL IS-670-LED integrating sphere and OL-770 VIS/NIR spectroradiometer. Continuous laser radiation after a quartz achromatic depolarizer was focused onto a sample located at the center of the sphere. The spectral power of the upconversion luminescence was measured using a spectroradiometer. The integrating sphere and the spectroradiometer were connected by an optical fiber. The experimental setup was corrected for spectral sensitivity using a Gooch & Housego reference halogen lamp with a known spectral output power. The power of the laser radiation incident on the sample was measured using a power meter based on an integrating sphere with high sensitivity.

The external energy yield (B$_{ex}$) of up-conversion luminescence was determined as the ratio of the power of upconversion luminescence in a certain spectral range to the power of laser radiation incident on the sample.

All measurements were performed at room temperature.

3. Experimental results

3.1. Up-conversion luminescence of BaY$_{1.8}$Lu$_{0.2}$F$_8$:Er crystals

In accordance with X-ray powder diffraction patterns (Fig. 1), for the synthesized BaY$_{1.8}$Lu$_{0.2}$F$_8$ crystals, the samples represented the same phase as their homologue BaY$_2$F$_8$, belonging to the monoclinic system, space group C12/m1 [16]. The differences in the position of the reflections are very small, although for the BaY$_{1.8}$Lu$_{0.2}$F$_8$ mixed crystal they are slightly shifted to the region of small angles.
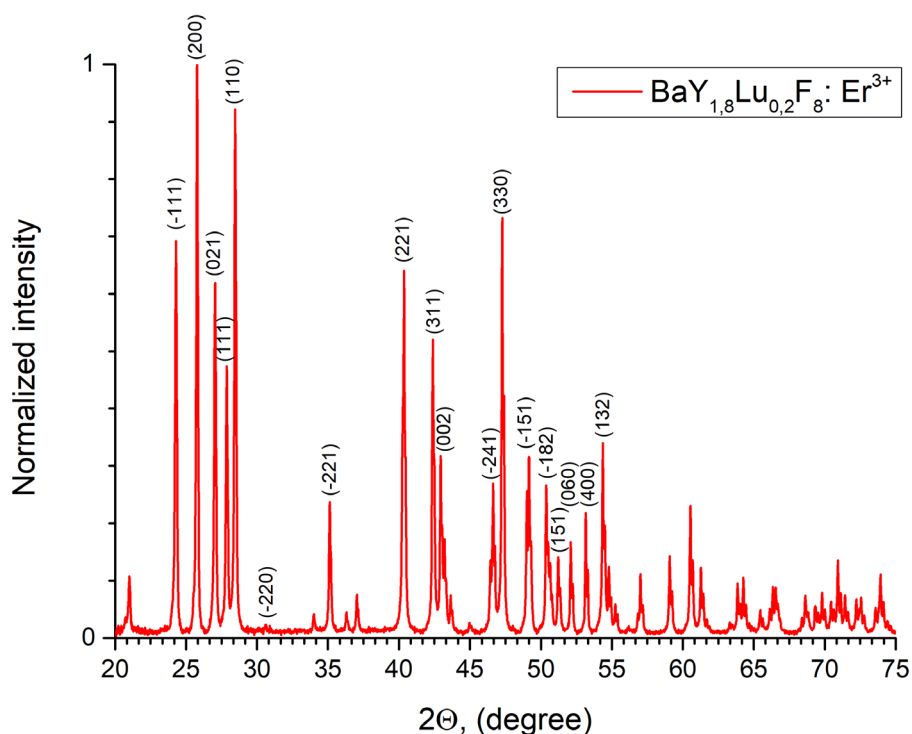

**Fig. 1.** X-ray pattern of the crystalline compound BaY$_{1.8}$Lu$_{0.2}$F$_8$:Er^{3+}

Condensed Matter and Interphases / Конденсированные среды и межфазные границы   2022;24(3): 387–396

A. S. Nizamutdinov et al.   Up-conversion luminescence in mixed crystals BaY$_{1.8}$Lu$_{0.2}$F$_8$ doped with Er^{3+} ions...

The absorption spectrum of the BaY$_{1.8}$Lu$_{0.2}$F$_8$:Er^{3+} crystal for the $^4I_{15/2} \rightarrow ^4I_{13/2}$ electronic transition of Er^{3+} ions in the spectral range 1400–1700 nm is shown at the Fig. 2 together with the spectrum of solar radiation above the atmosphere (the spectrum of the Sun AM0) and at the surface (the spectrum of the Sun AM1.5) of Earth. It can be seen that the absorption band of the BaY$_{1.8}$Lu$_{0.2}$F$_8$:Er^{3+} crystal overlaps well with the solar radiation spectrum. The dotted arrow in the spectrum also shows the wavelength of excitation of upconversion luminescence to the $^4I_{13/2}$ level of Er^{3+} ions in our investigation ($\lambda_{ex} \sim 1532$ nm).

The up-conversion luminescence spectra of the BaY$_{1.8}$Lu$_{0.2}$F$_8$:Er (20 at.%) crystal is shown at the Fig. 3, it consist of the electronic transitions $^2H_{9/2} \rightarrow ^4I_{15/2}$, $^2H_{11/2} \rightarrow ^4I_{15/2}$, $^4S_{3/2} \rightarrow ^4I_{15/2}$, $^4F_{9/2} \rightarrow ^4I_{15/2}$, $^4I_{9/2} \rightarrow ^4I_{15/2}$, $^4I_{11/2} \rightarrow ^4I_{15/2}$ of Er^{3+} ions. The highest luminescence intensity is observed for the band in the region of 1000 nm corresponding to the $^4I_{11/2} \rightarrow ^4I_{15/2}$ of Er^{3+} ions.

The evolution of luminescence spectra with power density of the 1532 nm laser excitation is shown at the Fig. 4. The intensity of anti-stokes luminescence rises with the excitation power and changes in the form of the spectra are observed in
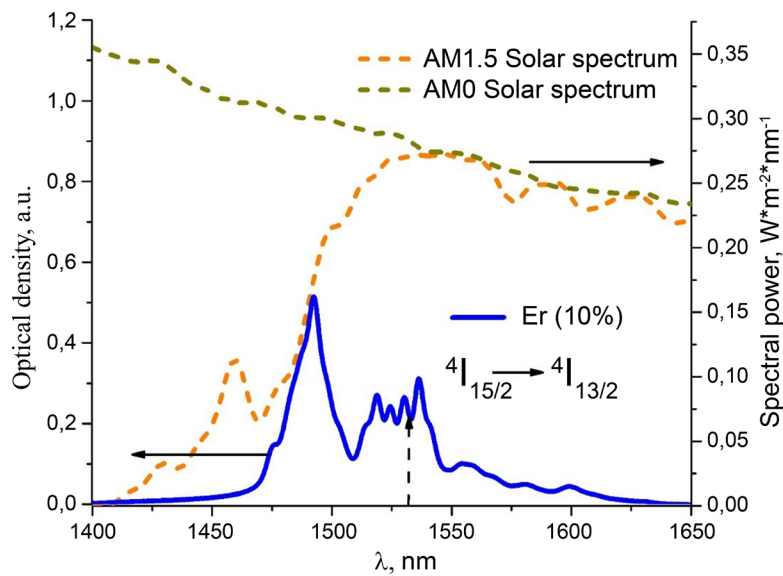
Fig. 2. Absorption spectrum of the BaY$_{1.8}$Lu$_{0.2}$F$_8$:Er^{3+} (10 at%) crystal for the $^4I_{15/2} \rightarrow ^4I_{13/2}$ transition of Er^{3+} ions and the spectrum of solar radiation above the atmosphere (AM0) and on the earth's surface (AM1.5)
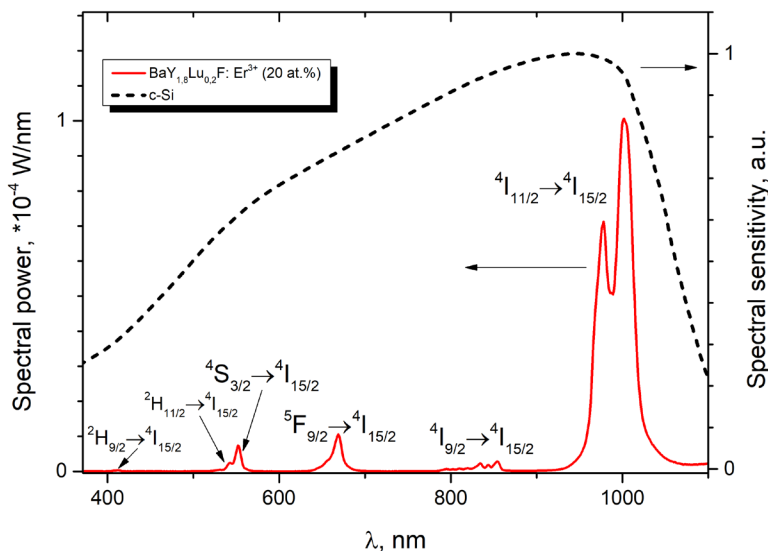
Fig. 3. Upconversion luminescence spectra of BaY$_{1.8}$Lu$_{0.2}$F$_8$:Er (20 at.%) crystals and spectral sensitivity of crystalline silicon

Condensed Matter and Interphases / Конденсированные среды и межфазные границы   2022;24(3): 387–396

A. S. Nizamutdinov et al.   Up-conversion luminescence in mixed crystals BaY$_{1.8}$Lu$_{0.2}$F$_8$ doped with Er^{3+} ions...
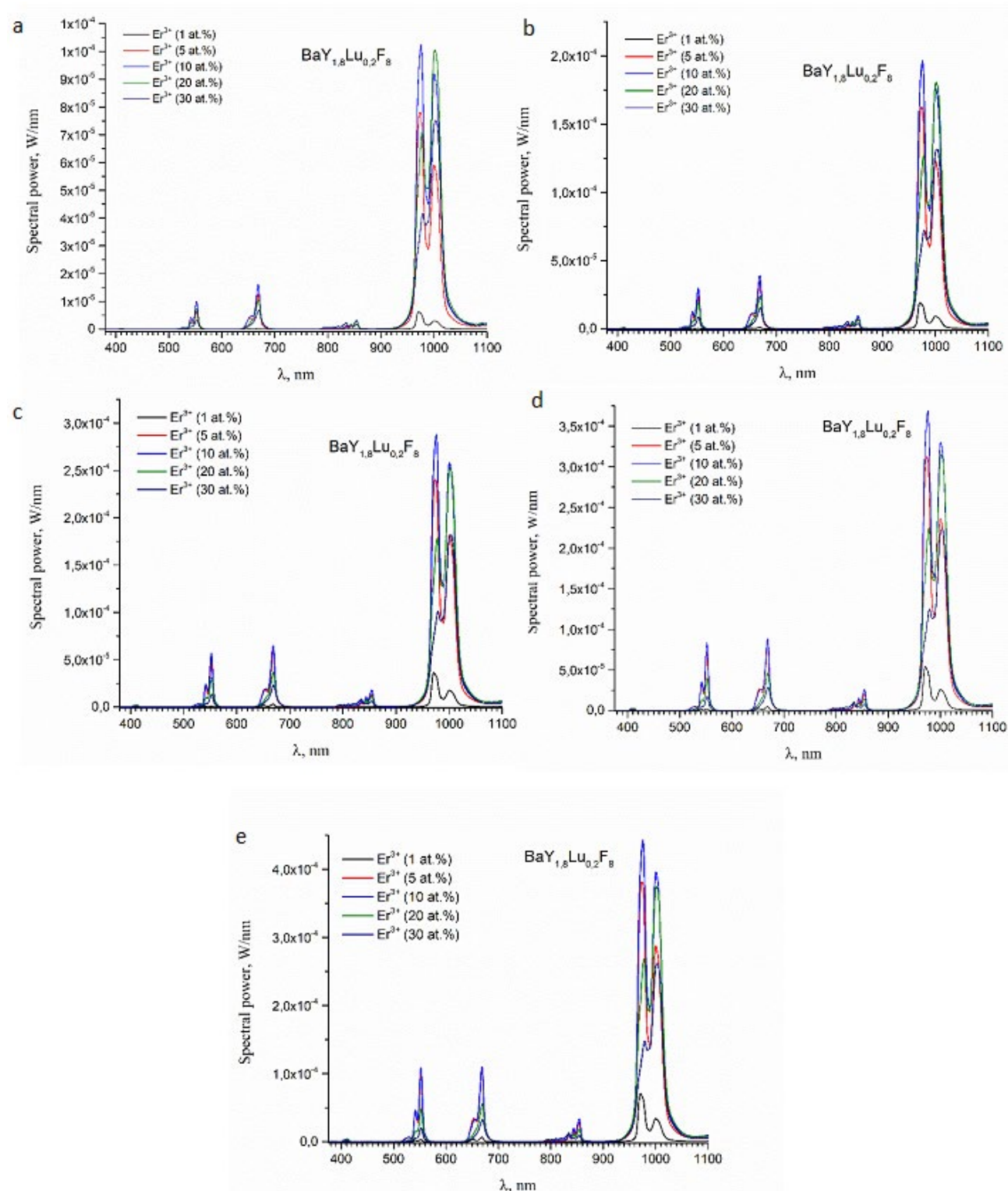
Fig. 4. Dependence of the intensity of the up-conversion luminescence of BaY$_{1.8}$Lu$_{0.2}$F$_8$:Er^{3+} crystals on the laser excitation power density: a) 6 W/cm^2, b) 12.7 W/cm^2, c) 19 W/cm^2, d) 25.5 W/cm^2, e) 32 W/cm^2

Condensed Matter and Interphases / Конденсированные среды и межфазные границы   2022;24(3): 387–396

A. S. Nizamutdinov et al.   Up-conversion luminescence in mixed crystals BaY$_{1.8}$Lu$_{0.2}$F$_8$ doped with Er^{3+} ions...

the investigated range from 6 W/cm^2 to 32 W/cm^2 which are discussed further.

The highest luminescence intensity for all electronic transitions of Er^{3+} ions in the range of 300–1100 nm is observed for the sample with a concentration of 10 at.% of Er^{3+} ions. The intensity of the up-conversion luminescence of Er^{3+} ions increases with increasing concentration up to 10 at.%, then concentration quenching is observed for samples with a concentration of 20 at.% and 30 at.%. This concentration dependence was observed for all values of the excitation power density.

The CCT and chromaticity coordinates of the radiation of up-conversion phosphors
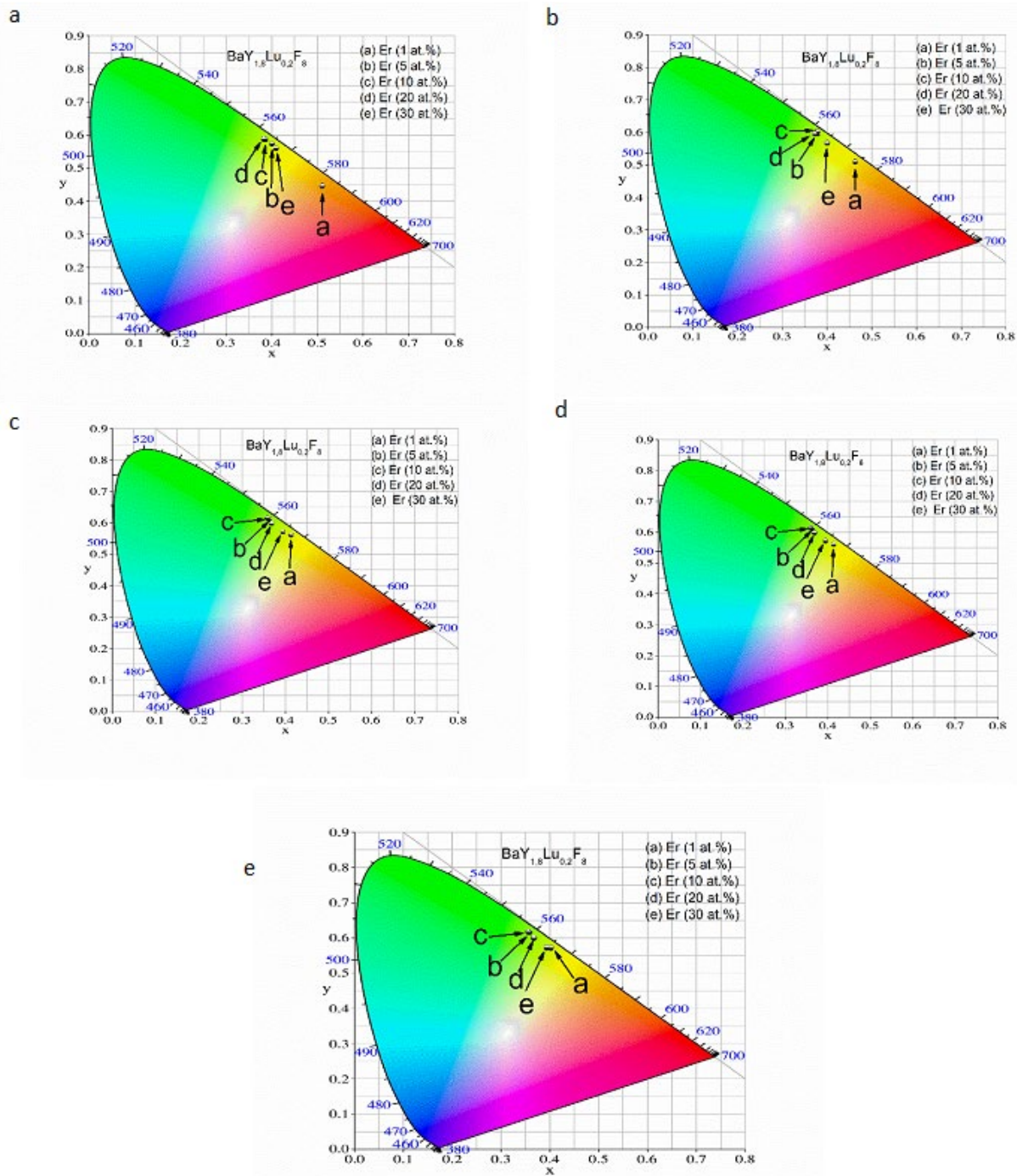
Fig. 5. Chromatic diagram of upconversion luminescence for BaY$_{1.8}$Lu$_{0.2}$F$_8$:Er crystals when excited by laser radiation with a wavelength of 1532 nm and a power density of 6 W/cm^2 (a), 12.7 W /cm^2 (b), 19 W/cm^2 (c), 25.5 W/cm^2 (d), and 32 W/cm^2 (e)

Condensed Matter and Interphases / Конденсированные среды и межфазные границы   2022;24(3): 387–396

A. S. Nizamutdinov et al.   Up-conversion luminescence in mixed crystals BaY$_{1.8}$Lu$_{0.2}$F$_8$ doped with Er^{3+} ions...

BaY$_{1.8}$Lu$_{0.2}$F$_8$:Er^{3+} were studied. Fig. 5 shows location at the chromatic diagram for the up-conversion luminescence of the studied crystals upon excitation by laser radiation with a power density of 6 W/cm², 12.7 W/cm², 19 W/cm², 25.5 W/cm², and 32 W/cm². The values of CCT and chromaticity temperatures are presented in Table 1.

The CCT and the chromaticity coordinates of the emission of fluoride phosphors depend on the excitation power density and the concentration of rare earth ions. For the BaY$_{1.8}$Lu$_{0.2}$F$_8$:Er^{3+} (20 at.%) sample, green-yellow emission is observed with a CCT of 4767-5002 K at an excitation power density of 6–32 W/cm². As the excitation power density increases, the CCT also increases.

Table 1. CCT values, chromaticity coordinates, internal and external energy yield of up-conversion luminescence in BaY$_{1.8}$Lu$_{0.2}$F$_8$: Er crystals

	BaY$_{1.8}$Lu$_{0.2}$F$_8$: Er (1 %)	BaY$_{1.8}$Lu$_{0.2}$F$_8$: Er (5 %)	BaY$_{1.8}$Lu$_{0.2}$F$_8$: Er (10 %)	BaY$_{1.8}$Lu$_{0.2}$F$_8$: Er (20 %)	BaY$_{1.8}$Lu$_{0.2}$F$_8$: Er (30 %)
Internal B$_{en}$ (6 W/cm²), %	2.3	17.8	20.4	10.7	6.9
Internal B$_{en}$ (12.7 W/cm²), %	3.2	19.4	19.0	9.9	6.2
Internal B$_{en}$ (19 W/cm²), %	4.5	20.5	19.5	9.3	5.7
Internal B$_{en}$ (25.5 W/cm²), %	5.1	20.2	19,0	8.9	5.4
Internal B$_{en}$ (32 W/cm²), %	5.6	18.7	18.3	8.6	5.1
External B$_{en}$ (6 W/cm²), %	0.4	6.4	9.4	9.0	6.5
External B$_{en}$ (12.7 W/cm²), %	0.6	6.9	9.3	8.3	5.8
External B$_{en}$ (19 W/cm²), %	0.7	7.1	9.3	7.8	5.4
External B$_{en}$ (25.5 W/cm²), %	0.8	7.1	9.1	7.4	5.1
External B$_{en}$ (32 W/cm²), %	0.9	7.0	8.9	7.1	4.8
CCT (6 W/cm2), K	2384	4469	4767	4704	4304
CCT (12.7 W/cm2), K	3339	4827	4943	4912	4453
CCT (19 W/cm2), K	3922	4992	5073	4959	4511
CCT (25.5 W/cm2), K	4249	5087	5141	4985	4553
CCT (32 W/cm2), K	4441	5149	5181	5002	4575
Chromaticity coordinates (6 W/cm2)	X= 0.5107 Y=0.4507	X=0.4010 Y=0.5786	X= 0.3866 Y=0.5918	X=0.3824 Y=0.5928	X=0.4096 Y=0.5644
Chromaticity coordinates (12.7 W/cm2)	X= 0.4630 Y=0.5136	X= 0.3792 Y=0.6006	X= 0.3718 Y=0.6070	X=0.3734 Y=0. 6003	X=0.4009 Y=0.5719
Chromaticity coordinates (19 W/cm2)	X= 0.4316 Y=0.5454	X= 0.3689 Y=0.6110	X= 0.3635 Y=0.6151	X=0.3704 Y=0.6030	X=0.3974 Y=0.5751
Chromaticity coordinates (25.5 W/cm²)	X= 0.4137 Y=0.5660	X= 0.3627 Y=0.6167	X= 0.3590 Y=0.6191	X=0.3686 Y=0.6033	X=0.3947 Y=0.5762
Chromaticity coordinates (32 W/cm²)	X= 0.4025 Y=0.5760	X= 0.3586 Y=0.6208	X= 0.3564 Y=0.6215	X=0.3676 Y=0.6042	X=0.3934 Y=0.5774

Condensed Matter and Interphases / Конденсированные среды и межфазные границы   2022;24(3): 387–396

A. S. Nizamutdinov et al.   Up-conversion luminescence in mixed crystals BaY$_{1.8}$Lu$_{0.2}$F$_8$ doped with Er^{3+} ions...

With an increase in the concentration of Er^{3+} ions from 1 at.% to 30 at.%, the CCT to a concentration of 10 at.% increases in the range of 2384–4767 K, and then decreases again to 4304 K at an excitation power density of 6 W/cm^2. The observed character of the increase in CCT with an increase in the concentration of Er^{3+} ions manifests itself for all studied excitation power densities. The dependence of CCT on the concentration of rare earth ions and the excitation power density is presented in Table 1.

3.2. Energy yield of upconversion luminescence of BaY$_{1.8}$Lu$_{0.2}$F$_8$:Er^{3+}

Internal and external energy yield are important characteristics when evaluating the application of BaY$_{1.8}$Lu$_{0.2}$F$_8$:Er crystalline compounds in photovoltaics to increase the efficiency of solar cells and protect securities. The internal energy yield of up-conversion luminescence in the range of 400–1100 nm was determined as the ratio of the radiation power to the absorbed excitation power for crystals with an Er^{3+} ion concentration of 1 at.%, 5 at.%, 10 at.%, 20 at.% and 30 at.% respectively. It can be seen that the maximum yield value corresponds to the sample with a concentration of 10 at.% Er^{3+} ions. The value of the internal energy output when excited by other power densities is presented in Table 1.

The maximum value of the external energy yield of the up-conversion luminescence was 9.4% at an excitation power density of 6 W/cm^2 for the BaY$_{1.8}$Lu$_{0.2}$F$_8$:Er^{3+} (10 at%) crystal which appears to be higher than that for BaY$_2$F$_8$:Er result from literature [15] and at the level of Yb^{3+} codoped luminophore BaF$_2$:Er,Yb [10].

4. Conclusions

In this work, we studied the upconversion luminescence characteristics of the concentration series of BaY$_{1.8}$Lu$_{0.2}$F$_8$:Er^{3+} crystals grown by the Bridgman method. The studied crystals showed intense up-conversion luminescence upon excitation of Er^{3+} ions to the ^{4}I$_{13/2}$ level by laser radiation with a wavelength of 1532 nm. The luminescence spectra consisted of electronic transitions ^{2}H$_{9/2}$→^{4}I$_{15/2}$, ^{2}H$_{11/2}$→^{4}I$_{15/2}$, ^{4}S$_{3/2}$→^{4}I$_{15/2}$, ^{4}F$_{9/2}$→^{4}I$_{15/2}$, ^{4}I$_{9/2}$→^{4}I$_{15/2}$, ^{4}I$_{11/2}$→^{4}I$_{15/2}$ Er^{3+} ions.

The maximum value of the external energy yield of the up-conversion luminescence was 9.4% at an excitation power density of 6 W/cm^2 for the BaY$_{1.8}$Lu$_{0.2}$F$_8$:Er^{3+} (10 at.%) crystal which appeared to be of optimal chemical composition. The maximum value of the internal energy yield of the up-conversion luminescence was 20.4% at an excitation power density of 6 W/cm^2 for the BaY$_{1.8}$Lu$_{0.2}$F$_8$:Er^{3+}(10 at.%) crystal.

Also the investigated crystals of BaY$_{1.8}$Lu$_{0.2}$F$_8$:Er^{3+} allow the control of the up-conversion luminescence spectra shape. By changing the concentration and power density of the excitation, it was possible to obtain up-conversion radiation with CCT in the range of 2384–5149 K.

Advantages revealed in this work for crystalline compounds BaY$_{1.8}$Lu$_{0.2}$F$_8$:Er^{3+} such as wide absorption bands in the infrared spectral range, a high external energy yield, and a controllable distribution of intensity of luminescence bands makes them prospective to improve the efficiency of double-sided solar cells.

Contribution of the authors

The authors contributed equally to this article

Conflict of interests

The authors declare that they have no known competing financial interests or personal relationships that could have influenced the work reported in this paper.

References

1. Lüthi S. R., Pollnau M., Güdel H. U., Hehlen M. P. Near-infrared to visible upconversion in Er^{3+}-doped Cs$_3$Lu$_2$Cl$_9$, Cs$_3$Lu$_2$Br$_9$, and Cs$_3$Y$_2$I$_9$ excited at 1.54 µm. *Physical Review B.* 1999;60(1): 162–178. https://doi.org/10.1103/PhysRevB.60.162

2. Wang Y., Ohwaki J. New transparent vitroceramics codoped with Er^{3+} and Yb^{3+} for efficient frequency upconversion. *Applied Physics Letters.* 1993;63(24): 3268–3270. https://doi.org/10.1063/1.110170

3. Alexandrov A. A., Mayakova M. N., Voronov V. V., Pominova D. V., Kuznetsov S. V., Baranchikov A. E., Ivanov V. K., Fedorov P. P. Synthesis of upconversion luminophores based on calcium fluoride. *Condensed Matter and Interphases.* 2020;22(1): 3–10. https://doi.org/10.17308/kcmf.2020.22/2524

4. Singh R., Madirov E., Busko D., Hossain I. M., Konyushkin V. A., Nakladov A. N., Kuznetsov S. V., Farooq A., Gharibzadeh S., Paetzold U. W.,

Condensed Matter and Interphases / Конденсированные среды и межфазные границы   2022;24(3): 387–396

A. S. Nizamutdinov et al.   Up-conversion luminescence in mixed crystals BaY$_{1.8}$Lu$_{0.2}$F$_8$ doped with Er^{3+} ions...

Richards B. S., Turshatov A. Harvesting sub-bandgap photons via upconversion for perovskite solar cells. *ACS Applied Materials and Interfaces*. 2021;13(46): 54874–54883. https://doi.org/10.1021/acsami.1c13477

5. Van Den Hoven G. N., Snoeks E., Polman A. Upconversion in Er-implanted Al$_2$O$_3$ waveguides. *Journal of Applied Physics*. 1996;79(3): 1258–1266. https://doi.org/10.1063/1.361020

6. Lyapin A. A., Gushchin, S. V., Kuznetsov S. V., Ryabochkina P. A., Ermakov A. S., Proydakova V. Yu., Voronov V. V., Fedorov P. P., Artemov S. A., Yapryntsev A. D., Ivanov V. K. Infrared-to-visible upconversion luminescence in SrF$_2$:Er powders upon excitation of the ^{4}I$_{13/2}$ level. *Optical Materials Express*. 2018;8(7): 1863–1869. https://doi.org/10.1364/OME.8.001863

7. Rubin J., Brenier A., Moncorge R., Pedrini C. Excited-state absorbtion and energy transfer in Er^{3+}-doped LiYF$_4$. *Journal of Luminescence*. 1986;36(1): 39—47. https://doi.org/10.1016/0022-2313(86)90029-3

8. Brede R., Heumann E., Koetke J, Danger T., Huber G., Chai B. Green up-conversion laser emission in Er-doped crystals at room temperature. *Applied Physics Letters*. 1993;63(15): 2030–2031. https://doi.org/10.1063/1.110581

9. Kaiser M., Würth C., Kraft M., Hyppänen I., Soukka T., Resch-Genger U. Power-dependent upconversion quantum yield of NaYF$_4$:Yb^{3+},Er^{3+} nano- and micrometer-sized particles-measurements and simulations. *Nanoscale*. 2017;9(28): 10051–10058. https://doi.org/10.1039/c7nr02449e

10. Madirov E. I., Konyushkin V. A., Nakladov A. N., Fedorov P. P., Bergfeldt T., Busko D., Howard I. A., Richards B. S., Kuznetsov S. V., Turshatov A. An up-conversion luminophore with high quantum yield and brightness based on BaF$_2$:Yb^{3+},Er^{3+} single crystals. *Journal of Materials Chemistry C*. 2021;9(10): 3493–3503. https://doi.org/10.1039/d1tc00104c

11. Liu Y., Zhou Z., Zhang S., Zhao E., Ren J., Liu L., Zhang J. Mechanisms of upconversion luminescence of Er^{3+}-doped NaYF$_4$ via 980 and 1530 nm excitation. *Nanomaterials*. 2021;11(10): 2767. https://doi.org/10.3390/nano11102767

12. Ivanova S., Pellé F. Strong 1.53 um to NIR–VIS–UV upconversion in Er-doped fluoride glass for high-efficiency solar cells. *Journal of the Optical Society of America B*. 2009;26(10): 1930–1937. https://doi.org/10.1364/JOSAB.26.001930

13. Shalav A., Richards B. S., Trupke T. Application of NaYF$_4$:Er^{3+} up-converting phosphors for enhanced near-infrared silicon solar cell response. *Applied Physics Letters*. 2005;86(1): 013505-1–013505-3. https://doi.org/10.1063/1.1844592

14. Ivaturi A., MacDougall, Sean K. W., Martín-Rodríguez R., Quintanilla M., Marques-Hueso J., Krämer, Karl W., Meijerink A., Richards, Bryce S. Optimizing infrared to near infrared upconversion quantum yield of β-NaYF$_4$:Er^{3+} in fluoropolymer matrix for photovoltaic devices. *Journal of Applied Physics*. 2013;114(1): 013505. https://doi.org/10.1063/1.4812578

15. Boccolini A., Faoro R., Favilla E., Veronesi S., Tonelli M. BaY$_2$F$_8$ doped with Er^{3+}: An upconverter material for photovoltaic application. *Journal of Applied Physics*. 2013;114(6): 064904. https://doi.org/10.1063/1.4817171

16. Kaminskii A. A., Sobolev B. P., Sarkisov S. E., Denisenko G. A., Ryabchenkov V. V., Fedorov V. A., Uvarova T. V. Physicochemical aspects of the synthesis of BaLn$_2$F$_8$-Ln^{3+} single crystals. Spectroscopy and stimulated emission of these crystals. *Izv. Akad. Nauk SSSR, Neorg. Mater*. 1982;18(3): 482–497. (In Russ.)

Information about the authors

Alexey S. Nizamutdinov, Cand. Sci. (Phys.–Math.), Senior Researcher, Associate Professor, Kazan Federal University (Kazan, Russian Federation).

https://orcid.org/0000-0003-1559-6671
anizamutdinov@mail.ru

Sergey V. Gushchin, postgraduate student, National Research Mordovia State University (Saransk, Russian Federation).

https://orcid.org/0000-0003-1680-337X
serg.guschin1703@gmail.com

Sergey A. Bukarev, postgraduate student, National Research Mordovia State University (Saransk, Russian Federation).

https://orcid.org/0000-0003-2781-5974
bukarevsa@yandex.ru

Alexey A. Shavelev, Junior Researcher, Kazan Federal University (Kazan, Russian Federation).

https://orcid.org/0000-0001-5700-6989
alexey.shavelev@gmail.com

Mikhail A. Marisov, Cand. Sci. (Phys.–Math.), Senior Researcher, Kazan Physical-Technical Institute, Kazan Federal University (Kazan, Russian Federation).

https://orcid.org/0000-0001-8425-7046
m.a.marisov@gmail.com

Ainur A. Shakirov, Junior Researcher, Kazan Federal University (Kazan, Russian Federation).

https://orcid.org/0000-0002-6140-3714
shakirov_1995@mail.ru

Airat G. Kiiamov, Cand. Sci. (Phys.–Math.), Senior Researcher, Kazan Federal University (Kazan, Russian Federation).

https://orcid.org/0000-0001-5376-7000
airatphd@gmail.com

Condensed Matter and Interphases / Конденсированные среды и межфазные границы   2022;24(3): 387–396

A. S. Nizamutdinov et al.   Up-conversion luminescence in mixed crystals BaY$_{1.8}$Lu$_{0.2}$F$_8$ doped with Er^{3+} ions...

Anna V. Astrakhantseva, Laboratory Assistant, Kazan Federal University (Kazan, Russian Federation)/
https://orcid.org/0000-0002-1670-3064
anya4324@gmail.com

Andrey A. Lyapin, Cand. Sci. (Phys.–Math.), Associate Professor, National Research Mordovia State University (Saransk, Russian Federation).
https://orcid.org/0000-0002-6963-9801
andrei_lyapin@mail.ru